Improved determination of the β-$\overline{\nu}_e$ angular correlation coefficient a in free neutron decay using the aSPECT experiment

Dissertation zur Erlangung des Grades

„Doktor der Naturwissenschaften“

am Fachbereich Physik, Mathematik und Informatik
der Johannes Gutenberg-Universität in Mainz

vorgelegt von

Christian Schmidt

geboren in Mainz

Mainz, den 27. Mai 2019

Abstract

The "Standard Model of particle physics" (SM) successfully explains an enormous number of experimental results and a wide variety of phenomena. Despite its great success the SM is incomplete. For example, it doesn't include the gravitational force and the baryon-asymmetry in our universe (matter over antimatter) is still an unsolved puzzle.

An unique opportunity to investigate the SM is the weak decay of the free neutron, $n \to pe\overline{\nu}_e + 782.3\,\mathrm{keV}$. This is described as purely left-handed, vector-axialvector ($V-A$) interaction within the framework of the SM. The low decay energy and the absence of nuclear structure allows for an excellent theoretical interpretation. Information gained by high precision measurements of observables in free neutron decay can be used to test for physics beyond the SM, e.g., to search for tensor (T) and scalar (S) interactions. In example, the measurement of different angular correlation coefficients allows for the determination of the ratio of the weak coupling constants, $\lambda = g_A/g_V$, which allows sensitive checks of the model's validity and limits.

The *a*SPECT experiment is a retardation spectrometer built to measure the proton energy spectrum in free neutron β-decay. From the shape of the spectrum, the β-$\overline{\nu}_e$ angular correlation coefficient a can be derived and thus $\lambda(a)$. In 2013, *a*SPECT had a successful beam time at the Institut Laue-Langevin, Grenoble (France). Different parameter settings of the spectrometer helped to trace instrumental systematics. Supportive follow-up measurements were conducted, e.g. to determine the spatial and temporal work function fluctuations of the electrodes, which is a source of one of the main systematic errors. These measurements were used as input for electromagnetic field computations and particle tracking simulations for a correction of systematics. The data of the runs in the individual configurations were combined and analysed using a multi-dimensional fit with a as free fit parameter.

This thesis gives a full representation of the almost completed analysis serving as draft for the final publication. Special focus is given on the systematic effects that could only be quantified by sophisticated electromagnetic field and particle tracking simulations. With this thesis, the *a*SPECT experiment, after 19 years of its proposal, comes to an end and can report on an improved determination of the angular correlation coefficient a:

$$a = -0.10476(85)\,.$$

This corresponds to $\frac{\Delta a}{a} \approx 0.8\,\%$, which is an improvement of a factor of 3.3 in comparison to the recent PDG 2018 average. Since one of the systematics has to be reviewed, this result is *preliminary*, but no significant change is expected.

Contents

List of Figures

List of Tables

1. Introduction

The understanding of our nature made enormous progress in the 20$^{\text{th}}$ century. The view on our laws of nature changed dramatically with the discovery of quantum mechanics, special and general relativity in the early 20$^{\text{th}}$. These breakthroughs finally paved the way to the development of the "Standard Model of particle physics" (SM). This theory of elementary particles and fields describes the weak, the electromagnetic, and strong interaction between six leptons and six quarks mediated by bosons.

Although the SM explains successfully an enormous body of experimental data it does have limitations. Although persistent attempts were made over many years it still doesn't incorporate general relativity. Further deficiencies are, e.g., the strong *CP* problem, the baryon asymmetry in our universe, or the origin of dark matter and energy. Therefore the question for physics beyond the SM arises, which is addressed by developing extensions of the SM, e.g., SUSY (supersymmetry) or novel explanations like string theory.

The neutron provides an excellent laboratory for probing the SM, since it experiences all four fundamental forces. The information gained by high-precision measurements with free neutrons can also be used to test for physics beyond the SM and are complementary to results in high energy experiments. The cosmological matter-antimatter symmetry, e.g., could be accounted for, if an electric dipole moment of the neutron (nEDM) would be found.

A free neutron is unstable. The low energetic β-decay of the free neutron n is the prototype semileptonic weak interaction:

$$n \rightarrow p + e^- + \overline{\nu}_e + 782.3\,\text{keV} \tag{1.1}$$

It decays weakly into a proton p, an electron e, and an electron-antineutrino $\overline{\nu}_e$ with a lifetime of about 15 min and a decay energy of about 782.3 keV. In the SM this process is described on the quark level, where a u quark of the proton (uud) decays into a d quark, which results in a neutron (ddu), by exchange of a W^- boson, which decays into an electron e and an electron-antineutrino $\overline{\nu}_e$ (see Figure 1.1). The differential β-decay rate, when observing only the electron and neutrino momenta and the neutron spin, is given by

$$d^3\Gamma \propto G_{\text{F}}^2 V_{\text{ud}}^2 p_{\text{e}} E_{\text{e}} (E_0 - E_{\text{e}})^2 \left(1 + a\frac{\vec{p}_{\text{e}} \cdot \vec{p}_\nu}{E_{\text{e}} E_\nu} + b\frac{m}{E_{\text{e}}} + \vec{\sigma}_{\text{n}} \cdot \left(A\frac{\vec{p}_{\text{e}}}{E_{\text{e}}} + B\frac{\vec{p}_\nu}{E_\nu}\right)\right) dE_{\text{e}} d\Omega_{\text{e}} d\Omega_\nu \tag{1.2}$$

with $\vec{p}_{\text{e}}$, $\vec{p}_\nu$, E_{e}, E_ν being the momenta and energies of the electron e and the electron-antineutrino $\overline{\nu}_{\text{e}}$, m the mass of the electron, G_{F} the Fermi constant, V_{ud} the first element of

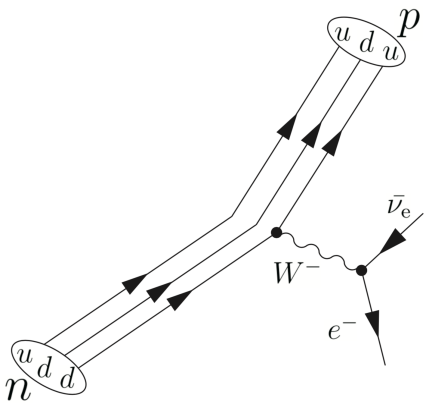

Figure 1.1.: Neutron decay in the standard model. A neutron (udd) decays in to a proton (duu), an electron e and an antineutrino $\overline{\nu}_e$ by a quark transformation $d \to u$ mediated by the exchange of a W^- boson.

the Cabibbo-Kobayashi-Maskawa (CKM) matrix, E_0 the decay energy and $\vec{\sigma}_\mathrm{n}$ the spin of the neutron. The decay rate provides several observables: The electron-antineutrino correlation coefficient a, the Fierz interference term b, the spin-electron correlation coefficient A (known as the β-asymmetry), and the spin-antineutrino correlation coefficient B. In the SM, the weak decay is described by a purely left-handed interaction, the $V-A$ theory. Within this, the angular correlation coefficients a, A, and B only depend on λ, the ratio of the weak axial-vector and vector coupling constants g_A and g_V, as follows:

$$a = \frac{1-|\lambda|^2}{1+3|\lambda|^2} \qquad A = -2\frac{|\lambda|^2+\lambda}{1+3|\lambda|^2} \qquad B = 2\frac{|\lambda|^2-\lambda}{1+3|\lambda|^2} \quad \text{with } \lambda = \frac{g_A}{g_V} \tag{1.3}$$

The comparison of λ values obtained from independent measurements of the angular correlation coefficients provides a test of the $V-A$ theory. In a purely left-handed symmetry the Fierz interference term should be $b = 0$ and can be investigated for an upper limit. The value of weak coupling constants is important in several fields: Cosmology, where it affects the production of light elements in the primordial nucleosynthesis, or particle physics, where it is used for neutrino detector calibration.

An independent measurement of the neutron lifetime τ_n in combination with λ allows for the determination of the element V_ud of the CKM matrix, since they are related as follows:

$$|V_\mathrm{ud}|^2 = \frac{(4908.6 \pm 1.9)\,\mathrm{s}}{\tau_n\left(1+3|\lambda|^2\right)}, \tag{1.4}$$

which is used for the important test of the unitarity of the first row of the CKM matrix:

$$|V_\mathrm{ud}|^2 + |V_\mathrm{us}|^2 + |V_\mathrm{ub}|^2 = 1\,. \tag{1.5}$$

A deviation from the unitarity would be a clear sign of physics beyond the SM (BSM), e.g., an additional quark generation. Since Equation (1.5) is mainly determined by V_{ud} and thus τ_n, a precise knowledge of the neutron lifetime is necessary. Currently, τ_n shows significant discrepancy ($\sim 4\sigma \approx 8\,\mathrm{s}$) between two types of experiments ("beam" and "bottle" measurements). Bottle experiments measure the number of neutrons remaining after a defined storing time, while in beam experiments the activity of the neutron beam and the decay products are measured simultaneously. The simplest explanation for the discrepancy would be an underestimation of systematic effects. Another possibility is a "dark" decay channel, which would not be observed in beam experiments leading to a shorter lifetime $\tau_{n,\mathrm{beam}} < \tau_{n,\mathrm{bottle}}$, which is the actual experimental finding. Then, the lifetime from bottle experiments would provide the correct value [GLG16, WG11, SVK$^+$05].

The *a*SPECT experiment ("*a*" spectrometer) had been constructed to measure a with a precision of $\Delta a/a \approx 0.3\%$ contributing to a determination of $\lambda(a)$ with $\Delta\lambda/\lambda \approx 0.08\%$. Since it is difficult to measure the angular distribution between the electron and the neutrino, a is inferred from the shape of the proton recoil spectrum. *a*SPECT measures the integral proton spectrum by means of magnetic adiabatic collimation with an electrostatic filter (MAC-E filter). Basically this means to measure a count rate against a retardation voltage. Thus, especially all retardation voltage dependent systematic effects directly influence the shape of the spectrum and therefore the observed value of a. This is the fundamental problem of high precision experiments like *a*SPECT. All systematics effects have to be determined quantitatively at a level that does not limit your result.

Now, 19 years after the proposal of the *a*SPECT experiment, the collaboration can report on a successful measurement of a with a precision of $\Delta a/a \approx 0.8\,\%$, which is an improvement by a factor of 3.3 in comparison to the latest, independent measurement of a. This value is derived from the data taken during the last beam time in summer 2013 at the Institut Laue-Langevin (Grenoble, France).

At the beginning of 2013 I started my doctoral thesis at the Johannes Gutenberg-Universtität Mainz under supervision of Prof. Dr. Werner Heil as part of the *a*SPECT collaboration. My Mainz colleagues, postdoc Dr. Marcus Beck and doctoral student Alexander Wunderle, who graduated in February 2017, and I improved several parts of the experiment based on knowledge basically gained from a failed beam time in 2011 and an off-line measurement in 2012. Finally, this led to the successful 2013 beam time with about 100 days of raw data taking, which I accompanied.

The essential part of my thesis was the investigation and quantitative determination of the following systematic effects: Magnetic field ratio $\langle r_{\mathrm{B}} \rangle$ (see Section 3.4.2), Retardation voltage $\langle U_{\mathrm{A}} \rangle$ (see Section 3.4.3), Edge effect (see Section 3.4.6), and Proton traps in the DV region (see Section 3.4.9). These effects could only be determined by sophisticated electromagnetic field and particle tracking simulations. I started from scratch with the implementation of a computational model of *a*SPECT. After validation, I conducted the tracking simulations and their analysis. Details are explained and discussed in the extensive, more technical Appendix C.

To obtain precise results from these simulations also supportive measurements were performed as part of my thesis: (i) A precision NMR measurement of the *a*SPECT magnetic field (see Section 3.4.2) and (ii) a thorough investigation of the spatial and temporal work function fluctuations of the electrodes defining the electric potential in the decay volume and the analysing plane (see Appendix A). The findings were implemented as part of the simulation.

Finally, I worked on the extraction of a by means of a global fit respecting all systematics (see Section 3.5). This included the assembly and final review of all systematic effects and experimental findings from supplementary measurements and investigations.

In parallel to the entire process of analysis, a draft of the final publication was prepared to be published in Physical Review C in summer 2019. This evolved simultaneously with the state of the analysis and was expanded and improved continuously, whereby I contributed essentially. As already mentioned, a majority of the systematic effects could only be quantified after the completion of the particle tracking simulation runs and their analysis. In this thesis I will present the *almost* final publication. For the final version the systematic effect "Proton backscattering" (see Section 3.4.7) is reviewed at present. This will be completed until the beginning of June 2019. According to the current knowledge, it is not expected that the preliminary angular correlation coefficient a to be presented in this thesis will differ significantly from the final result. Insofar, this thesis presents the expected final result of the *a*SPECT experiment, whereby, after 19 years of its proposal, it comes to a happy ending.

This thesis is organised as follows: Chapter 2 starts with a historical introduction into neutron β-decay and reviews previous and competing measurements. Chapter 3 presents the "Improved determ ination of the $\beta - \bar{\nu}_e$ angular correlation coefficient a in free neutron decay using the *a*SPECT experiment", which is the latest status of the publication. Thus, it gives a full review of the experiment, starting with an introduction, a description of the experiment and the measurement procedure, the discussion of the systematic effects, and finally the preliminary result and a conclusion. As Chapter 3 is written in publication writing style, there are several appendices giving a deeper insight in "Work function measurements using a Kelvin probe" (see Appendix A), "Proton recoil spectrum in case of finite n polarisation" (see Appendix B), and the "Electromagnetic field and particle tracking simulations" (see Appendix C).

2. Neutron β-decay

The *a*SPECT experiment measured the electron-antineutrino correlation coefficient a to so far unprecedented precision. In order to understand the implications on the SM a brief introduction into the theory of nuclear β-decay is given. First, a historical introduction to Fermi's and the $V-A$ theory is given, as well as the current description in the SM. The correlation between the measurable observables in free neutron β-decay will be discussed with special emphasis on the correlation coefficient a and the proton energy spectrum. Finally, recent and upcoming competing measurements will be presented.

2.1. Theory of neutron β-decay

2.1.1. Fermi's theory

Enrico Fermi was the first trying to work out a theoretical description of "β-radiation" in the thirties of the last century [Fer34]. Therefore, he used a description in analogy to the quantum theory of electromagnetic interaction. The corresponding Feynman graphs are shown in Figure 2.1. The Hamiltonian describing the electron-photon interaction (Figure 2.1a) is given as follows:

$$\mathscr{H} = e j_{\mu}^{\mathrm{em}} A^{\mu} \,. \tag{2.1}$$

Here, e is the electron charge representing the strength of the coupling, $j_{\mu}^{\mathrm{em}} = \overline{\Psi}_e \gamma_\mu \Psi_e$ is the electromagnetic current density, and A^{μ} is the 4-vector potential of the electromagnetic field. In general the Ψ's are 4-component Dirac spinors, in this case specifically the electron spinor

(a) Basic electron-photon vertex

(b) Point-like interaction of neutron β-decay

Figure 2.1.: Analogous Feynman graphs based on Fermi's first attempt of a description of β-decay.

field function Ψ_e and its adjoint function $\overline{\Psi}_e$. Following the *Bjorken and Drell* convention [BD64] the Dirac matrices $\gamma^\mu = (\gamma^0, \gamma^1, \gamma^2, \gamma^3)$ are given by:

$$\gamma^0 = \begin{pmatrix} \mathbf{1} & 0 \\ 0 & \mathbf{-1} \end{pmatrix}, \quad \gamma^k = \begin{pmatrix} 0 & \sigma^k \\ -\sigma^k & 0 \end{pmatrix} \text{ for } k = 1,2,3\,, \quad \gamma^5 = i\gamma^0\gamma^1\gamma^2\gamma^3, \tag{2.2}$$

where σ^k the Pauli matrices.

To describe the point-like interaction of the neutron decay in analogy to the electromagnetic interaction Fermi introduces several replacements:

$$A^\mu \rightarrow J_\mu^{\text{lep}} = \overline{\Psi}_e \gamma_\mu \Psi_{\bar{\nu}_e}, \tag{2.3}$$

$$j_\mu^{\text{em}} \rightarrow J_\mu^{\text{had}} = \overline{\Psi}_p \gamma_\mu \Psi_n, \tag{2.4}$$

$$e \rightarrow \frac{G_\text{F}}{\sqrt{2}} \tag{2.5}$$

The 4-vector potential is replaced by a leptonic electron-neutrino current J_μ^{lep}, the electromagnetic current by a hadronic current J_μ^{had}, and the electromagnetic coupling constant by the Fermi coupling constant $\frac{G_\text{F}}{\sqrt{2}}$[1]. Applying these transformation to Equation (2.1) gives the new Hamiltonian density:

$$\mathscr{H} = \frac{G_\text{F}}{\sqrt{2}} J_\mu^\dagger J^\mu + \text{h.c.}, \tag{2.6}$$

where J^μ comprises a hadronic and a leptonic contribution:

$$J_\mu = J_\mu^{\text{had}} + J_\mu^{\text{lep}}. \tag{2.7}$$

In first order, Fermi's theory gives a reasonable description for a broad range of weak interaction processes, but, as he already assumed, there must be a more general form of the Hamiltonian, which includes other possible Lorentz invariants than only the vector (V) interaction.

Selection rules

β-transitions are classified in *allowed* and *forbidden* decay modes. If the electron and neutrino do not carry orbital angular momentum away, the transition is *allowed*. Their selection rules are [GT36]

$$\Delta J = J_i - J_f = 0, \pm 1, \tag{2.8}$$

$$\pi_i \pi_f = +1, \tag{2.9}$$

[1] $G_F/(\hbar c)^3 = 1.166\,378\,7(6) \times 10^{-5}\,\text{GeV}^{-2}$, determined from measurements in muon decay [TBC+13].

Table 2.1.: Current-current interactions constructed by Gamow and Teller.

operator	name	number of matrices
$\overline{\Psi}\Psi$	scalar (S)	1
$\overline{\Psi}\gamma_\mu\Psi$	vector (V)	4
$\overline{\Psi}\gamma_\mu\gamma^\nu\Psi$	tensor (T)	6
$\overline{\Psi}\gamma_5\Psi$	pseudo-scalar (P)	1
$\overline{\Psi}\gamma_5\gamma_\mu\Psi$	axial-vector (A)	4

where $J_{i/f}$ and $\pi_{i/f}$ designate the spin and parity of the initial i and final f state. The pair of leptons can couple to a total spin $S=0$ (singlet state) and $S=1$ (triplet state). For singlet states only $\Delta J=0$ is allowed (Fermi decay). These transitions are mediated by a vector component. For triplet states $\Delta J=0,\pm1$ (Gamow teller decay, $0\to0$ forbidden) are allowed. These are mediated by axial-vector components. In nature, pure Fermi decays, like $^{14}\mathrm{O}\to{}^{14}\mathrm{N}+e^+\nu_e$, and pure Gamow Teller decays, like $^6\mathrm{He}\to{}^6\mathrm{Li}+e^-+\overline{\nu}_e$, are observed. In general, most transitions are mixtures, like neutron decay.

2.1.2. $V-A$ theory

In 1956 Lee and Yang [LY56] introduced a Hamiltonian, which includes four new current-current interactions (S, T, P, A) in addition to the vector interaction (V). These five different types of operators can be constructed from the 4×4 γ-matrices satisfying relativistic invariance (Table 2.1). They are named according to their transformation properties under spatial reflection. Then, the most general Hamiltonian is

$$\mathscr{H}=\frac{G_\mathrm{W}}{\sqrt{2}}\sum_{i\in\{S,V,T,P,A\}}\left\{L_i\left(\overline{\Psi}_p\Gamma_i\Psi_n\right)\left(\overline{\Psi}_e\Gamma_i(1-\gamma_5)\Psi_{\bar{\nu}_e}\right)+R_i\left(\overline{\Psi}_p\Gamma_i\Psi_n\right)\left(\overline{\Psi}_e\Gamma_i(1+\gamma_5)\Psi_{\bar{\nu}_e}\right)\right\}+\mathrm{h.c.}, \tag{2.10}$$

where G_W is a general weak coupling constant and the operators Γ_i's the current-current interactions:

$$\Gamma_S=1,\quad \Gamma_V=\gamma_\mu,\quad \Gamma_T=-i\frac{\left[\gamma_\mu,\gamma_\nu\right]}{2\sqrt{2}},\quad \Gamma_P=\gamma_5,\quad \Gamma_A=-i\gamma_\mu\gamma_5\quad . \tag{2.11}$$

The Hamiltonian is separated into left-handed (L_i) and right-handed (R_i) couplings [2]. This parametrisation highlights the handedness of the antineutrino, where $(1-\gamma_5)\Psi_{\bar{\nu}_e}$ is the left-handed projection and $(1+\gamma_5)\Psi_{\bar{\nu}_e}$ the right-handed projection of the antineutrino wave function. The coupling constants L_i and R_i, defining the strength of the particular interaction i, can only be determined experimentally. If $L_i\neq R_i$ parity is violated.

[2] A particle is right-handed if the direction of the spin and momentum are the same, left-handed if they are not. This corresponds to helicity eigenstate $h=+1$ and $h=-1$, respectively.

In 1957 Wu and her collaborators discovered maximal parity violation in the β-decay of ^{60}Co [WAH+57]. In general, it could be shown that leptons and antileptons involved in weak decays have opposite longitudinal polaristion, i.e. helicities. This reduced the choice of operators in Equation (2.10) down to two − the V and A operators. In 1958 Goldhaber, Grodzins, and Sunyar could determine the helicity of the neutrino to be $h = -1$, i.e. left-handed [GGS58].

Based on the aforementioned experimental results Feynman and Gell-Mann proposed the $V-A$ form of the Hamiltonian [FGM58]:

$$\mathscr{H} = \frac{G_W}{\sqrt{2}} \sum_{i=V,A} L_i \left(\overline{\Psi}_p \Gamma_i \Psi_n\right) \cdot \left(\overline{\Psi}_e \Gamma_i (1-\gamma_5) \Psi_{\bar{\nu}_e}\right) + \text{h.c.} \tag{2.12}$$

$$= g_V \left(\overline{\Psi}_p \gamma_\mu (1+\lambda\gamma_5) \Psi_n\right) \cdot \left(\overline{\Psi}_e \gamma_\mu (1-\gamma_5) \Psi_{\bar{\nu}_e}\right) + \text{h.c.}, \tag{2.13}$$

where

$$g_V = \frac{G_\text{W}}{\sqrt{2}} L_V, \quad g_A = \frac{G_\text{W}}{\sqrt{2}} L_A, \quad \lambda = \frac{g_A}{g_V}. \tag{2.14}$$

The vector coupling constant g_V corresponds to Fermi decays and the axial-vector coupling constant g_A to Gamow-Teller decays. The coupling constant g_V is approximately 1 and can be measured in ^{14}O decay for example. Neutron β-decay is a "mixed" transition, that is, it implies both, Fermi and Gamow-Teller contributions.

2.2. CKM matrix

In the quark model nucleons are not fundamental particles, but composed of three quarks. In there, neutron β-decay is described by a quark transformation $d \to u$. Weak decays, where a strange quark transforms into an up quark, $s \to u$ have been also observed, e.g. $K^+ \to \mu^+ \nu$ or $\Sigma^- \to n e^- \overline{\nu}$. This led to the assumption of weak eigenstates, which are linear combinations of the mass eigenstates of the three quark generations [Cab63, KM73]. The correlation of the weak eigenstates to the mass eigenstates is done by the so-called CKM matrix (Cabibbo-Kobayashi-Maskawa):

$$\begin{pmatrix} |d'\rangle \\ |s'\rangle \\ |b'\rangle \end{pmatrix} = \begin{pmatrix} V_{ud} & V_{us} & V_{ub} \\ V_{cd} & V_{cs} & V_{cb} \\ V_{td} & V_{ts} & V_{tb} \end{pmatrix} \begin{pmatrix} |d\rangle \\ |s\rangle \\ |b\rangle \end{pmatrix}, \tag{2.15}$$

where the primes correspond to the weak eigenstates and the unprimed to the mass eigenstates of the quarks. The matrix is predicted to be unitary. Deviations from unitarity would predict physics beyond standard model, e.g. a further quark generation, and is therefore an important test [Dub91, SBNC06, Abe08]:

$$|V_{ud}|^2 + |V_{us}|^2 + |V_{ub}|^2 \stackrel{!}{=} 1, \tag{2.16}$$

where $|V_{qq'}|^2$ describes the transition probability from $|q\rangle$ to $|q'\rangle$. The matrix can also be expressed in terms of four parameters, three angles and a phase. As heavier quarks don't contribute in first order, a single mixing parameter is sufficient to describe β-decay:

$$\left|d'\right\rangle = V_{ud}\,|d\rangle \approx \cos\theta_C\,|d\rangle\,, \tag{2.17}$$

where θ_C is the Cabibbo angle.

With these findings the coupling constants have to depend on the matrix element $|V_{ud}|$, thus

$$G_V = g_V \cdot |V_{ud}|\,, \qquad G_A = g_A \cdot |V_{ud}|\,. \tag{2.18}$$

2.3. Electroweak interaction and the standard model

At this point, the $V-A$ theory provides an excellent phenomenological statement about the observed charged weak interactions within first-order perturbation theory. But it has big difficulties to overcome divergences encountered in higher order. This makes the theory, at this state, to be not renormalisable.

In the 1960s, Weinberg, Salam and Glashow proposed that the weak and electromagnetic interaction can be treated as different manifestation of the so-called *electroweak* interaction [Gla61, Sal68, Wei67]. With this new theory the renormalisation problem was solved and first steps towards the development of the standard model was done. The symmetry between electromagnetic and weak interaction holds for large momentum transfers of about $q^2 \gg 10^4\,\mathrm{GeV}$. At low energies, the symmetry is *broken*. Then, the four mediating vector bosons of the electroweak interaction appear as one massless boson, the photon γ, and the others as massive bosons, W^+, W^-, Z^0 ($m_{W^\pm} = 80.379(12)\,\mathrm{GeV}$ and $m_{Z^0} = 91.1876(21)\,\mathrm{GeV}$ [THH+18]). By means of an additional $I = 3/2$ doublet of complex fields called Higgs scalars, the bosons are given their mass by the process of *spontaneous symmetry breaking*. The heavy mass of these bosons also explain the short range of the weak interaction, while the range of the electromagnetic interaction is not limited.

The interaction via a boson-exchange process introduces a *boson propagator term* of the form

$$\frac{1}{q^2 + m^2}\,, \tag{2.19}$$

where m is the boson mass and q the 4-momentum transfer. If $q \ll m$ the propagator can be considered as constant, but for high q it falls. In case of low momentum transfer the range of the weak interaction is limited to $\lesssim 10^{-3}\,\mathrm{fm}$ due to the heavy boson masses, which can be deduced from the uncertainty principle. This explains, why the point-like interaction is a good approximation in low energy processes.

The four mediating bosons are arranged in a triplet and a singlet as members of multiplets of "weak isospin" I and "weak hypercharge" Y. The corresponding bosons of the triplet

$(I=1)$ are $W_\mu = W_\mu^{(1)}, W_\mu^{(2)}, W_\mu^{(3)}$ and the one of the singulet $(I=0)$ is B_μ. Mathematically, W_μ correspond to SU(2) and B_μ to U(1), which is why the unification is accomplished as $\mathrm{SU(2)} \times \mathrm{U(1)}$.

The physical, charged bosons W_μ^+, W_μ^- and the neutrals Z_μ^0 and A_μ, which corresponds to the photon, are linear combinations of W_μ, B_μ:

$$W_\mu^\pm = \frac{1}{\sqrt{2}} \left(W_\mu^{(1)} \pm i W_\mu^{(2)} \right) \tag{2.20}$$

$$Z_\mu^0 = W_\mu^{(3)} \cos\theta_\mathrm{W} - B_\mu \sin\theta_\mathrm{W} \tag{2.21}$$

$$A_\mu = W_\mu^{(3)} \sin\theta_\mathrm{W} + B_\mu \cos\theta_\mathrm{W} \,, \tag{2.22}$$

where θ_W is the Weinberg angle (weak mixing angle), defined by

$$\tan\theta_\mathrm{W} = \frac{g}{g'} \quad . \tag{2.23}$$

Here, g is the coupling to the triplet field and g' the coupling to the singlet field.

However, in low energy processes such as neutron decay, non-local effects associated to the exchange of massive vector bosons are not observable. So, the four-fermion point-like approximation may be used.

2.4. Measurable parameters in free neutron β-decay

In the preceding sections the Hamiltonian of the weak interaction of the $V-A$ theory is derived. By means of Fermi's golden rule the transition rate W can be calculated as follows:

$$W = \frac{2\pi}{\hbar} \left| \mathscr{M}_{fi} \right|^2 \rho_e' \left(E_e \right) \,, \tag{2.24}$$

where ρ_e' is the phase space density of the final states and $\mathscr{M}_{fi}$ the transition matrix element, which is given by the Hamiltonian Equation (2.13).

In the modern form of the standard model the triple differential decay rate is then given by [JTW57]:

$$\begin{aligned} dW = {} & \frac{G_F^2 |V_{ud}|^2}{(2\pi)^4 \hbar} \rho_e' \left(E_e \right) dE_e d\Omega_e d\Omega_{\bar{\nu}_e} \xi \\ & \times \left(1 + a \frac{\vec{p}_e \vec{p}_{\bar{\nu}_e}}{E_e E_{\bar{\nu}_e}} + b \frac{m_e}{E_e} + \vec{\sigma}_n \left(A \frac{\vec{p}_e}{E_e} + B \frac{\vec{p}_{\bar{\nu}_e}}{E_{\bar{\nu}_e}} + D \frac{\vec{p}_e \times \vec{p}_{\bar{\nu}_e}}{E_e E_{\bar{\nu}_e}} \right) \right) \,, \end{aligned} \tag{2.25}$$

with $\vec{p}_\mathrm{e}$, $\vec{p_{\bar{\nu}_e}}$, E_e, $E_{\bar{\nu}_e}$ being the momenta and energies of the electron e and the electron-antineutrino $\overline{\nu}_\mathrm{e}$, m the mass of the electron, G_F the Fermi constant, V_ud the first element of the CKM matrix and $\vec{\sigma}_\mathrm{n}$ the spin of the neutron. The parameters a, A, b, B, D denote the different

correlation coefficients, which are partly depicted in Figure 2.2. The parameter ξ is described by the weak coupling constants $L_j, R_j\,(j = S,V,A,T)$:

$$\xi = \left(|L_S|^2 + |L_V|^2 + |R_S|^2 + |R_V|^2\right) + 3\left(|L_A|^2 + |L_T|^2 + |R_A|^2 + |R_T|^2\right). \tag{2.26}$$

Since the axial and tensor couplings are linked to the triplet state a factor of 3 arises. In the purely left-handed $V-A$ theory within the SM $L_S, L_T, R_A, R_S, R_V, R_T$ are predicted to be zero as well as b and D. Then

$$\xi = |L_V|^2 + 3\,|L_A|^2, \tag{2.27}$$

and the correlation coefficients a, A, B can be expressed by $\lambda = L_A/L_V$ and the phase angle ϕ between them:

$$a = \frac{1-|\lambda|^2}{1+3\,|\lambda|^2} \tag{2.28}$$

$$A = -2\frac{|\lambda|^2 + |\lambda|\cos\phi}{1+3\,|\lambda|^2} \tag{2.29}$$

$$B = 2\frac{|\lambda|^2 - |\lambda|\cos\phi}{1+3\,|\lambda|^2} \tag{2.30}$$

By measuring one of these correlation coefficients λ can be determined. A comparison of λ values from independent neutron decay measurements provides an important test of the $V-A$ model as the system is redundant and overdetermined. The current value is $\lambda = -1.2724(23)$ ([THH$^+$18], PDG 2018 average from neutron decay). Near the value $\lambda = -1.27$ the sensitivities for the correlation coefficients are given as follows:

$$\frac{\mathrm{d}a}{\mathrm{d}\lambda} \approx 0.298, \qquad \frac{\mathrm{d}A}{\mathrm{d}\lambda} \approx 0.374, \qquad \frac{\mathrm{d}B}{\mathrm{d}\lambda} \approx 0.076\,. \tag{2.31}$$

The aSPECT experiment measures the β-$\overline{\nu}_e$ angular correlation coefficient a, which is currently known to $a = -0.1059(28)$ ($\Delta a/a \approx 2.6\,\%$, [THH$^+$18] PDG 2018 average). Within the $V-A$ model a can take values from $-1/3$ (pure Gamow-Teller decay, $g_V = 0$) to $+1$ (pure Fermi decay, $g_A = 0$). In general, a is given by

$$a = \frac{1}{\xi}\left(|L_V|^2 - |L_S|^2 + |L_T|^2 - |L_A|^2 + |R_V|^2 - |R_S|^2 + |R_T|^2 - |R_A|^2\right). \tag{2.32}$$

Thus, a precise measurement of a can be used to search for scalar and tensor coupling constants $\neq 0$. Also, the non-zero value of a does not violate parity, as it does not contradict $L_i = R_i$, nor does it violate time-reversal invariance (all constants have to be real).

For more information of the β-decay of the neutron, the observables of it and its interactions, as well as limits from the neutron decay on the SM the reader is referred to [Abe08, Dub91, DS11, SBNC06].

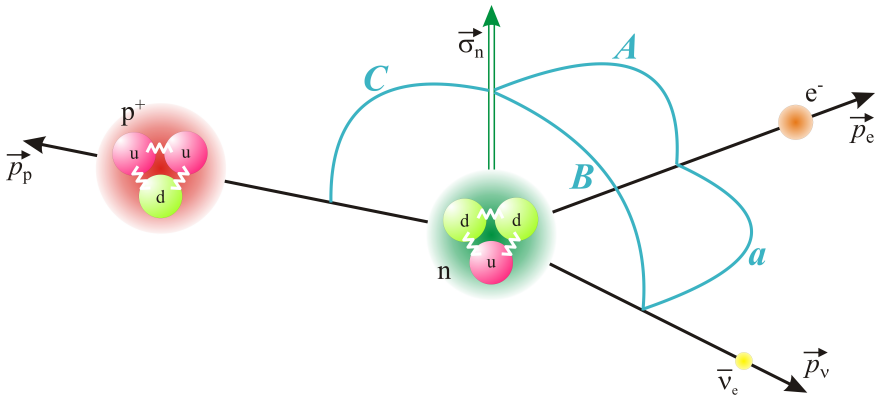

Figure 2.2.: Observable correlation coefficients in free neutron β-decay. The sketch shows a neutron with spin $\vec{\sigma}_n$ and the momenta of its decay products. The *a*SPECT experiment measures "little" a, which is the correlation between the electron $\vec{p}_e$ and neutrino momenta $\vec{p}_{\bar{\nu}_e}$.

2.5. The proton energy spectrum

The main objective of *a*SPECT is the determination of a from *unpolarised* neutron decay, in which case the differential decay rate can be written as:

$$dW \propto 1 + a\frac{|\vec{p}_e||\vec{p}_{\bar{\nu}_e}|}{E_e E_{\bar{\nu}_e}} \cos\theta_{e\bar{\nu}_e}\,. \tag{2.33}$$

Here, $\theta_{e\bar{\nu}_e}$ is the angle between the momenta of the electron $\vec{p}_e$ and the antineutrino $\vec{p}_{\bar{\nu}_e}$. The coefficient a indicates the preferred relative orientation of the electron and antineutrino momenta. In example, if $a = 0$, there is no preferred emission direction (isotropic), but if $a = +1$ the electron and antineutrino have much higher probability to be emitted in the same direction. For negative values of, in example $a = -1/3$, antiparallel emission is preferred. Due to kinematic reasons, momentum and energy conservation, this is directly linked to the observed proton recoil energies, which is depicted in Figure 2.3. This allows the determination of a from the shape of the proton recoil spectrum as can be seen in Figure 2.4. There, the proton energy spectrum is shown for three different values of a. The difference between the shape of the red dashed spectrum ($a = -0.3333$) and the blue spectrum ($a = -0.1059$) corresponds to a difference in a of about 200 %. The *a*SPECT experiment aims for $\Delta a/a \sim 1\,\%$. This means a precision of just $\sim 1/200$ of the observed change in shape of Figure 2.4.

Glück calculated the proton spectrum including several corrections to make the determination of λ possible to $\sim 0.1\,\%$, which corresponds to a precision in a of 0.03 % [Glü93]. The differential spectrum depends on the total proton energy $E_f = m_p c^2 + T_p$ and has the following

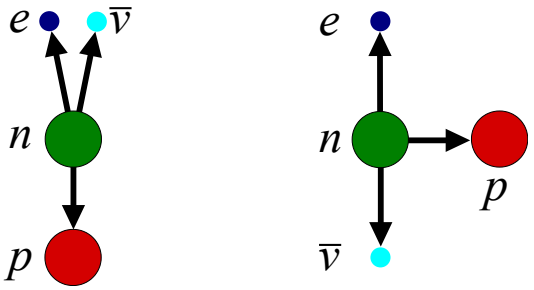

Figure 2.3.: Link between proton recoil energy and $\theta_{e\overline{\nu}_e}$. On the left, the emission angle $\theta_{e\overline{\nu}_e}$ between the direction of the electron e and antineutrino $\overline{\nu}_e$ is small, thus, due to momentum and energy conservation, the proton recoil energy is high. On the right, the angle is maximal, thus, the recoil energy is small.

form:

$$\omega_{0C\alpha}(E_f) = \tilde{\omega}_{0C}(E_f) \cdot (1 + 0.01 r_C(y))\,(1 + 0.01 r_\rho + 0.01 r_p(y))\,. \tag{2.34}$$

This equation is comprised of

- $\tilde{\omega}_{0C}(E_f)$, the proton spectrum including relativistic and Coulomb corrections of the $(1 + \frac{\pi\alpha}{\beta})$ approximation,
- $r_C(y)$, the higher order Coulomb correction,
- $r_p(y)$, the energy-dependent, model-independent, radiative correction, and
- $r_\rho = 1.505$, the energy- and model-independent, order-α correction.

The corrections $r_C(y)$ and $r_p(y)$ are plotted in Figure 2.5.

2.6. Previous and competing measurements of a

The first determination of a was carried out by *Grigoriev et al.* in the Soviet Union in 1967 [GGVN68]. The experiment measured the proton spectrum in coincidence at a fixed electron energy. By this method, background could be suppressed effectively. The proton energy could be determined by a time of flight measurement by means of an ellipsoidal electrostatic mirror. The result was

$$a = -0.091(39)\,, \tag{2.35}$$

which corresponds to $\Delta a/a \approx 43\,\%$ dominated by counting statistics.

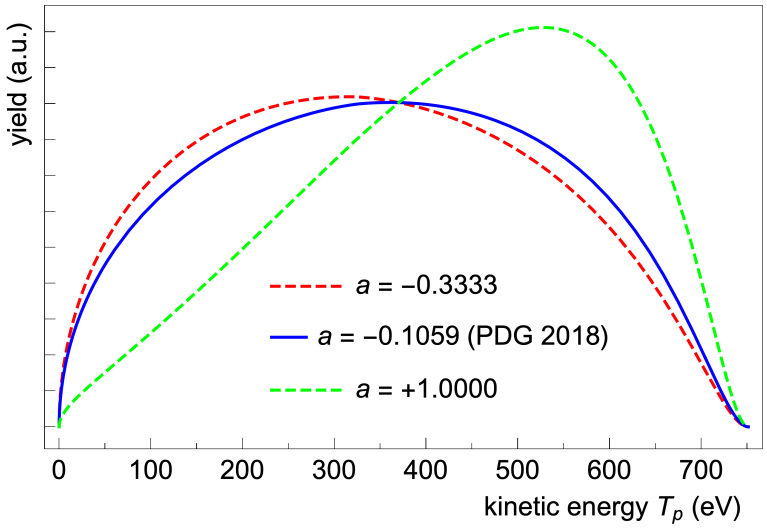

Figure 2.4.: Differential proton recoil spectrum. Shown is the differential proton recoil spectrum for three different a values: $a = -0.3333$ (pure Gamow-Teller transitions), $a = +1$ (pure Fermi transitions), and the current $a = -0.1059$ (PDG 2018 average). As can be easily seen, the more positive a is, the more high recoil energies are preferred, and vice versa.

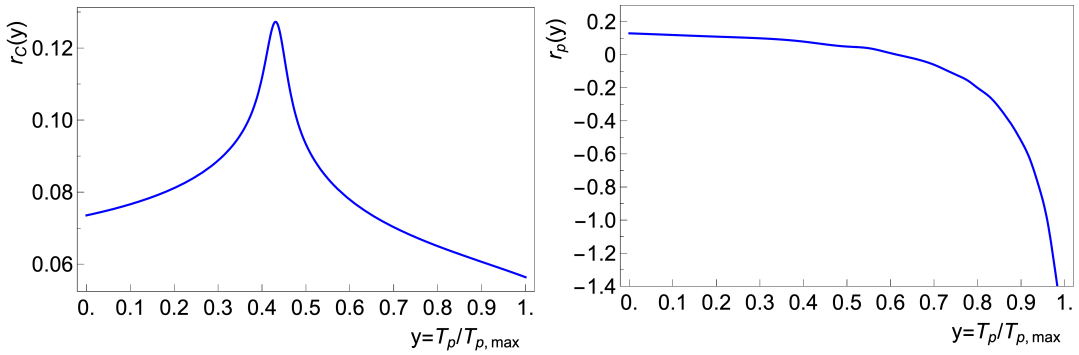

Figure 2.5.: Corrections to the proton energy spectrum $\tilde{\omega}_{0C}(E_f)$. (a) shows the higher order Coulomb correction and (b) the model-independent, radiative correction plotted against the fraction y of the maximal proton's kinetic energy $T_{p,max} \approx 751\,\text{eV}$. The curves are the result from a cubic interpolation of the values listed in TABLE III. and IV. from [Glü93].

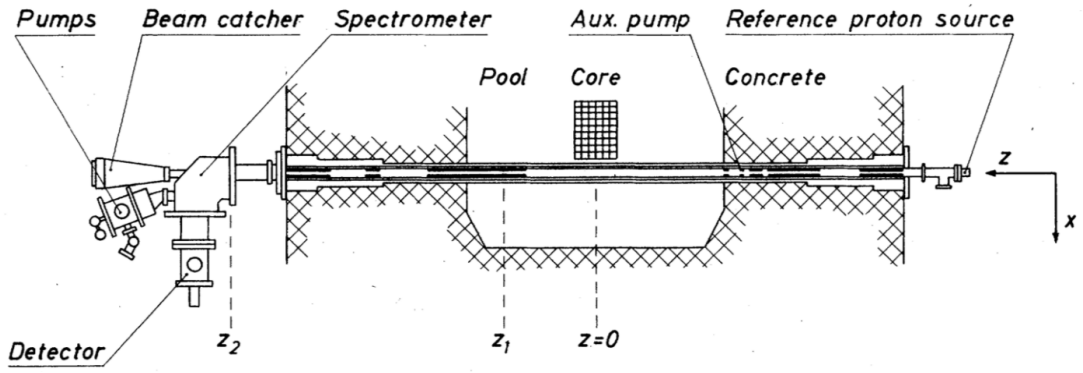

Figure 2.6.: Experimental setup by *Stratowa et al.* (Vienna, 1978). Fig. from [SDW78].

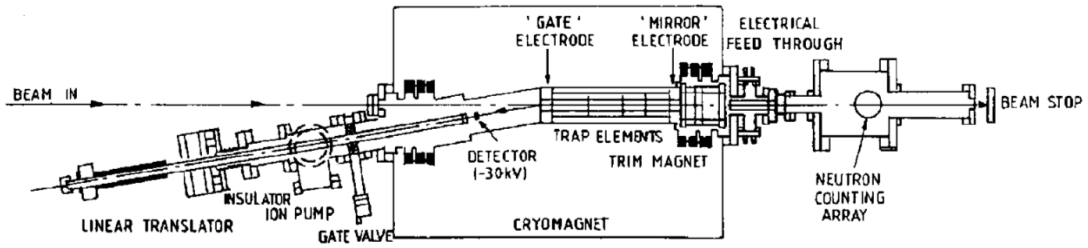

Figure 2.7.: Experimental setup by *Byrne et al.* (Grenoble, 2002). Fig. from [BDvdG$^+$02].

The first precise measurement was conducted by *Stratowa et al.* in Vienna in 1978 [SDW78]. They also derived a from the shape of the proton spectrum. Neutrons decayed in a tangential through tube of the ASTRA reactor ($z = 0$). By two apertures (z_1, z_2) only protons with 90° were selected, guided into a spectrometer (spherical condenser), and detected by an ion-electron converter detector (Figure 2.6). They obtained

$$a = -0.1017(51)\,, \tag{2.36}$$

which corresponds to $\Delta a/a \approx 5\,\%$. The leading systematics were energy-dependent factors in the transmission and the detection efficiency.

Only after 24 years in 2002 *Byrne et al.* performed a new measurement of a at the Institute Laue-Langevin (ILL) Grenoble [BDvdG$^+$02]. This experiment utilised a modified apparatus build to measure the neutron lifetime. It counted protons from a neutron beam passing a Penning-like trap. The trapped protons could be released by lowering the electric potential to one side of the trap ("gate" electrode, Figure 2.7). In this way the integral proton spectrum could be determined. Similar to aSPECT the proton momentum had to be transferred adiabatically to longitudinal momentum. This was one of the leading systematics of this experiment.

The value was determined to

$$a = -0.1054(55)\,, \tag{2.37}$$

which corresponds to $\Delta a/a \approx 5\,\%$. This is similar to the experiment by *Stratowa et al.* .

One of the current, competing experiments is aCORN [WBC$^+$09] conducted at the National Institute of Standards and Technology (NIST) in Gaithersburg (Maryland, USA). The experiment does not measure the shape of the proton spectrum, but realises the novel "wishbone asymmetry" first proposed by Yerozolimsky and Mostovoy [Yer04, BM94]. The spectrometer consist of a axial magnetic field with a β-spectrometer at one end and a proton counter at the other (Figure 2.8 (a)). The transverse electron and proton momenta are restricted by collimators and are detected in coincidence. It can be discriminated between two groups:

(i) Group I: Proton emitted towards proton detector and electron towards β-spectrometer.

(ii) Group II: Proton and electron are emitted towards β-spectrometer. In this case the proton gets reflected and is guided towards the proton detector, and thus is slower than a proton from group I.

Plotting the time of flight spectrum against the β energy E (Figure 2.8 (b)) reveals the two groups, the so-called "wishbone". The wishbone asymmetry $X(E)$ is related to a as follows:

$$X(E) = \frac{N_I(E) - N_{II}(E)}{N_I(E) + N_{II}(E)} = a\, f_a(E)\,, \tag{2.38}$$

where $f_a(E)$ is a geometric function.

In 2017 *Darius et al.* [DBD$^+$17] could determine a to

$$a = -0.1090 \pm 0.0030(\text{stat}) \pm 0.0028(\text{sys})\,, \tag{2.39}$$

which corresponds to $\Delta a/a \approx 3.8\,\%$[3]. The setup is sensitive even to tiny polarisation of the neutron beam ($\sim 0.6\,\%$), which was one of the main systematics. In 2014 aCORN was relocated to the neutron beam line NG-C, where data were collected from 2015 to 2016. The preliminary result presented in April 2019 expects $\Delta a/a \approx 2.1\,\%$ [WBD$^+$18].

The Nab experiment [Bow05, PAA$^+$09, BBPP14] is under construction at the Spallation Neutron Source (SNS) in Oak Ridge (Tennessee, USA). The experimental setup is shown in Figure 2.9 (a). It consists of two detectors and an axial guiding field between them passed by a neutron beam. Only the upper detector count protons, while both can count electrons. Nab measures the electron energy E_e and estimates the proton momentum p_p from the proton time of flight t_p (coincidence measurement). This allows the determination of the angle between electron and neutrino as follows:

$$\cos\theta_{e\nu} = \frac{p_p^2 - p_e^2 - p_\nu^2}{2 p_e p_\nu} \tag{2.40}$$

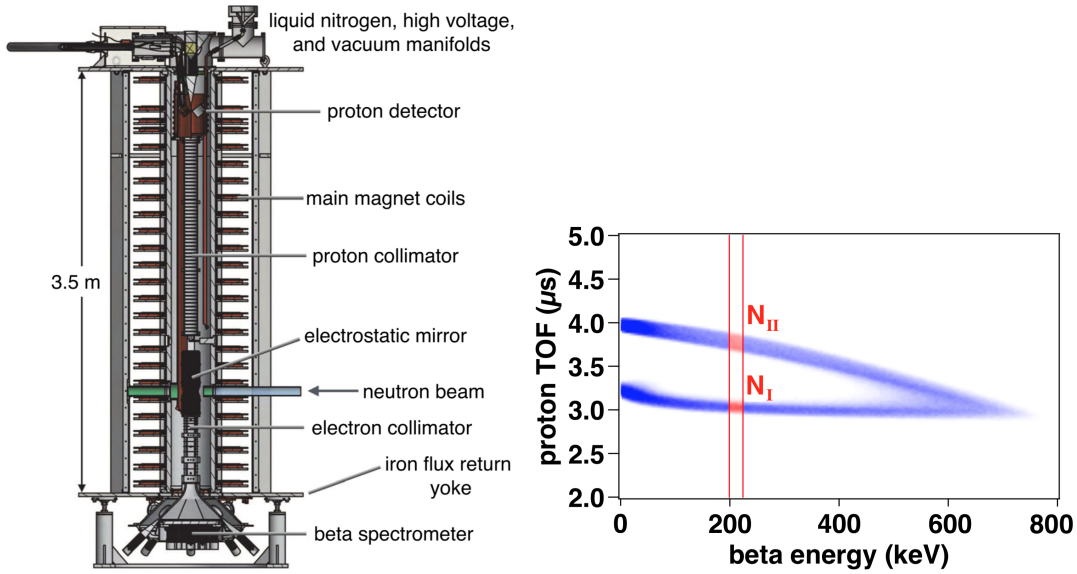

(a) (b)

Figure 2.8.: The aCORN experiment. (a) Experimental setup of aCORN (Gaithersburg, 2017). Fig. from [DBD+17]. (b) Wishbone asymmetry. The lower group are the direct protons (I) and the upper group the delayed protons (II). Fig. from [WBD+18].

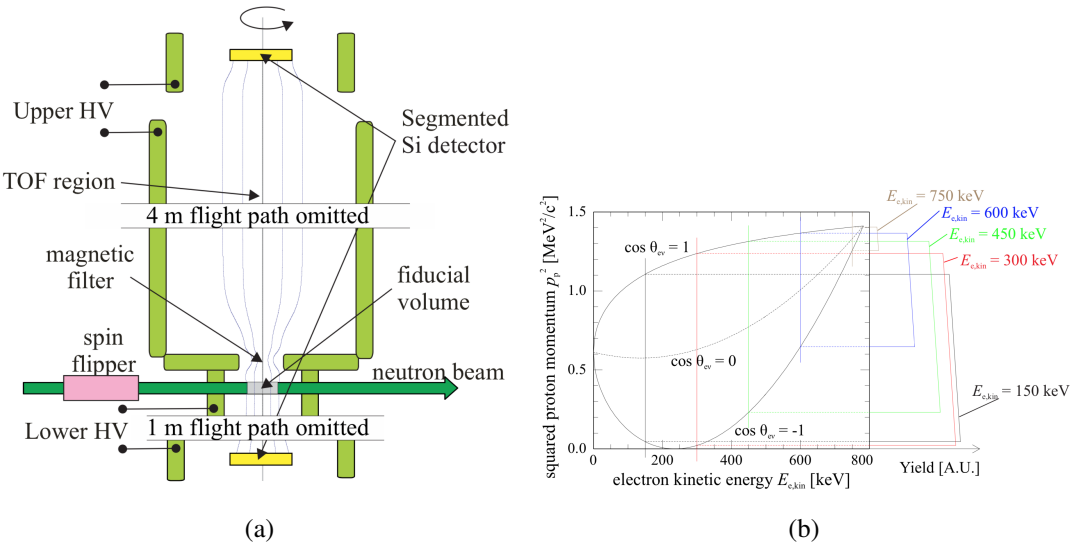

(a) (b)

Figure 2.9.: The Nab experiment. (a) Experimental setup of Nab. (b) Plot of phase space $\cos\theta_{ev}$. The projection of the squared proton momentum p_p^2 for a fixed electron energy E_e result in trapezes, which have slopes proportional to a. Both Figs. from [BAB+08].

The phase space of allowed values is shown in Figure 2.9 (b). For a fixed electron energy E_e, the decay rate will have a slope proportional to a. Nab aims for a determination of a with a precision of $\Delta a/a \approx 0.1\,\%$.

[3] Result from quadrature sum of statistical and systematic uncertainty (PDG convention).

3. Improved determination of the β-$\bar{\nu}_e$ angular correlation coefficient a in free neutron decay using the *a*SPECT experiment

3.1. Introduction

The free neutron presents a unique system to investigate the standard model of particle physics (SM). Its β-decay into a proton, an electron and an electron-antineutrino is the prototype semileptonic decay. The low decay energy allows a simple theoretical interpretation within the Fermi theory, which is a very good approximation of the underlying field theory at low energies. Due to the absence of nuclear structure this decay is easy to interpret with only minor theoretical corrections compared to nuclear β-decays.

While the neutron lifetime gives the overall strength of the weak interaction, neutron decay correlation coefficients depend on the ratio of the coupling constants involved, and hence determine its internal structure. Today, neutron β-decay gives an important input to the calculation of semileptonic charged-current weak interaction cross sections needed in cosmology, astrophysics, and particle physics. With the ongoing refinement of models, the growing requirements on the precision of these neutron decay data must be satisfied by new experiments.

The *a*SPECT experiment [BAB$^+$08, GBB$^+$05, ZBvdG$^+$00] has the goal to determine the ratio of the weak axial-vector and vector coupling constants $\lambda = g_\mathrm{A}/g_\mathrm{V}$ from a measurement of the β-$\bar{\nu}_e$ angular correlation in neutron decay. The β-decay rate when observing only the electron and neutrino momenta and the neutron spin and neglecting a CP-violating term is given by [JTW57]

$$d^3\Gamma \propto G_\mathrm{F}^2 V_\mathrm{ud}^2 p_\mathrm{e} E_\mathrm{e} (E_0 - E_\mathrm{e})^2 \left(1 + a\frac{\vec{p}_\mathrm{e}\cdot\vec{p}_\nu}{E_\mathrm{e}E_\nu} + b\frac{m}{E_\mathrm{e}} + \vec{\sigma}_\mathrm{n}\cdot\left(A\frac{\vec{p}_\mathrm{e}}{E_\mathrm{e}} + B\frac{\vec{p}_\nu}{E_\nu}\right)\right) dE_\mathrm{e} d\Omega_\mathrm{e} d\Omega_\nu \tag{3.1}$$

with $\vec{p}_e$, $\vec{p}_\nu$, E_e, E_ν being the momenta and energies of the beta electron and the electron-antineutrino, m the mass of the electron, G_F the Fermi constant, V_ud the first element of the Cabibbo-Kobayashi-Maskawa (CKM) matrix, E_0 the decay energy and $\vec{\sigma}_n$ the spin of the neutron. b is the Fierz interference coefficient. It vanishes in the purely vector axial-vector ($V-A$) interaction of the SM since it requires scalar (S) and tensor (T) interaction (see e.g.

[SBNC06, VWT15]). The correlation coefficients a and A are most sensitive to λ and can be used for its determination. The SM dependence of the beta-neutrino angular correlation coefficient a on λ is given by [JTW57, Abe08]

$$a = \frac{1-|\lambda|^2}{1+3|\lambda|^2}. \tag{3.2}$$

To date, the most accurate value of λ has been extracted from measurement of the β-asymmetry parameter A [MMD$^+$13, MMS$^+$18, BDA$^+$18]. However, determining λ from a yields complementary information since the experimental systematics are different and systematic effects are relevant in this type of high precision experiments.

λ together with the neutron lifetime τ_n can be used to test the unitarity of the top row of the CKM matrix [HT15] since it yields its first element V_{ud} according to [CMS18, MS06]:

$$|V_{\mathrm{ud}}|^2 = \frac{(4908.6 \pm 1.9)\,\mathrm{s}}{\tau_n\left(1+3|\lambda|^2\right)}, \tag{3.3}$$

where the error in the numerator reflects the uncertainty of electroweak radiative corrections. The neutron decay determination of V_{ud} is preferred as it is free of isospin breaking and nuclear structure corrections. Within the SM, neutron β-decay is described by two parameters only, i.e., V_{ud} and λ. Since more than two observables are accessible, the redundancy inherent in the SM description allows uniquely sensitive checks of the model's validity and limits [Dub91, PRMT07, KHB$^+$10, BCC$^+$12, CRM13, GANCS19], with strong implications in astrophysics [DS11]. Of particular interest in this context are the search for right-handed currents and for S and T interactions where the various correlation coefficients exhibit different dependencies. These investigations at low energy in fact are complementary to direct searches for new physics beyond the SM in high-energy physics (see e.g. [BCC$^+$12, CRM13, GJY$^+$18]).

The present precision of a measurements is $\Delta a/a \sim 3\,\%$ taking the PDG 2018 value $a = -0.1059(28)$ [THH$^+$18, SDW78, BDvdG$^+$02, DBD$^+$17]. The work with aSPECT presented here improved the measurement of the β-$\overline{\nu}_e$ angular correlation a to $\Delta a/a \sim 0.8\,\%$.

3.2. The Experiment

At aSPECT the β-$\overline{\nu}_e$ angular correlation is inferred from the energy spectrum of the recoiling protons from the β-decay of free neutrons. The shape of this recoil energy spectrum is sensitive to a, due to energy and momentum conservation: the proton gains a large recoil energy when the electron and neutrino are emitted in the same direction (dominant process for positive a) and only a small recoil energy when they are emitted in opposite directions (dominant for negative a). The resulting differential energy spectrum is shown for two different values of a in Figure 3.1 (a). The recoil energy spectrum in turn is measured with a

spectrometer using magnetic adiabatic collimation with an electrostatic filter (MAC-E filter) [BPT80, PBB$^+$92, LS85]. Such a MAC-E filter collimates the momenta of charged particles, protons in the case of *a*SPECT, into the direction of the magnetic field by guiding them from a high magnetic field B_0 into a low magnetic field region B_A. The inverse magnetic mirror effect provides for a conversion of their transversal energy into longitudinal energy. In the low magnetic field most of the kinetic energy of the proton therefore resides in its longitudinal motion, which is then probed by an applied retardation voltage U_AP. A variation of the retardation voltage yields a measurement of the integral proton energy spectrum (Figure 3.1 (b)). This technique in general offers a high luminosity combined with a high energy resolution at the same time. In order to extract a reliable value of the β-$\overline{\nu}_e$ angular correlation coefficient any effect that changes the shape of the integral proton energy spectrum has to be understood and quantified precisely. Examples are among others the transmission function of the MAC-E filter and background that depends on the retardation voltage.

3.2.1. The transmission function

As long as the protons move adiabatically through the MAC-E filter, the ratio of radial energies at emission and retardation points is given by $1/r_\mathrm{B}$, with $r_\mathrm{B} := \frac{B_\mathrm{A}}{B_0}$, where B_0 and B_A are the magnetic fields at the place of emission and retardation, respectively. This amounts to the energy resolution of *a*SPECT. Hence, the transmission function F_tr for isotropically emitted protons of initial kinetic energy T is a function both of U_A and r_B [GBB$^+$05, BAB$^+$08, Kon11]:

$$F_\mathrm{tr} = \begin{cases} 0 & \text{if } T \leq eU_\mathrm{A} \\ 1 - \sqrt{1 - \left(1 - \frac{eU_\mathrm{A}}{T}\right)/r_\mathrm{B}} & \text{if } eU_\mathrm{A} < T < \frac{eU_\mathrm{A}}{1-r_\mathrm{B}} \\ 1 & \text{if } T \geq \frac{eU_\mathrm{A}}{1-r_\mathrm{B}} \end{cases} \tag{3.4}$$

with e the elementary charge and $U_\mathrm{A} = \phi_\mathrm{A} - \phi_0$, the potential difference between the place of retardation (ϕ_A) and emission (ϕ_0). The place of retardation, the so-called analysing plane (AP), is defined as the plane, in which the kinetic axial energy of the protons in the magnetic flux tube from the decay volume (DV) to the detector becomes minimal. The AP of *a*SPECT is a surface in $\mathbb{R}^3$. It can be determined by particle tracking simulations given the known electric and magnetic field configurations. In case of homogeneous electric and magnetic fields inside the DV and AP electrode, the AP is simply the midplane of the AP electrode.

In the ideal case U_A is just the applied retardation voltage U_AP between the DV and AP electrode (see Figure 3.2). In reality, the electric potentials ϕ_A and ϕ_0 get slightly shifted and distorted by field leakage and locally different work functions of the electrodes creating these potentials. For the magnetic field ratio r_B, variations are caused by locally inhomogeneous B fields in the DV and AP region. Hence, U_A and r_B depend on the individual proton trajectories P_i. Therefore, they get replaced in Equation (3.4) by their averages $\langle U_\mathrm{A} \rangle$ and $\langle r_\mathrm{B} \rangle$, where the averages are over all trajectories of those protons that reach the detector[1]. For details

[1] To be precise, one would have to find $\langle F_\mathrm{tr} \rangle$ for an applied retardation voltage and initial kinetic energy T. Access

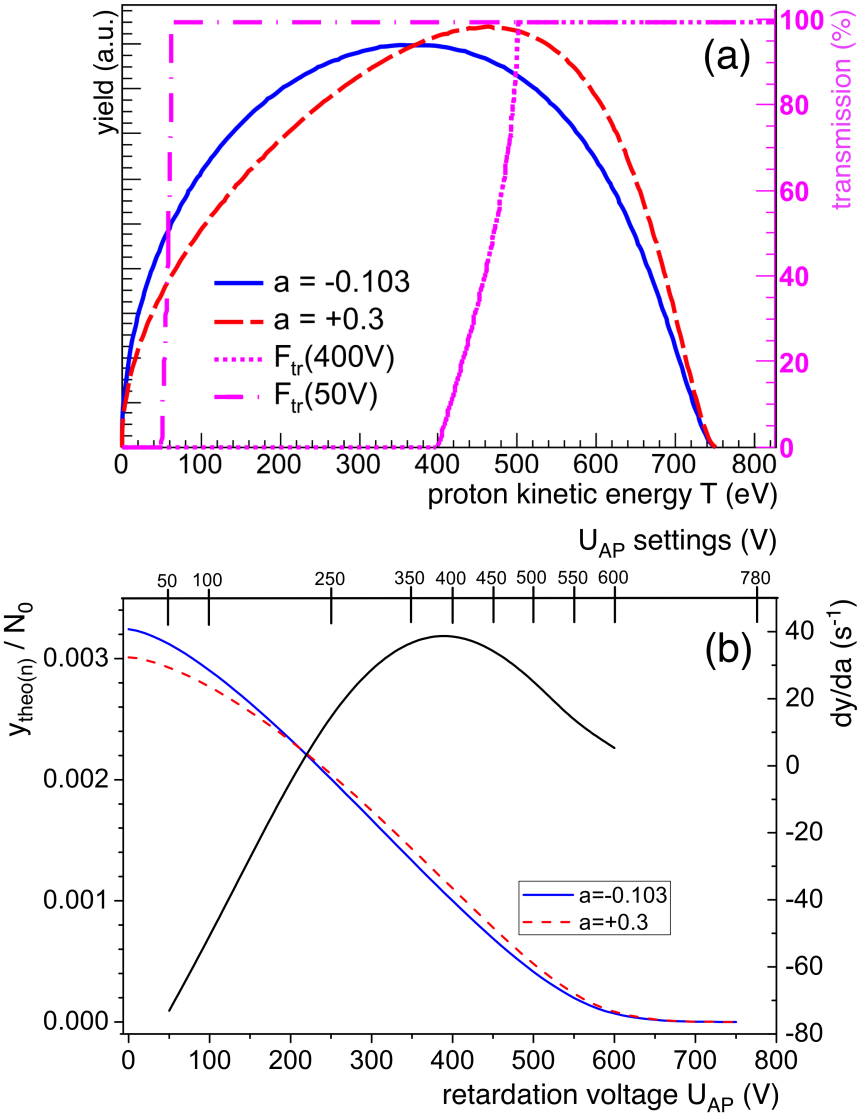

Figure 3.1.: (a) Expected proton recoil spectrum for $a = -0.103$ (blue solid line) which we use in the following as reference value (a_{ref}) and for an extreme value of $a = +0.3$ (red dashed line). The decay proton has its maximum energy at $T_{\mathrm{max}} = 751\,\mathrm{eV}$. Also shown are the respective transmission functions F_{tr} for the retardation potentials $U_{\mathrm{AP}} = 50\,\mathrm{V}$ and $U_{\mathrm{AP}} = 400\,\mathrm{eV}$ and $r_{\mathrm{B}} = 0.203$ (magenta lines). (b) The corresponding (normalised) integral proton spectra. Normalisation means that the are under the respective curve is 1, i.e., does not depend on a. The derivative dy/da (black solid curve) expresses the sensitivity of the yield $(y_{\mathrm{theo(n)}}/N_0)$ to changes in a which (in absolute numbers) is maximal at U_{AP} voltage settings of $\sim 50\,\mathrm{V}$ and $\sim 400\,\mathrm{V}$ (top horizontal axis). We do not use a lower voltage setting ($U_{\mathrm{AP}} < 50$ V), as it is potentially sensitive to background from the ionisation of residual gas.

on the determination of $\langle r_B \rangle$ and $\langle U_A \rangle$, see Sections 3.4.2 and 3.4.3. For more details on the transmission through MAC-E filters and the influence of the field configuration, see [GBB$^+$05, GDL$^+$13].

The uncertainties of $\langle U_A \rangle$ and $\langle r_B \rangle$ form the principal systematic uncertainties of *a*SPECT, albeit not the only ones. Two examples of transmission functions for *a*SPECT are included in Figure 3.1 (a). Simulations show [GBB$^+$05, Kon11] that the sensitivity of the measured a values on $\langle U_A \rangle$ and $\langle r_B \rangle$ is given by $\Delta a/a \sim 0.00012 \times \Delta\langle U_A \rangle/\text{mV}$ and $\Delta a/a \sim 10 \times \Delta\langle r_B \rangle/\langle r_B \rangle$. Therefore, a shift of $\Delta\langle U_A \rangle \sim 80\,\text{mV}$ or $\Delta\langle r_B \rangle/\langle r_B \rangle = 10^{-3}$ corresponds to a shift $\Delta a/a \sim 1\,\%$.

3.2.2. Experimental set-up

In 2013 *a*SPECT was set-up for a production beam time at the cold neutron beam line of PF1b [ADH$^+$06] at the Institut Laue-Langevin in Grenoble, France. Here we present the basic layout of the *a*SPECT experiment. Details are discussed in [BAB$^+$08, GBB$^+$05, ZBvdG$^+$00] and [Wun16, Mai14, Kon11, Gua11, Bor10, Sim10, Hor11]. Modifications of the experimental arrangement used for the measurement in 2013 with respect to the ones presented in the previous articles are shortly mentioned at the relevant places.

A schematic of the 2013 *a*SPECT spectrometer is shown in Figure 3.2. The longitudinal magnetic field of the MAC-E filter is created by a superconducting multi-coil system oriented in vertical direction [BAB$^+$08]. The neutron beam enters horizontally in the lower part of the *a*SPECT spectrometer at the height of the high magnetic field B_0 and is guided through the DV electrode towards the beam dump further downstream. Protons and electrons from neutron decays inside the DV electrode are guided adiabatically along the magnetic field lines. Downgoing protons are converted into upgoing protons by reflection off an electrostatic mirror electrode (EM) at $U_{EM} = 860\,\text{V}$ (Table 3.1) below the DV electrode, providing a 4π acceptance of *a*SPECT. The protons are guided magnetically towards the AP inside the main AP electrode (E14 in Table 3.1). Protons with sufficient energy pass through the AP and are focused onto a silicon drift detector (SDD) both magnetically and electrostatically. A reacceleration voltage of $U_{DC} = -15\,\text{kV}$ applied to an electrode surrounding the detector, the so-called detector cup (DC) electrode, is used in order to be able to detect the protons. A photograph of the set-up at PF1b is shown in Figure 3.3.

The main superconducting coils are operated in persistent mode. Additionally, there are two superconducting correction coils in driven mode to create a small magnetic field gradient across the DV, as well as a combination of external air-cooled coils in Helmholtz and Anti-Helmholtz configuration in the AP region. For more details regarding the magnetic fields and the *a*SPECT magnet system, see [GBB$^+$05, BAB$^+$08, Gua11, Wun16]. The whole set-up is surrounded by a magnetic field return yoke to reduce the stray magnetic field (see Figure 3.3), but does not affect significantly the internal magnetic field and its homogeneity [KGB$^+$14].

to $\langle F_{tr} \rangle$ including $\langle U_A \rangle$ and $\langle r_B \rangle$ is provided by particle tracking simulations, where the following relation to Equation (3.4) can be found: $\langle F_{tr} \rangle = F_{tr}(T, \langle U_A \rangle, \langle r_B \rangle)$.

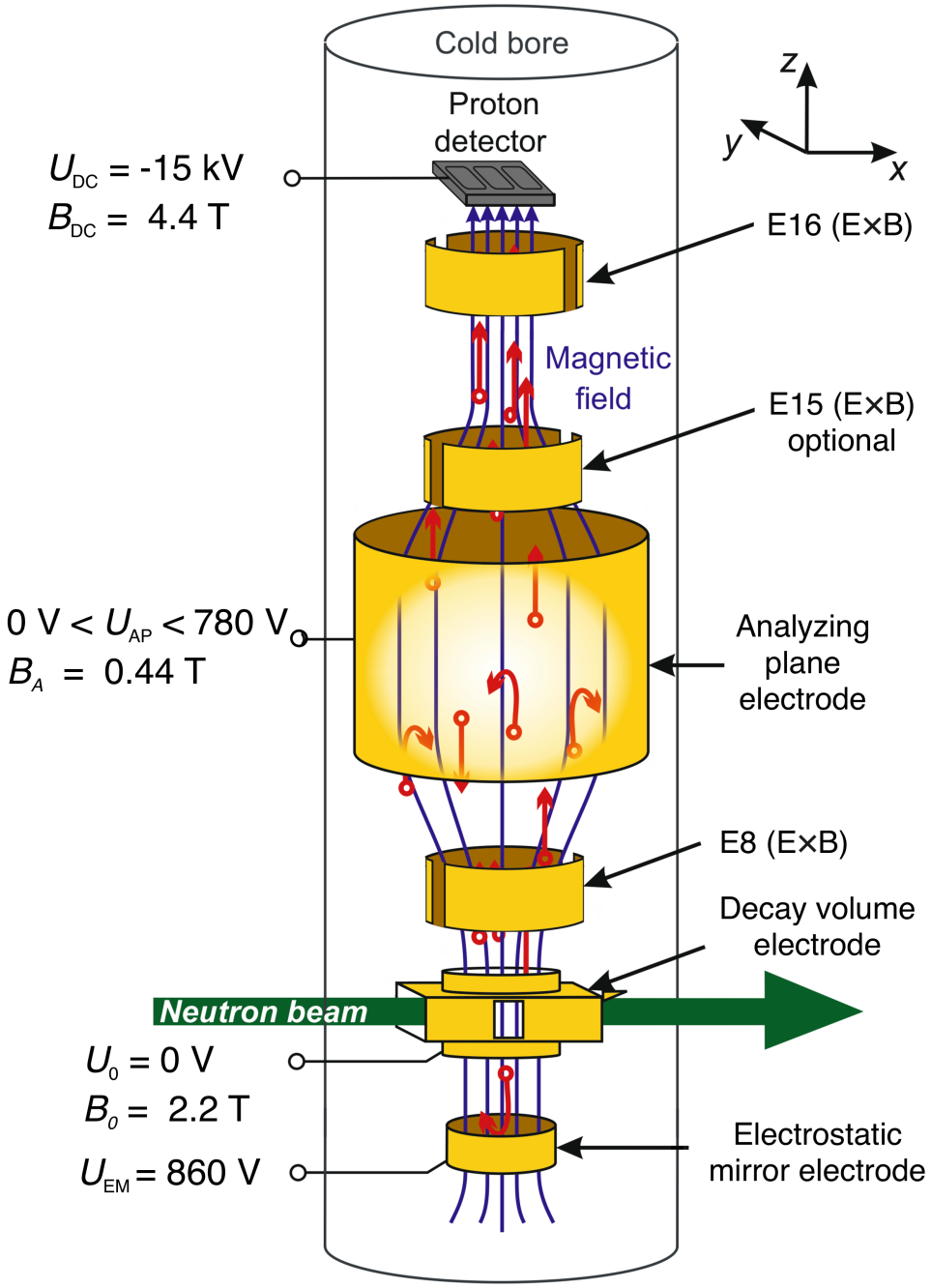

Figure 3.2.: Schematic of *a*SPECT. Only the most important electrodes are shown. The magnetic field is oriented in vertical direction (blue lines). The whole set-up is under ultra-high vacuum conditions.

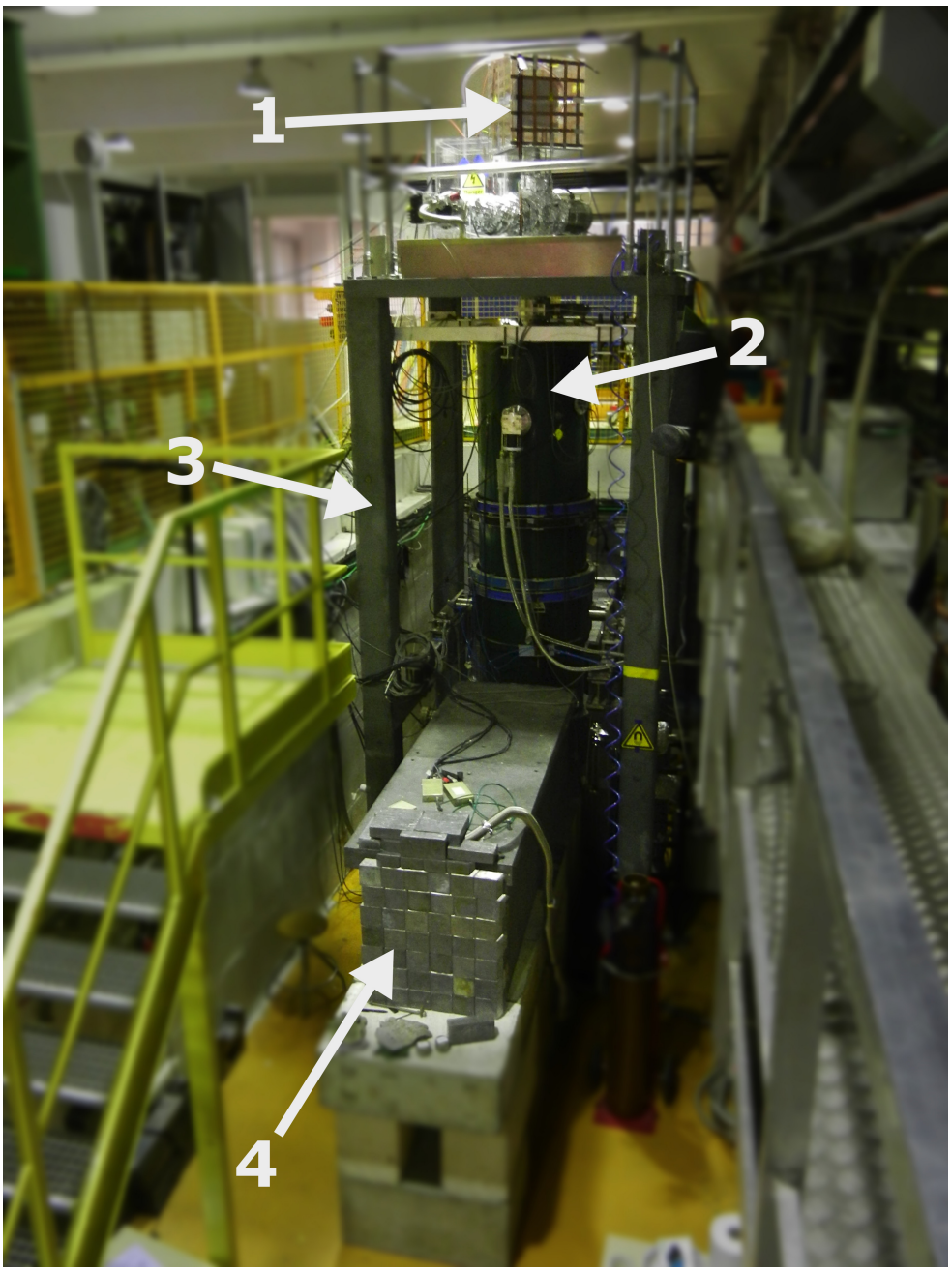

Figure 3.3.: The *a*SPECT set-up at the cold neutron beam line of PF1b at the ILL in 2013. Clearly visible are (1) the detector electronics on top, (2) the vertically aligned *a*SPECT cryostat system, (3) the massive magnetic field return yoke for the magnetic shielding and (4) the beam dump in front.

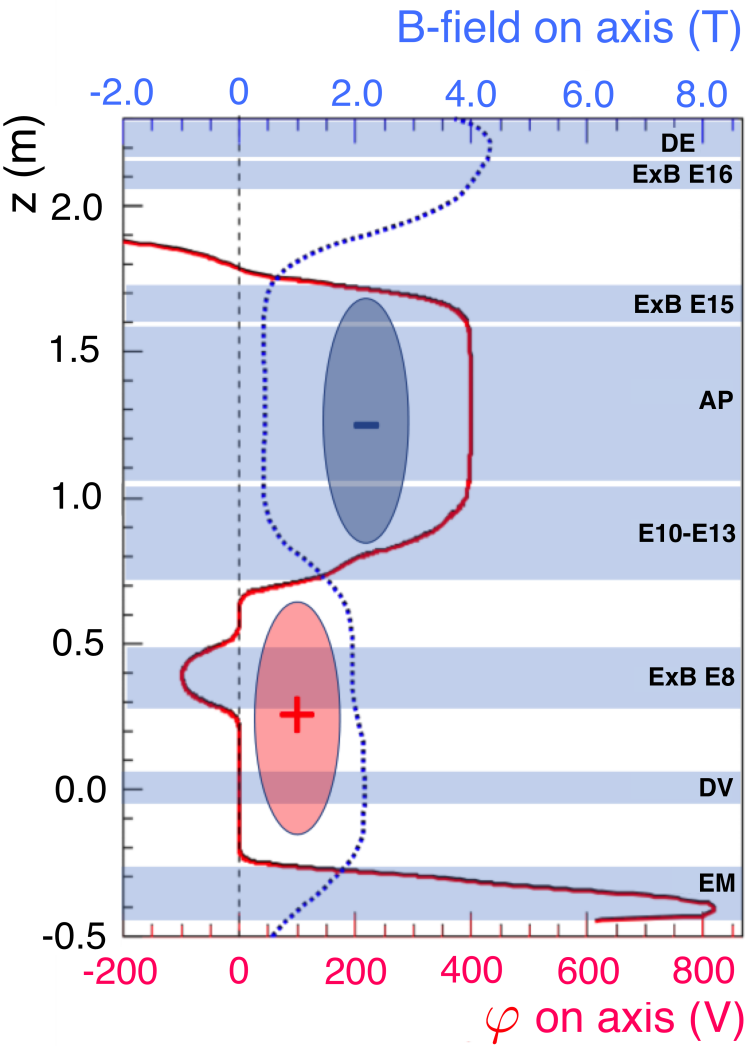

Figure 3.4.: Fields inside *a*SPECT along the vertical direction (z-axis). The magnetic field is shown in blue (dotted curve), the electric potential in red. The position of the electrodes as mentioned in the text and listed in Table 3.1 are indicated by horizontal bars (in blue). The most important Penning-like traps for positively (+) and negatively (-) charged particles inside *a*SPECT are indicated as ellipses.

During the beam time in 2013 the magnetic field was $B_0 \sim 2.2\,\mathrm{T}$ in DV region, $B_\mathrm{A} \sim 0.44\,\mathrm{T}$ around the AP and $B_\mathrm{DC} \sim 4.4\,\mathrm{T}$ at the position of the detector.

The electrode system creating the electric potentials has been described in detail in [GBB+05, BAB+08, Gua11, Kon11]. Between the DV and the main AP electrode the electrode system contains cylindrical electrodes with subsequently higher potential (electrodes E10 to E13 in Table 3.1). Their purpose is to avoid steep gradients of the electric potential to achieve a sufficiently adiabatic motion of the decay protons from the DV to the AP [GBB+05]. They also help to minimise field leakage into the main AP electrode (E14). The resulting electric potential along the vertical axis of the *a*SPECT spectrometer is shown in Figure 3.4 together with the course of the magnetic field strength. Between the AP and DV electrode, the voltage U_AP is applied. The applied voltage U_AP is supplied by a precision power supply[2]. A voltage divider further provides the voltages for the electrodes above and below the main AP electrode, see Table 3.1. U_AP is measured with a precision of $< 13\,\mathrm{mV}$ at a second connection to the main AP electrode using a precision voltmeter[3] (Section 3.4.3). Typical voltages applied to the relevant electrodes during the 2013 beam time are shown in Table 3.1. The nomenclature is from [BAB+08]. Besides the new DV and AP electrodes major differences compared to [BAB+08] are the omission of the diaphragm electrode E7, the segmentation of the mirror electrode E1 into two parts for improved adiabatic motion during reflection of the protons, and the change of E15 above the main AP electrode to a dipole electrode, cf. Figure 3.2.

The DC electrode as well as the upper $E \times B$ drift electrode E16 are made of stainless steel (316LN), which has been electropolished to reduce field emission. Furthermore, the thickness of about 3 cm of the DC electrode housing the SDD reduces the environmental background seen by the detector. All other electrodes are made of OFHC copper (mostly CW009A). They are gold-coated galvanically with a thickness of $1\,\mu\mathrm{m}$ and an underlayer of $10\,\mu\mathrm{m}$ silver. Most electrodes have got a cylindrical shape. The DV and AP electrodes, in contrast, are made from flat segments (Figure 3.5). This is one difference to previous setups of *a*SPECT. Flat electrodes lead to a more homogeneous work function on the electrode surface during manufacture [Kon11]. In addition, they allow a measurement of the work function of the electrodes using a scanning Kelvin probe, see Appendix A. The DV and AP electrodes were made from the same slab of copper and the electrode surfaces were machined and treated identically[4]. Both the DV and AP electrodes were polished before coating using a non-magnetic polish.

In between beam times aging of the surfaces was observed due to diffusion of Cu into the Ag layer and to some extend into the final top layer of Au [TP76, Pin79], leading to increased surface roughness contributing to increased field emission and as a result to an increased background during a beam time in 2011. As a consequence, the Au coating with its underlayer of

[2] FuG Elektronik GmbH model HCN 0,8M-800.

[3] Agilent model 3458A multimeter.

[4] Except for the bottom plate of the DV electrode: this plate had a mechanical defect, a deep scratch. To remove this the plate was remachined some time after manufacture. This led to slightly different surface properties, visible in the work function measurements, see Appendix A.

Table 3.1.: Typical voltage settings with respect to the DV during the 2013 beam time. In the case shown here E15 was not used as $E \times B$ drift electrode (symmetric). When operated in $E \times B$ mode to reduce background, side L of E15 was switched to the same voltage as E11 (asymmetric). For details of the electrodes see [BAB+08].

Electrode	Voltage (V)	Comments
E1	$+860$	EM mirror electrode
E8 (L/R)	$-1/-200$	Lower $E \times B$ drift electrode
E10	$0.4 \times U_{\mathrm{AP}}$	Variable
E11	$0.7125 \times U_{\mathrm{AP}}$	Variable
E12	$0.9000 \times U_{\mathrm{AP}}$	Variable
E13	$0.9925 \times U_{\mathrm{AP}}$	Variable
E14	U_{AP}	Main AP electrode, variable
E15 (L/R)	$0.9875 \times U_{\mathrm{AP}}$	$E \times B$ drift electrode (optional), variable
E16 (L/R)	$-1750/-2250$	Upper $E \times B$ drift electrode
E17	-15000	DC electrode

Ag was simply renewed shortly before a scheduled beam time. Prior to the assembly all electrodes were cleaned in an ultrasonic bath using the cleaning sequence soap (P3 Almeco 36), deionised water, solvent (isopropyl), and again deionised water. Before final installation any visible dust that had accumulated on the electrodes was removed using lint-free tissue. Using the identical material, identical production procedures like machining, polishing and coating and handling the electrodes identically resulted in similar properties of the work function and its dependence on environmental conditions like the formation of surface adsorbates with their dependence on temperature and pressure. After the production beam time in 2013 and until the measurement of the work function of the electrodes with the Kelvin probe, the electrodes were stored in a commercial deep freeze at a temperature of $< -18\,^{\circ}\mathrm{C}$. Since the diffusion coefficient follows an Arrhenius equation, the lower temperature effectively suppresses the aforementioned diffusion processes [PB72]. Additionally, the electrodes were enclosed individually in plastic bags filled with Argon to avoid contamination. The measured long-term stability of the work function of the electrodes after the beam time shows that these measures effectively suppressed the deterioration of the surfaces. Consequently, no significant change of their work function was the finding, see Appendix A.

Inside *a*SPECT, the neutron beam is shaped in front of the DV and further downstream towards the beam dump by several ^{6}LiF apertures [Bor10]. These apertures have been mounted originally on non-conductive Borosilicate glass plates. To avoid any potential charge up effect and therefore field leakage into the DV, the glass plates have been replaced by conductive

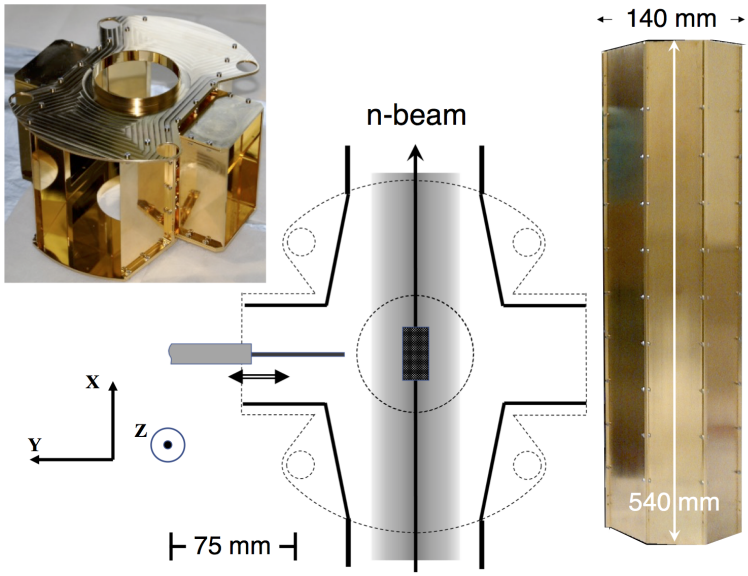

Figure 3.5.: Photograph of the DV electrode (left) and the main, octagonally shaped AP electrode (right) as used during the 2013 beam time. The sketch shows the collimated neutron beam (in gray) as it passes through the DV electrode. The dark area indicates the projection (to $z = 0$) of the fiducial decay volume in which the protons are magnetically focussed along the flux tube onto the two pads (2, 3) of the SDD. The side ports of the DV electrode are used for pumping and lateral access, e.g., beam profile measurements.

plates made out of BN and TiB_2[5] [Mai14, Wun16]. For the same reason the ^{6}LiF apertures have been sputtered with Ti.

A manipulator installed at the cross-piece on a side port of the spectrometer at the height of the DV electrode provides the possibility to insert probes into the centre of the DV electrode (Figure 3.5). It was used, among others, to insert Cu foils for measurements of the neutron beam intensity profile inside the DV, removing the necessity to extrapolate from beam profile measurements further up- and downstream of the DV, which had introduced a significant uncertainty in the past. ^{63}Cu and ^{65}Cu of the foil are activated by neutrons from the beam with half-lives of 12.7 h of ^{64}Cu and 5.1 min of ^{66}Cu. The X-rays and β^+ particles of ^{64}Cu in the activated Cu foil are imaged using a X-ray imaging plate and an image plate scanner. In Figure 3.6 the horizontal projection (y-axis) of the measured neutron beam profile is shown. Along the incident neutron beam the beam profile does not change, at least not across the effective neutron decay length of ~ 3 cm. This section is defined by the magnetic projection (in x-direction) of the decay protons along the flux tube onto the two detector pads (2, 3) of the SDD (cf. Figure 3.7). A flux tube is a generally tube-like (cylindrical) region of space which fulfils $\int B \cdot dA = \text{const}$. Both the cross-sectional area (A) of the tube and the field contained may vary along the length of the tube, but the magnetic flux is always constant. Therefore, for the radial displacement (r) of the decay protons along the symmetry axis (z) of the aSPECT cryostat it follows to a good approximation:

$$r(z) = r_{\mathrm{DV}} \sqrt{B_0/B(z)}\,. \tag{3.5}$$

Also shown in Figure 3.6 is a distribution measured using a reduced beam profile. The latter was used to investigate an important systematic effect of aSPECT, the edge effect, see Section 3.4.6.

Inside the aSPECT system an ultra-high vacuum is maintained by means of cascaded turbomolecular pumps, one at the height of the DV electrode and two at the detector. The cold bore of the cryostat, with temperatures locally reaching down to ~ 50 K, is acting as a cryopump. Furthermore, good vacuum conditions are maintained by internal getter pumps[6] at the height of the lower $E \times B$ electrode E8 and just below the DV electrode as well as an external getter pump[7] at the height of the DV electrode. With this vacuum set-up a pressure of $p_{\mathrm{DV}} \sim 5 \cdot 10^{-10}$ mbar was achieved close to the DV electrode after several weeks of pumping. This is far below the critical pressure for proton scattering off residual gas (cf. Section 3.4.10, [GBB$^+$05]). Despite the very good vacuum of aSPECT, the remaining residual gas gets ionised and trapped in Penning-like traps, created by the B- and E-fields of the spectrometer. The most prominent ones are indicated by ellipses in Figure 3.4. Stored protons, ions and electrons are removed to a large extent from these traps by two longitudinally split dipole electrodes, above the DV electrode (E8) and above the main AP electrode (E15) by

[5] ESK, DiMet Type 4.
[6] SAES type CapaciTorr C 400-2 DSK.
[7] SAES type CapaciTorr C 500-MK5.

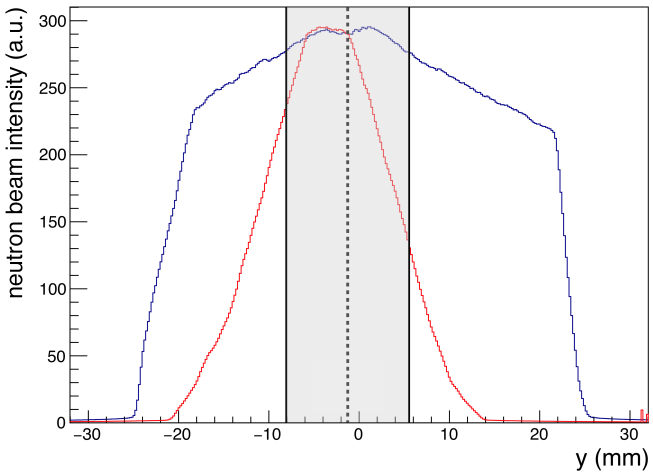

Figure 3.6.: Measured neutron beam profiles (projection onto the horizontal y-axis) for standard (blue) and reduced (red) beam size. The latter was used to investigate systematic effects. The shaded area represents the magnetic projection of the central pad (2) of the SDD onto the y-axis in the DV (cf. Equation (3.5)).

their $E \times B$ drift motion[8], see Figures 3.2 and 3.4. Hence, the low vacuum level (the vacuum gradually improved during the whole production run) and the removal of stored particles by $E \times B$ drifts reduces the retardation voltage-dependent background as one of the potential sources of systematics to an acceptable level. This background stems from positively charged rest gas ions ionised in the AP region (Section 3.4.5, [Mai14, Wun16]). The $E \times B$ electrode E16 does not serve for trap cleaning but is used to pre-accelerate protons which have passed the AP (ensuring that they overcome the increasing magnetic field) and to tune their alignment onto the detector.

The SDD for proton counting consists of an array of three detector pads of an area of $(10 \times 10)\,\mathrm{mm}^2$ each[9], see Figure 3.7 ([SHM+07, Sim10]). It has an entrance window of 30 nm thickness made from aluminium. The effective thickness of the silicon deadlayer behind this window was determined to $(45 \pm 4)\,\mathrm{nm}$ using a SRIM2008 [ZZB10] simulation. Use of a SDD with its intrinsic low electronic noise compared with Si PIN diodes, combined with a thin deadlayer, permits to lower the reacceleration voltage to $U_{\mathrm{DC}} = -15\,\mathrm{kV}$[10]. This significantly reduces field emission. The reacceleration voltage is provided by a high-voltage

[8] Charged particles moving in crossed E- and B-fields have a drift motion perpendicular to both fields [Jac98]. Due to this $E \times B$ drift, stored charged particles move outside of their storage volume, where they usually hit the electrode walls and are of no longer concern.

[9] pnSensor UM-141101.

[10] With a kinetic energy of $\sim -15\,\mathrm{kV}$ protons have a range of $\sim 280\,\mathrm{nm}$ in silicon (simulated with SRIM2008). This is much larger than the effective deadlayer of $\sim (30+45)\,\mathrm{nm}$ and the protons can easily be detected, see Figure 3.8.

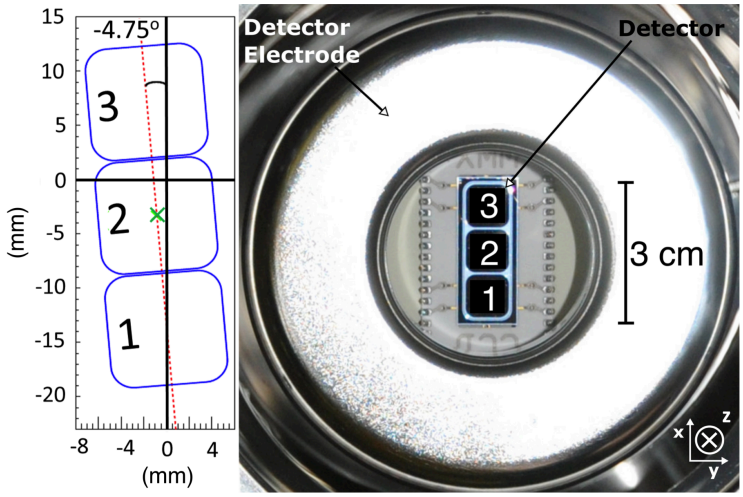

Figure 3.7.: The SDD with its three detector pads is mounted inside the detector cup electrode featuring a wall thickness of 3 cm, which is at the reacceleration potential of -15 keV. An offline analysis showed that the DC-electrode was not fully centred. The drawing on the left shows the aligment of the three detector pads with respect to the *a*SPECT coordinate system.

power supply[11].

Signals from the SDD are read out by a custom-built preamplifier and spectroscopy amplifier with logarithmic amplification (shaper). The shaped signals are digitised with a sampling ADC (12 bit, 50 ns resolution) [BAB+08, MGK+06, SGB+09]. Figure 3.8 shows a pulse-height spectrum (cf. Section 3.4.8) taken during the beam time. The proton peak is well separated from the electronic noise. The SDD is also sensitive to the β-particles from the decay of the neutron. They are clearly visible above the proton region in Figure 3.8 and steadily continue into the proton region, as can be deduced from a measurement at $U_{\mathrm{AP}} = 780\,\mathrm{V}$, where all decay protons are blocked by the potential barrier. Low energetic β-particles, indeed, form the dominant background in the proton region, see Figure 3.8. On the other hand, the highest energy β-particles from neutron decay will not lose all their energy in the active region of only $\sim 450\,\mu$m (depending on their impact angle). Therefore and because of the logarithmic amplification, the β spectrum trails off at intermediate β energies.

To determine the exact position of the detector with respect to the DV electrode, a copper wire of length $l \approx 8\,$cm aligned along the z-axis was mounted on the manipulator and then inserted into the DV electrode from the side ports. This wire was first activated in the neutron beam and then moved perpendicularly to the beam direction (beam off). By detecting

[11] Type: FuG HCN 35-35000.

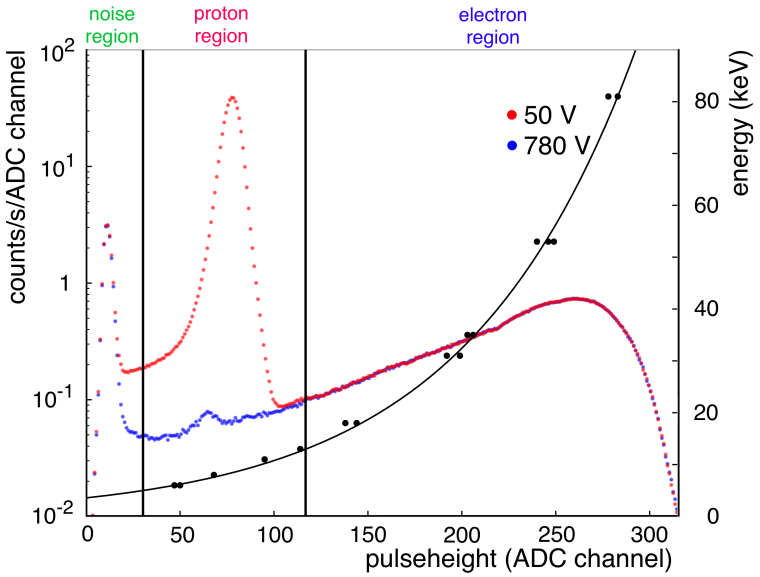

Figure 3.8.: Pulse height spectrum of protons and electrons from neutron decay (in red) measured at ILL in 2013 (config 1, cf. Table 3.3). The proton peak is well separated from the noise. A background measurement at $U_{\mathrm{AP}} = 780\,\mathrm{V}$ is shown in blue. The small peak visible in the 780 V spectrum is caused by ionised rest gas and reduced in later configurations, see Section 3.4.5. The two vertical lines denote the chosen lower (ADC channel: 29) and upper (ADC channel: 120) integration limits for the proton region. Demonstration of the logarithmic amplification of the SDD electronic (black solid curve) using characteristic X-rays of energy E (black circles). The right axis indicates the X-ray energy.

the emitted electrons from the activated copper with the SDD, the magnetic projection of the detector in y direction onto the DV electrode was determined. In order to measure the corresponding magnetic projection of the detector in x direction, i.e. along the beam direction, a second activated Cu wire ($l \approx 15\,\mathrm{mm}$) placed parallel to the y-axis was scanned along the x-axis [Mai14]. These measurements showed that the DC electrode was not fully centred in the cryostat (cf. Figure 3.7). As a consequence, the magnetic flux tube from one of the detector pads, pad 1, was partially crossing one of the electrodes (E12) of *a*SPECT. This was confirmed off-line by particle tracking simulations. On the one hand, this pad therefore experienced a significantly higher and also fluctuating background. On the other hand, some of the decay protons would scatter off this electrode, whereby they will lose an unspecified amount of energy. Therefore, the data from this detector pad could not be used for the analysis of a.

In a beam time in 2008 [SGB$^+$09] saturation effects in the detector electronics caused by the high energetic β-particles from neutron decay were observed [Sim10, Kon11]. This was solved by a reduction of the amplification of the preamplifier and a new spectroscopy amplifier with logarithmic amplification, see Figure 3.8. The logarithmic amplification was checked using a ^{133}Ba source and characteristic X-rays from Cu, Fe and Pb excited by the radiation from the ^{133}Ba source. This improvement also allowed to measure the energy spectrum of the β-particles during the beam time in 2013 (see Figure 3.8), limited at higher energies only by the thickness of the sensitive area of the detector of $450\,\mu$m.

Two systematic effects are associated with the proton detection: first, even though the proton energy at the detector varies only from 15.00 keV to 15.75 keV, the energy-dependence of the backscattering of the protons at the SDD has to be taken into account at the precision needed for *a*SPECT (Section 3.4.7). Second, since the diaphragm E7 described in [BAB$^+$08] has been omitted in the electrode system, the beam profile is much wider than the detector, see Figure 3.6. Since the profile is non-uniform and asymmetric over the projected area of the detector, protons close to the edges of the detector may be falsely detected or lost depending on their radius of gyration and azimuthal phase with which they arrive at the SDD. This energy-dependent so-called edge effect has to be taken into account in the analysis (Section 3.4.6).

3.3. Measurement with *a*SPECT

Several beam times were taken with *a*SPECT at the cold neutron beam line of PF1b [ADH$^+$06] at ILL. The beam time in 2008 showed that the spectrometer was fully operational but the aforementioned saturation effect of the detector prevented a result on a. This saturation effect was solved for a beam time in 2011. However, strong discharges, mostly inside the AP trap (Figure 3.4), again foiled a successful beam time: Temporal fluctuations of the measured background count rate, as well as their strong dependence on the retardation voltage precluded a meaningful data analysis. At times, an exponential increase in the background events was seen. To prevent saturation of the detector and to empty the trap, the retardation voltage had to be prematurely zeroed. Such Penning discharges in systems with good vacuum and crossed

magnetic and electric fields can be initiated by field emission and may be self-amplifying due to a feedback from secondary ionisation of the residual gas under a range of specific conditions (see e.g. [BVB+10]). Such discharges of similar high-voltage induced background have been observed at other experiments in the past [FBP+16, FGV+14, KSB+05]. For *a*SPECT it was found that degradation of some electrode surfaces had caused increased field emission leading to these discharges. The above-mentioned improvements eliminated that problem. This was shown with measurements in 2012 in an offline zone in the ILL neutron hall, see [Mai14]. The beam time of 100 days in 2013 then constituted the production measurement for a new determination of a.

3.3.1. The measurement procedure

The 2013 beam time consisted of measurement runs with a typical duration of half a day. Initially, the experimental settings were tuned and optimised. This included finding the settings for the $E \times B$ electrodes to minimise the background and to optimise the steering of the protons onto the detector[12] with respect to count rate, edge effect, etc.. After this optimisation procedure the experimental settings were kept constant for several days in a row for measurements of a. Measurements runs with the same settings of electrodes and magnetic fields are grouped into a so-called configuration for the data analysis (see Table 3.2). In order to study the major systematic effects (Section 3.4), dedicated measurements were taken at detuned settings of the electrodes and/or different beam profiles to study the enhanced effect.

Within a measurement run measurements were organised in sequences of applied voltages U_{AP} that were repeated until a run was stopped. A typical measurement sequence used is shown in Figure 3.9. In order to eliminate first order temporal drifts (time scale $> 30\,\mathrm{min}$) during the measurements, e.g. due to a variation of the neutron flux, the measurement sequence was not in ascending or descending order of U_{AP} but alternated the voltage as shown. Each measurement at a given voltage U_{AP} in the measurement sequence consists of its own measurement cycle:

- Initially the neutron beam is blocked and U_{AP} is set to $U_{\mathrm{AP}} = 0\,\mathrm{V}$. Data taking starts at $t = 0\,\mathrm{s}$. After $t_{\mathrm{AP,\,on}} = 10\,\mathrm{s}$, the AP electrode is ramped up to U_{AP} (cf. Table 3.2)[13]
- Between $20\,\mathrm{s} \leq t \leq 40\,\mathrm{s}$, instrumental- and environmetal-related background is measured.
- At $t_{\mathrm{n,on}} \sim 40\,\mathrm{s}$, the neutron beam is switched on by means of a fast neutron shutter (B_4C) placed in the neutron beam line about 5 m upstream of the DV electrode [Mai14].

[12] The $E \times B$ electrodes can steer the protons by $\mathcal{O}(\mathrm{mm})$ at the place of the detector.

[13] The time to ramp up (down) to $\sim 97\,\%$ of the full potential difference is about 5 s. The measurement cycle was only continued after reaching sufficient stability of U_{AP} (using the feedback from the precision voltmeter [Sim10].

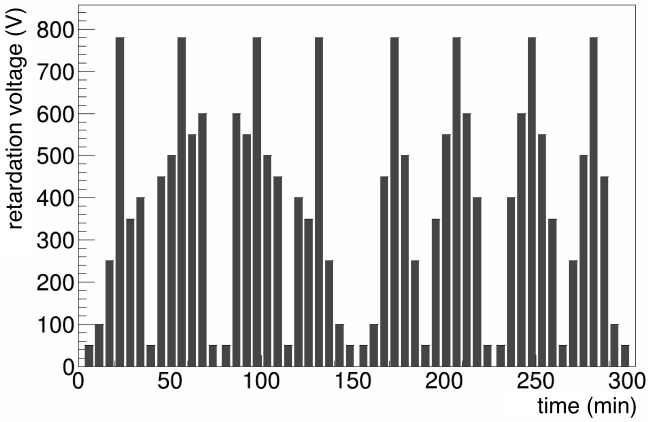

Figure 3.9.: Measurement sequence of the 2013 beam time which repeats after 300 min until data taking is stopped. Each bar in the diagram corresponds to a measurement cycle of ~ 5 min duration for the respective value of U_{AP} and has a time structure as shown in Figure 3.16 of Section 3.4.5.

- For pre-defined shutter opening times t_{op} of 50 s, 100 s, and 200 s, the decay protons are counted. After $t_{\mathrm{n,off}}$, background is measured again for about $\Delta t_{\mathrm{int}} \sim 20$ s in order to extract a possible retardation voltage-dependent background (Section 3.4.5).
- Approximatively 30 s after closing the shutter, U_{AP} is ramped down again to ensure that stored particles in Penning-like traps (cf. Figure 3.4) are definitely gone.
- After another ~ 50 s, data taking is completed for that particular measurement cycle. The individual sections of data acquisition add up to a total duration of about 5 min. The timing diagram of such a cycle is shown in Figure 3.16 of Section 3.4.5 in which background contributions are discussed in more detail.

Each measurement sequence contains an above-average number of 50 V and 780 V measurement cycles. The 50 V measurements with the highest proton count rate are needed with good statistics in order to normalise the integral proton spectrum and are also used to check the temporal stability of the incoming neutron flux. The 780 V measuring cycles (cf. Figure 3.8) together with the recorded background measurements during shutter off serve for a complete background analysis (Section 3.4.5).

3.3.2. Data analysis

The measurements of Table 3.2 were used for the analysis of a. They include measurement configurations $c = 1, 2$ (ON), $3, 7$ with changes of the optimal parameter settings in order to investigate their influence on a. In configurations $c = 4, 5,$ and 6, the neutron beam profile has

been reduced to considerably enhance a major systematic effect, i.e., the edge effect. With $c = 2$ (OFF) - mirror off in config 2 - the 4π symmetry of proton detection was broken, increasing the sensitivity to trapped protons in the DV region as well as to non-isotropic emission of the protons with respect to the spin of the decaying neutron in case of a finite beam polarisation.

The data analysis was performed for each detector pad (p) individually. For a given configuration (c), the pulse-height spectra of the individual measurement cycles with the same retardation voltage settings i ($i = 1,\ldots,10$, in total) were added (counts) to a sum spectrum (cf. Figure 3.8). From these sum spectra the integral count rates within the proton region can be calculated by dividing them by the measuring time accordingly. The proton region encloses the proton peak, which is located around pulse height channel 80. The lower integration limit was set at ADC channel 29 to exclude low energy electronic noise. The upper integration limit was set to safely include the high energy tail of the proton peak while minimising the amount of β-electron events (background) in the proton region. Consequently, some fraction of the protons, tail events below the lower integration limit and backscattered protons, as well as some pile-up events above the upper integration limit are not counted but lost. How these loss effects have been taken care of is discussed in Sections 3.4.7 and 3.4.8, respectively. In the proton region, typical count rates for aSPECT are $\sim 450\,\mathrm{cps}$ at $U_{\mathrm{AP}} = 50\,\mathrm{V}$ and $\sim 6\,\mathrm{cps}$ without protons ($U_{\mathrm{AP}} = 780\,\mathrm{V}$). Above the upper integration limit, the count rate of β-electron events is $\sim 70\,\mathrm{cps}$ independent of voltage settings.

3.3.3. Fit procedure

To simplify expressions, the indexing c and p for a given configuration and detector pad is omitted hereinafter. For the analysis of a from the integral proton recoil spectra, a fit is performed to the measured data, with a as one of the free fit parameters. In the ideal case without any systematic effect, this fit would be a χ^2 minimisation of the fit function $f_{\mathrm{fit}}(U_{\mathrm{AP}}, r_{\mathrm{B}}; a, N_0)$ to the measured proton spectrum. f_{fit} would only consist of the theoretical recoil energy spectrum $\omega_{\mathrm{p}}(T,a)$ (see Appendix B) folded with the transmission function $F_{\mathrm{tr}}(T, U_{\mathrm{AP}}, r_{\mathrm{B}})$ (Equation (3.4)) and a prefactor N_0 in units of cps (the second fit parameter) which serves to match the measured count rate spectrum:

$$\begin{aligned} f_{\mathrm{fit}}(U_{\mathrm{AP}}, r_{\mathrm{B}}; a, N_0) &= N_0 \int_0^{T_{\max}} \omega_{\mathrm{p}}(T,a) \cdot F_{\mathrm{tr}}(T, U_{\mathrm{AP}}, r_{\mathrm{B}})\, dT \\ &=: y_{\mathrm{theo}}(U_{\mathrm{AP}}, r_{\mathrm{B}}; a, N_0)\,. \end{aligned} \tag{3.6}$$

The χ^2 function in this case is given by

$$\chi^2 = \sum_{i=1}^{n} \frac{\left(y_{\mathrm{exp},i} - f_{\mathrm{fit}}(U_{\mathrm{AP}}, r_{\mathrm{B}}; a, N_0)\right)^2}{\left(\Delta y_{\mathrm{exp},i}\right)^2}\,, \tag{3.7}$$

where U_{AP} is the applied retardation voltage at measurement point i. The dead time-corrected count rates in the proton region are denoted by $y_{\mathrm{exp},i}$ (cf. Section 3.4.8) with $\Delta y_{\mathrm{exp},i}$ as their

Table 3.2.: Typical voltage settings of the *a*SPECT spectrometer during the 2013 beam time. When operated in dipole mode to reduce background, different voltages are applied on side L and R of E15, with side L set to the same voltage as E11 (asymmetric case, see Table 3.1). Configurations 3 to 7 use -200/-5 V instead of -1/-200 V for the lower $E \times B$ electrode. In configuration 6, the electric field direction of the dipole electrode E8 was repeatedly inverted.

Configuration name	Settings	Effect to be studied
Config 1	Equal to Table 3.1	Standard data taking
Config 2	Repeatedly switched mirror on/off	Proton traps in DV, see Section 3.4.9
Config 3	E15L = E11	U_{AP}-dependent background see Section 3.4.5
Config 4	Config 3 with reduced beam profile	Edge effect and U_{AP}-dependent, background, see Section 3.4.6
Config 5	Config 1 with reduced beam profile	Edge effect, see Section 3.4.6
Config 6	Config 5, E8 repeatedly interchanged	Influence of lower $E \times B$ on edge effect, see Section 3.4.6
Config 7	Config 3 with E3=+4 V, E6=−4 V	To prevent proton traps in the DV, see Section 3.4.9

statistical uncertainties. The theoretical proton recoil spectrum $\omega_{\mathrm{p}}(T,a)$ is given by Eq. (3.11) in [Glü93]. This spectrum includes relativistic recoil and higher order Coulomb corrections, as well as order-α radiative corrections. These corrections are precise to a level of $\Delta a/a \sim 0.1\,\%$.

The χ^2 fit of Equation (3.7), however, shows a strong correlation (> 0.9) among the fit parameters N_0 and a with a correspondingly large correlated error on the extracted value of the β-$\bar{\nu}_e$ angular correlation coefficient a. In order to reduce this correlation considerably, the proton integral count rate spectrum is fitted by a distinctly better fit function largely orthogonalised with respect to the fit parameters N_0 and a according to

$$\begin{aligned} f_{\mathrm{fit(n)}} &= \int_0^{T_{\max}} N_0 \cdot \omega_{\mathrm{p(n)}}(T,a,r_{\mathrm{B}}) \cdot F_{\mathrm{tr}}(T,U_{\mathrm{AP}},r_{\mathrm{B}})\, dT \\ &=: y_{\mathrm{theo(n)}}\,. \end{aligned} \tag{3.8}$$

Here, a normalised differential proton recoil spectrum is used with

$$w_{\mathrm{p(n)}}(T,a,r_{\mathrm{B}}) = \mathrm{norm}(a,r_{\mathrm{B}}) \cdot \omega_{\mathrm{p}}(T,a)\,. \tag{3.9}$$

The normalisation factor $\mathrm{norm}(a, r_\mathrm{B})$ is given by

$$\mathrm{norm}(a, r_\mathrm{B}) = \left(\int_0^{751\mathrm{V}} \frac{y_\mathrm{theo}(U_\mathrm{AP}, r_\mathrm{B}; a, N_0)}{N_0}\, dU_\mathrm{AP} \right)^{-1} \tag{3.10}$$

to provide a theoretical integral proton spectrum $y_\mathrm{theo(n)}$ of area N_0 which does no more depend on a in contrast to the integral value of y_theo of Equation (3.6).

In the actual conduction of the experiment one has to deal with systematic effects, like shifts and inhomogeneities of the applied electric and magnetic fields or background and its possible dependency on the retardation voltage, etc., which alter the measured integral proton spectrum. This can be taken into account by additional functions f_sys which modify the spectrum accordingly. For each systematic effect (j) the function depends on a set of fit parameters $\{fpar_j\}$ representing the coefficients of a polynominal expansion up to order 4 of the quantities U_AP[14], T, or y_theo. The polynomial approach with these variables (including the constant function as zero order polynomial function) is sufficient to describe all possible modifications on the spectrum's shape by the investigated systematic effects listed in Section 3.4.

The corresponding fit function is then given by

$$\begin{aligned} &f_\mathrm{fit(n)}\left(U_\mathrm{AP}, r_\mathrm{B}, y_\mathrm{theo(n)}; a, N_0, \{fpar_{j=1}\}, \{fpar_{j=2}\}, \cdots\right) \\ &= N_0 \cdot \left(\int_0^{T_\mathrm{max}} \omega_\mathrm{p(n)}(T, a, \langle r_\mathrm{B}\rangle) \cdot F_\mathrm{tr}(T, \langle U_\mathrm{A}\rangle, \langle r_\mathrm{B}\rangle)\, dT \right)_{f_\mathrm{sys}^{j'}} + \sum_{j \neq j'} f_\mathrm{sys}^{j}\left(U_\mathrm{AP}, r_\mathrm{B}, y_\mathrm{theo(n)}; \{fpar_j\}\right) . \end{aligned} \tag{3.11}$$

The integral expression indexed by $f_\mathrm{sys}^{j'}\left(U_\mathrm{AP}, r_\mathrm{B}, T; \{fpar_j\}\right)$ means that for certain systematic errors (j') the corresponding function is included as a modification of the integral expression: Concerning the transmission function $F_\mathrm{tr}(T, \langle U_\mathrm{A}\rangle, \langle r_\mathrm{B}\rangle)$, one has to describe the average retardation potential $\langle U_\mathrm{A}\rangle$ as a function of U_AP, i.e., $\langle U_\mathrm{A}\rangle = f_\mathrm{sys}^{\langle U_\mathrm{A}\rangle}\left(U_\mathrm{AP}; fpar_{\langle U_\mathrm{A}\rangle}\right)$ (cf. Section 3.4.3) and to replace the magnetic field ratio $\langle r_\mathrm{B}\rangle \rightarrow f_\mathrm{sys}^{\langle r_\mathrm{B}\rangle}\left(\{fpar_{\langle r_\mathrm{B}\rangle}\}\right)$, a zero order polynomial function (cf. Section 3.4.2). Proton backscattering in the deadlayer (dl) of the SDD is taken into account by modifying the energy recoil spectrum $\omega_\mathrm{p(n)}(T, a, r_\mathrm{B}) \rightarrow f_\mathrm{sys}^\mathrm{dl}\left(T; \{fpar_\mathrm{dl}\}\right) \cdot \omega_\mathrm{p(n)}(T, a, r_\mathrm{B})$ (cf. Section 3.4.7).

The fit parameters we introduce in f_sys^{j} may have correlations with the value of a as a result of the χ^2 minimisation. To get a statistically meaningful handle on these correlations, we combine the data acquired for the determination of a with *supplementary* measurements and simulations of the different systematic effects to an overall data set. From the now more comprehensive fit to this overall data set we can determine the value and uncertainty of a

[14] In the argument of f_sys^{j} we have set $\langle U_\mathrm{A}\rangle = U_\mathrm{AP}$ since corrections on the applied retardation voltage U_AP are of 2^nd order here.

including correlations with the respective parameters used to correct for systematic effects. In general the additional measurements/simulations of systematic effects (j) are described by n_j measured values $y^j_{\mathrm{sys},k}$ with $k = 1,\ldots,n_j$. Together with their functional descriptions $g^j_{\mathrm{sys}}\left(U_{\mathrm{AP}}, T, r_{\mathrm{B}}, y_{\mathrm{exp}}, y_{\mathrm{theo(n)}}; \{gpar_j\}\right)$, they are implemented in the χ^2-fit of the overall data set as

$$\chi^2 = \sum_{i=1}^{n} \frac{(y_{\mathrm{exp},i} - f_{\mathrm{fit(n)}}(U_{\mathrm{AP}}, r_{\mathrm{B}}, y_{\mathrm{theo(n)}}; a, N_0, \{fpar_{j=1}\}, \{fpar_{j=2}\}, \ldots))^2}{(\Delta y_{\mathrm{exp},i})^2} + \sum_j \sum_{k=1}^{n_j} \frac{(y^j_{\mathrm{sys},k} - g^j_{\mathrm{sys}}(U_{\mathrm{AP}}, T, r_{\mathrm{B}}, y_{\mathrm{exp}}, y_{\mathrm{theo(n)}}; \{gpar_j\}))^2}{(\Delta y^j_{\mathrm{sys},k})^2} \,. \tag{3.12}$$

The first term on the right hand side of Equation (3.12) is the original χ^2 Equation (3.11) now including all systematic corrections in the fit function to describe the measured count rate spectrum at the measurement points i.

The second term - the double sum - describes the fit $g^j_{\mathrm{sys}}\left(U_{\mathrm{AP}}, T, r_{\mathrm{B}}, y_{\mathrm{exp}}, y_{\mathrm{theo(n)}}; \{gpar_j\}\right)$ on the supplementary measurements or simulations $y^j_{\mathrm{sys},k}$ with error bars $\Delta y^j_{\mathrm{sys},k}$, where the sum over j encompasses all systematic investigations applied. As in the case of f^j_{sys}, we have set $\langle U_{\mathrm{A}} \rangle = U_{\mathrm{AP}}$ in the argument of g^j_{sys}. f^j_{sys} and g^j_{sys} may or may not be the same function. This depends on how we get access to the relevant systematic effect through the supporting measurements/simulations and on how these results have to be transferred to f^j_{sys} in order to make the appropriate correction on the systematic effect (j) in the integral proton spectrum. That is why the parameter set $\{fpar_j\}$ and $\{gpar_j\}$ which enter into the fit may be different for a given systematic effect. This, for example, is the case when describing the background with its retardation voltage-dependent part (cf. Section 3.4.5).

The 'comprehensive' fit has to be applied to each pad and measurement configuration individually, since the systematic effects may vary between pads and configurations. However, for the final result both detector pads and all selected configurations have to be included in the final global fit with a being the same fit parameter for all, but all other systematics individual for the respective pad (p) and configuration (c). Formally, the so-called global χ^2 fit can be expressed as

$$\chi^2_{\mathrm{global}} = \sum_c \sum_p \chi^2_{c,p} \tag{3.13}$$

introducing here again the c and p dependency of the χ^2 function (expressions on the right-hand side of Equation (3.12) and adding them up accordingly.

The routine we employed is based on Wolfram Mathematica and has been used for other experiments in the past [HKH$^+$04, TAB$^+$13, AHK$^+$14].

3.3.4. Field and particle tracking simulations

In order to understand the behaviour of the experimental set-up and to determine several systematic uncertainties quantitatively, simulations of the electric and magnetic fields were performed, as well as particle tracking simulations. For this purpose, the open-source KASPER simulation framework is used, containing the KGeoBag, KEMField, and KASSIOPEIA packages [FGT+17, Cor14, Fur15]. The EM field and particle tracking simulation routines of KASPER were originally developed and used for *a*SPECT, then modified and hugely improved at KIT and MIT for the KATRIN experiment to determine the neutrino mass.

The *a*SPECT coils and electrodes geometry is implemented using the KGeoBag software package for designing generic 3-dimensional models for physics simulations. This geometry is forwarded to KEMField for electromagnetic potential and field calculations. At that point the applied currents, voltages (see Table 3.1) as well as the measured work functions of the particular electrode segments have to be set as input parameters. The different methods used for charge density and field calculation are described in [LŠA06, Hil17, Glu11]. The calculated fields together with the geometrical arrangement are then used for the particle tracking, performed with the KASSIOPEIA package [FGT+17]. In KASSIOPEIA, the track contains the initial particle state (position, momentum vector, and energy) as well as the current state which is consecutively updated as the simulation progresses. The equation of motion is solved at each step using an 8^{th} order Runge-Kutta algorithm. KASSIOPEIA also stores parameters like path length, elapsed time, number of steps in the trajectory calculation and exit condition identification containing the reason why track calculation was stopped, i.e., particle hits the detector plane, an electrode surface or is trapped in Penning-like field configurations. In the particle tracking simulation the weighting with the measured beam profile is taken into account.

To achieve the required precision on the simulated systematic corrections, $\sim 10^{10}$ protons had to be tracked with KASSIOPEIA resulting in a multi-core CPU computing time of $\sim 0.5\,\text{y}$[15]. In addition, 40 weeks of single GPU computation time with KEMField was necessary to solve the charge density distribution for the different electrostatic configurations. For details of the simulations see Appendix C.

3.4. Quantitative determination of the systematic effects

The systematic uncertainties relevant in this analysis lie in the knowledge of the transmission function and any effect that shows a dependence on the recoil energy or the retardation voltage. The relevant experimental systematic effects in no order of strength are

A. Temporal stability and normalisation,

B. Magnetic field ratio $\langle r_{\text{B}} \rangle$,

[15] Mogon high performance cluster of Mainz university [mog19].

C. Retardation voltage $\langle U_\mathrm{A} \rangle$,

D. Background,

E. Edge effect,

F. Proton backscattering and lower integration limit,

G. Dead time and pile-up,

H. Proton traps in the DV region,

I. Miscellaneous effects.

In the following we explain each effect, show with which method it was investigated and what its influence on the proton spectrum or on a is. Systematic effects are taken into account down to $\Delta a/a \leq 0.1\,\%$. In addition to these major systematics there are some minor systematics which have been shown to be small enough to not significantly influence the experimental result at the present level of precision. These are the adiabatic motion of the proton that has been taken care of in the design of the spectrometer, electron backscattering at the electrodes below the DV and higher order corrections in the fit function.

3.4.1. Temporal stability and normalisation

The temporal stability of the measurement was checked via the measured count rates in the proton region at 50 V retardation voltage where we have the highest event rates. The resulting good statistics can be utilised to trace possible systematic drifts and non-statistical fluctuations. Figure 3.10 shows the sequence of count rates (central pad) for the 50 V measurement runs in config 1 according to the scheme depicted in Figure 3.9. The individual 50 V runs were 200 s long (shutter opening time), resulting in a relative statistical accuracy of $\sim 0.34\,\%$ per pad at an average count rate of about 445 Hz. The distribution of the count rates around their common mean (standard deviation) essentially reproduces the expected error from pure counting statistics. In config 1, for example, a total of 193 runs at 50 V were conducted within 3.5 days including an interruption of about 30 h. For the central pad the average count rate is 445.65(11) Hz which after dead-time correction enters as data point $y_\mathrm{exp}^{\mathrm{config1,\,pad2}}(50\,\mathrm{V})$ in the integral proton spectrum (see Figure 3.1 (b)). Table 3.3 shows the average count rates at 50 V for the seven measurement configurations and the results of the respective χ^2 fits (constant fit). The distribution of count rates in all measurement configurations clearly indicate the absence of drifts $> 1\,\mathrm{Hz/day}$ (estimated conservatively). The influence of linear drifts on a exactly cancels as long as the drift period T_D is an integer multiple (n) of $t_0 \sim 150\,\mathrm{min}$ as can be deduced from Figure 3.9 with the worst case scenario when the drift kinks at a half-integer multiple of t_0. For the latter case we estimated the influence on a to be less than 0.1 % (relative) assuming a drift period of one day.

Table 3.3.: Average count rates in the proton region at 50 V for the different configurations (central detector pad). In case of $\chi^2/\nu > 1$, the error bars on the average count rates were scaled with $\sqrt{\chi^2/\nu}$.

Configuration	Start time	Average count rate at 50 V(s^{-1})	χ^2/ν
Config 1	06/28/2013	445.65(11)	1.07
Config 2 (ON)	07/05/2013	445.57(27)	1.06
Config 3	07/26/2013	452.33(15)	1.27
Config 4	07/30/2013	395.82(21)	0.97
Config 5	08/01/2013	393.07(25	1.51
Config 6	08/04/2013	389.79(32)	0.61
Config 7	08/05/2013	443.36(16)	0.95

The average count rates for the other retardation voltage settings were extracted in a similar manner which then provide the remaining data points $y^{c,p}_{\mathrm{exp}}(U_{\mathrm{AP}})$ to determine the shape of the integral proton spectra differentiated according to configuration (c) and detector pad (p). In all cases the statistical error bars were scaled with $\sqrt{\chi^2/\nu}$ if the constant χ^2 fit to the temporal sequence of the rates showed a reduced χ^2 of $\chi^2/\nu > 1$ (ν: degrees of freedom).

3.4.2. Magnetic field ratio $\langle r_{\mathrm{B}} \rangle$

To precisely determine $\langle r_{\mathrm{B}} \rangle$, a proton-based NMR system[16] has been developed [Gua11]. It consists of two z-shaped glass tubes of inner diameter 2.5 mm and outer diameter 4 mm. Each glass tube is filled with a 1:1 mixture of acetone and ethanol which stays liquid down to 150 K. The central part of the z-shape is surrounded by a solenoidal NMR coil of ~ 1 cm length, which is oriented horizontally in the B-field of *a*SPECT (see inset of Figure 3.11 (a)).

The resonant circuits ($Q \sim 150$) were tuned to the respective resonance frequencies of ~ 92 MHz and ~ 18 MHz of the local B-fields inside the DV and AP electrode and finally matched to the standard impedance of the connecting lines (50 Ω).

Shortly after the 2013 beam time, the *a*SPECT spectrometer was brought to room temperature, and the whole electrode system including the detector setup was removed. To provide both free access to the inner part of the spectrometer and the necessary temperature conditions for the NMR probe measurements, an inverted, non-magnetic Dewar was built and fitted inside the bore tube of the spectrometer. After cooling down and ramping the magnetic field up again with the same current settings as before, the field along the z-axis was measured. The two probes measured simultaneously at fixed distance, with the lower probe positioned around

[16] The fields inside *a*SPECT were scanned with a Hall probe sufficient to bridge the dynamic field range along the entire flux tube and to measure B-fields with a relative accuracy of $\sim 5 \cdot 10^{-3}$.

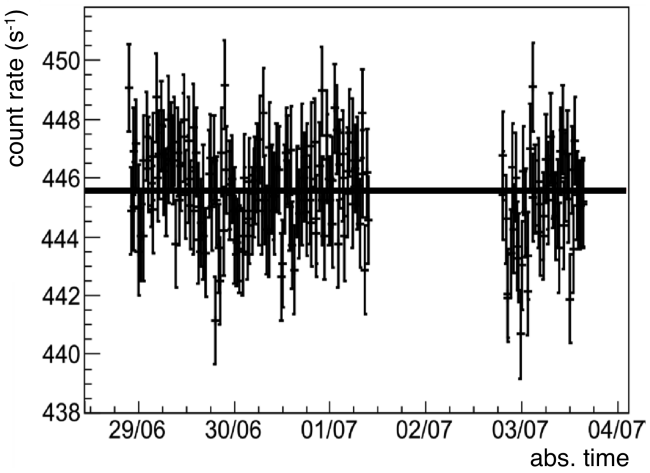

Figure 3.10.: Temporal sequence of 50V runs for config 1. Plotted are the average count rates of the central detector pad for the individual measurement runs of 200 s duration. The distribution of data points around their common mean(solid line) corresponds to the drawn error bars resulting from pure counting statistics. A constant fit to the data gives: $\chi^2/\nu = 1.07$.

the centre of the DV electrode and the upper probe at the place of the local field maximum at the height of the AP electrode. The measured fields are shown in Figure 3.11. They are used to confirm the quality of field simulations with KEMField for the given coil configuration of *a*SPECT and the respective current settings. Minor adaptations due to the influence of the return yoke on the internal magnetic field [KGB$^+$14] as well as environmental fields were taken into account.

The field simulations were used to determine the off-axis fields inside the DV and AP electrode. From the known field configuration and the beam profile measurements the magnetic field ratio $\langle r_\mathrm{B} \rangle$ as result of the particle tracking simulation was determined. For details see Appendix C.4.

When electrode E15 was used as dipole electrode (config 3, config 4, config 7), the local magnetic field maximum in the AP region had to be slightly shifted ($\sim -3\,\mathrm{cm}$) by means of the external anti-Helmholtz coils (AHC). The resulting field changes in the DV and AP region were considered with their impact on $\langle r_\mathrm{B} \rangle$. Table 3.4 shows the $\langle r_\mathrm{B} \rangle$ values from particle-tracking simulations differentiated by detector pad and configuration.

This simulation-based error analysis must be extended by an offset error common to all $\langle r_\mathrm{B} \rangle$ values. The main contribution comes from the uncertainty of the exact position ($\pm 1\,\mathrm{mm}$) of the two NMR samples in axial direction (cf. Figure 3.11) with $(\Delta\langle r_\mathrm{B} \rangle / \langle r_\mathrm{B} \rangle)_\mathrm{pos.} = 1.7 \cdot 10^{-5}$. Although the field ratio is quite robust to repeated ramping the superconducting magnets

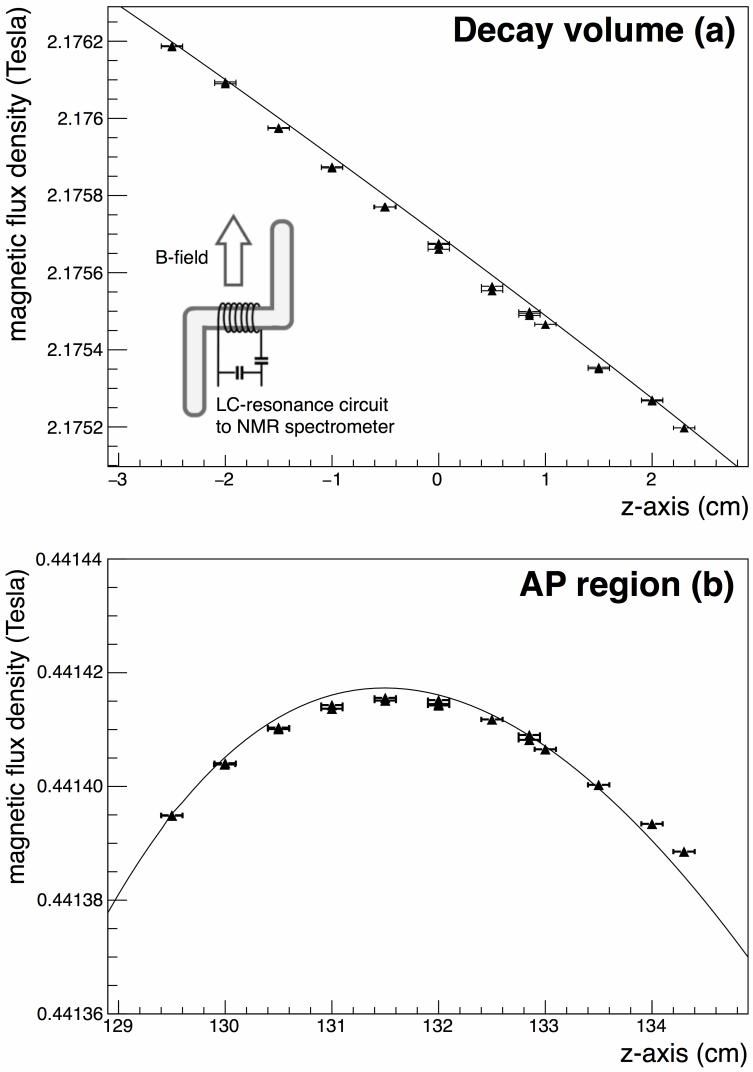

Figure 3.11.: NMR measurements of the magnetic field on-axis around the centre position of the DV and the AP electrodes. The uncertainties in the field measurement correspond to the symbol size and mainly reflect the measurement reproducibility. The positioning error of the NMR probe was estimated to be $\pm 1\,\mathrm{mm}$. The solid lines are the results from KEMField field simulations based on the known *a*SPECT coil configuration as well as the current settings used in the 2013 beam time. (a) The B-field inside the DV exhibits a small axial gradient of $\sim 2 \cdot 10^{-4}\,\mathrm{T/cm}$ to ensure that no decay protons get trapped by the magnetic mirror effect between the DV and EM. Inset: Sketch of NMR probe used to measure the fields. (b) In the AP region the B-field has a tiny, local maximum to provide sufficiently adiabatic motion close to the AP [GBB+05, GDL+13].

Table 3.4.: Simulated $\langle r_B \rangle$ values. The uncertainty is dominated by Monte Carlo statistics. Possible influences of beam position variation (± 1 mm) and differences due to standard and reduced beam profile on $\langle r_B \rangle$ are included in the given uncertainty which is $\sim 6 \cdot 10^{-6}$ relative. The table lists the start values obtained from simulations/measurements and the corresponding fit results. The error given with the fit results is the uncertainty in $c_0^{\langle r_B \rangle}$, the value in the last line ('offset') indicates $c_{0,\mathrm{offset}}^{\langle r_B \rangle}$ and its uncertainty.

	$c_0^{\langle r_B \rangle}$: Config 1, 2, 5, 6 (symmetric)	$c_0^{\langle r_B \rangle}$: Config 3, 4, 7 (asymmetric)
Pad 2 fit start value	0.2028870(12)	0.2028897(12)
Pad 2 fit result	0.2028870(15)	0.2028897(15)
Pad 3 fit start value	0.2028930(12)	0.2029001(12)
Pad 3 fit results	0.2028930(15)	0.2029001(15)

	$c_{0,\,\mathrm{offset}}^{\langle r_B \rangle}$: Config 1,..., 7
Pad 2/3 start value	$0. \pm 4.0 \cdot 10^{-6}$
Pad 2/3 fit result	$-2.9 \cdot 10^{-8} \pm 4.9 \cdot 10^{-6}$

down and up[17], moving the detector mechanics, changing the status of nearby valves, etc., the influences of which were estimated and included in the error budget (cf. Table 3.4) resulting in a total offset error of $< 2 \cdot 10^{-5}$ (relative).

To include these results into the fit procedure of Equation (3.12) we have to set $y_{\mathrm{sys}}^{\langle r_B \rangle} = \langle r_B \rangle$ and $\Delta_{\mathrm{sys}}^{\langle r_B \rangle} = 1.2 \cdot 10^{-6}$ (cf. Table 3.4) and further $g_{\mathrm{sys}}^{\langle r_B \rangle} = c_0^{\langle r_B \rangle}$ with $c_0^{\langle r_B \rangle}$ as free fit parameter. In the fit function of Equation (3.11) one has to replace $\langle r_B \rangle \to f_{\mathrm{sys}}^{\langle r_B \rangle} = c_0^{\langle r_B \rangle} + c_{0,\,\mathrm{offset}}^{\langle r_B \rangle}$. The parameter $c_{0,\,\mathrm{offset}}^{\langle r_B \rangle}$ is a restricted fit parameter in the fitting procedure which is Gaussian distributed around zero mean with standard deviation $\sigma = 2 \cdot 10^{-5} \cdot \langle \bar{r_B} \rangle = 4.1 \cdot 10^{-6}$. This way the offset error on $\langle r_B \rangle$ is taken into account. In Table 3.4 the corresponding fit results for $\langle r_B \rangle$ including error bars are listed.

[17] The superconducting magnet shows a kind of hysteresis, which is a small, but known, effect [SSS68]). It disappears after the coils are warmed up above their critical temperature of $T_{\mathrm{crit}} = 9$ K, which was applied systematically for field changes.

3.4.3. Retardation voltage $\langle U_{\mathrm{A}} \rangle$

Like $\langle r_{\mathrm{B}} \rangle$, the retardation voltage $\langle U_{\mathrm{A}} \rangle$ directly enters the transmission function Equation (3.4). Sources of uncertainties of $\langle U_{\mathrm{A}} \rangle$ are

1. the measurement precision of the applied voltage,
2. inhomogeneities and instabilities of the potential in the DV and the AP region due to spatial and temporal variations of the work function of the DV and AP electrodes, and
3. inhomogeneities of the potential in the DV and AP region due to field leakage.

3.4.3.1. Measurement precision of the applied voltage

The retardation voltage U_{AP} was measured continuously at the readback connections of the AP and the DV electrode using the Agilent 3458A multimeter. Each voltage reading was integrated for 4 s to achieve the required precision. The multimeter was calibrated at least annually and was working within specification during the beam time 2013, i.e., the corresponding precision of each measurement of the retardation voltage was $\Delta U_{\mathrm{AP,\,Agilent}} < 13\,\mathrm{mV}$ for all voltages. The short-time voltage stability was found to be better than 1.5 mV on the 1000 V scale.

3.4.3.2. Impact of spatial and temporal variations of the work function

*a*SPECT utilises gold-coated electrodes to obtain inert electrode surfaces, to achieve a high temporal stability of the surface properties, and to avoid any potential surface charges on an electrically insulating oxide layer [Dob74]. The work function of these electrodes modifies the actual retardation voltage measured between the DV and AP electrode. The work function (WF) of gold varies by up to $\Delta \mathrm{WF}^{\mathrm{Au}}/e \sim 500\,\mathrm{mV}$ depending on its crystalline structure and orientation [Hay12]. Besides, a WF decrease of as much as one volt may occur on exposure of water vapor to gold (humidity) [WF72]. All in all, this is significantly larger than the desired uncertainty of $\Delta\langle U_{\mathrm{A}} \rangle < 30\,\mathrm{mV}$ needed to keep retardation voltage related uncertainties of a below 0.3 %. Since only WF differences are relevant, the problem is largely relaxed if only common drift modes are present. Furthermore, WF differences may be greatly compensated if the electrodes have passed the same manufacturing process. This particularly applies for the DV and AP electrodes where we used the measures as described in Section 3.4.2 for the production process, cleaning procedures and depositary. Nonetheless, great efforts were made to measure precisely the WF of the individual electrode segments by means of a scanning Kelvin Probe. The WF investigations were conducted after the 2013 beam time in extensive measuring campaigns in the years 2014 and 2015. The time span of almost two years was also important to trace possible drifts and fluctuations of the WF. The safe knowledge about the actual WF during the 2013 run under the given measuring conditions in *a*SPECT was a

cornerstone to meet the required accuracies in the specification of the potential distribution inside the DV and AP electrodes. (details are presented in Appendix A).

3.4.3.3. Field leakage

Both the DV electrode and its surroundings are on ground potential to prevent possible field leakage into the DV. However, the WF of the DV electrode and those of the materials in immediate vicinity, i.e., bore tube (stainless steel), BN (TiB_2 enriched) collimation guide, and Ti-coated LiF frames are different, leading to field leakage into the DV through the large openings of the DV electrode (cf. Figure 3.5). The WF of these materials were measured and are shown in Table 3.5. The maximal WF difference between materials is $\Delta\mathrm{WF}/e \sim 500\,\mathrm{mV}$, with the bore tube and collimation materials more negative than the DV electrode, leading to a small potential bump for the protons inside the DV electrode. The potential distributions in the DV and AP region were finally simulated using re-scaled WF, i.e., from the measured relative WF the WF average of all DV and AP electrode segments was subtracted. Since only potential differences are relevant this measure is of no relevance.

Figure 3.12 shows the potential distribution along the z-axis inside the DV electrode and the adjacent electrodes which like the DV electrode are kept at ground potential. The distribution simulated by KEMField is essentially a superimposition of the potential drop between top and bottom plate of the DV electrode (cf. Figure 3.5) caused by the measured WF differences of $\sim 100\,\mathrm{meV}$ and the potential bump due to field leakage. For config 7, the red curve is the relevant one, since the adjacent electrodes were put at $\pm 4\,\mathrm{V}$ to prevent protons from being trapped in the DV region.

The AP electrode with an aspect ratio of 3.6:1 is long compared to its diameter and shielded at both ends by overlapping electrodes with only slightly lower potential (cf. Table 3.1). Field simulations show that the residual field leakage results in a homogeneity of the potential in the AP region of better than 2 mV. This can be deduced from Figure 3.13 where the shallow potential maximum is plotted for an applied retardation voltage of 400 V. It peaks at $z \sim 131\,\mathrm{cm}$, i.e., it ideally overlaps with the position of the local B-field maximum (see Figure 3.11). However, the inclusion of the electrodes' WF which were only accessible to measurement after the 2013 beam time somewhat lowers the actual potential values inside the AP electrode and makes the distribution slightly asymmetric. Still, sufficient overlap with the local B-field maximum is given. Similar results were obtained for config 3 and config 4 (E15 dipole electrode used in $E \times B$ mode), where both the E- and B-field maxima were shifted by $\sim 3\,\mathrm{cm}$ towards the DV region.

3.4.4. The effective retardation voltage $\langle U_\mathrm{A} \rangle$

The inhomogeneities of the potential in the DV and AP region lead to a slight shift of the effective retardation voltage $\langle U_\mathrm{A} \rangle$ from the applied voltage U_AP. Figure 3.14 shows the corresponding deviations $\Delta U_\mathrm{AP} = \langle U_\mathrm{A} \rangle - U_\mathrm{AP}$ determined from particle tracking simulation for a

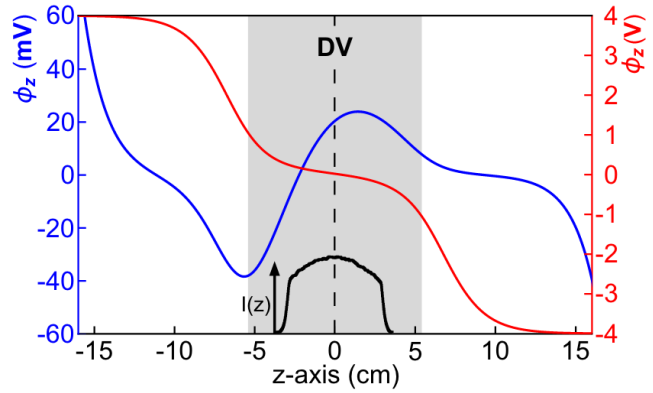

Figure 3.12.: Simulation of the potential distributions along the z-axis in the DV region. The blue curve (left axis) shows the potential for configurations 1-6 based on the measured work functions of the DV electrode and surrounding materials. The red curve (right axis) shows the resulting potential for config 7 where the electrodes below and above the DV were set to +4 V and -4 V, respectively. Inset $I(z)$: Measured beam profile along the z-axis (intensity in arbitrary units).

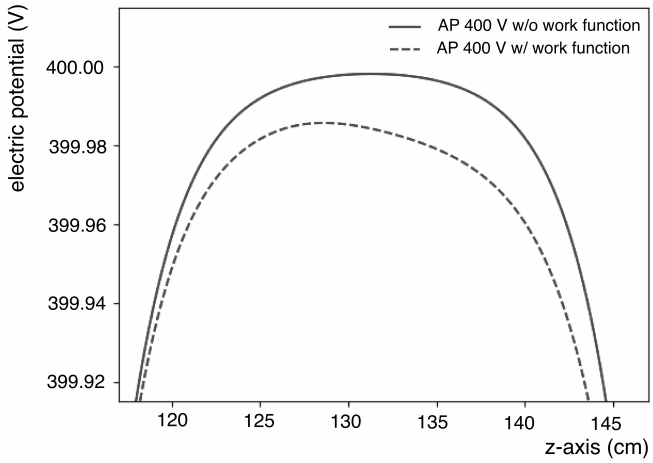

Figure 3.13.: Simulated potential distribution along the z-axis in the AP region with the retardation voltage set to 400 V. A symmetric distribution around $z \sim 131$ cm (solid curve) is the result if only field leakages are considered. The inclusion of the electrodes' WF leads to an asymmetric shape with somewhat lower potential values and a slightly shifted position of the maximum (dashed curve).

Table 3.5.: Measured WF differences between materials at *a*SPECT and the Kelvin probe tip: $\mathrm{WF_{rel}} := \mathrm{WF_{tip}} - \mathrm{WF_{mat}}$. The individual measurements have a measurement uncertainty of $\pm 30\,\mathrm{meV}$, whereas the average WF differences of the DV and AP electrode segments could be determined more precisely on a statistical basis (see Appendix A). The fact that the titanium-containing materials for the collimation show a higher WF than the gold-coated electrodes can be attributed to titanium oxide layers which lead to a significant increase of the WF of the substrate [GCP06].

Location	Surface material	Relative work function
DV electrode (average)	Au	$(113 \pm 12)\,\mathrm{meV}$
AP electrode (average)	Au	$(127.4 \pm 2.5)\,\mathrm{meV}$
Bore tube	Stainless steel 316L	$(-85 \pm 30)\,\mathrm{meV}$
Collimation	BN with TiB_2	$(-240 \pm 30)\,\mathrm{meV}$
Collimation	Ti-coated LiF	$(-394 \pm 30)\,\mathrm{meV}$

total of four selected voltages (see Appendix C.4). The error bars give the statistics of the MC simulation and include the uncertainties from a $\pm 1\,\mathrm{mm}$ variation of the true beam position as well as changes of the beam profile (standard/reduced). The functional dependence can be described by a straight line; however, a distinction must be made between the individual detector pads and configuration runs with symmetrical or asymmetrical setting of the E15 electrode.

The corresponding assignment in the fit procedure according to Section 3.3.3 is then:

$$\begin{aligned} y_{\mathrm{sys}}^{\langle U_\mathrm{A}\rangle}(U_{\mathrm{AP},k}) &= (\langle U_\mathrm{A}\rangle_k - U_{\mathrm{AP,\,k}}) \quad \text{with } k = 1,\cdots,4\,. \\ \Delta y_{\mathrm{sys}}^{\langle U_\mathrm{A}\rangle} &: \text{corresponding error bars from Figure 3.14} \\ g_{\mathrm{sys}}^{\langle U_\mathrm{A}\rangle} &= c_0^{\langle U_\mathrm{A}\rangle} + c_1^{\langle U_\mathrm{A}\rangle} \cdot U_{\mathrm{AP}} \\ f_{\mathrm{sys}}^{\langle U_\mathrm{A}\rangle} &= U_{\mathrm{AP}} + g_{\mathrm{sys}}^{\langle U_\mathrm{A}\rangle} + c_{\mathrm{AP,\,offset}}^{\langle U_\mathrm{A}\rangle} \end{aligned} \tag{3.14}$$

As in case of $\langle r_\mathrm{B}\rangle$ (cf. Section 3.4.2) the simulation-based errors must be extended by an offset error $c_{\mathrm{AP,\,offset}}^{\langle U_\mathrm{A}\rangle}$ common to all $\langle U_\mathrm{A}\rangle$ values. In the fit procedure, $c_{\mathrm{AP,\,offset}}^{\langle U_\mathrm{A}\rangle}$ is again a restricted fit parameter which is Gaussian distributed around zero mean with standard deviation $\sigma_{\mathrm{AP,\,offset}} := \Delta U_{\mathrm{AP,\,offset}} 30\,\mathrm{mV}$. In Table 3.6 the different contributions to $\sigma_{\mathrm{AP,\,offset}}$ are listed. Details are discussed in Appendix A.

Table 3.6.: Uncertainties from WF measurements and U_{AP} reading. For details, see Appendix A.

Effect	Uncertainty
Temporal changes of the WF differences between DV and AP electrode	$\Delta\mathrm{WF}_{\mathrm{DV/AP}}/e \leq 20\,\mathrm{mV}$
Transferability of WF measurements to UHV conditions inside *a*SPECT	$\Delta\mathrm{WF}_{\mathrm{UHV}}/e \leq 10\,\mathrm{mV}$
Influence of temperature gradients inside *a*SPECT on WF differences	$\Delta\mathrm{WF}_{\mathrm{grad}T}/e \leq 10\,\mathrm{mV}$
Measurement precision of applied voltage	$\Delta\mathrm{U}_{\mathrm{AP}}^{\mathrm{Agilent}} \leq 13\,\mathrm{mV}$
Influence of WF measurement uncertainties on particle tracking results	$\Delta\mathrm{U}_{\mathrm{AP}}^{\mathrm{p\text{-}tracking}} \leq 10\,\mathrm{mV}$
$\sigma_{\mathrm{AP,\,offset}}$ (quadratic sum)	30 mV

3.4.5. Background

The measured background in the proton region for the most part stems from electrons from neutron β-decay. Further contributions to the detected background are instrumental/environmental background, i.e., background measured with beam off[18], and other beam induced background, like γ-rays from neutron capture reactions and positive rest gas ions from secondary ionisation processes in Penning-like traps of the *a*SPECT spectrometer.

Independent of its origin, the background can be categorised into a component that depends on the retardation voltage and one that does not. The latter can be readily tolerated since it simply represents a count rate offset in the integral proton spectrum which can be considered as free fit parameter in the fit function of the χ^2 minimisation. Thus, this background (if small) may only slightly worsen the purely statistical sensitivity in the determination of a.

On the contrary, an U_{AP}-dependent background changes the shape of the spectrum and therefore the value of a extracted from the fit, if no quantitative description of its functional dependence is given and taken into account accordingly. In previous beam times, the origin of the U_{AP}-dependent background was investigated and measures to reduce or even to get rid

[18]This also includes the tail of the electronic noise leaking into the proton integration window (cf. Figure 3.8).

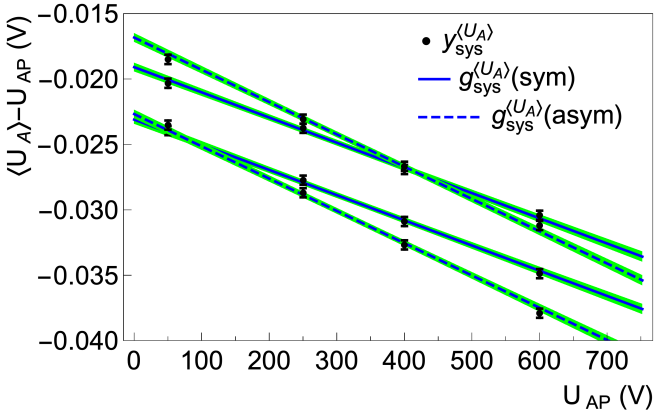

Figure 3.14.: Deviation $\Delta U_{\mathrm{AP}} = \langle U_{\mathrm{A}} \rangle - U_{\mathrm{AP}}$ extracted from particle tracking simulations for $U_{\mathrm{AP}} = 50, 150, 400,$ and $600\,\mathrm{V}$. A linear dependence on U_{AP} is the finding. However, there are differences in slope and intercept for the respective detector pad 2/3 (upper/lower pair of curves) and symmetric/asymmetric settings of the E15 electrode. The error bars are dominated by the statistics of the particle tracking simulation. Further drawn are the global fit results of $g_{\mathrm{sys}}^{\langle U_{\mathrm{A}} \rangle}$ (cf. Equations (3.12) and (3.13)) for the overall dataset.

of it were implemented.

The main source of the retardation voltage-dependent background is residual gas ionisation due to electrons from neutron decay and field electron emission in combination with Penning-like traps inside *a*SPECT which amplify this kind of background. Field emission often originates from microprotrusions and particulate contamination on the surface of the electrode, which enhances the local electric field. With the consequent and sustainable measures to improve the electrode surface quality (cf. Section 3.3), this particular source of ionisation could be largely eliminated. Beam off measurements during the 2013 run have shown that the field emission induced ion count rate in the proton region is $\sim 5 \cdot 10^{-3}\,\mathrm{cps}$ and its impact on a is negligibly small ($\ll 0.1\,\%$) [Mai14].

Looking at the composition of the rest gas inside *a*SPECT at low pressure and low temperature, hydrogen (H_2) accounts for the largest fraction[19]. The small bump in the proton region of the pulse height spectrum at 780 V (cf. Figure 3.8) stems from collisions of trapped low-energy electrons in the AP region with hydrogen molecules. These secondary electrons are mainly produced by the β-electrons from neutron decay whose trajectories along the magnetic flux tube hit the AP electrode [KD03, RD77]. The ionisation cross section for electron impact on H_2 is highest for energies around 50 eV [PGG09, YSH$^+$08], the energy range of secondary electrons which can be easily stored in the Penning-like trap around the AP electrode (cf. Fig-

[19]Measurements were performed with a mass spectrometer Pfeiffer Vacuum QMG-220 mounted at one of the *a*SPECT side ports. We identified the ratios $H_2 : H_20 : N_2$ as $1 : 0.16 : 0.17$ [Mai14].

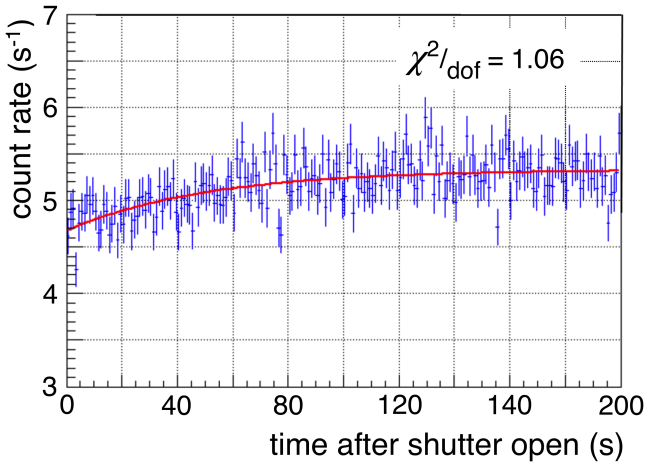

Figure 3.15.: Evolution of the background count rate in the proton region as a function of the time after opening the fast neutron shutter for $U_{AP} = 780\,V$. The red solid curve is a fit to the data: $y = p_0 + p_1 \cdot (1 - \exp(-t/\tau_s))$. The constant part of the background, p_0, is calculated to be 4.67(6) cps, the non-constant part shows an exponential saturation behaviour with $\tau_s = 51(10)\,s$ being the characteristic time constant and $p_1 = 0.66(6)$ cps the resulting count rate after saturation is reached. These background investigations were carried out in the commissioning phase before the runs config 1 to config 7 used in the analysis. During commissioning, the somewhat higher residual gas pressure produced a higher non-constant background ($\sim$ factor of 2) as compared to config 1 (cf. Figure 3.17).

ure 3.4).

H_2^+ (H^+) ions that are produced above the AP (or have sufficient energy to pass the AP) are accelerated towards the detector electrode (ions produced below the AP are stored and removed by the $E \times E$ electrode E8). If they hit the detector, they will cause background events with an energy similarly to the one of decay protons. Depending on the applied AP voltage the trap depth for those low energy electrons changes and with it the yield of hydrogen ions, leading to the retardation voltage dependent background. This background component cannot be measured directly during normal data taking due to the presence of protons from neutron decay, which result in a signal much larger than the background. Only for the 780 V measurement the background is directly accessible. Figure 3.15 shows the evolution of the background count rate in the proton integration window after opening the fast neutron shutter (cf. Section 3.3.1 for the measuring sequence). The retardation voltage-dependent background represents the non-constant part, the lapse of which reflects the filling of the trap, where saturation is reached after a characteristic time constant of about 50 s. Note that the data in Figure 3.15 were taken during commissioning at a higher pressure than during data taking.

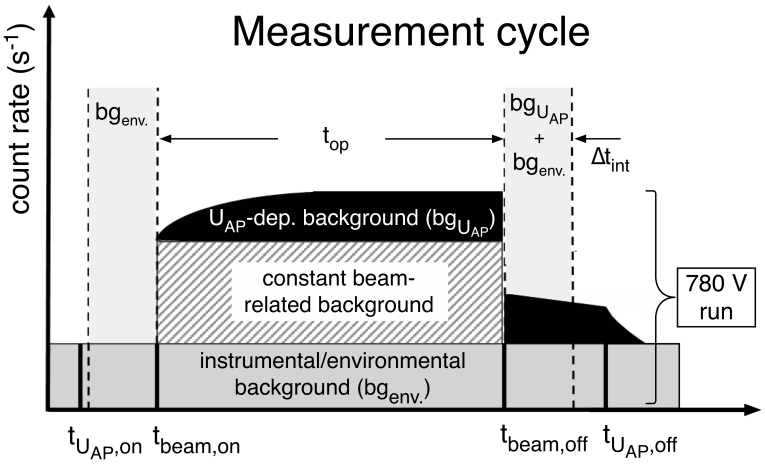

Figure 3.16.: Temporal sequence of a measurement cycle showing the different background contributions (not to scale). The U_{AP}-dependent background ($\mathrm{bg}_{U_{\mathrm{AP}}}$) can be extracted from the counting rate difference of two measurement intervals (Δt_{int}) displaced in time, one before shutter opening ($t_{\mathrm{beam,\,on}}$), the other immediately after closing the shutter ($t_{\mathrm{beam,\,off}}$), i.e., the regions enclosed by vertical dashed lines. For $t \geq t_{\mathrm{beam,\,off}}$, the trap empties again with the time constant τ_{s} allowing to monitor the yield of the rest gas ions ($\mathrm{bg}_{U_{\mathrm{AP}}}$).

For all other voltage settings, this background component must be extracted from the measured count rates in two distinguished time windows of the measurement cycle, the temporal sequence of which is depicted in Figure 3.16.

As consistency check, the 780 V measurement cycle apart from a known conversion factor should give the same values for the retardation voltage dependent background rate, once directly extracted from the integral value of the proton-like peak in the pulse height spectrum of Figure 3.8 (I) and then from the measurement procedure depicted in Figure 3.16 (II). A simple background model to describe the build up of ($\mathrm{bg}_{U_{\mathrm{AP}}}$) and its relaxation after shutter closed predicts for the ratio R of the time-averaged background rates with shutter open and after closing the shutter:

$$R = \frac{1-\tau_{\mathrm{s}}/\tau_{\mathrm{op}}}{\tau_{\mathrm{s}}/\Delta t_{\mathrm{int}}\,(1-\exp(-\Delta t_{\mathrm{int}}/\tau_{\mathrm{s}}))} = (0.9 \pm 0.1)\,. \tag{3.15}$$

Equation (3.15) holds for $t_{\mathrm{op}} \gg \tau_{\mathrm{s}}$ which is valid for $t_{\mathrm{op}} = 200\,\mathrm{s}$. The chosen time interval is $\Delta t_{\mathrm{int}} = 20\,\mathrm{s}$ (cf. Figure 3.16). The error bar reflects the uncertainty in τ_{s}. The direct comparison $\langle \mathrm{bg}^{\mathrm{I}}_{780\,\mathrm{V}} \rangle / \langle \mathrm{bg}^{\mathrm{II}}_{780\,\mathrm{V}} \rangle \sim 0.9$ confirms the expected ratio (cf. Figure 3.17).

Since the vacuum conditions inside aSPECT continuously improved during the 2013 measurement run, the background from ionised rest gas atoms was steadily decreasing. In addition, the electrode E15 was used as a dipole electrode ($E \times B$ drift electrode) which consider-

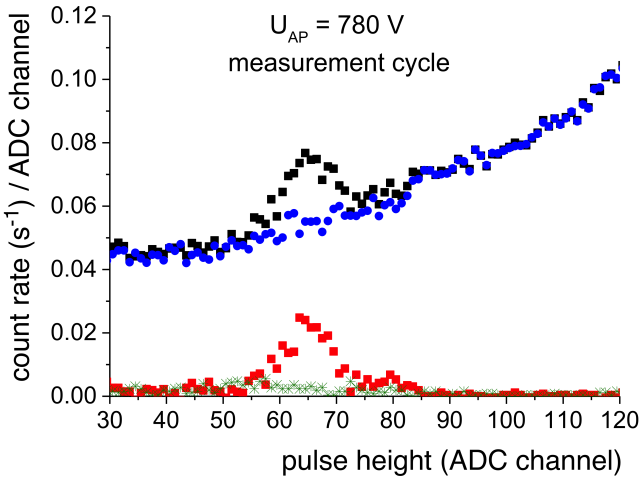

Figure 3.17.: Pulse height spectra measured at $U_{\mathrm{AP}} = 780\,\mathrm{V}$ within the proton integration window for config 1. Red squares: Spectrum of $\mathrm{bg}^{\mathrm{II}}_{780\,\mathrm{V}}$ extracted from the difference measurement (cf. Figure 3.16) with $\langle \mathrm{bg}^{\mathrm{II}}_{780\,\mathrm{V}} \rangle \sim 0.34\,\mathrm{cps}$. Black squares: Spectrum measured with beam on (shutter opened) with instrumental/environmental background (green stars) already subtracted. Subtraction of $\mathrm{bg}^{\mathrm{I}}_{780\,\mathrm{V}} = \mathrm{bg}^{\mathrm{II}}_{780\,\mathrm{V}} \cdot R$ according to the background model yields the blue data points (essentially electrons from neutron decay) with an integral count rate of $\sim 5.75\,\mathrm{cps}$.

ably reduced the number density of secondary electrons trapped in the AP region. Therefore, from config 3 on no AP voltage-dependent background could be identified anymore. Figure 3.18 shows the extracted background component $\left(\mathrm{bg}_{\mathrm{env}} + \mathrm{bg}^{\mathrm{II}}_{U_{\mathrm{AP}}}\right)_{\mathrm{pad\ 2}}$ immediately after $t_{\mathrm{beam,\ off}}$ at the different U_{AP} voltage settings for config 1 and config 3. To incorporate the retardation voltage dependent background in the fitting procedure, the data have to be added as $y^{\mathrm{bg}}_{\mathrm{sys},k}$ to the overall dataset with their statistical errors $\Delta y^{\mathrm{bg}}_{\mathrm{sys},k}$. To these data the following function has been fitted

$$g^{\mathrm{bg}}_{\mathrm{sys}}\left(U_{\mathrm{AP}}; c^{\mathrm{bg}}_0, c^{\mathrm{bg}}_2\right) = c^{\mathrm{bg}}_0 + c^{\mathrm{bg}}_2 \cdot (U_{\mathrm{AP}})^2 \,. \tag{3.16}$$

From config 3 on the constant fit function $g^{\mathrm{bg}}_{\mathrm{sys}} = c^{\mathrm{bg}}_0$ was sufficient to describe the data. The retardation voltage dependent term is then included in the fit function of Equation (3.11) according to

$$f^{\mathrm{bg}}_{\mathrm{sys}} = R \cdot \left(c^{\mathrm{bg}}_2 \cdot (U_{\mathrm{AP}})^2\right) + c_{\mathrm{bg}} \,. \tag{3.17}$$

The first term on the RHS has been multiplied by the conversion factor R to adapt it to the real voltage dependent background during 'beam on'. The second term represented by the free fit parameter c_{bg} includes all constant background components. After the first two config runs, $f^{\mathrm{bg}}_{\mathrm{sys}}$ of Equation (3.17) could be replaced by $f^{\mathrm{bg}}_{\mathrm{sys}} = c_{\mathrm{bg}}$.

3.4.6. Edge effect

The so-called edge effect originates from the gyration of the protons in the magnetic field. The radius of gyration, r_{g}, is the radius of the circular motion of a charged particle (q) of mass m in the presence of a uniform magnetic field given by

$$r_{\mathrm{g}} = \frac{m v_{\perp}}{|q|B} \,, \tag{3.18}$$

where $v_{\perp}$ is the component of the velocity perpendicular to the direction of the magnetic field B. Hence transmitted protons which arrive close to the edges of the detector[20] have a certain probability to be either detected or not, due to their gyration[21]. The probability to be detected depends on the initial transverse energy $T_{\perp} = T \sin^2\theta$ of the proton and thus via the transmission function on the retardation voltage. Given a homogeneous spatial distribution of the incident neutron beam in the DV, the gain and loss of protons at the edges of the detector cancel. From the measured beam intensity profiles along the y-axis both for the standard and reduced beam size (cf. Figure 3.6) an almost linear drop in intensity $-|dI/dy|$ at the site of the detector edges is the finding. This is shown in Figure 3.19 (a) illustrating the relative count

[20] The detector reaches its full response at a distance < 0.1 mm from its edges [Sim10]. This was measured at PAFF at Technische Universität München [MHP+07].

[21] The gyration radius of the protons at the height of the detector ($B_{\mathrm{DV}} = 4.4$ T) is $r_{\mathrm{g}} < 1.3$ mm.

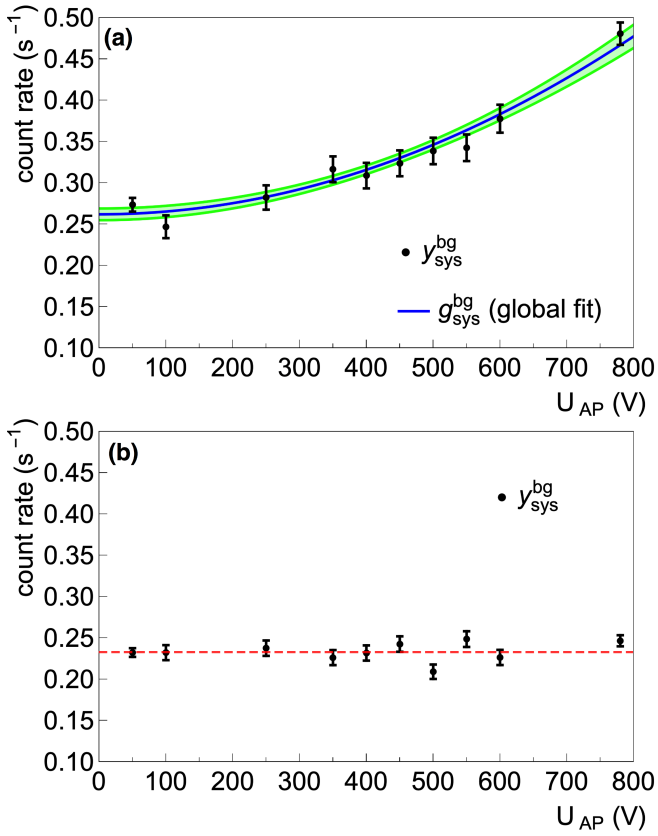

Figure 3.18.: Measured retardation voltage-dependent background in the proton region with pad 2. Shown is the count rate in the measurement interval immediately after $t_{\text{beam, off}}$ (cf. Figure 3.16) in dependence of the applied retardation voltage U_{AP} for config 1 (a) and config 3 (b). A clear increase of the count-rate is the finding for config 1, whereas a voltage dependency is no longer observed (dashed horizontal line to guide the eyes) for config 3 (as well as for the subsequent configuration runs). The constant instrumental /environmental background contributes with $\langle \text{bg}_{\text{env}} \rangle \sim 0.14\,\text{cps}$. Further drawn is the fit result of $g^{\text{bg}}_{\text{sys}}$ for the global fit to the config 1 dataset.

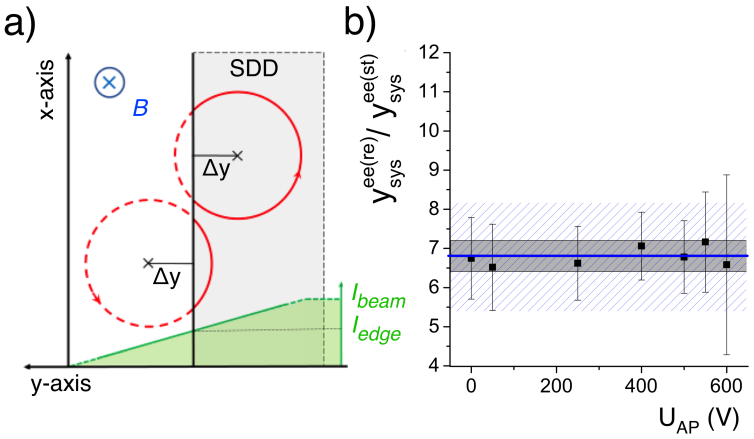

Figure 3.19.: (a) Relative count rate losses $\varepsilon(\Delta y)$ due to the edge effect shown for two gyrating protons of the same r_g at mean distance $\Delta y \leq r_g$ left and right from the detector edge. From elementary geometrical considerations it results for $|dI/dy|/I_{edge} \cdot r_g \ll 1$: $\varepsilon(\Delta y) = (|dI/dy|/I_{edge}) \cdot \Delta y \cdot (1 - \arccos(\Delta y/r_g)/\pi)$. (b) Ratio $\left(y_{sys}^{ee(re)}/y_{sys}^{ee(st)}\right)_{U_{AP}}$ of relative count rate losses for the reduced and standard beam profile from particle tracking simulations. Within the error bars, no dependence on the chosen retardation voltage settings (7 in total) can be observed (black horizontal line and grey shaded area represent the mean and its standard error). This finding coincides with the simple expression $\varepsilon_{re}/\varepsilon_{st}$ from Equation (3.20) which gives (6.9 ± 1.4) (mean and σ-error shown in blue).

rate losses $\varepsilon(\Delta y)$ by the example of two gyrating protons at the height of the detector plane in case of $|dI/dy| > 0$. For the average relative loss rate across the width L of the detector pad one obtains:

$$\begin{aligned} \langle \varepsilon(r_g) \rangle_L &= \frac{2\sqrt{B_0/B_{DV}}}{L} \cdot |dI/dy| \cdot \frac{I_{edge}}{\langle I_{beam} \rangle} \cdot \int_0^{r_g} \varepsilon(\Delta y) dy \\ &\approx \frac{2\sqrt{2}}{L} \cdot \frac{|dI/dy|}{\langle I_{beam} \rangle} \cdot \frac{3r_g^2}{8}, \end{aligned} \tag{3.19}$$

where $\langle I_{beam} \rangle$ is the average beam intensity across the detector acceptance (shaded area in Figure 3.6). The factor $\sqrt{B_{DC}/B_0} \approx \sqrt{2}$ compensates for the reduced slope (cf. Equation (3.5)) of $|dI/dy|$ if this quantity is extracted from Figure 3.6. For a given retardation voltage U_{AP} one can formally introduce an effective gyration radius (squared), $r_{g,\,eff}^2(U_{AP})$, which comprises the spectrum of gyration radii for transmitted protons which hit the detector. The latter number must be determined by particle tracking simulations to give precise numbers for the average relative loss rates, in particular their dependence on U_{AP}.

However, for the standard (st) and reduced (re) beam profile the ratio of the relative count rate losses results in a simple expression

$$\frac{\varepsilon_{\mathrm{re}}}{\varepsilon_{\mathrm{st}}} \approx \frac{|dI/dy|_{\mathrm{re}}}{|dI/dy|_{\mathrm{st}}} \cdot \frac{I^{\mathrm{st}}_{\mathrm{beam}}}{I^{\mathrm{re}}_{\mathrm{beam}}}\,, \tag{3.20}$$

which directly can be calculated from Figure 3.6 (or Table 3.3) giving: $\varepsilon_{\mathrm{re}}/\varepsilon_{\mathrm{st}} = (6.9 \pm 1.4)$. The error bar mainly results from the uncertainties in determining the actual slopes $|dI/dy|$ at the detector edges.

More precise numbers for the edge effect, particularly its dependence on the retardation voltage, are obtained from particle tracking simulations (see Appendix C.4). In these simulations, a homogeneous profile in the DV has been simulated. The actual profiles were then implemented by weighting the simulated homogeneous start distribution with the measured profile distributions. The relative loss rate $y^{\mathrm{ee}}_{\mathrm{sys}} = 1 - \Re$ then results from the ratio $\Re$ of the simulated hits at the detector with the actual beam profile and the homogeneous one. This procedure easily allows to vary the position of the beam in the DV region relative to the detector to determine the uncertainty due to an overall position uncertainty of ± 1 mm. The simulations have been performed for each detector pad and measurement configuration separately. It turned out that the differences in the edge effect for pad 2 and 3 are marginal. The same is true for the differences between configurations measured with the same beam profile. Therefore, results of the different pads and configurations have been combined. The resulting relative edge-effect losses at different retardation voltages are shown in Figure 3.20. The uncertainty $\Delta y^{\mathrm{ee}}_{sys}$ incorporates the MC statistics and the uncertainty in the beam position (± 1 mm). For the ratio $\left(y^{\mathrm{ee(re)}}_{\mathrm{sys}}/y^{\mathrm{ee(st)}}_{\mathrm{sys}}\right)_{U_{\mathrm{AP}}}$ we obtain the data points depicted in Figure 3.19 (b). Within error bars, these ratios show no dependence on the retardation voltage with their mean given by $\langle y^{\mathrm{ee(re)}}_{\mathrm{sys}}/y^{\mathrm{ee(st)}}_{\mathrm{sys}}\rangle = (6.8 \pm 0.4)$. This result is in very good quantitative agreement with the ratio $\varepsilon_{\mathrm{re}}/\varepsilon_{\mathrm{st}}$ (cf. Equation (3.20)) in which only the characteristics of the respective beam profile[22] enter. The data depicted in Figure 3.20 can be described by the function

$$g^{\mathrm{ee}}_{\mathrm{sys}}\left(U_{\mathrm{AP}};\{c^{\mathrm{ee}}_0, c^{\mathrm{ee}}_2, c^{\mathrm{ee}}_4\}\right) = c^{\mathrm{ee}}_0 + c^{\mathrm{ee}}_2 \cdot \left(U_{\mathrm{AP}}\right)^2 + c^{\mathrm{ee}}_4 \cdot \left(U_{\mathrm{AP}}\right)^4\,. \tag{3.21}$$

The relative edge-effect losses are then included in the fit function of Equation (3.11) according to

$$f^{\mathrm{ee}}_{\mathrm{sys}} = -g^{\mathrm{ee}}_{\mathrm{sys}}\left(U_{\mathrm{AP}};\{c^{\mathrm{ee}}_0, c^{\mathrm{ee}}_2, c^{\mathrm{ee}}_4\}\right) \cdot y_{\mathrm{theo(n)}} \tag{3.22}$$

with $y_{\mathrm{theo(n)}}$ from Equation (3.8).

[22] This comparison serves as a consistency test between a simple estimation and a complex simulation of the edge effect, which of course increases the confidence in the results.

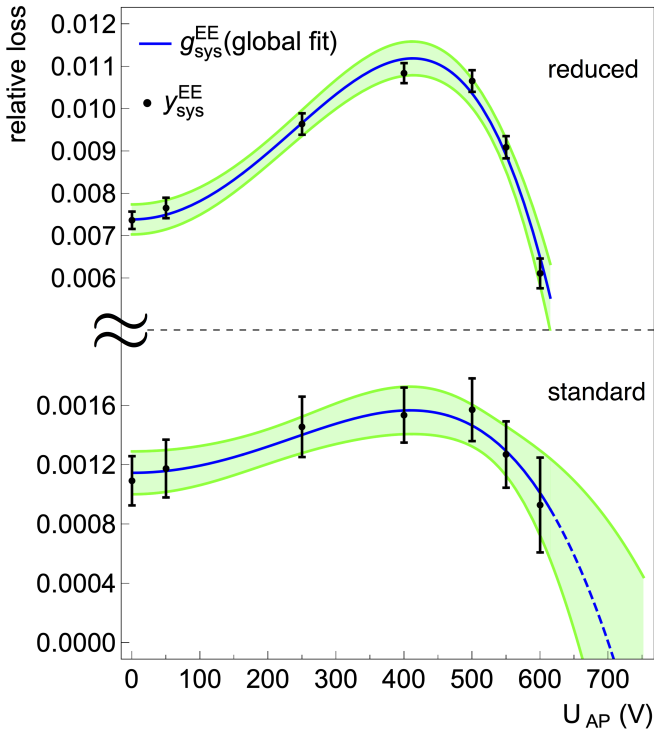

Figure 3.20.: Simulation of the retardation voltage dependence of the relative edge-effect losses $y_{sys}^{ee(st)}$ and $y_{sys}^{ee(re)}$ for the standard and reduced beam profile, respectively. Further drawn is the fit result of $g_{sys}^{ee(re)}(U_{AP})$ and $g_{sys}^{ee(rst)}(U_{AP})$ for the global fit to the overall data set.

3.4.7. Proton backscattering and lower integration limit

Protons that reach the detector can get backscattered, mostly due to scattering off the nuclei of the detector material. Consequently, these protons lose only a fraction of their kinetic energy in the detector. This is the dominant process that causes the low-energy tail of the proton peak in the pulse height spectrum in Figure 3.8. This backscattering is energy- and angle-dependent and even the small variation in proton energy in the range of $15.00\,\mathrm{keV} < (15.00\,\mathrm{keV} + T) < 15.75\,\mathrm{keV}$ may lead to an energy-dependent detection efficiency that can change the value of the a coefficient.

Protons which fall below the lower integration limit of the proton region and thus are not counted can be divided into two classes: a) Protons that deposit some energy in the active volume of the SDD and b) protons that do not deposit any energy in the active volume, i.e., protons that are already stopped in the deadlayer due to nuclear straggling. The former number can be determined by extrapolation of the low energy tail of the proton spectrum from the lower integration limit to zero energy for each retardation voltage. The latter is determined as a function of the proton energy T from the simulation package SRIM2008 [ZZB10]. The simulation uses the effective thickness of the deadlayer ($\sim 75\,\mathrm{nm}$) and an angle of incidence of 10° of the protons onto the detector. This angle is close to the average angle of incidence determined from particle tracking simulations of isotropically emitted protons through aSPECT. Further it is considered that backscattered protons towards the AP electrode which still stay in the magnetic flux tube will have a second chance after motion reversal due to reflection on the increasing potential to hit the detector, etc. However, some protons do not pass the deadlayer even after multiple attempts.

Figure 3.21 shows the fraction of protons $y^{\mathrm{dl}}_{\mathrm{sys},k}(k = 1, \cdots, 8)$ at initial energy T_k that do not interact in the active volume as a result of this simulation with $\Delta y^{\mathrm{dl}}_{\mathrm{sys},k}$ the statistical uncertainties. Therefore, the differential proton spectrum $\omega_{\mathrm{p(n)}}(T, a, r_{\mathrm{B}})$ has to be modified by the fractional losses of protons in the deadlayer which show an energy dependence of $\sim 1 \cdot 10^{-3}$. This correction is implemented in the fit by modifying Equation (3.11), so that

$$\omega_{\mathrm{p(n)}}(T, a, r_{\mathrm{B}}) \rightarrow f^{\mathrm{dl}}_{\mathrm{sys}} \cdot \omega_{\mathrm{p(n)}}(T, a, r_{\mathrm{B}}) \tag{3.23}$$

with $f^{\mathrm{dl}}_{\mathrm{sys}}(T) = 1 - g^{\mathrm{dl}}_{\mathrm{sys}}(T)$. The simulated data in Figure 3.21 can be described by a straight line $g^{\mathrm{dl}}_{\mathrm{sys}} = c^{\mathrm{dl}}_0 + c^{\mathrm{dl}}_1 \cdot T$.

The number of protons that do interact in the active volume, but deposit an energy below the detection threshold, was determined from the measured proton pulse height spectra. For the high statistics configurations config 1, config 3 and config 7, each detector pad and each retardation voltage the background spectrum at 780 V was subtracted from the corresponding pulse height spectrum to get the pure proton contribution. Each of these spectra was then fitted just above the lower integration limit using an exponential function [Leo94] (Figure 3.22, red line). Extrapolating the exponential function towards pulse height channel zero (Figure 3.22, green line), the loss due to the lower integration limit can be determined as a function of U_{AP} for each pad and configuration (green area in Figure 3.22). As this is a pure detector effect,

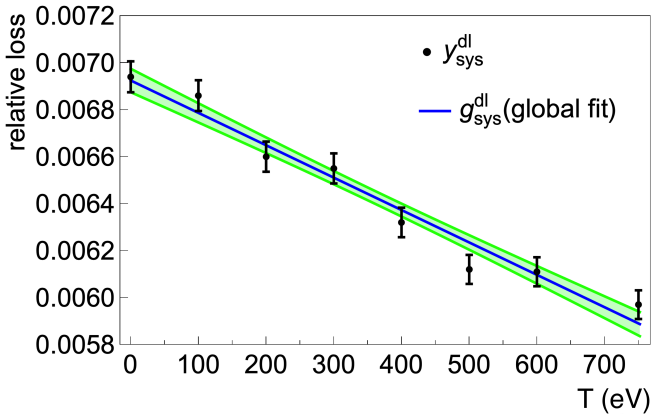

Figure 3.21.: Simulation of the fractional loss y^{dl}_{sys} of protons that do not reach the active volume of the detector but are stopped in the deadlayer due to backscattering. Further drawn is the global fit result of g^{dl}_{sys} to the overall dataset as a function of the initial kinetic energy of the protons.

the data from the different configurations can be combined per pad and retardation voltage, to achieve better statistics. In Figure 3.23, the loss of protons y^{tail}_{sys} is shown as a function of the retardation voltage. The uncertainties Δy^{tail}_{sys} are due to the quality of the exponential fit and therefore the extrapolation to ADC channel zero. The data points at 550 V and 600 V have got very low statistics, causing a bigger uncertainty of the extrapolation. The loss can be described by a straight line $g^{tail}_{sys}(U_{AP}) = c^{tail}_0 + c^{tail}_1 \cdot U_{AP}$ and is incorporated into the fit function of Equation (3.11) by

$$f^{tail}_{sys}(U_{AP}) = -g^{tail}_{sys}(U_{AP}) \cdot y_{theo(n)}\,, \tag{3.24}$$

where this correction is the same for each configuration and pad.

3.4.8. Dead time and pile-up

The dead time of the DAQ as well as the pile up both depend on the total count rate. This rate in turn depends, a.o., on the retardation voltage. Hence, both effects introduce a retardation voltage-dependent effect. As described in [Sim10], *a*SPECT uses a sampling ADC[23]. If a trigger has occured, the ADC values for a time window of 4 μs (event window) are stored in a memory buffer (cf. Figure 3.24). A second event arriving within this time will be recorded in the same event window. Due to the nature of the trigger (the DAQ system processes an event in 0.2 μs) the next event window has a minimum time difference of $T_{dead} = 4.2\,\mu$s. As per event window only one event, namely the first one, is counted in the analysis, a non-extendable dead

[23] Sampling frequency is 20 MHz, resulting in time bins with a width of 50 ns.

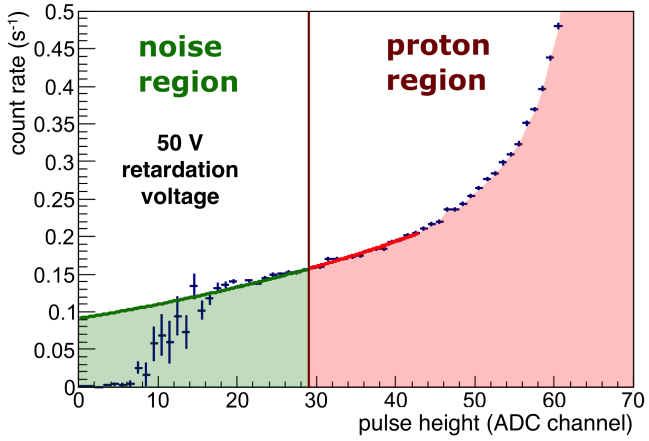

Figure 3.22.: Low energy region of the pulse height spectrum at $U_{\mathrm{AP}} = 50\,\mathrm{V}$ of config 1/ pad 3 after background subtraction measured at 780 V. The lower integration limit is depicted by the vertical line. The exponential fit to the pulse height spectrum just above the threshold (red line) is extrapolated to zero (green line). The corresponding area (in green) represents the loss of protons which deposit energy in the active volume of the SDD but fall below the lower integration limit.

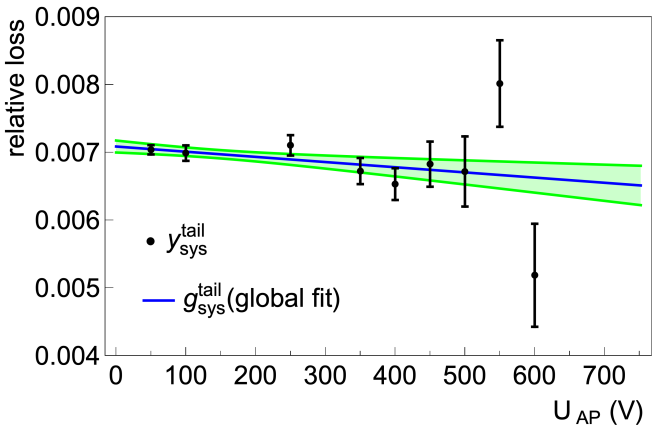

Figure 3.23.: Retardation voltage dependence of the proton loss $y^{\mathrm{tail}}_{\mathrm{sys}}$ in the active volume due to the lower integration limit. The relative loss is the green area in Figure 3.22 divided by the sum of red and green areas. Further drawn is the fit result of $g^{\mathrm{tail}}_{\mathrm{sys}}$ for the global fit to the overall dataset.

time correction [Leo94] has been performed in the following way

$$y_{\mathrm{exp}} = \frac{y_{\mathrm{exp}}^{\mathrm{meas}}}{1 - y_{\mathrm{tot}}^{\mathrm{meas}} \cdot T_{\mathrm{dead}}} \,. \tag{3.25}$$

$y_{\mathrm{tot}}^{\mathrm{meas}}$ is the total count rate detected[24], whereas $y_{\mathrm{exp}}^{\mathrm{meas}}$ is the measured integral count rate in the proton region. This correction for the dead time has been applied to the pulse height spectra of each pad, retardation voltage and configuration separately, resulting in $y_{\mathrm{exp},i}^{c,p}$ used for the analysis (cf. Section 3.3.3). It is important to know T_{dead} precisely in order to apply a good correction. With ΔT_{dead} unknown by $\pm 50\,\mathrm{ns}$, the uncertainty results in a negligible systematic error of $\Delta a/a \approx \pm 0.04\,\%$. This has been extracted from Equation (3.6) using the reference value a_{ref} [Kon11]. In the dead time correction of Equation (3.25) it is assumed that the events are occurring randomly, i.e., obey Poisson statistics. This, however, is not fulfilled since in aSPECT a maximum of 13.1 % of the decay electrons can be detected in coincidence with their correlated proton [Kon11]. In the experiment in the limit $U_{\mathrm{AP}} \to 0\,\mathrm{V}$ (Figure 3.1 (b)) we observe a slightly larger number of $N_{\mathrm{el}}/N_{\mathrm{p}}\,(0\,\mathrm{V}) \approx 16\,\%$, due to electron backscattering [Kon11]. The influence of these correlated events on the deadtime correction (Equation (3.25)) has been investigated by MC simulations. The total count rate can be decomposed according to

$$\begin{aligned} y_{\mathrm{tot}}^{\mathrm{meas}}(U_{\mathrm{AP}}) &= N_{\mathrm{p}}(U_{\mathrm{AP}}) + N_{\mathrm{el}} + N_{\mathrm{noise}} \\ &\equiv \left(0.68 \cdot N_{\mathrm{p}}(U_{\mathrm{AP}}) + N_{\mathrm{el}} + N_{\mathrm{noise}}\right) + 2 \cdot \left(0.16 \cdot N_{\mathrm{p}}(U_{\mathrm{AP}})\right) \,. \end{aligned} \tag{3.26}$$

The first term on the RHS represents the uncorrelated count-rate events, which are randomly distributed. The second term gives the rate of correlated electron/proton pairs. The time difference between correlated pairs (TOF spectrum) can be parametrised by a log-normal distribution

$$y = U_{\mathrm{peak}} \cdot \exp\left(-\frac{1}{2}\left(\frac{\ln\left((t-t_0)/\tau\right)}{\sigma}\right)^2\right) , \tag{3.27}$$

where the minimum TOF of decay protons detected with their correlated electrons is $t_0 = 7.2\,\mu\mathrm{s}$ for $U_{\mathrm{AP}} = 50\,\mathrm{V}$ up to $t_0 = 10\,\mu\mathrm{s}$ for $U_{\mathrm{AP}} = 600\,\mathrm{V}$ with $\tau \approx 2.8\,\mu\mathrm{s}$ and $\sigma \approx 0.7$, typically [Kon11]. In the MC simulation, the count rate events from $0.16 \cdot N_{\mathrm{p}}(U_{\mathrm{AP}})$ are again randomly distributed over the unit time interval of 1 s and the associated proton events are added with a time offset that reflects the TOF spectrum. Finally, dead time losses are determined by the query: $t_{i+1} - t_i \leq 4.2\,\mu\mathrm{s}$ in chronological order of the simulated events which differ due to the retardation voltage dependence of the total count rate (cf. Equation (3.26)). The simulation showed that the inclusion of correlated events in the dead time correction shifts the a coefficient by $|(a_{\mathrm{corr}} - a_{\mathrm{uncorr}})/a_{\mathrm{uncorr}}| = 0.1\,\%$ compared to Equation (3.25) which assumes

[24] In config 1 (pad 2), the total count rate at 50 V was $y_{\mathrm{tot}}^{\mathrm{meas}} \approx 530\,\mathrm{cps}$ with the following partial count rates in the respective integration regions: 439 : 74 : 17 for $N_{\mathrm{p}}(50\,\mathrm{V}) : N_{\mathrm{el}} : N_{\mathrm{noise}}$.

a purely statistically distributed event rate. Therefore, in our dead time correction this effect was taken into account.

For a proper pulse height determination, possible multiple pulses within the same event window have to be separable. In Figure 3.24, two pulses are shown occurring within one event window. To determine the correct pulse height of the first pulse, a spline interpolation $f_{\text{spline}}(t)$ has been performed. Using a simple curve sketching, pulse maxima, inflection points, etc. can be identified which allows to reconstruct the true pulse height (i.e., that of the first, triggering event) even in case of overlapping pulses. This method works down to a separation time between the two pulses of $\Delta t_{\text{s}} \sim 0.5\,\mu\text{s}$ (Figure 3.25). Two pulses with closer separation can only be partially differentiated or not at all which will lead to pile-up events. This effect is rate- and thus U_{AP}-dependent and has to be accounted for. In a first step, all events with two clearly separated peaks and the first peak having a pulse height in the proton region are identified. To this pulse height of the first peak, the pulse height of the second is added. If the sum of both pulse heights is higher than the upper integration limit, the event is selected. This selection ensures that only events from the proton region are taken, in which a pile up would push the first peak out of the proton region[25].

By counting all separable double pulses in the event window and creating their distribution as a function of their respective separation times Δt_{s}, the fraction of pile up events can be determined (cf. Figure 3.25). An almost constant number C_0 of counts per time bin is observed in the range $1\,\mu\text{s} < \Delta t_{\text{s}} < 2\,\mu\text{s}$. For $\Delta t_{\text{s}} \leq 1\,\mu\text{s}$ the number of separable pulses starts to decrease due to pile up, for $\Delta t_{\text{s}} > 2\,\mu\text{s}$ the second pulse maximum starts to move out of the event window. The number of pile up events is then extracted by extrapolating the constant C_0 to $\Delta t_s = 0\,\mu\text{s}$ and integrating the missing counts represented by the grey shaded area in Figure 3.25. The integral number of missing events divided by the measurement time is then the rate of pile up events used as correction. This procedure was performed for the high statistics runs config 1, 3, 7, for each pad and retardation voltage separately. The resulting count rate loss $y_{\text{sys}}^{\text{pile up}}$ as a function of the actual count rate in the proton region, y_{exp}, is shown in Figure 3.26 with the statistical uncertainties $\Delta y_{\text{sys}}^{\text{pile up}}$. The resulting functional dependence can be used as a correction for all configurations, as it originates from the DAQ being independent of the individual configurations. Hence, the pile up correction $y_{\text{sys}}^{\text{pile up}}$ shown in Figure 3.26 has been included in the fit as common correction with

$$g_{\text{sys}}^{\text{pile up}}(y_{\text{exp}};\{c_0^p,c_2^p\}) = c_0^p + c_2^p \cdot \left(y_{\text{exp}}(U_{\text{AP}})\right)^2 , \tag{3.28}$$

$$f_{\text{sys}}^{\text{pile up}} = -\left(c_0^p + c_2^p \cdot (y_{\text{theo(n)}})^2\right) . \tag{3.29}$$

As the pile up is a loss of count rate, it has to enter with a negative sign in the fit function of Equation (3.11).

[25] Pile up events which would still be within the proton region are not considered, as they are counted anyway.

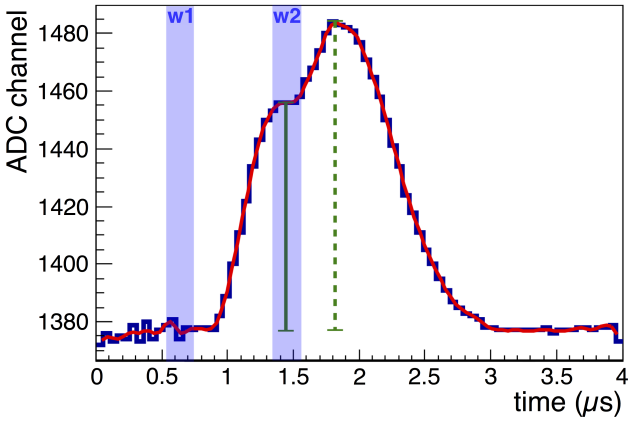

Figure 3.24.: Example of two individual proton events within one event window. The signal as recorded by the ADC is shown in blue, the spline interpolation in red. The position of the two events is indicated by the vertical green lines. The trigger algorithm is based on the comparison of two windows (w1, w2) within the shift register the data from the ADC is continuously shifted through. If the mean values of those two windows differ by more than an externally set threshold, the trigger condition is fulfilled. Window w1 is used to determine the baseline (first 15 time bins of 0.75 μs), whereas w2 is separated from w2 by 0.8 μs. For the subsequent signal analysis, the baseline is subtracted in each case (cf. Figure 3.8).

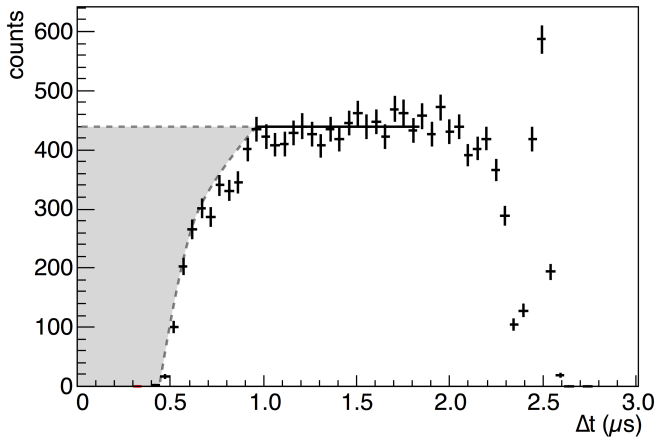

Figure 3.25.: Quantitative determination of pile up events (blue area) within the event window. The counts per time bin (50 ns) of the separated events (crosses) which reach a plateau at $1\,\mu\text{s} \leq \Delta t_\text{s} \leq 2\,\mu\text{s}$ are extrapolated to $\Delta t_\text{s} \to 0\,\mu\text{s}$. The integral number of pile up events divided by the measurement time is then the rate of pile up events. The data shown are from config 1 (pad 2) at $U_\text{AP} = 0\,\text{V}$ with the total measuring time of 38600 s. The reduction of the distribution above $2\,\mu\text{s}$ is caused by the finite length of the event window in which the maximum of the 2$^\text{nd}$ pulse no longer falls.

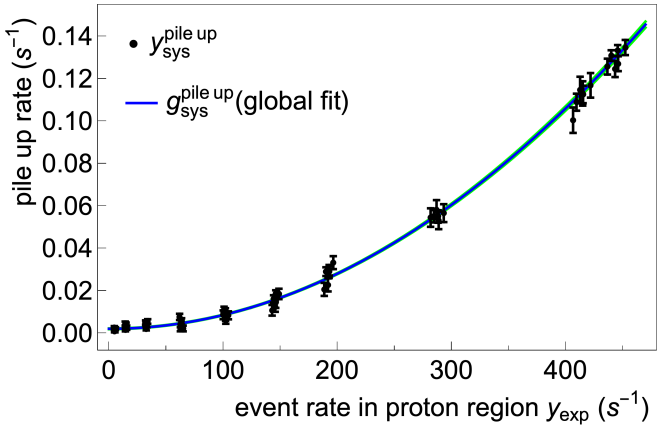

Figure 3.26.: Pile up rate $y_\text{sys}^\text{pile up}$ as function of the event rate y_exp in the proton region. Since y_exp depends, a.o., on the retardation voltage, the pile up results in a retardation voltage-dependent loss. Data taken from config 1, 3, 7, pad 2 and 3 are bundled in clusters for a given retardation voltage setting. Further drawn is the global fit result of $g_\text{sys}^\text{pile up}$ to the overall data set.

3.4.9. Proton traps in the DV region

Protons with low kinetic energy T and emission angle close to 90° with respect to the magnetic field can be trapped in the DV region. For example, the applied axial magnetic field gradient ($dB/dz < 0$) across the DV (cf. Figure 3.11 (a)) was a targeted measure to prevent such protons to be trapped between the DV and EM by the magnetic mirror effect, if they have been emitted into the rear hemisphere. In combination with an inhomogeneous electric potential ϕ_0, Penning-like traps can easily be created inside the DV region. Therefore, great care has been taken in the design of the electrode system of the *a*SPECT spectrometer to avoid these traps. In axial direction, the beneficial effect of field leakages from the positively-charged EM electrode (+860 V) and the negatively charged $E \times B$ electrode E8 (-1l-200 V) to some extent prevents protons from being stored in the DV region. WF inhomogeneities of the various electrode segments, however, lead to the actual potential inside the DV region as shown in Figure 3.12.

Protons with low longitudinal energy can be trapped by this potential and thus are lost for the measurement. Such a loss would bias the measured a value. To investigate traps inside the DV and their effect on a we performed

1. particle tracking simulations including the measured work function distributions in the DV along with an analytical approach to quantify the retardation voltage-dependent losses due to stored protons in the DV region,

2. measurements of a with an additional extraction field in the DV.

3.4.9.1. Particle tracking simulations

In the simulation (see Appendix C.4), protons are generated throughout the DV weighted with the measured neutron beam profile. Here, we only consider protons from the fiducial decay volume, which under optimal conditions would be losslessly guided along the magnetic flux tube onto the two detector pads (2, 3). In the actual B- and E-field configuration, their motion is tracked and if a proton is trapped or can leave the flux tube in radial direction by $E \times B$ drift, this proton is counted as lost. Figure 3.27 (inset) shows the yield of trapped protons as a function of the kinetic energy of the proton at its decay point inside the fiducial volume and the emission angle. The corresponding relative loss of protons $y^{\mathrm{tr}}_{\mathrm{sys},k}$ as a result from particle tracking simulations is shown in the same figure as a function of the retardation voltage ($k = 1,\ldots,9$). The uncertainties $\Delta y^{\mathrm{tr}}_{\mathrm{sys},k}$ shown in Figure 3.27 include statistical uncertainties from the Monte Carlo simulations as well as the uncertainties of the WF and field leakages and the uncertainty of the neutron beam profile. This loss is implemented in the fit function by

$$\begin{aligned} g^{\mathrm{tr}}_{\mathrm{sys}}\left(U_{\mathrm{AP}};\{c^{\mathrm{tr}}_0,c^{\mathrm{tr}}_1\}\right) &= c^{\mathrm{tr}}_0 \cdot U^{-2}_{\mathrm{AP}} + c^{\mathrm{tr}}_1 \cdot U_{\mathrm{AP}}\,, \\ f^{\mathrm{tr}}_{\mathrm{sys}} &= -g^{\mathrm{tr}}_{\mathrm{sys}} \cdot y_{\mathrm{theo(n)}}\,. \end{aligned} \tag{3.30}$$

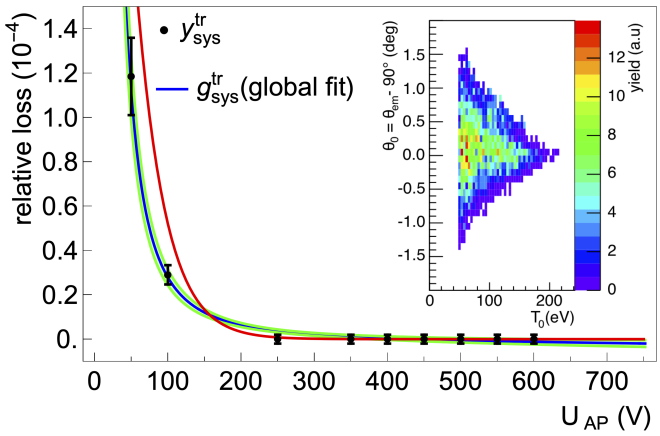

Figure 3.27.: Relative loss y^{tr}_{sys} due to trapped protons in the DV region as a function of the retardation voltage. The black data points are from particle tracking simulations whereas the red solid line is the result of an analytical calculation ($y^{tr,\,cal}_{sys}$) under simplified assumptions (proton trajectories: on-axis). Further drawn is the global fit result of g^{tr}_{sys}. Inset: Conditions for protons to be stored in the DV region. Shown is the colour-coded yield (a.u.) for the parameter space θ_0 and T_0, the proton emission angle $\theta_0 = \theta_{em} - 90°$ and its kinetic energy T_0 at the decay point.

For an analytical calculation of the expected relative proton losses in the DV region, one can use Eq. (3) from [GBB+05], which describes the longitudinal energy $T(P)$ of the proton at any trajectory point P and which after some manipulation using $T(z) = 0$ (on-axis trajectories are only considered) can be written as:

$$\theta_0 = \sqrt{\frac{B_0}{B_z}\left(\frac{e\phi_z - e\phi_0}{T_0}\right) - \frac{B_0 - B_z}{B_z}}\,. \tag{3.31}$$

T_0 is the proton kinetic energy at decay point z_0 with ϕ_0, B_0 the respective local electric potential and magnetic field. Correspondingly we have ϕ_z, B_z along the z-axis. θ_0 is the proton emission angle at z_0 related to the direction perpendicular to B_0 which causes proton reflection at position z. Using the distribution of the electric potential and the magnetic field along the z-axis in the DV region (Figure 3.12), the maximum emission angle $\theta_0^{\max}$ referred to 90° can be determined: $\theta_0^{\max}(T_0, z_0) = \max|\theta_0(T_0, z_0; V_z, B_z)|$. This angle also represents the relative number of stored protons of energy T_0 at z_0 for isotropically emitted protons, since we have: $2 \cdot \{\int_0^{\theta_0^{\max}} 2\pi \cos\theta d\theta / 4\pi\} \approx \theta_0^{\max}$.

The weighting with the normalised beam profile $I(z_0)$ (cf. Figure 3.12) along the z-axis gives $\langle\theta_0^{\max}(T_0)\rangle = \int_{-5\,\mathrm{cm}}^{+5\,\mathrm{cm}} I(z_0) \cdot \theta_0^{\max}(T_0, z_0) dz_0$ which to a good approximation can be parametrised by $\langle\theta_0^{\max}(T_0)\rangle = 0.00485 \cdot \exp\left(-(T_0 - 50\,\mathrm{eV})/39\,\mathrm{eV}\right)$ rad. Finally, the relative count rate loss due to trapped protons can be determined by including the differential proton spectrum and the transmission function:

$$y_{\mathrm{sys}}^{\mathrm{tr,\,cal}} = \frac{\int \langle\theta_0^{\max}(T_0)\rangle \cdot \omega_{\mathrm{p}}(T_0, a) \cdot F_{\mathrm{tr}}(U_{\mathrm{AP}}, r_{\mathrm{B}}; a, T_0) dT_0}{\int \omega_{\mathrm{p}}(T_0, a) \cdot F_{\mathrm{tr}}(U_{\mathrm{AP}}, r_{\mathrm{B}}; a, T_0) dT_0} \tag{3.32}$$

The result is shown in Figure 3.27, where $y_{\mathrm{sys}}^{\mathrm{tr,\,cal}}$ is plotted versus U_{AP} for $a_{\mathrm{ref}} = -0.103$. The relative loss rate is about 30 % higher than the one derived from particle tracking simulations. This is reasonable since the simplifications made, i.e., x, y-dependence of the electric potential (off-axis) were not taken into account, slightly overestimate the actual losses.

3.4.9.2. Measurement with additional extraction field

In order to quantify the effect of trapped protons on a, an E-field was applied along the z-axis of the DV electrode, strong enough to extract any trapped proton. To generate such a field, the connecting electrodes below and above the DV electrode have been set to +4 V and -4 V, respectively. This does not change the mean potential in the DV, but generates an electric field of the order of 6 V/m along the z-axis, see Figure 3.12. This field prevents protons from being stored in the DV region. A measurement of a with this field (config 7) coincides with a derived from config 1[26] within their respective uncertainties (cf. Section 3.5). In the fit routine of Equation (3.11), $f_{\mathrm{sys}}^{\mathrm{tr}}$ was not used for config 7.

[26] In config 1 to 6 these electrodes like the DV electrode are at ground potential.

3.4.10. Miscellaneous effects

3.4.10.1. Proton scattering off residual gas

The transmission of protons through /aspect/ may be modified by scattering of the protons off residual gas atoms. Three different kinds of collision can be distinguished: The protons may be neutralised by charge exchange processes, or change their energy and direction due to elastic or inelastic scattering. This problem has already been taken into account in the design phase of *a*SPECT: In order to be negligible for an experiment at the 0.3 % level, the residual gas pressure between the DV and the AP has to be below 10^{-8} mbar [GBB^{+}05]. With all the vacuum improvements in place since the offline beam time in 2012, a pressure of $\sim 5 \cdot 10^{-10}$ mbar was achieved close to the DV electrode, well below this critical pressure.

3.4.10.2. Adiabaticity

The calculation of the integral proton spectrum in Figure 3.1 (b) is based on exact adiabatic proton motion from DV to AP. The adiabaticity of the protons in the /aspect/ spectrometer was tested in [GBB^{+}05] by high-precision tracking simulations for various magnetic fields and for $U_{\mathrm{E8}} = -3\,\mathrm{kV}$ dipole potential of the lower $E \times B$ electrode E8. According to Table I of [GBB^{+}05], the relative change of a due to non-adiabaticity at $B_0 = 2.2\,\mathrm{T}$ is smaller than $4 \cdot 10^{-4}$. The proton motion adiabaticity improves with smaller absolute values of U_{E8} (due to the smaller kinetic energy of the protons in the E8 region), and we used $U_{\mathrm{E8}} = 200\,\mathrm{V}$ in our measurements (cf. Table 3.1). Therefore, the systematic relative change of the a value due to non-adiabaticity is far below $4 \cdot 10^{-4}$ in our measurements.

3.4.10.3. Doppler effect due to neutron motion

The motion of the decaying particle also changes the observed energies of the outgoing particles relative to the energies in the centre-of-mass system (CMS) of the decaying particle according to:

$$T_{\mathrm{LAB}} = T_{\mathrm{CMS}} + \frac{m_p}{m_n} T_{\mathrm{n}} + 2 \sqrt{\frac{m_p}{m_n}} \sqrt{T_{\mathrm{CMS}} \cdot T_n} \cos\theta_{\mathrm{CMS}}\,, \tag{3.33}$$

where θ_{CMS} is the polar angle in the CMS and $T_{\mathrm{n}} \approx 4\,\mathrm{meV}$ is the average energy of the cold neutron beam at PF1B. In *a*SPECT the magnetic field is transverse to the neutron beam and protons are detected with 4π acceptance. We find therefore a large cancellation of Doppler effects. After averaging over all θ_{CMS} angles (cf. Equation (3.33)), the lab energies of the protons are systematically higher by $\Delta T \sim 4\,\mathrm{meV}$ than their corresponding CMS energies. From Section 3.2.1 one can estimate this effect on a by $\Delta a/a \approx 0.005\,\%$ if ΔT is attributed to a corresponding uncertainty in the retardation voltage of $\Delta U_{\mathrm{AP}} = \Delta T/e$. A more refined analysis done by [GBB^{+}05] predicts even smaller relative changes. Hence, we do not expect any essential systematic uncertainty from the Doppler effect at our current level of accuracy.

3.5. Fit results and extraction of a

In order to get a first impression of the quality of the raw data, the individual configurations are fitted separately without any systematic correction. For that we use the (normalised) theoretical integral proton spectrum (cf. Equation (3.8)) and consider the background signal by a constant term, c_{bg}, which besides N_0 and a is another free fit parameter of the fit function given by:

$$f_{\mathrm{fit}}(U_{\mathrm{AP}}, r_{\mathrm{B}}; a, N_0, c_{\mathrm{bg}}) = y_{\mathrm{theo(n)}}(U_{\mathrm{AP}}, r_{\mathrm{B}}; a, N_0) + c_{\mathrm{bg}}\,. \tag{3.34}$$

Figure 3.28 shows the ideogram of a values for each configuration (j). The ideogram was built in the same manner of the PDG review [THH$^+$18] to convey information about possibly inconsistent measurements. Each data point is represented by a Gaussian with a central value a_j, error σ_{a_j}, and area proportional to $1/\sigma_{a_j}$. The standard deviation includes the correlated error from the fit. The contribution of the purely statistical error $\sigma_{a_j}^{\mathrm{stat}}$ (uncorrelated error) is indicated by the inner ticks at the error bars of the individual a values and shows that the total error σ_a is essentially the uncorrelated one. The uncorrelated error from the fit can be deduced from $\sigma_a^{\mathrm{stat}} = \left(\sum_i (1/\Delta a_i)^2\right)^{-1/2}$ with $\Delta a_i = \Delta y_{\mathrm{exp},i} / \left(dy/da\right)_i$. The $\Delta y_{\mathrm{exp},i}$ are the statistical uncertainties of the measured count rates $y_{\mathrm{exp},i}$ at the respective retardation voltage settings[27] (i). The derivative $(dy/da)_i$ expresses the sensitivity of $y_{\mathrm{exp},i}$ to changes in a at measurement point (i) of the integral proton spectrum (cf. Figure 3.1 (b)).

The central peak of the ideogram which culminates at $a \simeq -0.106$ comprises the configuration runs (blue) with the standard parameter settings. At its wings a shoulder towards positive a values and a bump structure on the opposite side can be identified. For configuration runs 4, 5, 6a, and 6b (green data points) with the reduced beam profile, the enhanced edge effect leads to a shift in a towards negative values with the common mean at $a \simeq -0.111$. On the other hand, the weakly prominent shoulder can be attributed to config 2b (red data point), where the electrostatic mirror was switched off.

The reduced χ^2/ν values to test the goodness of the fit are listed in Figure 3.28 for the individual configuration runs. The errors of the extracted a values were scaled with $\sqrt{\chi^2/\nu}$ whenever the condition $\chi^2/\nu \geq \chi^2_{\nu,\alpha}/\nu$ was met. The $\chi^2_{\nu,\alpha}$ value is derived from $\int_{\chi^2_{\nu,\alpha}}^{\infty} f_\nu\left(\chi^2\right) d\chi^2 = \alpha$ with $f_\nu\left(\chi^2\right)$ being the χ^2 distribution function with ν degrees of freedom. We took the significance level $\alpha = 0.05$ according to the PDG guidelines [THH$^+$18].

In order to investigate the effect of the individual systematic corrections onto a and its uncertainty it seems obvious to take the χ^2 function of Equation (3.12) which includes all systematic corrections and to extract the a value for the data set of the particular configuration run. Then in a second step, the fit procedure is repeated but now with the systematic effect of interest turned off. Any change in a should therefore be attributable to the influence of the systematic effect under investigation. This procedure, however, does not lead to unambiguous quantitative results on the influence of the respective systematic effect on a. This is due to

[27] For $U_{\mathrm{AP}} = 50\,\mathrm{V}$], the Δy_{exp} values for the different configurations are listed in Table 3.3.

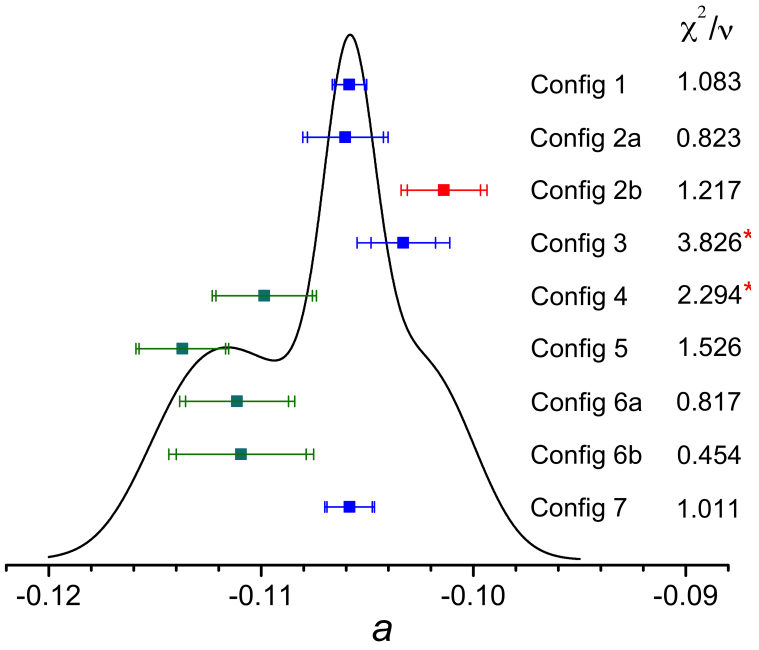

Figure 3.28.: Ideogram of a values for each configuration fitted separately without any systematic correction. The blue data points are derived from configuration runs with standard parameter settings. Forced enhancement of the edge effect by a reduced beam profile leads to more negative a values (green data points), whereas config 2b (EM off) shows the trend from systematic shifts to positive a values. The total error from the fit is shown together with the uncorrelated error which reflects the count rate statistics and which essentially constitutes the total error. The error bars are scaled with $\sqrt{\chi^2/\nu}$ whenever $\chi^2/\nu \geq \chi^2_{\nu,\alpha}$ is met (details see text) which is indicated by an asterisk (*). The degrees of freedom are $\nu = 15$ in this case.

the fact that with the removal and addition of a systematic effect, the correlations between the fit parameters also change, which in turn influences the value on a as result of the χ^2 minimisation. This is particularly the case when it comes to small systematic shifts which lie within the statistical (uncorrelated) error. In order to get an overview of the contribution of the systematic effects discussed in Section 3.4, a different procedure is chosen: Starting point is the integral proton spectrum $y^{a_{\mathrm{ref}}}_{\mathrm{theo(n)}}(U_{\mathrm{AP}}, r_{\mathrm{B}}; a_{\mathrm{ref}}, N_0) + c_{\mathrm{bg}}$ to which the reference value $a_{\mathrm{ref}} = -0.103$ of the β-$\bar{\nu}_e$ angular correlation coefficient is assigned. The count rate amplitude N_0 is adapted to the measured count rates in the respective configuration runs (cf. Table 3.3), as well as the constant background of $c_{\mathrm{bg}} \sim 6\,\mathrm{cps}$ measured at 780 V. In the next step, this spectrum is modified with the contributions of the systematic effect under investigation. For instance in case of the edge effect, the function $f^{\mathrm{ee}}_{\mathrm{sys}} = -\left(c^{\mathrm{ee}}_0 + c^{\mathrm{ee}}_2 \cdot U^2_{\mathrm{AP}} + c^{\mathrm{ee}}_4 \cdot U^4_{\mathrm{AP}}\right) \cdot y^{a_{\mathrm{ref}}}_{\mathrm{theo(n)}}$ is added which describes the relative count rate losses due to this effect (cf. Equations (3.21) and (3.22))). The coefficients were determined from the global fit to the overall data set. Finally, a χ^2 fit yields the potential change of a according to

$$\chi^2 = \sum_{i=1}^{10} \frac{1}{(\Delta y_{\mathrm{theo(n)},i})^2} \cdot (y^{a_{\mathrm{ref}}}_{\mathrm{theo(n)},i} \cdot (1 - c^{ee}_0 - c^{ee}_2 \cdot U^2_{\mathrm{AP},i} - c^{ee}_4 \cdot U^4_{\mathrm{AP},i} + c_{\mathrm{bg}}) - f^a_{\mathrm{fit}})^2 \qquad (3.35)$$

with the fit function given by $f^a_{\mathrm{fit}} = y^a_{\mathrm{theo(n)}}(U_{\mathrm{AP}}, r_{\mathrm{B}}; a, \widetilde{N}_0) + \widetilde{c}_{\mathrm{bg}}$. Prior to a χ^2 fit, the respective count rate at measurement point (i) (cf. Figure 3.1 b) was modified by an offset count rate which is Gaussian distributed around zero mean with standard deviation $\Delta y_{\mathrm{theo(n)},i}$. For $\Delta y_{\mathrm{theo(n)},i}$ we take a statistical error ~ 5 times smaller in total than the actual count rate error for config 1. This measure is a compromise between measurement sensitivity to trace tiny systematic shifts and the goodness of fit testing with a reduced χ^2 of $\chi^2/\nu \leq 2$.

Table 3.7 shows the influence of systematics discussed in Section 3.4 on the extracted value a_{fit} from the fit.

The expected finding here is the dominant shift of the a value by the edge effect with reduced beam profile, which was already observed in the raw data fits without systematic corrections (cf. Figure 3.28). From the ratio of the relative count rate losses for the standard (st) and reduced (re) beam profile, see Equation (3.20), we further expect $(a^{\mathrm{re}}_{\mathrm{fit}} - a_{\mathrm{ref}})/(a^{\mathrm{st}}_{\mathrm{fit}} - a_{\mathrm{ref}}) \approx \varepsilon_{\mathrm{re}}/\varepsilon_{\mathrm{st}}$. This functional relationship matches well within the specified error bars of $\varepsilon_{\mathrm{re}}/\varepsilon_{\mathrm{st}} = (6.8 \pm 0.4)$, see Section 3.4, and $(a^{\mathrm{re}}_{\mathrm{fit}} - a_{\mathrm{ref}})/(a^{\mathrm{st}}_{\mathrm{fit}} - a_{\mathrm{ref}}) = (8.8 \pm 1.8)$. In the latter case, the relative uncertainty of the a_{fit} values with $\delta a_{\mathrm{fit}}/a_{\mathrm{ref}} \simeq 0.2\,\%$ determines this error.

Among the configuration runs with the standard parameter settings the listed systematic effects may add up to a relative shift in a of $\delta a_{\mathrm{sys}}/a \sim 1\,\%$. All in all, this is a relatively small effect for the systematic corrections on the measurement values. The error on the individual systematic corrections (j) listed in Table 3.7 can be estimated from the corresponding error band on g^j_{sys} as a result of the global fit. Taking, for example, the edge effect (standard beam

[28] Relative change of a using the fit result of the retardation voltage-dependent background in config 1 (cf. Figure 3.18 (a)). For config 2, this value is already reduced by a factor of ~ 2 and there will be no shift in a for the subsequent configuration runs.

Table 3.7.: Relative changes of a values as result of a χ^2 fit in which a reference integral proton spectrum ($a_{\mathrm{ref}} = -0.103$) was modified by systematic effects as discussed in Section 3.4. The relative uncertainty of the extracted a_{fit} values is $\sim 0.2\,\%$, essentially determined by the chosen statistical errors $\Delta y_{\mathrm{theo(n),\,i}}$ at the data points (i) of the integral proton spectrum. The respective U_{AP} and r_{B} offset error does not change the input reference value a_{ref}, but only increases its uncertainty as result of the fit [28].

	Section	a_{fit}	$\frac{a_{\mathrm{fit}}-a_{\mathrm{ref}}}{\lvert a_{\mathrm{ref}}\rvert}\,(\%)$
No systematic	—	-0.1031	-0.1
U_{AP}-dep. background	3.4.5	-0.1044	-1.4
Trapped protons in DV	3.4.9	-0.1028	+0.3
Edge effect (standard)	3.4.6	-0.1041	-1.1
Edge effect (reduced)	3.4.6	-0.1121	-8.8
Lower integration limit	3.4.7	-0.1030	$< \lvert 0.1\rvert$
Pile up	3.4.8	-0.1029	+0.1
Deadlayer	3.4.7	-0.1023	+0.7
$\langle U_{\mathrm{AP}}\rangle$	3.4.3	-0.1025	+0.5
U_{AP} offset	3.4.3	a_{ref}	0.0 ± 0.3
$\langle r_{\mathrm{B}}\rangle$	3.4.2	-0.1030	$< \lvert 0.1\rvert$
r_{B} offset	3.4.2	a_{ref}	0.0 ± 0.1

profile) as one of the major systematic corrections, $\Delta g_{\mathrm{sys}}^{\mathrm{ee,st}} / g_{\mathrm{sys}}^{\mathrm{ee,st}} <\sim 15\,\%$ can be inferred from Figure 3.20. Thus, the relative uncertainty on the extracted a value due to the edge effect correction (st) is $\Delta a / a^{\mathrm{ee,st}} \leq |-0.011 \cdot 0.15| \sim 0.15\,\%$. In a similar way, this can be done for the other systematic corrections shown in Table 3.7 in order to get an estimate on their relative contributions to the overall uncertainty in a. To derive the total error on a (including the correlated error) in the right way, however, the global fit needs to be performed.

Figure 3.29 shows the results from the fit procedures (cf. Section 3.3.3) now with all systematic errors and their uncertainties included. The extracted a_c values for the individual configuration runs were obtained from a fit in which independent fit parameters a_c for the β-$\overline{\nu}_e$ angular correlation coefficient have been assigned to each configuration run (c). This approach leads to equal corrections of systematic effects as far as they are relevant for the respective configuration runs and indicates in the distribution of the a_c values whether those do scatter statistically or not. Besides the a value extracted from config 2b ((EM) off), all other values behave as expected, which manifests in the depicted Gaussian ideogram (back) of Figure 3.29. The ideogram shown in red which includes the config 2b value, on the other hand, shows a pronounced tail towards positive a values. By ~ 3 standard deviations, this

value deviates from the peak position of the ideogram(s). The latter, in turn, matches almost perfectly with the extracted $\langle a \rangle$ value from the global fit, in which the overall data set (except config 2b) was fitted with only one common fit parameter for a.

We can identify two reasons why this non-standard measurement of config 2b does not allow us to extract a precise value on a via the χ^2 fit:

1. Protons which are emitted into the rear hemisphere are guided along the magnetic field lines onto the bottom flange (stainless steel) of the aSPECT spectrometer ($B \sim 0.11\,\mathrm{T}$) if the electrostatic mirror (EM) is off. The angle- and energy-resolved intensity distributions of reflected H^+ ions were measured, e.g., in [SKD+17] for incident proton beams in the energy range $< 1\,\mathrm{keV}$. So a fraction of them is backscattered and may pass the AP if they can overcome the magnetic mirror below the DV and if their energy is higher than the applied retardation potential. Accordingly, one may expect a change of the integral proton spectrum which, however, cannot be quantitatively determined with sufficient accuracy. In case of EM 'on' (for all other configurations), there is no backscattering off materials, but rather it is a reversal of motion without energy loss.

2. A neutron beam polarisation of $P \sim 3\,\%$ is needed to get the same change of the integral spectrum than with about 10 % change of a. In config 2b, aSPECT operated as a 2π spectrometer (electrostatic mirror off) and the differential proton recoil spectrum $\omega_\mathrm{p}(T,a)$ (cf. Figure 3.1 a) must be supplemented by a $\cos\vartheta$ term (see Appendix B) according to

$$W(T,a,c) = \omega_\mathrm{p}(T,a) + P \cdot \omega_\mathrm{ps}(T,a) \cdot \cos\vartheta\,, \tag{3.36}$$

   where ϑ is the angle between neutron spin and proton momentum and c denotes the product $c = P \cdot \cos\vartheta$. The second term vanishes for $P = 0$ and/or in case of a 4π detection of the decay protons (for the latter reason all other configurations are insensitive to a residual polarisation). The H113 beam is nominally unpolarised, but the neutron guide wall of the ballistic ^{58}Ni/Ti supermirror guide [ADH+06] could cause a slight unwanted neutron polarization as observed on the NG-6 beam of the aCORN experiment [DBD+17]. Moreover, one must assume that the polarisation is not homogeneously distributed over the beam profile. The lack of knowledge about the finite beam polarisation and its spatial distribution in the decay volume does not allow to determine the model function of the integral proton spectrum from Equation (3.36) good enough.

Both aspects, therefore, suggest not to take config 2b into account in the final data analysis. Hence, the value for the β-$\overline{\nu}_e$ angular correlation coefficient a obtained from the aSPECT experiment (cf. Figure 3.29) is

$$\langle a \rangle = -0.10476 \pm 0.00085\,, \tag{3.37}$$

which results in a relative uncertainty of $\Delta a/a = 0.81\,\%$ in the determination of this quantity.

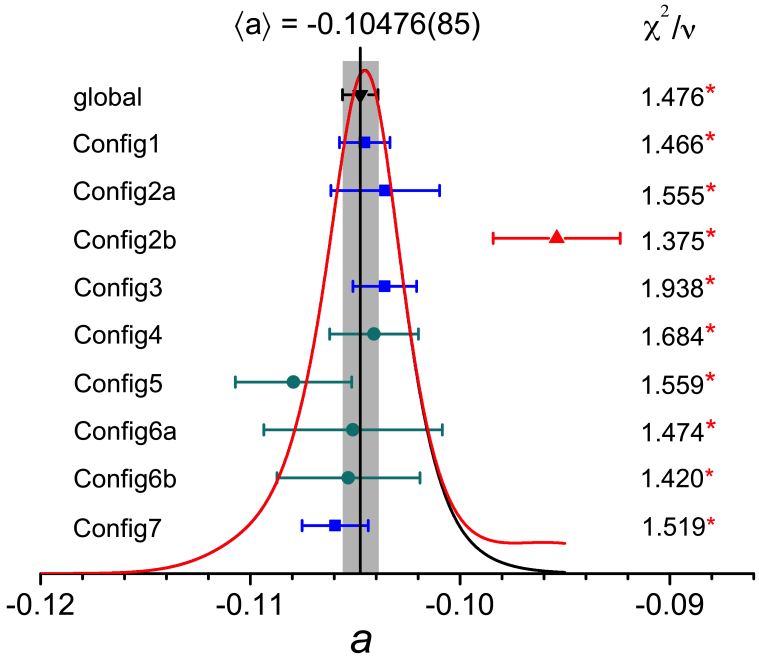

Figure 3.29.: Global fit results on a with systematic corrections included. Ideograms (black-/red) of extracted a values where independent fit parameters a_j for the β-$\overline{\nu}_e$ angular correlation coefficient have been assigned to each configuration run (j), The red one included the outlier value of a from config 2b, where aSPECT operated as 2π spectrometer (EM off). The global fit to the overall dataset (except config 2b) with only one common fit parameter for a yields $\langle a \rangle = -0.10476(85)$ for the production beam time in 2013 (black vertical line with error band indicated by gray bar). All error bars are scaled with $\sqrt{\chi^2/\nu}$, since $\chi^2/\nu \geq \chi^2_{\nu,\alpha}/\nu$ is always fulfilled in the case of $\nu > 100$ (d.o.f. for the global fit).

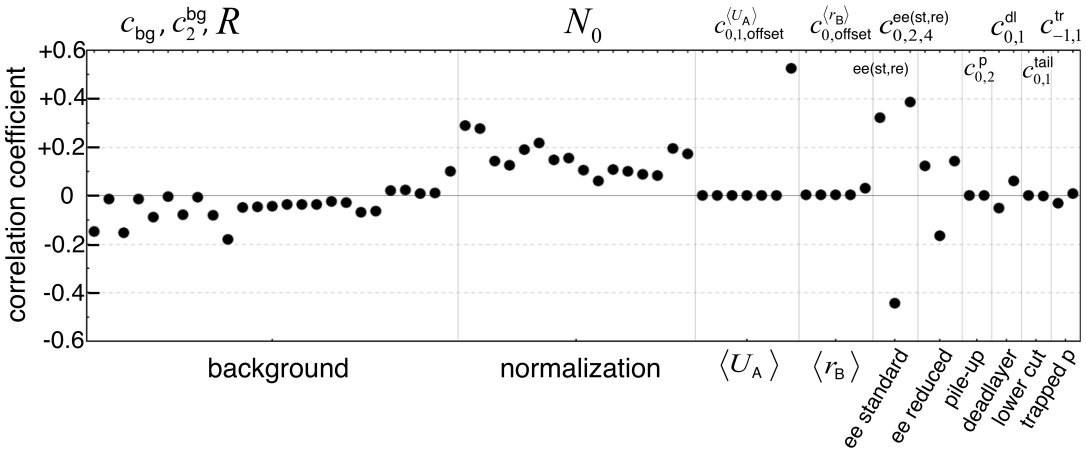

Figure 3.30.: Linear relationship (correlation) coefficient of a with various fit parameters (67 in total) as result of the global fit to the overall data set. Most of the parameters show correlation coefficients $< |0.2|$ which is weak and likely insignificant. Strong correlations, i.e., values that surpass $|0.8|$ are not found. Moderate correlations (+0.5) are found for $c_{\text{offset}}^{\langle U_A \rangle}$ to describe the offset error common to all $\langle U_A \rangle$ values and for the parameters $c_{0,2,4}^{ee(sr)}$ ($\sim |0.4|$) to correct for the edge effect (standard beam profile). A further breakdown according to detector pads (p) and configuration run (c) was not made in this correlation.

The error on a is the total error. Besides the statistical error it contains the uncertainties of the systematic corrections and the correlations among the fit parameters which enter the variance-covariance matrix to calculate the error on the derived quantity from the fit. Figure 3.30 shows the correlation coefficients between a and the various fit parameters which in most cases are $< |0.2|$.

Our new value is in good agreement with the present PDG value of (-0.1059 $\pm$ 0.0028) [THH$^+$18] for the β-$\overline{\nu}_e$ angular correlation coefficient of the free neutron but with the overall accuracy improved by a factor of 3.3. Using Equation (3.2) one can deduce a value for the ratio of the weak axial-vector and vector coupling constant $\lambda = g_A/g_V$ given by

$$\lambda = (-1.2693 \pm 0.0028) \tag{3.38}$$

Figure 3.31 shows the status of λ measurements (including our result) in which the distinction is made between measurements which determine the λ value from the beta-asymmetry A (blue data points) respectively from the β-$\overline{\nu}_e$ angular correlation coefficient a (red data points).

There is a general trend visible (in chronological order of the published results) towards more negative λ values. A systematic difference at the 1-2 σ level cannot be identified be-

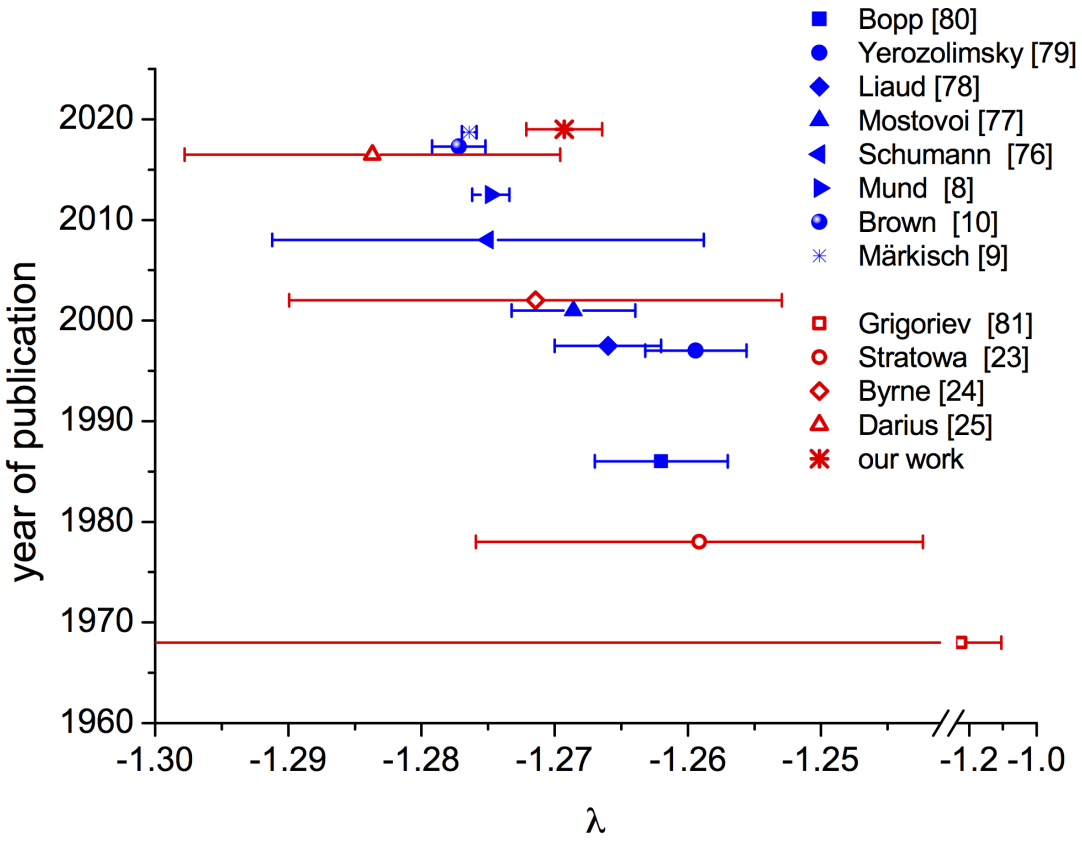

Figure 3.31.: Published results on λ derived from β-asymmetry measurements (blue data points) and from $\beta - \bar{\nu}_e$ angular correlation measurements (red data points) [MMS$^+$18, BDA$^+$18, MMD$^+$13, SKD$^+$08, MKS$^+$01, LSK$^+$97, YKMS97, BDH$^+$86, DBD$^+$17, BDvdG$^+$02, SDW78, GGVN68].

tween the two different measures of λ extraction, although comparable accuracies are obtained with the most recent results.

Under the assumption of the conserved vector current (CVC) hypothesis, experimentally determined values for λ directly determine g_{A}. This serves as a benchmark for lattice QCD calculations and determines the relationship among parameters of the weak hadronic current. Recent improvements in lattice QCD calculations which approach the per-cent-level determination in the physical point [ACH$^+$17, CNR$^+$18, LYD$^+$18, GJY$^+$18, OHM$^+$18, CDMD$^+$19] show promising agreement between theory and experiment. A comparison of experimental values for g_{A} with lattice values by itself constitutes a new physics test of non-standard couplings [GAC16].

3.6. Conclusion and outlook

In summary, we have measured the β-$\overline{\nu}_e$ angular correlation coefficient a with aSPECT resulting in a fractional precision of $\sim 0.8\,\%$. This result is in good agreement with the present PDG value but with the overall accuracy improved by a factor of 3.3. Within the SM, the correlation coefficients in neutron β-decay can be expressed in terms of one parameter, λ, which is the ratio of the weak coupling constants: $\lambda = g_{\mathrm{A}}/g_{\mathrm{V}}$. With $a = -0.10476(85)$ we obtain $\lambda = -1.2693(28)$. This value deviates by 1.5σ from the most recent λ measurement of the Perkeo collaboration [MMS$^+$18], which was determined via the β-asymmetry parameter A. This experimental situation calls for further improvements in the measurement accuracy; in particular being on par with the Perkeo result in terms of accuracy presents a major challenge.

The 4π detection of the decay protons with the aSPECT spectrometer which is based on the electrostatic MAC-E filter principle helps to a great deal to suppress unwanted systematics. From the analysis of the systematic effects we are confident that with an upgrade of the present spectrometer, a relative accuracy of $\Delta a/a \sim 0.2\,\%$ can be reached.

The essential improvements in the order of their importance are:

1. WF differences of polycrystalline gold surfaces as well as their temporal fluctuations result in the current uncertainty of $da/a \sim 0.3\,\%$. For this reason, gold single crystal layers have to be used as the inner surface of the DV and AP electrodes in order to reduce patch effects (cf. Figure A.1 (a)) to insignificance and to provide a homogeneous WF distribution across the electrode surface [MY12]. Surface dipoles caused by adsorption of contaminants if exposed to ambient conditions may lead to potential changes of the electrode, but those are spatially uniform for Au surfaces in a defined crystallographic orientation [LKS$^+$03]. As only the potential difference between the DV and AP electrode is of relevance, this WF offset (and its possible temporal drift) drops out. In this context, the current accuracy ($\sim 13\,\mathrm{mV}$) in the voltage measurement must be improved accordingly.

2. The electrode system has to be redesigned. In particular, the use of a broader magnetic

flux tube onto the enlarged SDD detector area of 3×3 pads should be realised. The uncorrelated statistical error at present contributes with $\sim 0.4\,\%$ to the total error and was obtained within ~ 20 days effective data taking time at the PF1b beam line at ILL with two detector pads in operation. This measure will allow to reach a statistical limit of $\Delta a/a_{\mathrm{stat}} \sim 0.1\,\%$ within 100 hours of effective data taking.

3. The major remaining systematic correction (after having eliminated the retardation voltage-dependent background by improved vacuum conditions) is the edge effect and proton backscattering at the SDD detector. At present, the edge effect corrections (standard beam profile) are under control to a level of $\Delta a/a \sim 0.1\,\%$. A better adapted collimation of the incoming neutron beam will reduce the slope dI/dy (cf. Equation (3.19)) of the beam profile in the DV and along with it the edge effect correction. Proton backscattering at the SDD has been thoroughly investigated (cf. Section 3.4.7) and is under control at the level of $\Delta a/a \sim 01.\,\%$.

The envisaged relative accuracy in the determination of a in turn will result in a determination of λ of $\Delta\lambda/\lambda \sim 4 \cdot 10^{-4}$. This is the sensitivity range which was recently achieved by the PERKEO collaboration. From neutron decay data, not only a precise $V-A$ SM value of λ can be extracted. Of particular interest is the search for right-handed currents and for S and T interactions where the measurement of τ_n, A and a, e.g., exhibit different dependencies [GJL95]. A common fit to the neutron decay data is all the more predictive on "Beyond the Standard Model" contributions if comparable accuracies are achieved.

A. Work function measurements using a Kelvin probe

The work function (WF) of different electrodes and its variation across the surface of each electrode was measured after the 2013 beam time by means of a Kelvin probe. Kelvin probe systems are vibrating capacitor systems and are based on the experimental approaches of [M.R98] and [Zis32]. The capacitor is formed by the sample electrode and the gold-plated tip ($= 2\,\mathrm{mm}$) of the Kelvin probe. The term relative work function ($\mathrm{WF_{rel}}$) in the context of Kelvin probe measurements tells that the WF of the electrode is measured relative to the WF of the probe tip, i.e., $\mathrm{WF_{rel}} := \mathrm{WF_{tip}} - \mathrm{WF_{sample}}$. The Kelvin probe used at ambient conditions (KP Technology SKP150150) is a scanning Kelvin probe system with scan size $(15 \times 15)\,\mathrm{cm}^2$ specified to have a precision of 1-3 meV. It is contained in an enclosure for reproducible and stable results. The enclosure contains an open container of saturated $\mathrm{MgCl_2{\cdot}6H_2O}$ solution to stabilise the air humidity at $(33.2 \pm 0.1)\,\%$. The latter is monitored by means of a humidity sensor. Prior to each WF scan the electrodes were wiped with isopropyl using fine-grade wipers (BEMCOT M-3) in order to receive similar initial conditions with lowest levels of lint and particles. After having put an electrode under the Kelvin probe for a scan measurement the environmental conditions have to stabilise. From the WF scans (step sizes of 1 mm or 3 mm) the average $\overline{\mathrm{WF}}_{\mathrm{rel}}$ of each electrode was computed as well as the RMS fluctuation across its surface. Figure A.1 (a) gives an example of a WF scan for segment AP-83 as part of the AP electrode.

The time for the system to stabilise for reproducible results on the level of $\sim 3\,\mathrm{meV}$ strongly depends on the air humidity at the time of placing the sample into the enclosure. WF changes accompanying the adsorption/desorption of water on gold surfaces have been investigated in [WF72]. Repeated scans after lock-up showed that it takes several days up to one week to reach stable conditions. This characteristic stabilisation time is too long to perform all necessary scans of the DV and AP electrode segments which had to be cut into smaller pieces (28 DV and 40 AP segments) to fit into the scanning area. As a good compromise we took the time span overnight ($\sim 12\,\mathrm{h}$) for the system to stabilise, which allowed us to scan two electrode sample pieces per day. The choice of a shorter time span than the one required to equilibrate the sample electrode with the environment causes a larger uncertainty in the measured WF averages. This is shown in Figure A.1 (b) for repeated $\overline{\mathrm{WF}}_{\mathrm{rel}}$ measurements of a single AP electrode segment (AP-83). The RMS fluctuations are $\sim 26\,\mathrm{meV}$ around the common mean of $\langle \overline{\mathrm{WF}}_{\mathrm{rel}} \rangle \sim 92\,\mathrm{meV}$. Therefore, for all the single-unit $\overline{\mathrm{WF}}_{\mathrm{rel}}$ measurements of electrode segments we take the somewhat higher value

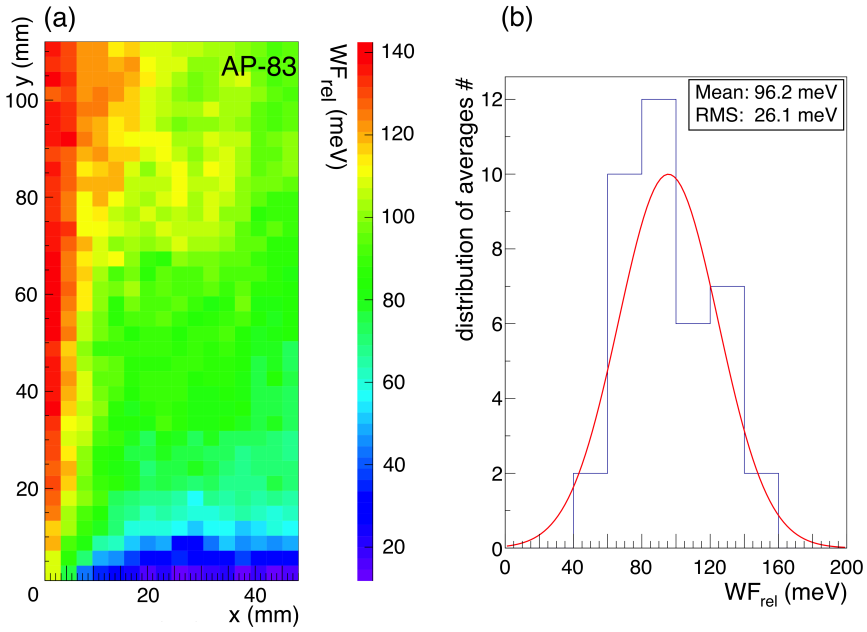

Figure A.1.: WF scan of a flat electrode segment (AP-83) of size $48 \times 108\,\mathrm{mm}^2$. (a) The colour map shows the $\mathrm{WF}_{\mathrm{rel}}$ distribution (meV) across the surface with $\overline{\mathrm{WF}}_{\mathrm{rel}} = 92.76\,\mathrm{meV}$ and RMS fluctuation of 24.73 meV. Scan time: $\sim 1.5\,\mathrm{h}$. (b) Repeated $\overline{\mathrm{WF}}_{\mathrm{rel}}$ measurements for segment AP-83 using a time span overnight ($\sim 12\,\mathrm{h}$) for the system to stabilise. To a good approximation the $\overline{\mathrm{WF}}_{\mathrm{rel}}$ distribution can be described by a Gaussian function (solid curve) with mean $\langle\overline{\mathrm{WF}}_{\mathrm{rel}}\rangle 96.2\,\mathrm{meV}$, $\sigma = 26.1\,\mathrm{meV}$, and $\delta\langle\overline{\mathrm{WF}}_{\mathrm{rel}}\rangle \sim 4.2\,\mathrm{meV}$ (error on mean value determined on a statistical basis).

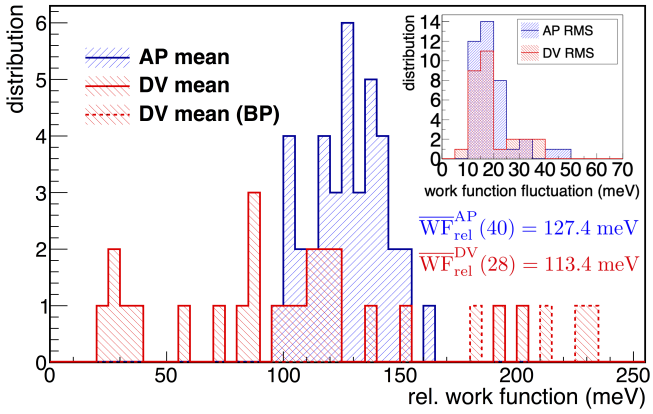

Figure A.2.: Distribution of $\overline{\mathrm{WF}}_{\mathrm{rel}}$ for each segment of the DV (red) and the AP electrode (blue). The bars indicated in dashed red are from the bottom part (BP) of the DV electrode which was re-machined and led to slightly different surface properties. Otherwise the $\mathrm{WF}_{\mathrm{rel}}$ averages of both electrodes overlap to quite some extent. Inset: Distribution of the RMS fluctuation of $\mathrm{WF}_{\mathrm{rel}}$ across each electrode. All electrodes show a remarkably similar behavior of their WF fluctuations.

$unit[pm30]meV$ as common uncertainty. Figure A.2 shows the distribution of the $\overline{\mathrm{WF}}_{\mathrm{rel}}$ values for the DV and the AP electrode segments and the distribution of the RMS fluctuation across the individual surfaces.

The quantity of interest for *a*SPECT is the difference of the potentials of AP and DV. Any common change or drift of the WF will drop out in this difference. Since the Au-coated electrodes were manufactured and treated in the same way, most of the changes due to adsorbates, temperature, as well as temporal drifts are expected to cancel in the difference. The challenge lies in the quantification of residual changes. The issue of the quantification of the residual change of the WF difference between AP and DV electrodes can be subdivided into four categories:

- Accuracy of the WF measurements
- Temporal changes of the WF
- Transferability of WF measurements to UHV conditions inside *a*SPECT, and
- Influence of the temperature differences on WF

A.1. Accuracy of the WF measurements

The exact electrode geometry with the segments' associated relative WF is implemented and used as input in KEMField for electromagnetic field and potential calculations in the DV and the AP region. For the AP electrode segments, the complete WF pattern (see Figure A.1 (a)) was taken into account, while only the mean value was used to characterise the WF across the surface of a DV electrode segment. This is due to the fact that the flux tube inside the AP electrode passes closer to the surfaces of the segments than in the DV, where WF differences (patch sizes of $\sim 3 \times 3\,\mathrm{cm}^2$) are smeared out by the appropriate distance[1]. The impact of the measurement uncertainty ($\pm 30\,\mathrm{meV}$) on the extracted values $\langle U_\mathrm{A} \rangle$ is considered in the particle tracking simulation by modifying the measured WF of the individual electrode segments statistically with WF offsets generated from a Gaussian distribution with mean zero and $\sigma = 30\,\mathrm{meV}$. The resulting RMS fluctuations in $\langle U_\mathrm{A} \rangle$ are then taken as error on the common mean.

A.2. Temporal changes of the WF

The measurements of the work function took place in 2014 and 2015 whereas the production beam time for the measurement of the beta-neutrino angular correlation was in summer 2013 and the gold plating of the electrodes was performed in early spring 2013. On these time scales one has to consider the issue of a changing WF over time.

Since only the difference between the WF of the AP and the DV electrode is of interest at *a*SPECT, the relatively large number of electrode segments can be used to investigate possible WF changes over time. A total of 40 electrode segments is used and divided into two subsets (i, j) of 20 pieces each. The pairwise WF difference $\Delta\overline{\mathrm{WF}}_{i,j=i+20} := \overline{\mathrm{WF}}_i - \overline{\mathrm{WF}}_{j=i+20}$ of two segments, one from each subset, is calculated for the chosen division and the segment numbering used. This procedure was performed in a measuring campaign in 2014 and then approximately one year later in 2015. It has the advantage that on a statistical basis the measurement uncertainty of $\pm 30\,\mathrm{meV}$ largely drops out and a potential temporal effect can be observed. Figure A.3 shows the distribution of the differences $\overline{\mathrm{WF}}_{i,\mathrm{diff}} = \Delta\overline{\mathrm{WF}}_{i,j=i+20}\,(2014) - \Delta\overline{\mathrm{WF}}_{i,j=i+20}\,(2015)$. From this we can deduce the average change of $\langle \overline{\mathrm{WF}}_\mathrm{diff} \rangle = (5 \pm 6)\,\mathrm{meV}$. This is compatible with zero. The uncertainty yields the limit on the temporal stability of 11 meV.

For the 2013 measurement run we take 20 meV as a conservative upper limit for possible WF differences between the DV and AP electrode due to aging effects.

[1] The minimal distance of the effective decay volume to one of the DV electrodes is $> 40\,\mathrm{mm}$ (cf. Figure 3.5), i.e., larger than the patch sizes . Therefore, we can use for each segment its surface-averaged WF [BTS+13].

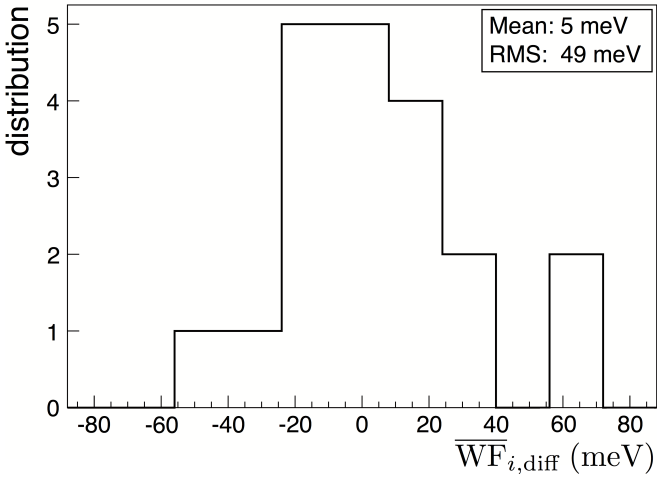

Figure A.3.: Distribution of the WF differences $\overline{\mathrm{WF}}_{i,\mathrm{diff}}$ used to extract temporal WF changes within a time span of about one year.

A.3. Transferability of WF measurements to UHV conditions of *a*SPECT

In the 2013 beam time, the electrodes were mounted in *a*SPECT with the surface adsorbates still present. Since the electrodes are located in the cold bore of the superconducting magnet, they cannot be baked out. Therefore, adsorbates like water are not fully removed under vacuum and the modification of the WF or what is more relevant to our case: the change in WF differences had to be investigated. To experimentally check WF changes, we put two electrode segments of *a*SPECT in a Kelvin probe at vacuum (end pressure $\sim 2 \cdot 10^{-5}$ mbar) which had been set-up for WF measurements for the KATRIN experiment. To get reliable and stable values the work functions were measured after the system had been stabilised. In order to have an almost simultaneous WF comparison, only line scans (~ 15 min) across the surfaces were performed, one immediately after the other with the samples in alternation. Figure A.4 shows the sequence of the average relative WF extracted from such line scans for both electrode samples. During the initial phase of pumping down relatively large $\overline{\mathrm{WF}}_{\mathrm{rel}}$ changes of ~ 100 meV can be observed since the 'simultaneity' of the alternating sample scans was not given due to the big temporal WF gradient. This stabilises at a pressure of around 10^{-3} mbar. What follows is a steady decrease of the WF of both samples, but with a stable WF difference of ~ 20 meV. The scans were stopped overnight (~ 12 h). Continuation of scans at the end pressure of $\sim 10^{-5}$ mbar showed stable WF conditions at a WF difference of ~ 10 meV. From these investigations we deduce: In going to UHV conditions inside *a*SPECT one has to assume an additional uncertainty of 10 meV in the WF differences of the AP and DV electrodes measured under ambient conditions.

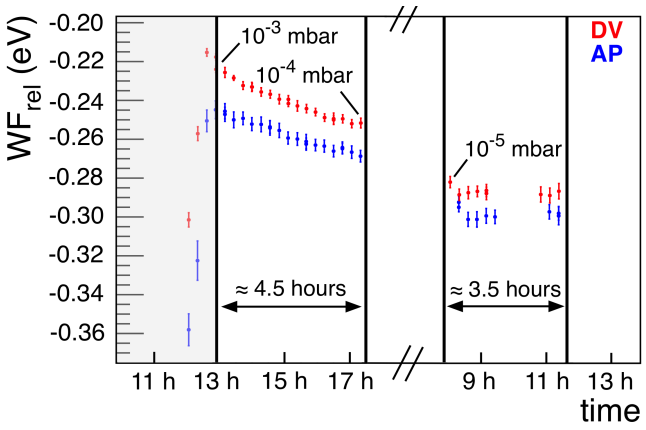

Figure A.4.: Time sequence of line scans showing the extracted means of the relative WF during evacuation of a UHV Kelvin probe. The two electrode samples were measured alternately.

A.4. Influence of the temperature differences on WF

The work function exhibits a small dependence on the temperature [RL15, HSW79]. We have measured temperatures at the electrode system in several places close to our electrodes during the off-line beam time in 2012. Temperatures varied between 80 K and 120 K, i.e. by $\Delta T = 50\,\mathrm{K}$. Using the formalism from [RL15] based on first principles we can deduce a maximum work function difference of $\Delta\overline{\mathrm{WF}}_T = 10\,\mathrm{meV}$ between the DV and AP electrode. This is consistent with an older phenomenological method [HSW79] and constitutes an additional uncertainty to the measurement accuracy.

B. Proton recoil spectrum in case of finite n polarisation

In the following we largely refer to the paper of F. Glück et al. [GJL95]. Recoil-order effects and radiative corrections are neglected. The differential proton recoil spectrum $W(T,a,c)$ in case of a finite neutron polarisation, P, is given by

$$W(T,a,c) = \omega_{\mathrm{p}}(T,a) + P \cdot \omega_{\mathrm{ps}}(T,a)\cos\vartheta \tag{B.1}$$

where ϑ is the angle between neutron spin and proton momentum and T is the kinetic energy of the proton. The respective spin-dependent and spin-independent terms $\omega_{\mathrm{ps}}(T,a)$ and $\omega_{\mathrm{p}}(T,a)$ can be expressed as

$$\omega_{\mathrm{ps}}(T,a) = +\frac{1}{8}(A+B)\left(F_{\max}(T) - F_{\min}(T)\right) \tag{B.2}$$

and

$$\omega_{\mathrm{p}}(T,a) = w_{\max}(T,a) - w_{\min}(T,a) \tag{B.3}$$

with

$$(A+B) = -4\lambda / \left(1+3\lambda^2\right) \text{ or} \tag{B.4}$$

$$(A+B) = -\sqrt{1+2a-3a^2} \tag{B.5}$$

using Equation (3.2).

By defining the following constants:

$$\Delta = m_{\mathrm{p}} - m_{\mathrm{n}} = 1.293318 \cdot 10^6\,\mathrm{eV} \tag{B.6}$$

$$m_{\mathrm{e}} = 0.5110034 \cdot 10^6\,\mathrm{eV}, \tag{B.7}$$

$$m_{\mathrm{n}} = 939.5656 \cdot 10^6\,\mathrm{eV}, \tag{B.8}$$

$$T_{\mathrm{m}} = \left(\Delta^2 - m_{\mathrm{e}}^2\right) / \left(2m_{\mathrm{n}}\right), \tag{B.9}$$

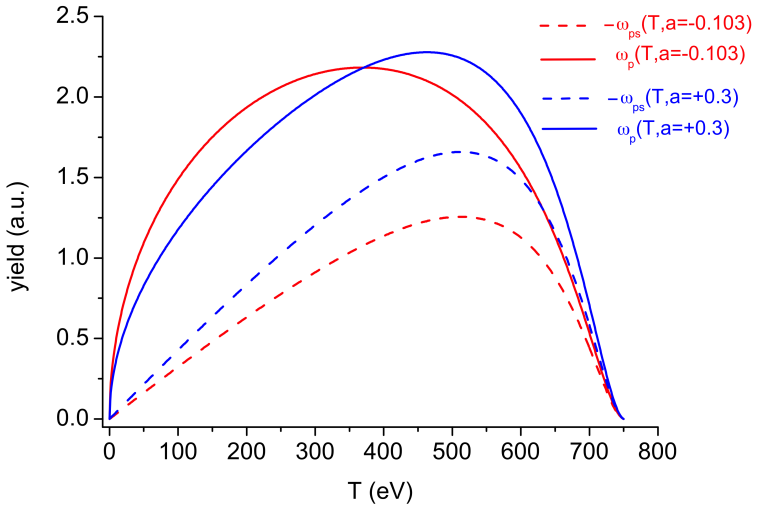

Figure B.1.: Spin-independent $\omega_{\mathrm{p}}(T,a)$ and the spin-dependent component $\omega_{\mathrm{ps}}(T,a)$ of the differential proton recoil spectrum $W(T,a,c)$ from Equation (B.1) for $a_{\mathrm{ref}} = -0.103$ and for an extreme value of $a = +0.3$. Note that $\omega_{\mathrm{ps}}(T,a)$ is negative, but for the yield we have $W(T,a,c) > 0$ for all $\cos\vartheta$ values since $|\omega_{\mathrm{ps}}(T,a)| < |\omega_{\mathrm{p}}(T,a)|$. The yield is given in (a.u.). To get prefactors for the absolute numbers, see [GJL95].

and further the T-dependent terms:

$$p(T) = \sqrt{2(m_n - \Delta)T + T^2}, \tag{B.10}$$

$$E_{\min}(T) = \frac{1}{2}\left(\Delta - T - p(T) + \frac{m_e^2}{\Delta - T - p(T)}\right), \tag{B.11}$$

$$E_{\max}(T) = \frac{1}{2}\left(\Delta - T + p(T) + \frac{m_e^2}{\Delta - T + p(T)}\right), \tag{B.12}$$

$$x_{\min}(T) = 2E_{\min}(T) - \Delta, \tag{B.13}$$

$$x_{\max}(T) = 2E_{\max}(T) - \Delta, \tag{B.14}$$

we obtain for

$$F_{\max(\min)} = \frac{\Delta\, x_{\max(\min)}^3}{3p} - \frac{m_{\mathrm{e}}^2 x_{\max(\min)}^2}{2p} - \Delta\, p x_{\max(\min)}, \tag{B.15}$$

and

$$w_{\max(\min)} = \frac{1}{2}(1+a)\, E_{\max(\min)}^2 \left(\Delta - \frac{2}{3}E_{\max(\min)}\right) + a\, m_{\mathrm{n}} E_{\max(\min)}\,(T - T_{\mathrm{m}})\ . \tag{B.16}$$

Figure B.1 shows the differential spectra $\omega_{\mathrm{p}}(T,a)$ and $\omega_{\mathrm{ps}}(T,a)$ for $a = a_{\mathrm{ref}} = -0.103$ and $a = +0.3$.

C. Electromagnetic field and particle tracking simulations

In Section 3.4 all major systematics influencing a are presented. Not all of these could be determined by pure analysis of experimental data or additional measurements. In particular the systematics B. Magnetic field ratio $g_{\mathrm{sys}}^{\langle r_{\mathrm{B}} \rangle}$ (Section 3.4.2), C. Retardation voltage $g_{\mathrm{sys}}^{\langle U_{\mathrm{A}} \rangle}$ (Section 3.4.3), E. Edge effect $g_{\mathrm{sys}}^{\mathrm{ee}}$ (Section 3.4.6) and H. Proton traps in the DV region $g_{\mathrm{sys}}^{\mathrm{tr}}$ (Section 3.4.9) could only be quantified by sophisticated particle tracking simulations.

To perform these simulations a full computational model of the aSPECT experiment had to implemented and validated. The first step was to create the geometry with all relevant parts, e.g., the electrode and coil system. Based on this, electromagnetic field calculations had to be carried out including optimisation and validation to get precise results. As final step, about 10^{10} protons were tracked and analysed to obtain the data y_{sys}^{j} for the systematic corrections g_{sys}^{j} mentioned above.

To solve the electromagnetic fields based on the electric potential and current distributions as well as to track and analyse the amount of protons sufficient computing power was necessary. The Johannes Gutenberg-Universität Mainz runs the supercomputer MOGON I and II providing 298 TFLOPS or 2000 TFLOPS, respectively (standard desktop computer $\sim$ 0.05 TFLOPS[1]). Both supercomputers were among the 100 fastest supercomputer in the world at launch time. This performance was necessary to carry out all required simulations within a reasonable time frame.

Not only raw computing power is important, also your simulation software have to be efficient. For this purpose the C++ based software framework KASPER was used. The routines were originally developed and used for aSPECT, then modified and hugely improved at KIT and MIT for the needs of the KATRIN collaboration, which aims to improve the limit of the neutrino mass down to 0.2 eV/c^2 (90% CL) or discover the actual mass, if it is larger than 0.35 eV/c^2. No other joint tool for implementation of complex geometries, electromagnetic field calculations and particle tracking is available. There exists tools for each task separately, e.g. GEANT4 for particle tracking and COMSOL for electromagnetic field calculations, but a combination of different software usually leads to lack of performance and flexibility. The software package is open-source and publicly available at `https://github.com/KATRIN-Experiment/Kassiopeia`.

In this appendix a detailed description of the performed simulations will be given. Ap-

[1] FLOPS - Floating-point operations per second. Unit of measure for computer performance.

pendix C.1 introduces the C++ simulation framework KASPER, with focus on the utilised modules KGeoBag, used for modelling arbitrary 3D geometries, KEMField, used for calculation of electromagnetic fields, and Kassiopeia, used for proton particle tracking based on KEMField and KGeoBag. Appendix C.2 describes details of the implementation of the *a*SPECT geometry with KGeoBag. Besides the straight forward construction of the electrode and coil system additional components like the neutron density distribution in the decay volume and the positioning of the detector are discussed. In Appendix C.3 the methods used for solving the electro- and magnetostatic configurations of *a*SPECT are discussed. Finally, Appendix C.4 gives details on the performed particle tracking simulations with Kassiopeia and their analysis for each systematic effect separately.

C.1. The C++ simulation framework KASPER

The software framework KASPER is an objected-oriented C++ coded toolset comprised of several semi-independet modules for simulation and (KATRIN specific) analysis. All modules can be compiled on MacOS and Linux systems using the CMake build system. There is the possibility to link against ROOT [BR97] data analysis and Visualisation Toolkit (VTK) [SML06] libraries. When linked against ROOT the user can use the ROOT file format files for simulation in- and output. VTK offers the opportunity, e.g., for easy visualisation of simulated electromagnetic fields and particle tracks. Furthermore, KASPER can exploit parallel frameworks, for example OpenCL reducing computation time for electromagnetic field computations drastically. The user interface is based on configuration files in the XML style format.

In the following an overview of the used modules is given:

- **KGeoBag**: Module for the construction of 3D geometries for simulation.
- **KEMField**: Module for electromagnetic field simulations based on the geometry provided by KGeoBag. Supports parallelisation system utilising both the OpenCL and MPI libraries.
- **Kassiopeia**: Module for particle tracking simulations. Based on the geometry from KGeoBag and the electromagnetic fields by KEMField, particles can be generated, propagated through the electromagnetic field and conditionally terminated.

Each module will be introduced in the sections below in a more general way with focus on the applied methods. Details on the practical implementation and application concerning simulations for *a*SPECT will be presented in Appendices C.2 and C.3.

C.1.1. KGeoBag - Module for modeling 3D geometries

The KGeoBag module plays a central role for particle tracking simulations with Kassiopeia. It allows the user to construct 3D models of their experiments and operate on them. It is

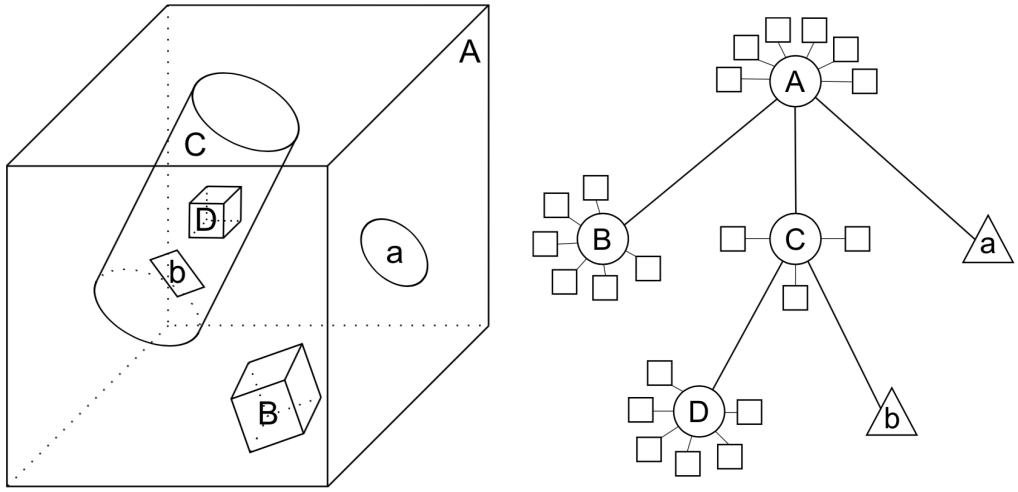

(a) Nested shapes.

(b) Tree structure of KGeoBag.

Figure C.1.: Structure of KGeoBag geometry tree. Representation of surfaces by small letters/triangles, spaces by capital letters/circles, and boundary surfaces by squares. Shapes can be nested into each other as depicted in (a). This can be visualised by a tree structure (b). Figure from [Gro15].

not only possible to define the bare geometrical properties but also non-geometrical ones. In example, electric potentials and currents can be related to surfaces or spaces as well as tracking navigation properties like terminators, e.g., a particle track should stop when it hits a given surface. This section contains some XML example listings to give the reader an impression of the code, but they won't be discussed in detail.

C.1.1.1. Shapes and structure

KGeoBag differentiates between two basic shapes: surfaces and spaces. Each shape's dimension and position is created in its own coordinate system. Single shapes are related to each other by nesting them in a common space. This space in turn can be nested again, and so on (Figure C.1a). When a shape is placed in a space a transformation like rotation and displacement can be applied. The relation between the geometric objects is internally represented by a tree as depicted in Figure C.1b.

C.1.1.2. Extensions - Discretisation and electromagnetic configuration

For the solution of the electrostatic configuration the partial differential equations of the system have to be solved. Since an analytically solution would be extremely difficult one uses numerical methods. Therefore the geometry have to be discretised. KEMField uses the

Boundary Element Method (BEM) to be explained in Appendix C.1.2.2. This means, that the discretisation of the geometry is restricted to the system boundaries, e.g. the electrode surfaces, which are divided in small triangles. The composite of the triangles of a discretised surface is called "mesh". The finer the mesh is, the better the accuracy of the solution, e.g. the computed electric potential. But the computation time will also increase with the number of mesh elements (= number of triangles). Especially in high field regions at corners or sharp edges, many mesh elements have to be used in order to obtain reasonable field and potential values.

The geometry created with KGeoBag provides direct options for the creation of the mesh. In example, a cylindrical electrode is created by drawing a line in x-y-plane and rotating it by 2π around the x-axis:

```
<!--cylindrical electrode, radius(y): 0.1m, height(x): 1.0m-->
<rotated_poly_line_surface
name="cylindrical_surface"
rotated_mesh_count="16">
        <poly_line>
                <start_point
                x="-0.5"
                y="0.1"/>
                <next_line
                x="0.5"
                y="0.1"
                line_mesh_count="32"
                line_mesh_power="2."/>
        </poly_line>
</rotated_poly_line_surface>
```

Listing C.1: Code example for creating a cylindrical electrode.

In this case the rotation is discretizied in 8 pieces (`rotated_mesh_count`) and in 16 pieces along the symmetry axis (`line_mesh_count`). The option `line_mesh_power` causes a gradually reduction in size of the mesh elements towards the edges of the cylindrical electrode. The result from this code is show in Figure C.2.

For electromagnetic field calculations with KEMField, to be discussed in the following chapter, KGeoBag also features an extension to assign voltages to surfaces (electrode voltage), and electric currents and windings to spaces (magent current). The following code example assigns 100.0 V to the surface `cylindrical_surface` from the listing above:

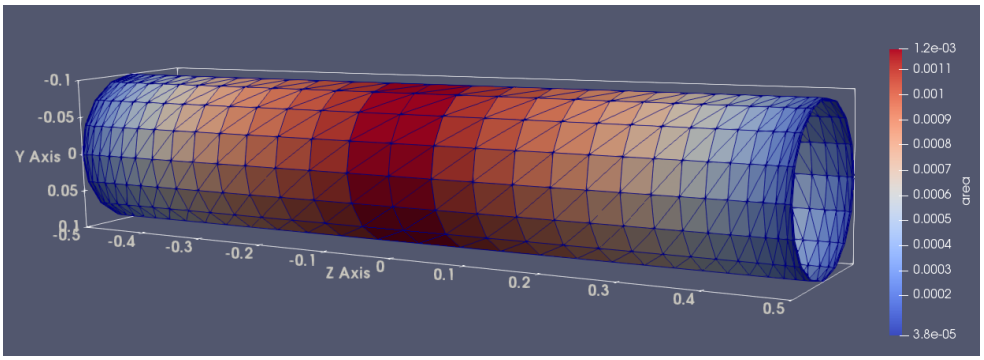

Figure C.2.: Meshed cylindrical electrode. Shown is the result from Listing C.1. KGeoBag creates a cylinder by rotating a line around the z-axis. The resulting mesh of triangles is defined by the three options: `rotated_mesh_count="16"` the discretisation in ϕ, `line_mesh_count="32"` the discretisation in z-direction and the `line_mesh_power="2."` reducing the size of mesh elements towards the edges of the cylinder. In consequence the number of mesh elements is $(16 * 32) * 2 = 1024$. The factor of 2 arises from the fact that each quadratic element is divided into two triangles.

```
1 <!--Assignment of 100V to cylindrical_surface-->
2 <electrostatic_dirichlet
3 name="cylindrical_electrode"
4 surfaces="cylindrical_surface"
5 value="100.0"
6 />
```

Listing C.2: Code example for assigning voltage to a surface.

In this manner the full *a*SPECT geometry is build, meshed and configured electro- and magnetostatically.

C.1.2. KEMField - Module for electromagnetic field computations

By means of KGeoBag the geometry and the electromagnetic configuration has been defined. Based on this, the next step on the way to particle tracking simulations is the computation of the electromagnetic fields. The module KEMField processes the discretised geometry from KGeoBag to solve linear equation systems in context of the BEM. For this task KEMField provides more than one method differing in precision and computation time. This section briefly introduces the applied methods.

C.1.2.1. Magnetostatic field computation

The computation of the magnetostatic field is, in comparison to the computation of the electrostatic field, a straight forward task. The reason for this is, that in general the distribution of the magnetic sources (currents) are known. Like *a*SPECT many experiments utilise axial symmetric field configurations generated by coils, which means a symmetric distribution of the magnetic sources. This results in a significant simplification of the equation systems to solve.

Direct method

The direct approach is the solution of the Biot-Savart law:

$$d\vec{B} = \frac{\mu_0}{4\pi} \frac{I d\vec{s} \times \vec{r}}{r^3} . \tag{C.1}$$

The formula denotes an infinite element of a wire $d\vec{s}$ carrying a constant electric current I with μ_0 the permeability constant. By integration over the element one gets the magnetic flux density $\vec{B}(\vec{r}\,)$ at an arbitrary position $\vec{r}$ in space. For complex shapes discretised in N elements, the total magnetic flux density is given by the sum of all contributions $\vec{B}_i$:

$$\vec{B}_{\text{tot}} = \sum_{i=1}^{N} \vec{B}_i . \tag{C.2}$$

The order of the discretisation N determines the accuracy of the numerical approximation and the computation time. This method can be applied to arbitrary complex geometries but does not take advantage of symmetries.

Elliptical integrals

For a thin axial symmetric coil the Biot-Savart law Equation (C.1) using cylinder coordinates can be expressed in terms of the complete elliptical integrals of first (Equation (C.3)), second (Equation (C.4)), and third (Equation (C.5)) kind [Gar63]:

$$K(k) = \int_0^{\pi/2} d\phi \frac{1}{\sqrt{1 - k^2 \sin^2 \phi}} , \tag{C.3}$$

$$E(k) = \int_0^{\pi/2} d\phi \sqrt{1 - k^2 \sin^2 \phi} , \tag{C.4}$$

$$\Pi(n,k) = \int_0^{\pi/2} d\phi \frac{1}{\left(1 - n^2 \sin^2 \phi\right) \sqrt{1 - k^2 \sin^2 \phi}} . \tag{C.5}$$

For an extended coil an integration in radial and axial direction is required. The result is simply the superposition of the field of a full cylinder minus the field of the inner cylinder resulting in the field of a coil with radial thickness $R_{\max} - R_{\min}$ and axial length $Z_{\max} - Z_{\min}$:

$$B_z = \hat{B}_z(Z_{\max}) - \hat{B}_z(Z_{\min}), \tag{C.6}$$
$$B_r = \hat{B}_r(R_{\max}) - \hat{B}_r(R_{\min}) \tag{C.7}$$

with

$$\hat{B}_z = -\frac{\mu_0 \lambda}{\pi} \frac{(z-Z)R}{(r+R)S} \left(K(k) + \frac{R-r}{2R} \left(\Pi(n,k) - K(k) \right) \right), \tag{C.8}$$
$$\hat{B}_r = -\frac{\mu_0 \lambda}{\pi} \frac{R}{S} \left(2\frac{E(k)-K(k)}{k^2} + K(k) \right), \tag{C.9}$$

and

$$S = \sqrt{(r+R)^2 + (z-Z)^2}, \tag{C.10}$$
$$k^2 = \frac{4rR}{S^2}, \tag{C.11}$$
$$n^2 = \frac{4rR}{(r+R)^2}, \tag{C.12}$$

where $\lambda = \frac{dI}{dz}$ is the linear current density, and (z,r) the axial and radial position to be calculated. In comparison to the direct method the use of elliptical integrals for axial symmetric geometries has the advantage that no discretisation of the coil is necessary. Although you have an analytical solution, the integrals have to be computed numerical which slows down particle tracking.

Zonal harmonic expansion

The zonal harmonics are special spherical harmonics of the form $P_l(\cos\theta)$. The zonal harmonic expansion method makes use of expressing the magnetic flux density by Legendre polynomials and their derivatives [Glu11]. These are calculated at so-called source points z_i located on the symmetry axis, e.g. the coil axis. Depending on the distance ρ_i between the point $P_i(r,z)$ to be computed to the nearest source point z_i there are two types of expansions: The central expansion if $\rho_i < \rho_i^{\text{cen}}$ and the remote expansion if $\rho_i > \rho_i^{\text{rem}}$, where ρ_i^{cen} and ρ_i^{rem} denote the minimal and maximal distance between the source point and magnetic sources, respectively (Figure C.3).

For the central expansion with $\rho_i < \rho_i^{\text{cen}}$ the expansion is given by

$$B_r = -\sin\theta \sum_{n=1}^{\infty} \frac{B_n^{\text{cen}}}{n+1} \left(\frac{\rho}{\rho^{\text{cen}}} \right)^n P_n'(\cos\theta)\,, \tag{C.13}$$

$$B_\phi = 0\,, \tag{C.14}$$

$$B_z = \sum_{n=0}^{\infty} B_n^{\text{cen}} \left(\frac{\rho}{\rho^{\text{cen}}} \right)^n P_n(\cos\theta) \tag{C.15}$$

with B_n^{cen} the central expansion coefficients of the n-th grade Legendre polynomial P_n. In case of $\rho_i > \rho_i^{\text{rem}}$ the remote expansion takes effect:

$$B_r = -\sin\theta \sum_{n=2}^{\infty} \frac{B_n^{\text{rem}}}{n} \left(\frac{\rho^{\text{rem}}}{\rho} \right)^n P_n(\cos\theta)\,, \tag{C.16}$$

$$B_\phi = 0\,, \tag{C.17}$$

$$B_z = \sum_{n=0}^{\infty} B_n^{\text{rem}} \left(\frac{\rho^{\text{rem}}}{\rho} \right)^n P_n'(\cos\theta) \tag{C.18}$$

with B_n^{rem} being the remote expansion coefficients of the n-th grade Legendre polynomial P_n.

Now the central and remote coefficients at the source points have to be calculated only once in advance and stored to disk. This increases the calculation speed by a factor of 10 to 100 in comparison to the elliptical integral method. As can be seen in Figure C.3 there are regions with $\rho^{\text{cen}} < \rho < \rho^{\text{rem}}$. For these cases the zonal harmonics are not valid and elliptical integrals are used automatically. For *a*SPECT all relevant field points for particle tracking could be computed by the zonal harmonics method since the coils are far away from the protons flux tube.

C.1.2.2. Electrostatic field computation

The computation of the electric field for the *a*SPECT electrode system is more complex than the computation of its magnetic field from the coil system. In case of the coil system the magnetic sources (electric currents) are known but for the electrode system they are not (electric charges). Only the boundary conditions are set by applying electric potentials as done by KGeoBag. The aim is to find a charge density distribution on the electrodes' surfaces which satisfies these boundary conditions, which is also know as the *Dirichlet problem* [Jac98]. With the knowledge of the charge density distribution it is possible to compute the electric field at an arbitrary position.

To solve the electrostatic problem the boundary element method in combination with the efficient Robin Hood algorithm was used, to be explained in the following.

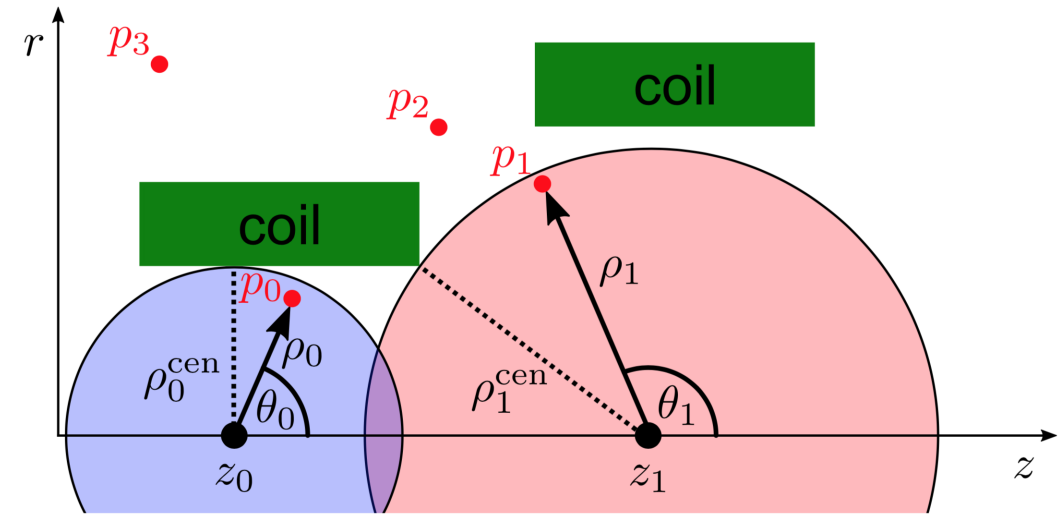

(a) Central expansion.

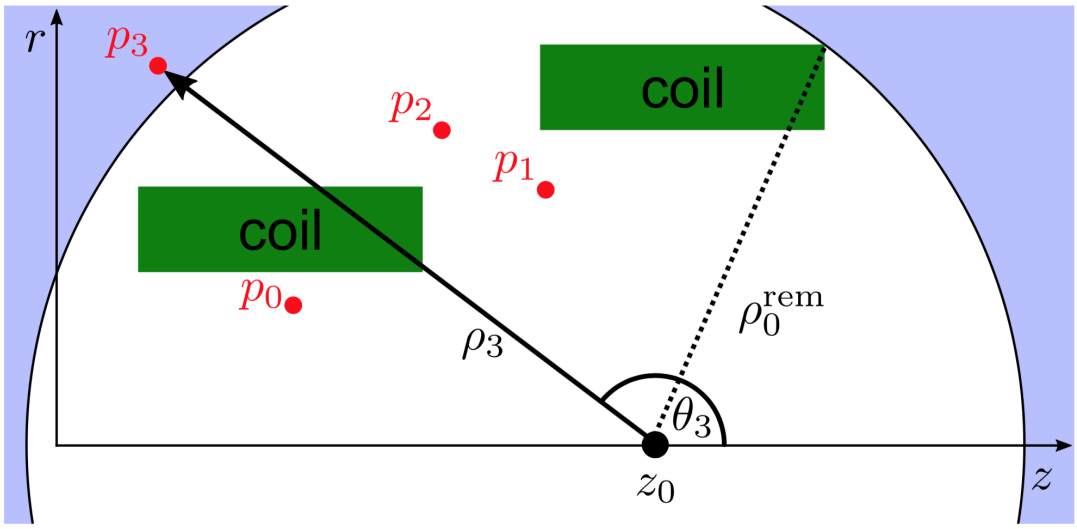

(b) Remote expansion

Figure C.3.: Types of zonal harmonics expansion. (a) Central expansion. Illustrated are two coils with rectangular cross section (green) and the central expansion region for the on-axis source points z_0 (blue disk) and z_1 (red disk) defined by the shortest distance to the magnetic source ρ_0^{cen} and ρ_1^{cen} (dashed lines), respectively. In this case the points p_0 and p_1 can be calculated using the central expansion, p_2 and p_3 cannot since they are not in the convergence region. (b) Remote expansion. Illustrated are two coils with rectangular cross section (green) and the remote expansion region for the on-axis source point z_0 (blue area) defined by the maximal distance to the magnetic source ρ_0^{rem}. In this case p_3 can be calculated using the remote expansion. As explained above p_0 and p_1 are covered by the central expansion. The point p_2 is either inside the central nor the remote expansion region, therefore elliptical integrals have to be used.

Boundary element method

Two common approaches are used to solve physical systems numerically: the *finite element method* (FEM) and the *boundary element method* (BEM). Both methods aim to solve the partial differential equation (PDE) of the physical system numerically. In the case of FEM the entire system is discretised in finite elements, even the empty space. In the case of BEM only the boundaries of the system have to be discretised. For that reason the number of mesh elements is much smaller leading to less consumption of computer memory. Since the electrostatic problem of *a*SPECT can be fully described by boundary surfaces (infinitesimal thin electrodes), BEM is better suited.

The discretisation of a surface is shown in Figure C.2. In general, a surface S is divided in N elements S_j:

$$S = \sum_{j}^{N} S_j \,. \tag{C.19}$$

Each element S_j shall carry a constant, homogeneous charge density σ_j. The boundary conditions, which are the applied voltages, can be related to this quantity by the following equation:

$$U_i = \sum_{j=1}^{N} C_{ij}\sigma_j \,. \tag{C.20}$$

U_i is the potential at the centre of the element i respecting all other elements j. The contribution of a single element j is determined by calculation of the so-called Coulomb matrix elements $C_{ij} = C_j(\vec{r}_i)$, which is an integration over the mesh element S_j:

$$C_i(\vec{r}_j) = \int_{S_j} \frac{1}{|\vec{r}_i - \vec{r}_S|}\, d^2\vec{r}_S \,. \tag{C.21}$$

Precise and fast integration over S_j is crucial for the performance of particle tracking simulations. Methods were investigated and optimised by [Hil17] and [Cor14].

To obtain the charge densities σ_j the linear equation system Equation (C.20) has to be solved. This can be done by a diagonalisation algorithm, e.g. the Gauss-Jordan method. For this direct method, the minimum required computer memory scales with $\mathcal{O}(N^2)$ since the entire matrix C_{ij} have to be kept in memory. In example, 10^4 mesh elements would consume about 2 GB of memory. Even worse are the required arithmetic operations scaling with $\mathcal{O}(N^3)$. With typical computer hardware this direct method is practically limited to geometries with about $N \lesssim 10^5$ mesh elements. For geometries which exceed this number, like *a*SPECT with about $9 * 10^5$ mesh elements, the so-called iterative Robin Hood method is utilised [LŠA06, LŠA08, FLC$^+$12]. The electrode system of *a*SPECT is not completely axial symmetric as there are, e.g. dipole electrodes. For that reason algorithms to solve for the charge density distribution can not take advantage of symmetry like for the magnetic field calculation.

Robin Hood method

The Robin Hood method is a numerical method specially developed for solving electrostatic boundary problems iteratively. The algorithm behaves similar to the natural process of charge redistribution. Electric charges on an ideal conductor will redistribute until the boundary becomes an equipotential surface even if there are additional charges in the proximity of the conductor. In this way Gauss' law is satisfied. The Robin Hood algorithm makes use of this simple strategy [FLC+12].

Let us consider the discretised cylindrical electrode S (Figure C.2). Each triangle S_j with area A_j is assigned with a randomised, initial charge density σ_j. The algorithm starts with the computation of U_i for each boundary element (cf. Equation (C.20)). The resulting list of potentials is searched for the two elements S_m and S_n with potential U_m and U_n differ the most from the equipotential condition. Between these elements charge is moved from one to the other element so that the equipotential condition is satisfied: $U'_m = U'_n$. The new potentials are given by

$$U'_m = U_m + C_{mm}\ \delta\sigma_m + C_{mn}\ \delta\sigma_n \tag{C.22}$$

$$U'_n = U_n + C_{nn}\ \delta\sigma_n + C_{nm}\ \delta\sigma_m\,. \tag{C.23}$$

The changes in charge densities $\delta\sigma_m, \delta\sigma_n$ are calculated by

$$\delta\sigma_m = \frac{A_n(U_n - U_m)}{A_n(C_{mm} - C_{nm}) + A_m(C_{nn} - C_{mn})} \tag{C.24}$$

$$\delta\sigma_n = \frac{A_m(U_m - U_n)}{A_n(C_{mm} - C_{nm}) + A_m(C_{nn} - C_{mn})} \tag{C.25}$$

with the net charge exchange $\delta q_{\text{total}} = A_m\ \delta\sigma_m + A_n\ \delta\sigma_n = 0$. Due to the charge redistribution the potentials U_i for all other elements have changed. The algorithm starts again with the computation of the U'_i's and moves charge from one element to another again. This is proceeded until a user-defined accuracy limit is reached. The concept can easily be adapted for the case electrodes are held at fixed potentials.

Due to the algorithm of the Robin Hood method only the current approximate solution of Equation (C.20) have to be kept in memory and not the entire matrix C_{ij}. Therefore the required storage scales with $\mathcal{O}(N)$ instead of $\mathcal{O}(N^2)$ for the direct method. The number of arithmetic operations scale with $\mathcal{O}(N^2)$. This makes the Robin Hood method suitable for bigger geometries also with $N > 10^5$. One further advantage is the high parallelisation capability of the method since each step consists of $\mathcal{O}(N)$ independent calculations. That allows to make use of modern graphic processors units' (GPU) parallel architecture with a factor of hundred of cores more in comparison to standard computer processing units (CPU).

C.1.2.3. Electrostatic field solver

KEMField provides several methods for the calculation of the electrostatic field and potential at an arbitrary point in space produced by the computed charge density distribution. In the

following two methods used for the *a*SPECT 's particle tracking simulations will be presented.

Direct method

The simplest approach to compute the field and potential at an arbitrary point $\vec{r}$ is to calculate the contribution from each surface element S_j and sum them up:

$$U(\vec{r}) = \frac{1}{4\pi\varepsilon_0} \sum_{j=0}^{N} \sigma_j \int_{S_j} \frac{1}{|\vec{r}-\vec{r}_j|} d\vec{r}_j \,, \tag{C.26}$$

$$\vec{E}(\vec{r}) = \frac{1}{4\pi\varepsilon_0} \sum_{j=0}^{N} \sigma_j \int_{S_j} \frac{\vec{r}-\vec{r}_j}{|\vec{r}-\vec{r}_j|^3} d\vec{r}_j \,. \tag{C.27}$$

This is done by integrating over each element (triangle) S_j with its constant charge density σ_j, where ε_0 is the permittivity constant. Because this method does not make use of any approximation it has the highest precision. The computation time for this methods scales with the number of surface elements N and the used integration technique.

Interpolation of field maps

Instead of direct computation of the electrostatic field and potential at each point one can use precomputed points on a 3D grid, a so-called field map. The field calculation is then performed by interpolating between the grid points. In the case of a 3D grid an arbitrary point is surrounded by eight grid points. The simplest "interpolation" is the use of the nearest neighbour, which is obvious the worst approximation. Much more precise results can be obtained by tricubic interpolation, which is the 3D case for cubic interpolation. A cubic interpolation connects two neighbouring points by a third degree polynominal respecting several boundary conditions. Figure C.4 shows a comparison between the nearest neighbour method and the cubic interpolation for the 1D case.

C.1.3. Kassiopeia - Module for particle tracking

Kassiopeia is the particle tracking module [FGT+17] of the KASPER package. It allows to generate particles, propagate them through electromagnetic fields, conditionally terminate them, and store selected information of the particle processing to disc.

The aim of particle tracking is to simulate the dynamic physical state of a given particle with fixed mass m and charge q in electromagnetic fields. The process of simulation evolves the initial particle state $(t_0, \vec{r}_0, \vec{p}_0)$ until a predefined termination condition is fulfilled and the simulation is stopped. All information of the dynamic physical state calculated by the simulation algorithm are accessible and are organised in the data structure to be explained in the following.

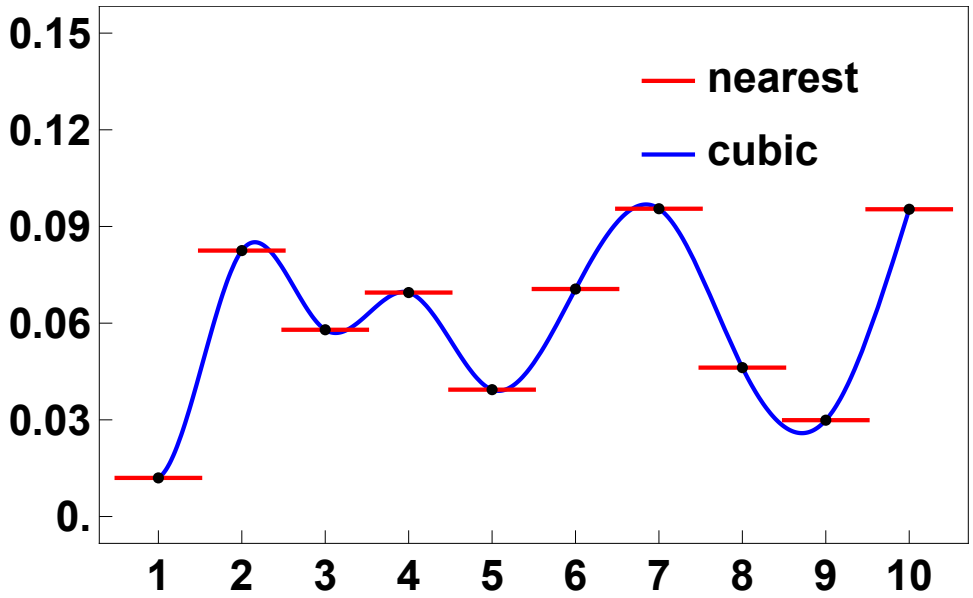

Figure C.4.: 1D interpolation methods. The black markers represent an arbitrary data set. The red line is the result for the "nearest neighbour method". The blue line is a cubic spline.

C.1.3.1. Organisation structure

The output data from the simulation progress are organised in four levels (Figure C.5):

- **Step:** The lowest level of organisation is a step. It represent one iteration of the particle's physical state evolution from $(t_i, \vec{r}_i, \vec{p}_i)$ to $(t_{i+1}, \vec{r}_{i+1}, \vec{p}_{i+1})$ by solving the equations of motion. During each step it is also checked if a termination condition is fulfilled, in example, an electrode surface is crossed. The data of a step is given by the single iterations $(t_i, \vec{r}_i, \vec{p}_i)$.

- **Track:** The collection of steps from the particle's origin until its termination is called a track. The data of a track are represented by the initial state $(t_0, \vec{r}_0, \vec{p}_0)$ and the final state $(t_K, \vec{r}_K, \vec{p}_K)$.

- **Event:** The next level of organisation is an event. The particle and its initial state $(t_0, \vec{r}_0, \vec{p}_0)$ is created by an event generator. The primary track from such an event can split into a secondary track, e.g., in the case of radioactive decay. The collection of these multiple tracks is called an event. For the *a*SPECT simulations an event and a track are almost identical.

- **Run:** The highest level of organisation is called Run. It is the collection of multiple events and represents a full particle tracking simulation.

With t_i representing the time, $\vec{r}_i$ the cartesian position, and $\vec{p}_i$ the cartesian momentum vector at step i.

C.1.3.2. Physical state evolution

The evolution of a particle in Kassiopeia begins with its generation, followed by tracking, and finally its termination at a certain state. More details of these three stages are explained in the following sections.

Generation of particles

The initialisation of an event always starts with the generation of a particle. For the definition of a particle the PDG's ID-scheme is used [THH+18]. The proton's ID is given by "2212" (electron "11"). By means of this ID Kassiopeia knows about the intrinsic particle properties like q and m.

In addition the seven dynamic initial conditions of the particle are generated: the initial time t_0, the position in space $\vec{r}_0$, and the initial momentum vector $\vec{p}_0$. For each initialisation of these initial conditions a so-called value generator is used. In example, a value generator gives random starting positions $\vec{r}_0$ in a fixed volume, e.g. decay volume. These can be uniformly distributed or drawn from a user-specified probability function. Kassiopeia offers several value generators, which will not further discussed.

For *a*SPECT it is more practical to generate the kinetic energy T_0 and direction of the particle in spherical coordinates (θ_0, ϕ_0) instead of the cartesian momentum vector $\vec{p}$.

Tracking of particles

The core of Kassiopeia is the calculation of particle tracks by solving the equations of motion. In electromagnetic fields the motion is described by the Lorentz equations. Kassiopeia numerically integrates these first order ordinary differential equations. Besides the exact representation of the Lorentz equations there is the adiabatic representation, which holds in the case where the electric and magnetic field is approximately constant over a single cyclotron motion. Details on both set of equations are presented in the following. Furthermore the used integrator and the step control mechanism is briefly mentioned.

Exact tracking

The exact tracking propagates the particle with mass m and charge q through the electromagnetic fields $\vec{E}$ and $\vec{B}$. The state of the particle is described by the time t, its position $\vec{r}$ and

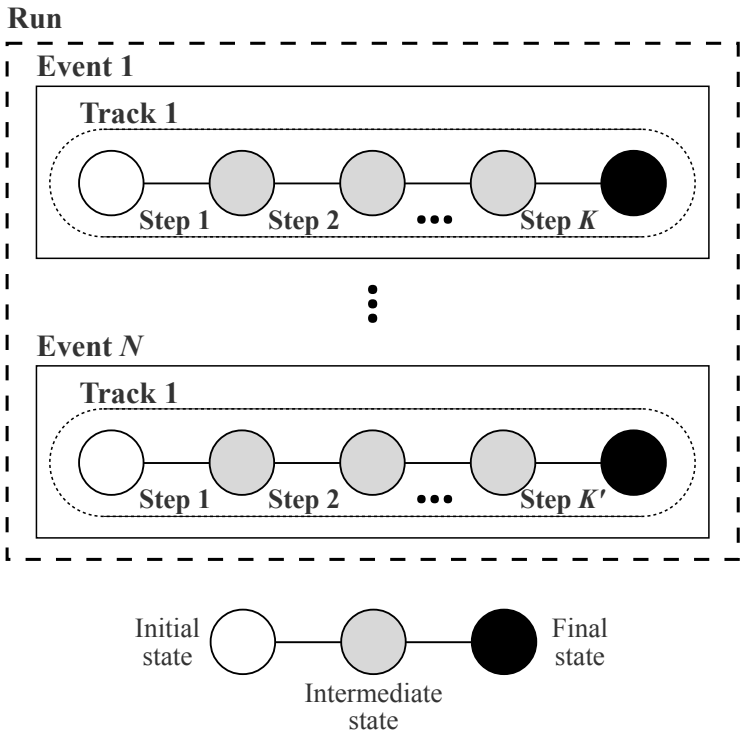

Figure C.5.: Structure of particle state evolution. The lowest level in particle tracking is a "Step" representing the lowest iteration in the particle's evolution. The next higher level is a "track" consisting of multiple (intermediate) steps represented by an inital and final state. An "Event" can consist of multiple tracks, in example, if the primary track is divided into two, e.g., by radioactive decay. This scenario is not depicted since it was not used for particle tracking simulations for *a*SPECT. The highest level in in the organisation structure is the "Run". It represents a single execution of an entire configured particle tracking simulation. Figure based on [Gro15].

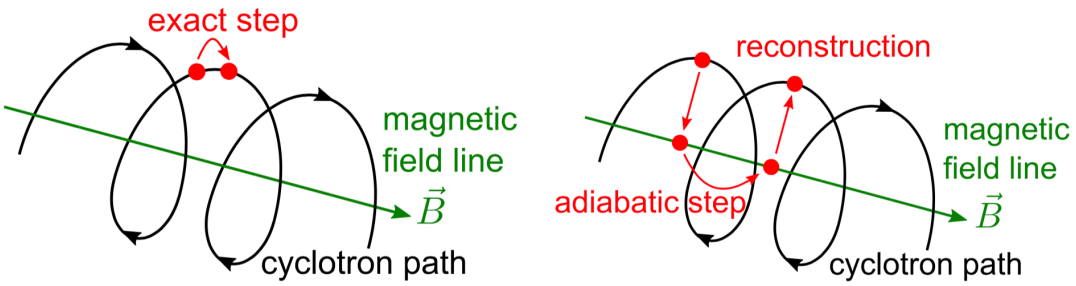

Figure C.6.: Comparison of exact tracking to adiabatic tracking. The left and right figures show the same cyclotron path (black) of a particle (red) gyrating around a magnetic field line (green). On the left exact tracking is depicted where the full Lorentz equation is solved to calculated the real position of the particle on its cyclotron path. Since a strong path curvature exists small steps are necessary (exact step). On the right adiabatic tracking is presented. In this case the gyration centre is tracked and the position due to cyclotron motion reconstructed. As the change in curvature of the gyration centre track is less strong larger steps are sufficient (adiabatic step). Figure taken from [Gro15].

its momentum vector $\vec{p}$. The corresponding differential equations are given by:

$$\frac{d\vec{r}}{dt} = \frac{\vec{p}}{\gamma m}, \tag{C.28}$$

$$\frac{d\vec{p}}{dt} = q\left(\vec{E}(\vec{r},t) + \frac{\vec{p}\times\vec{B}(\vec{r},t)}{\gamma m}\right), \tag{C.29}$$

where γ is the relativistic Lorentz factor. Since no simplification on this equations was applied its called exact tracking.

Adiabatic tracking

A particle moves adiabatic if the magnetic and electric field remains approximately constant during one cyclotron motion. This means the adiabatic invariant $\gamma\mu$ is conserved, where μ is the magnetic moment due to the cyclotron motion of the particle. In that case the particle follows and gyrates around a single magnetic field line. That in turn means, that the path of the guiding centre of the gyration is in first order identically to the path of the magnetic field line. Due to this fact, Equations (C.28) and (C.29) can be simplified. In contrast to exact tracking where the track is calculated along the real path of cyclotron motion, adiabatic tracking calculates the path of the guiding centre and reconstructs the real position due to cyclotron motion (Figure C.6).

The guiding centre representation is given by

$$\frac{d\vec{r}_\mathrm{c}}{dt} = \frac{p_\parallel}{\gamma m}\frac{\vec{B}(\vec{r}_\mathrm{c},t)}{B_\mathrm{c}(\vec{r}_\mathrm{c},t)}\,, \tag{C.30}$$

$$\frac{dp_\perp}{dt} = \frac{p_\perp p_\parallel}{2\gamma m\vec{B}(\vec{r}_\mathrm{c},t)}\nabla\vec{B}(\vec{r}_\mathrm{c},t)\cdot\frac{\vec{B}(\vec{r}_\mathrm{c},t)}{B_\mathrm{c}(\vec{r}_\mathrm{c},t)}\,, \tag{C.31}$$

$$\frac{dp_\parallel}{dt} = -\frac{p_\perp^2}{2\gamma m B(\vec{r}_\mathrm{c},t)}\nabla B(\vec{r}_\mathrm{c},t) + q\vec{E}(\vec{r}_\mathrm{c},t)\cdot\frac{\vec{B}(\vec{r}_\mathrm{c},t)}{B_\mathrm{c}(\vec{r}_\mathrm{c},t)}\,, \tag{C.32}$$

$$\frac{d\phi_\mathrm{c}}{dt} = \frac{q}{\gamma m}\vec{B}(\vec{r}_\mathrm{c},t) \tag{C.33}$$

with $\vec{r}_\mathrm{c}$ the guiding centre, $p_{\perp,\parallel}$ the momentum perpendicular or parallel to the magnetic field, respectively, and ϕ_c the phase of the gyration needed to reconstruct the real position [Nor61]. These equations are valid in absence of drifts, e.g., caused by $E\times B$ electrodes (magnetron motion).

Equations (C.30) to (C.32) can be extended to consider drifts due to magnetron motion, resulting in ([FGT+17, Nor61]):

$$\frac{d\vec{r}_{\mathrm{c,\,drift}}}{dt} = \frac{d\vec{r}_\mathrm{c}}{dt} + \frac{\vec{E}(\vec{r}_\mathrm{c},t)\times\vec{B}(\vec{r}_\mathrm{c},t)}{B(\vec{r}_\mathrm{c},t)^2} + \frac{2p_\parallel^2+p_\perp^2}{qm(\gamma+1)B(\vec{r}_\mathrm{c},t)^3}\vec{B}(\vec{r}_\mathrm{c},t)\times\vec{\nabla}B(\vec{r}_\mathrm{c},t)\frac{\vec{B}(\vec{r}_\mathrm{c},t)}{B(\vec{r}_\mathrm{c},t)}\,, \tag{C.34}$$

$$\frac{dp_{\parallel,\,\mathrm{drift}}}{dt} = \frac{dp_\parallel}{dt} + \frac{q\gamma m}{p_\parallel}\vec{E}(\vec{r}_\mathrm{c},t)\cdot\frac{d\vec{r}_\mathrm{c}}{dt} - \frac{p_\perp^2}{2p_\parallel B(\vec{r}_\mathrm{c},t)}\left(\vec{\nabla}\vec{B}(\vec{r}_\mathrm{c},t)\cdot\frac{d\vec{r}_\mathrm{c}}{dt}\right)\cdot\frac{\vec{B}(\vec{r}_\mathrm{c},t)}{B(\vec{r}_\mathrm{c},t)}\,, \tag{C.35}$$

$$\frac{dp_{\perp,\,\mathrm{drift}}}{dt} = \frac{dp_\perp}{dt} + \frac{p_\perp}{2B(\vec{r}_\mathrm{c},t)}\left(\vec{\nabla}\vec{B}(\vec{r}_\mathrm{c},t)\cdot\frac{d\vec{r}_\mathrm{c}}{dt}\right)\cdot\frac{\vec{B}(\vec{r}_\mathrm{c},t)}{B(\vec{r}_\mathrm{c},t)}\,. \tag{C.36}$$

One advantage of adiabatic tracking is the reduction of necessary integrations to be performed. Furthermore, less steps for the calculation of a particle track are needed, because the track of the gyration centre does not exhibit such strong changes in comparison to exact tracking, where the real position of the particle is calculated (Figure C.6).

Integrator

For the exact or adiabatic tracking the corresponding first order differential equations (Equations (C.30) to (C.31) or Equations (C.30) to (C.32), respectivley) have to be solved. This is done by numerical integration by means of the 8$^{\mathrm{th}}$ order Runge-Kutta algorithm (details, e.g., [But08]).

Step control

Step control is a mechanism to set conditions on the number of steps required to perform a full track. In example, if one lets the algorithm perform large spatial steps for the particle

in comparison to the change of the electromagnetic fields, this will lead to a loss in accuracy of the track. As each step includes the calculation of the electric and magnetic field at the current position, which is the most time consuming task in particle tracking, one have to adjust this parameter carefully. Kassiopeia provides several control mechanism. The simplest are realised by controlling the time or the distance between Step i and Step $i+1$. A more advanced step control is based on the current magnetic field: one can define a single step as a fraction of a single cyclotron motion.

Termination of particles

The user have to define conditions when a particle is terminated and the tracking of it stops. In example, a particle can be terminated, when it leaves a defined volume, it hits an electrode surface or exceeds a defined number of steps. After a particle is terminated a new event is generated and a new track starts.

C.1.3.3. Simulation output

Raw data

The user have to be aware of the fact that in general not all data from a simulation can be stored to disk. In example, a typical single track for aSPECT consists of about 10^3 steps. The description of the entire physical state of a particle involves seven quantities $(t_i, \vec{r}_i, \vec{p}_i)$. To be statistically significant usually 10^9 tracks are needed. To summarise, one needs at least $\left(10^3 \cdot 7 \cdot 10^9\right) \cdot 8\,\text{Byte} = 56\,\text{TByte}$ of disk space for the essential quantities. Therefore the user have to think thoroughly about the analysis procedure in advance and select on this basis the data to store. Often the information about the initial and final state (start and end of a track, see Figure C.6) and the cause of termination are sufficient for analysis. This reduces the required storage by $\sim 10^3$ instantaneous. Simulation output can also be conditionally, e.g., the maximal/minimum longitudinal energy of a track including the position at maximum/minimum value can be stored.

The selected data are stored to disk in a tree of the ROOT data structure [BR97]. Kassiopeia also provides reader classes for easy data access. The user greatly benefit from that when linking his analysis tools against the Kassiopeia libraries.

Visualisation

Kassiopeia can create a file of the VTK format [SML06]. VTK is an open-source toolkit system for 3D computer graphics, image processing, and visualisation. It can render scientific data and has a number of visualisation algorithms. However, the VTK file format can not only store the geometric objects from KGeoBag, it can also store, e.g., the applied potentials and the simulated trajectories of the particles in space. As well the fieldmaps from KEMField are stored in the VTK file format and are therefore easy visualisable. In pratice, the open-source

application Paraview [AGL05] is used to open VTK files, get access to the scientific data and visualise them. Providing this easy access to data is of great advantage for analysis.

C.2. *a*SPECT computational model

In the last Appendix C.1 the simulation software package KASPER was introduced with emphasize on the methods to be applied on the simulations. In this section details on the implementation in practice are given. Of course, the computational model describes *a*SPECT only as good as its input parameters. Therefore, several supportive measurments were performed and used as input data for the simulation, also to be discussed in the following.

C.2.1. Implementation of the *a*SPECT geometry with KGeoBag

The geometrical model of *a*SPECT was implemented with great care. This is essential as in particular the geometry defines the boundaries for the electromagnetic field calculations. This in turn means a too detailed model increases the complexity of the boundary problem to solve and this in turn the required computation power. Therefore, always simplifications have to be applied.

The experimental setup is described in Section 3.2.2. It can be divided in three main parts: the superconducting coil system, the electrode system, and the detection system. Furthermore the neutron beam is basically a part of the experimental setup. In the following the implementation of each part is presented.

C.2.1.1. Superconducting coil system

The magnetic field is generated by a set of 15 superconducting, axial symmetric coils mounted inside the cryostat. As they are not accessible, the positions and dimensions of the coils could not be measured directly. Therefore, in a first step, the theoretical values of the coils (dimensions, positions, windings) from the design drawings were used to calculated the magnetic field analytically (general analytical solution for axial symmetric coils with rectangular cross section in [GS63]). This solution was compared to Hall probe ($\Delta B/B \sim 10^{-3}$) and much more precise proton-based NMR measurements ($\Delta B/B \sim 10^{-5}$). Minor deviations between these measurements and the analytical magnetic field calculations could be corrected on by shifting coils on-axis by several millimetres. This was done by a χ^2 fit to the measured field data. The fit function was simply represented by the superposition of the single 15 coils. As free fit parameters the z-positions of the coils were used. Due to vibrations during transportation of the cryostat and strong forces when the magnet is ramped up such deviations are easily possible. Finally, the adapted parameters from the fit were used for the magnetic field simulation with KEMField instead of the parameters from the manufacturer.

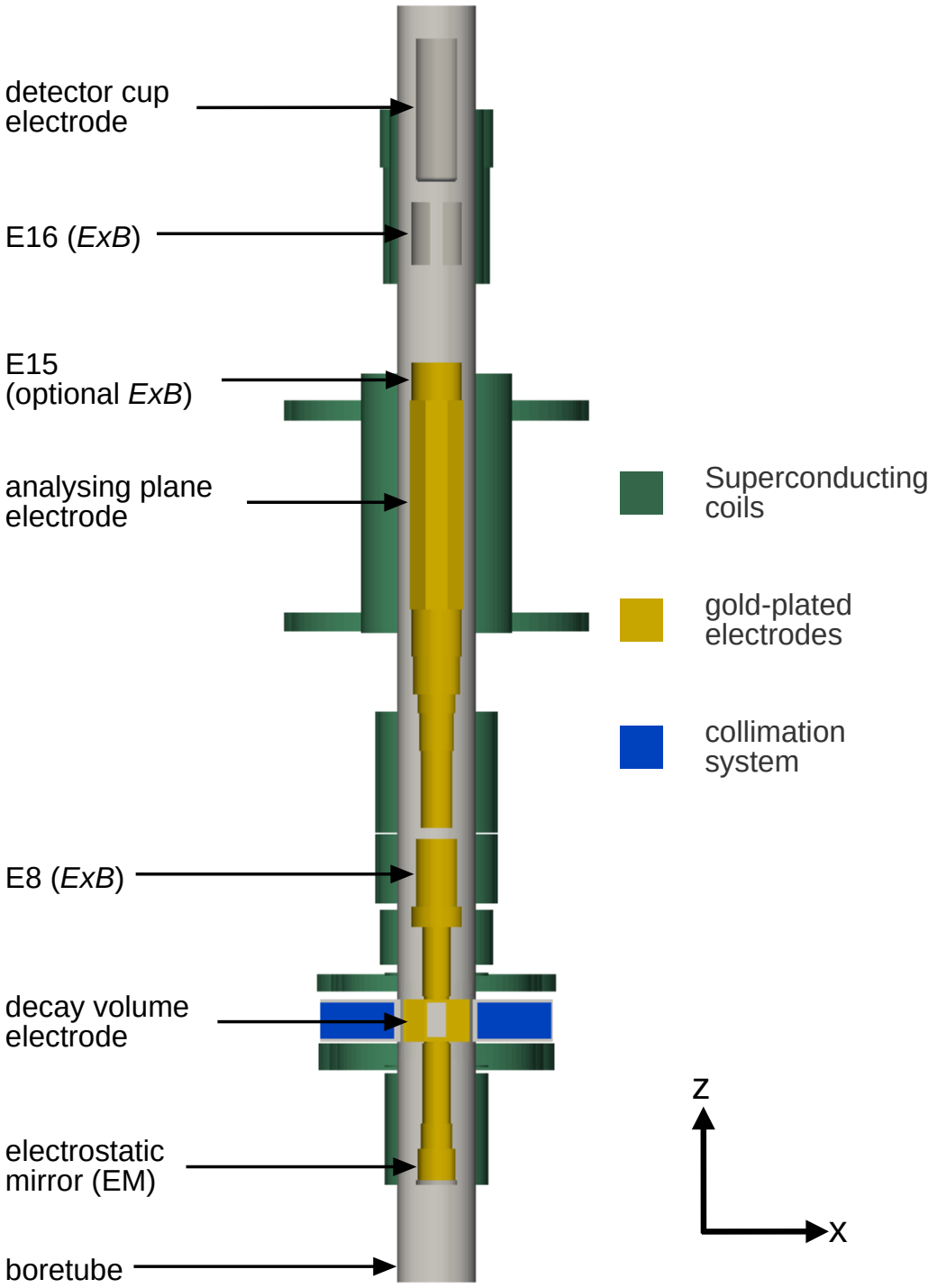

Figure C.7.: Geometrical model of *a*SPECT. Shown is the geometrical model of *a*SPECT as implemented in KGeoBag visualised by means of *Paraview*. The boretube (grey) and the superconducting coils (green) are sliced to uncover the electrode system (golden). At height of the decay volume electrode the collimation system (blue) can be seen. Important electrodes are labelled (compare this with Figure 3.2).

C.2.1.2. Electrode system

The electrode system (see Figure C.7) is assembled out of ~ 16 single electrodes outside of the cryostat. The electrode system is then pushed into the cold bore and fixed. To obtain the geometrical data the electrode system was measured and documented in detail immediately prior to mounting to and after dismounting from the cold bore. All electrodes are implemented as surfaces with no thickness.

The electrostatic mirror at the very end of the electrode system is a close-mesh wire system in the x-y-plane to prevent background by incident electrons from neutron decay but also providing a homogeneous potential barrier for the high energetic protons. The electrostatic solution of such tiny structures would cost unnecessarily computation power. Therefore the mirror was simplified by a simple surface at potential of the wire system.

During operation the electrode system is at 120 K. The electrodes are built out of Cu. Therefore an expansion coefficient of $\alpha_{\mathrm{Cu}} = 0.99770458$ [Hah70] was calculated and taken into account leading to an integral shrinking of about -2.5 mm in z-direction.

At least the bore tube and the internal collimation are electrodes leading to field leakage due to work function differences inside the decay volume as described in Section 3.4.3. Both components' geometry were measured and are part of the computational model.

C.2.1.3. Detection system

The detection system is mounted independently on the top of *a*SPECT. For measurements the detector cup electrode holding the detector itself has to be moved in the high magnetic field inside the cold bore by the so called "detector insertion mechanics". The z-position of the detector (detector plane) inside the cold bore could be determined indirectly by measuring the moved distance. Since the heavy detector cup is only supported by a long tube in z-direction, the centre of the detector cup electrode and thus the detector itself can easily be shifted off-axis. Also there can be an angle between the alignment of the detector pads and the direction of the neutron beam (x-direction). In order to determine the correct position of the detector, an activated copper wire was moved parallel to the x- and y-axis through the decay volume while all electrostatic fields were off (Section 3.2). From the resulting count rates the pure magnetic projection of the three detector pads in the decay volume can be deduced (for details see [Mai14]). By means of simulations of magnetic field lines this could be re-projected to the detector plane shown in Figure C.8.

C.2.1.4. Neutron density distribution in the decay volume

Due to inhomogeneous electromagnetic fields in the decay volume and a finite detector size systematic uncertainties can also depend on the density distribution of the neutrons in the decay volume. This neutron beam profile was measured by activating a copper foil placed in the centre of the decay volume parallel to the y-z-plane (Figure C.9). Already described in Section 3.2. The neutron beam is guided to the decay volume through a collimation system

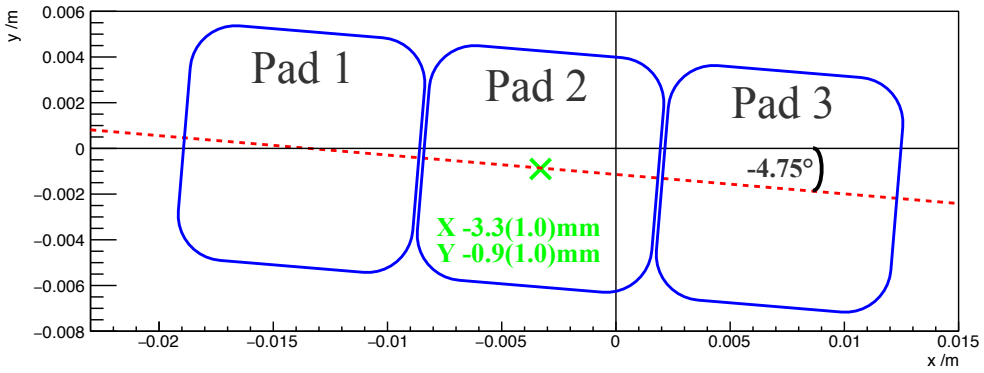

Figure C.8.: Positioning of the detector pads. An activated copper wire was moved parallel to the x- and y-axis through the decay volume with all electrostatic fields switched off. By means of the wire position dependent count rates the magnetic projection of the detector in the decay volume could be constructed. This measured magnetic projection could be re-projected to the detector plane by simulating magnetic field lines from the decay volume to the detector plane. The result is shown in this figure. The centre of the detector (green cross) is shifted by $(x,y) = (-3.3(1.0)\,\mathrm{mm}, -0.9(1.0)\,\mathrm{mm})$ off the symmetry axis of the bore tube and turned with respect to the x-axis by $-4.75°$.

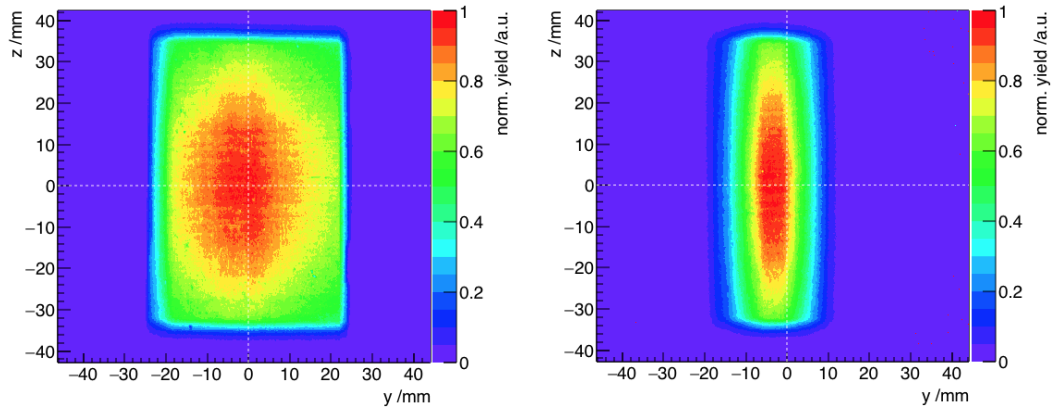

(a) Standard beamprofile

(b) Reduced beamprofile

Figure C.9.: Neutron beam profiles from copper foil activation. (a) The standard neutron beam profile as result of the collimation system measured in the centre of the decay volume. (b) The reduced neutron beam profile as result of an additional aperture of 15×75 mm in front of the collimation system.

with a length of 40 cm therefore divergence of the beam profile inside the decay volume is negligible.

C.3. Electromagnetic field computations on *a*SPECT

The path of a proton through *a*SPECT is determined by its initial conditions and the experienced electromagnetic fields. In particular, these parameters are the decisive factors whether a proton is counted at the detector or not. Of course, this also holds for the tracking simulations solving the equations of motions (Appendix C.1.3.2). Essentially, the simulated fields are determined by two key points: the boundary conditions of the electromagnetic problem, which are input parameters to the simulation, and the precision of the utilised computational method. This section will discuss details on the latter.

C.3.1. Magnetic field computation

The computation of the magnetic field is less elaborate and challenging due to the fact, that the magnetic sources are known and the coils are arranged axial symmetric.

For the numerical computation of the magnetic field the zonal harmonic expansion method as described in Appendix C.1.2.1 was used. For the coil system source points in 1 mm increments with 1000 expansion coefficients at each point were set. This is rather dense and

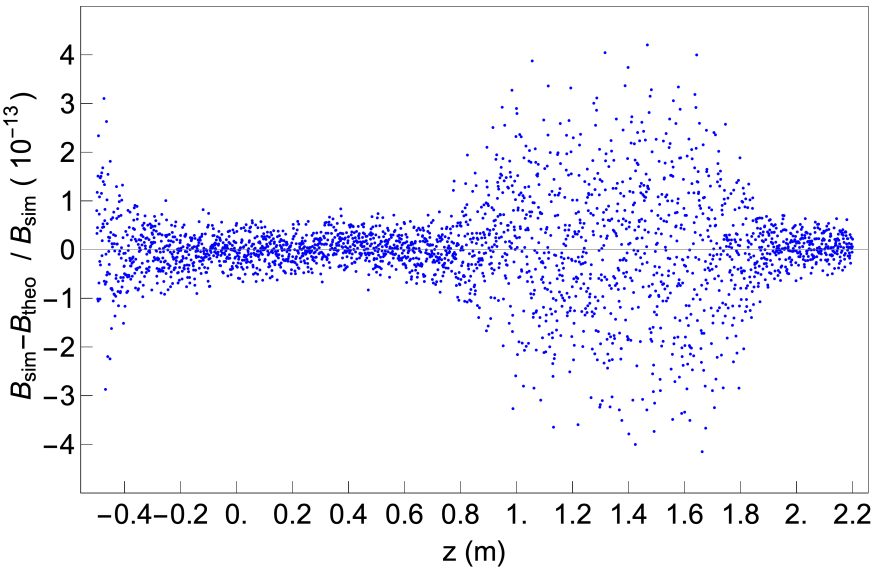

Figure C.10.: Relative precision of simulated magnetic field for the *a*SPECT coil system. The blue points present the relative precision $\frac{B_{z,\,sim}-B_{z,\,theo}}{B_{z,\,sim}}$ for the full *a*SPECT coil system, where $B_{z,\,theo}$ is the analytical solution and $B_{z,\,sim}$ the result from the simulation with the zonal harmonic method. The precision is relative at a $<$ 10^{-12} level for all points. This is the numerical limit as can be seen in the analysing plane region ($\sim 1.2-1.6\,\mathrm{m}$), where the relative precision is about a factor 5 lower since the field is a factor 5 lower.

probable not necessary, but the performance of the method is extremely high. The computation of all source points' coefficients, which has only to be done a single time, requires less than a minute. To compute a magnetic field point inside the convergence radius it takes just several μs. It will turn out, that this fraction of time can be neglected in contrary to the much longer computation time needed by the electric field calculation and therefore does not thwart proton tracking.

In Figure C.10 the relative precision $\frac{B_{z,\,sim}-B_{z,\,theo}}{B_{z,\,sim}}$ for the full *a*SPECT coil system is depicted, where $B_{z,\,theo}$ is the analytical solution and $B_{z,\,sim}$ the result from the simulation with the zonal harmonic method. The field is coincidence for all field points relative at $< 10^{-12}$ level. This is by far precise enough.

C.3.2. Electrostatic charge density and field computation

This section outlines the method to find sufficient mesh parameters, compares the much faster field computation by field maps to the most accurate integrating field solver, and give details on the implementation of the measured work function distributions.

C.3.2.1. Optimisation of the mesh

The computation of the electrostatic field is more complex and more expensive in comparison to the computation of the magnetic field. This is owed two fundamental differences: The first one is the non-axial symmetric electrode system and the second one the non-existent knowledge of the (electric) sources. The later requires an additional step: the extensive computation of the electric charge densities on the electrodes' surfaces. And since the axial symmetry is broken due to several dipole electrodes, the charge density distribution will also exhibit no symmetry. As a result the field computation will be more elaborate, too.

For the computation of the charge density distribution the Robin Hood method as explained in Appendix C.1.2.2 was applied. All necessary information are provided by KGeoBag: the meshed electrodes' geometries and the electrodes' potentials (see Appendix C.1.1.2). While the geometries and potentials are external input parameters the meshing has to be specified by the user. This is crucial since the grade of discretisation has significant impact on the precision of the resulting charge density and the computing power consumption. In the following the optimisation of the meshing will be discussed.

The procedure on the optimisation of the meshing will be demonstrated on a sub set of electrodes E10 - E11 - E12 - E13 - E14 (octagonal AP electrode) - E15 (dipole electrode) depicted in Figure C.11. The mesh for the single cylindrical electrodes are defined by two parameters: the line mesh count and the radial mesh count. The first specifies the discretisation in z-direction and the second in ϕ-direction (as introduced in Appendix C.1.1.2). These parameters determine the area size of the resulting mesh elements S_{ij} as shown in Figure C.12a. The mesh power was set equal 2. The resulting charge density as result of the Robin Hood method is depicted in Figure C.12b as an example.

To check if the level of discretisation is sufficient to obtain precise results the radial mesh count (RMC) and the line mesh count (LMC) were increased stepwise. For simplification each electrode will be assigned with the same LMC and a fixed RMC of 128. After each refinement of the LMC, the charge density distribution and the corresponding electric potential on-axis were calculated $U_{\mathrm{LMC}}(z)$ and the results compared. In Figure C.13 the absolute of the difference of two electric potentials $|\Delta U| = U_{\mathrm{LMC}}(z) - U_{\mathrm{LMC'=LMC\cdot 2}}(z)$ are plotted. The LMCs for the differences are chosen in a way that the triangular mesh elements are half of their size (LMC'=LMC·2). The plot shows local maxima in the regions of electrode transitions, where the charge densities exhibit the strongest gradients (compare Figure C.12b), while inside long electrodes the minima are placed (e.g. E14 at $z = 1.34\,\mathrm{m}$). The potential differences $|\Delta U|$ decrease by about half an order of magnitude when the mesh elements are bisected in size. For $\mathrm{LMC} \to \infty$ the solution converges, of course. In example, the blue curve satisfies $|\Delta U(z)| < 10^{-2}\,\mathrm{V}\ \forall z$, which means that a further refinement of the LMC can only result in a gain of precision below $10^{-2}\,\mathrm{V}$. Therefore the solution is stable on this level. In this way the LMC and RMC was investigated for the full electrode system to be stable on $< 5\,\mathrm{mV}$.

The final mesh consists of about $9 * 10^5$ triangles. The Robin Hood method requires about 8 h to solve for the charge density distribution on a *NVIDIA GeForce GTX TITAN* graphic card

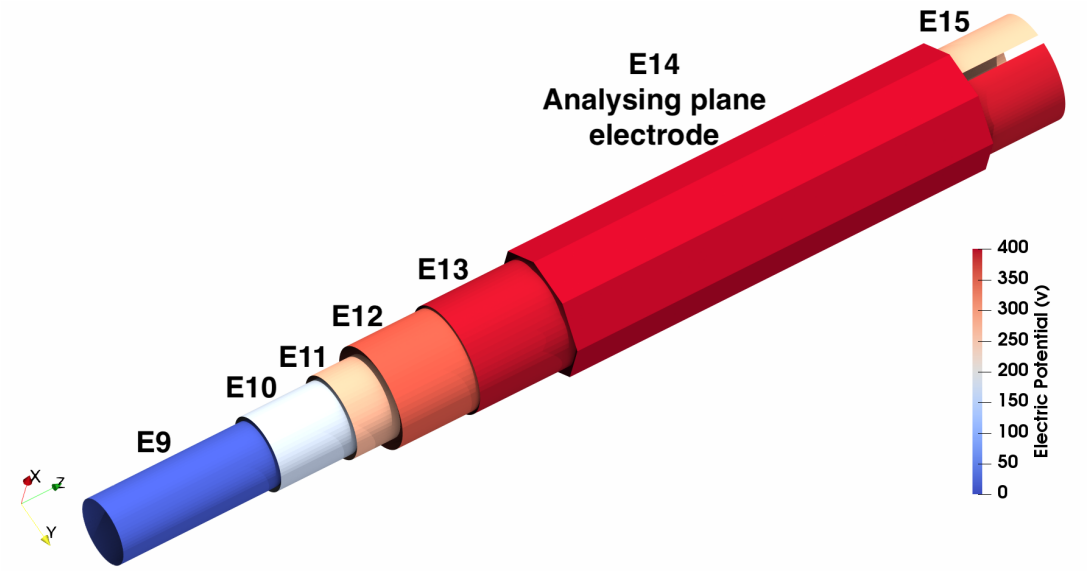

Figure C.11.: Visualisation of electrodes E10 to E15. The figure shows the set of electrodes E10 to E15, where E14 is the octagonal analysing plane electrode and E15 one of the dipole electrodes. The colours indicate the applied electric potentials. In this case E14 is set to 400 V. The other electrodes are set as factor of this voltage (see Table 3.1).

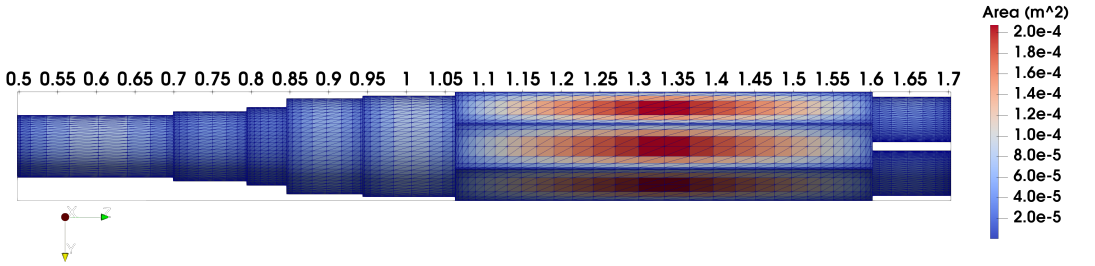

(a) Meshed E10 to E15 electrodes and element sizes.

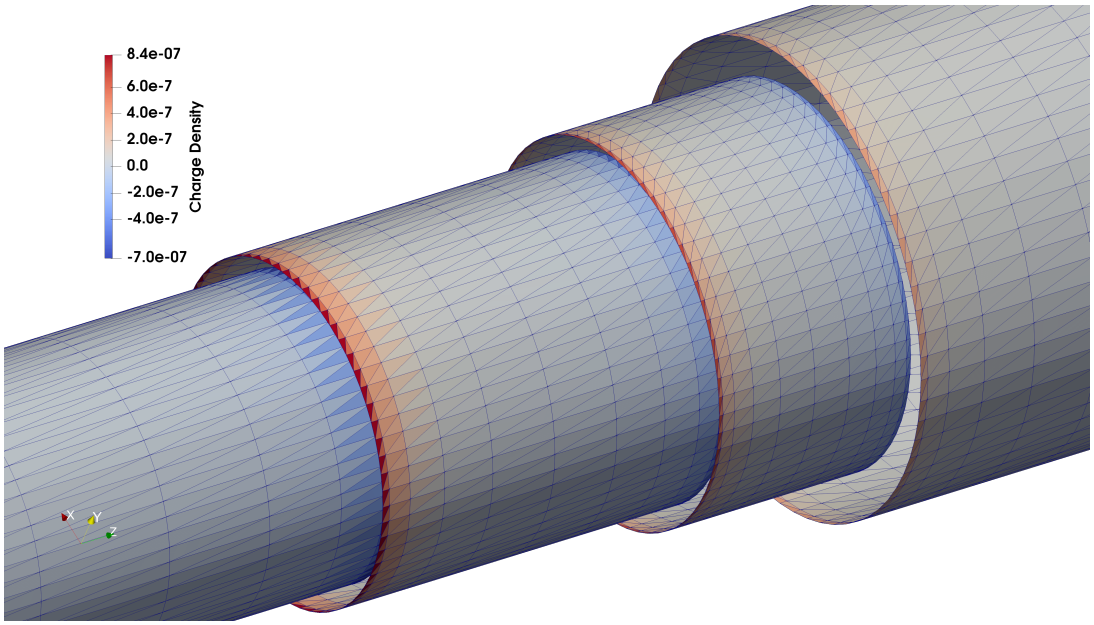

(b) Charge density distribution of E9 to E12.

Figure C.12.: Visualisation of meshing and charge density distribution. (a) The cylindrical electrodes show a line mesh count of 10 and a radial mesh count of 64. The octagonal E14 electrode consists of 8 rectangular plates each meshed in 8 pieces for the short and 32 pieces for the long side. The colour illustrates the area size of the triangular mesh elements (red > blue). The mesh power of 2 leads to smaller (blueish) elements towards the edges of the electrodes. (b) The figure shows the charge density of the single mesh elements as result of the Robin Hood method. In the region of electrode transitions the gradient in the charge density is higher, for which reason the mesh power was applied. In this case, the setted discretisation is to coarse to allow a smooth gradient.

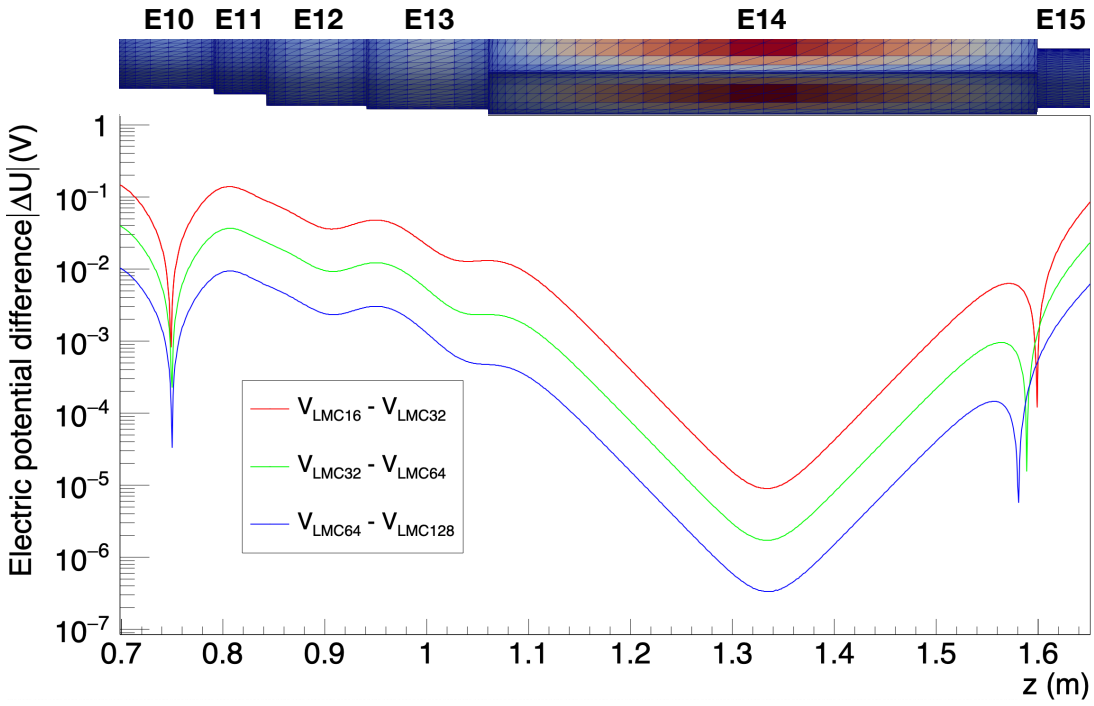

Figure C.13.: Potential convergence due to linear mesh refinement. Plotted is the difference of two electric potentials $\Delta U(z) = U_{\mathrm{LMC}\,n} - U_{\mathrm{LMC}\,n+16}$ resulting from their individual charge density computations ($\log_{10}$ scale). On the top of the frame the electrode system is shown in proper size ratio. It can be seen that the difference $\Delta U(z)$ decreases in all regions after each iteration. While the difference between the first two iterations, the black and the blue line is rather large, the difference between the last two iterations is much smaller.

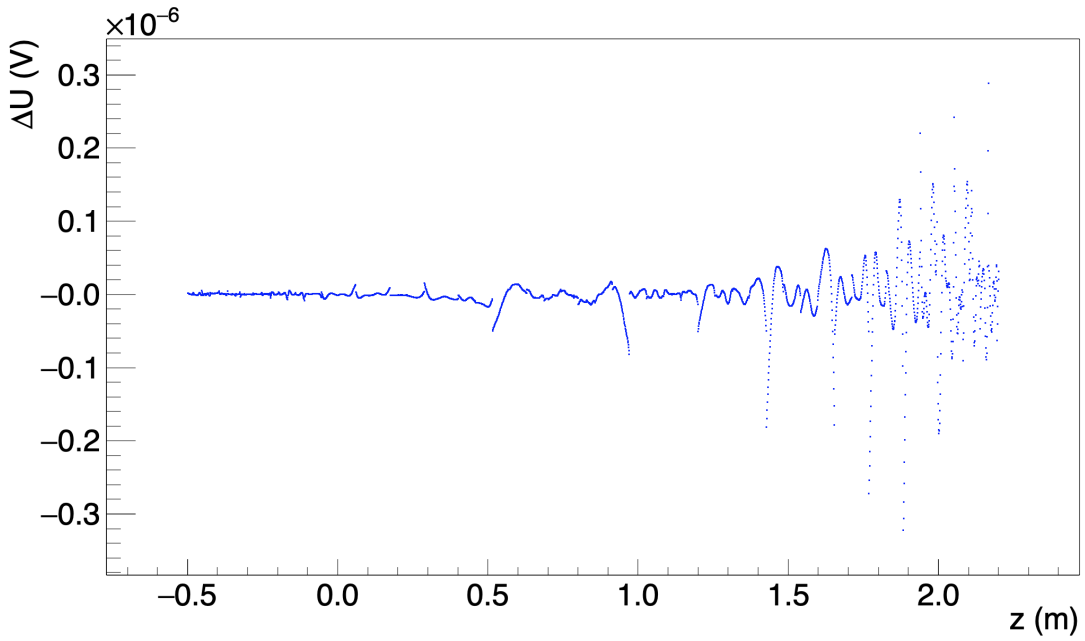

Figure C.14.: Comparison integrating field solver vs. field map. The blue data points show the electric potential difference $\Delta U(z) = U_{IFS}(z) - U_{FM}(z)$ between the integrating field solver (IFS) and the field map (FM). The deviations are well below $< 10^{-6}$ V.

(in case with no work function applied).

C.3.2.2. Field map vs. integrating field solver

For the computation of the electric field and potential during proton tracking the integrating field solver is too slow to obtain the required simulation statistics in reasonable time. A much faster method is the usage of field maps for the different electrostatic configurations. The field maps have to be computed only once in advance and can then be loaded to RAM for the proton tracking simulations. It was found that a grid constant of 2 mm results in short evaluation times and precise values (Figure C.14). Each field map covers only the magnetic flux tube, which results in an acceptable RAM consumption of about 5 GB per map/simulation. The Mogon cluster provides enough capacitances to cover this requirement even for a large number of parallel simulations (up to $\sim$ 18000).

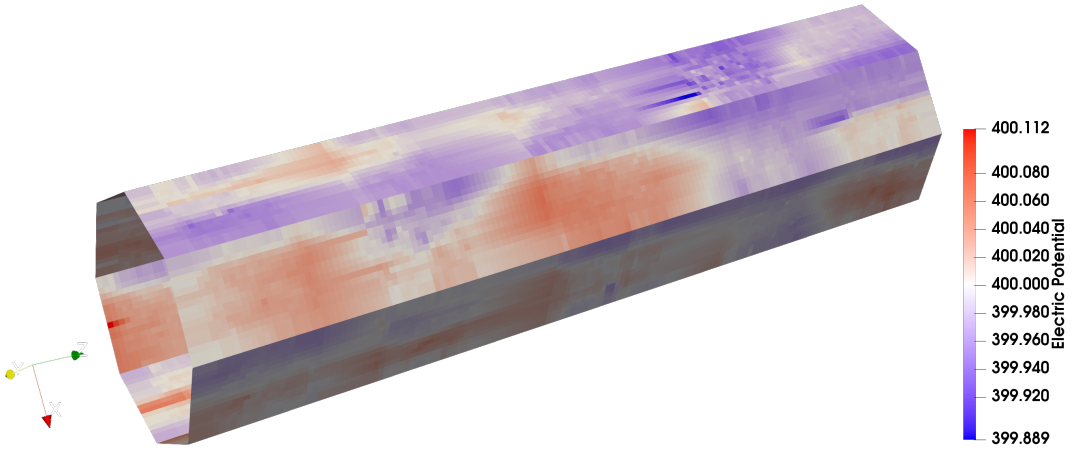

Figure C.15.: Analysing plane electrode E14 with corrected voltage. Shown is the octagonal analysing plane electrode. The colours indicate the corrected electric voltage due to the work function fluctuations: reddish > 400 V, white = 400 V, blueish < 400 V. The distribution on the surfaces also exhibits the patchy structure due to the different crystal orientation of gold emerging from the process of electroplating.

C.3.2.3. Special case implementation of work function

As described in Section 3.4.3, and Appendix A extensive work had been done to quantify and investigate the work function fluctuations of our electrodes. To determine the influence on a these had to be implemented in the simulations. In case of the decay volume electrode and the surrounding elements (boretube and collimation with LiF apertures) the mean values of the measured work function fluctuations could be applied since the magnetic flux tube to the detector is always far enough from these surfaces and the work function fluctuations will smooth out. For the analysing plane electrode this is not the case. To measure the work function of the octagonal analysing plane electrode with our Kelvin probe, it was build to be dismountable in eight long plates, which were finally cutted in five pieces each, resulting in 40 electrode parts. Every part's work function fluctuation was scanned with a grid constant of 3 mm. In this way the work function distribution over each of the eight long plates could be reconstructed as discrete grid. This grid was interpolated and could finally be used to assign the corrected voltage to the computational model of the analysing plane electrode. Therefore the underlying geometry of the analysing plane electrode was constructed out of squares of ~ 3 mm each with the corrected voltage applied. The result is shown in Figure C.15.

The solution of the charge density distribution with all measured work functions implemented last for a single electrostatic configuration two weeks on a GPU.

C.4. *a*SPECT proton particle tracking simulations

In the preceding sections details on the implementation of the geometry and the electromagnetic field computations has been depicted. This section gives details on the configuration of the performed tracking simulations. Essentially, this means setting up the particle generator, the tracking method, and the applied terminators. The following settings are shared to large extent by all simulations. Subtleties will be mentioned in the sections concerning the individual simulations.

C.4.1. Configuration and validation of tracking simulations

C.4.1.1. Generator

In *a*SPECT the source of protons is the neutron beam running through the decay volume electrode in $+x$-direction. Protons decay all along the way of the beam. Tracking all of them would be waste of computing time, of course, since only protons with the opportunity to be counted by the detector are of interest. For this reason it is sufficient to specify a proportioned *decay volume* that covers only the projected volume to the detector pads. This decay volume was determined by simulating regular grids of protons in the $x-y$-plane, which are started at different z-positions inside decay volume electrode. For all protons incident on the detector pads the initial positions were requested from the simulation output. With this information the decay volume could be derived. Account has been taken of angular and energy dependence of this volume due to $E \times B$ drifts and the different measurement configurations. The resulting decay volume was enlarged a little just to be safe not to lose any protons.

For simulations the protons were distributed homogeneous over the decay volume. To take account for the real neutron distribution the homogeneous distribution is weighted with the measured beam profile (Figure 3.6) during analysis. This allows, e.g., to investigate the edge effect for different beam profiles (uniform, standard, reduced) from a single simulation and thus saves a huge amount computation time.

Protons were emitted isotropically, which means $\vartheta = [0; 2\pi)$ and $\phi = [0; \pi)$ respecting the correct spherical distribution. The proton energy distribution follows the differential proton spectrum with $\omega_{\mathrm{p}}(T, a(\lambda_{\mathrm{PDG}}) = -0.105656)$ including relativistic and higher order Coulomb corrections, as well as radiative corrections (see [Glü93]). The value $a(\lambda_{\mathrm{PDG}}) = -0.105656$ is calculated from $\lambda_{\mathrm{PDG}} = -1.2723$ (best estimate of λ from PDG in 2015).

C.4.1.2. Tracking

As described in Appendix C.1.3.2, Kassiopeia provides exact tracking and adiabatic tracking with drift terms. Both methods were compared by simulation of discrete tracks. Only negligible differences could be found as already investigated by [GBB$^+$05], which confirms the excellent adiabatic properties of *a*SPECT. For this reason the faster adiabatic tracking could

be applied. The step control was set to be 1/32 of a cyclotron motion. Finer resolutions have been found not to result in a different path of the proton.

C.4.1.3. Terminators

Every simulated proton track needs to be stopped at a certain point of its physical state evolution. This is ensured by the configuration of terminators. All of the terminators were carefully checked to take effect. Hereafter all of them are listed and explained:

Detector death

The best that could happen to a proton, is being detected. Therefore, a plane at the z-position of the detector was defined. A track that crosses this surface is stopped and marked as "detector death". If such a proton is an actual count in the simulation, is decided during analysis. Therefore the analysis script checks if the $x-y$ incident position in the detector plane is located inside one of the pads or not (cf. Figure C.8).

Surface death

In principle, a proton from decay follows a certain magnetic field line towards the detector. Due to widening of the magnetic flux tube towards the analysing plane or repeated $E \times B$ drifts in case of trapping, there is a probability that it hits an electrode surface. The first is especially the case for pad 1, which was not taken into account for analysis of a, since its projection to the decay volume touched the electrode system. If a track hits a surface, it is stopped and marked as "Surface death".

Minimal kinetic energy death

If a proton is generated with a kinetic energy $T_0 < e*(U_{\mathrm{AP}} - 500\,\mathrm{mV})$ it is terminated instantaneously and marked as "Minimal kinetic energy death". Since the transmission condition even for $\theta_0 = 0^\circ$ cannot be fulfilled (cf. Equation (3.4)), such a proton has no chance to reach the detector and would be trapped until another terminator takes action (e.g. "Surface death" due to $E \times B$ drift). The choice of 500 mV gave the possibility to investigate protons near the transmission condition. This terminator speeds up particle tracking significant especially for higher analysing plane voltages, since uninformative protons are not tracked. It would be even possible not to generate these protons, but in this case statistical information of the initial spectrum is lost.
Default setting: Proton track is stopped at "Step 0" if $T_0 < e*(U_{\mathrm{AP}} - 500\,\mathrm{mV})$.

AP reflection death

A proton, that is reflected, which means $+p_z \rightarrow -p_z$, between the lower $E \times B$ electrode (E8) and the analysing plane ($z \sim 1.34\,\mathrm{m}$), does obviously not fullfill the transmission condi-

tion and is for most simulations of no interest. Then the proton is marked as "AP reflection death".

Trapped death

A proton that changes its sign of the momentum vector $\pm p_z \rightarrow \mp p_z$ is reflected either by the electrostatic mirror, the magnetic gradient in the decay volume (magnetic mirror effect for protons with just tiny longitudinal energy in $-z$-direction), or by the retardation voltage on its way towards the analysing plane (in case of ideal electromagnetic field). This means, that after at least two reflections the particle had the chance to pass the analysing plane. Therefore, after $N_{\mathrm{ref}} > 2$ reflections the track can be stopped in principle. The value of N_{ref} depends on the matter to investigate. To determine the reason of trapping, more particle observables have to be considered, e.g., positions of the reflections. However, if the terminator takes action the track is marked as "Trapped death".
Default setting: Proton track is stopped after 2 reflections.

Outside death

If the proton's position is found to be outside the volume of the bore tube, it is marked as "Outside death". This terminator is for safety reasons only.

Maximal steps death

For whatever reasons non of the aforementioned terminators take action, the particle would be processed forever. Processing means the computation of further "Steps". This case is intercepted by the "Maximal steps death", a terminator, which stops the track after a user-defined number of steps. The maximum number of allowed steps was set to $5 * 10^5$. Only a fraction of about 10^{-5} protons were found to be stopped by this terminator. All of these had initial kinetic energies below 10 eV and initial polar angles to the z-direction of $\sim 90^\circ$. Therefore this effect is negligible.
Default setting: Proton track is stopped if the number of steps exceed $5 * 10^5$.

C.4.2. Edge effect

This section gives a more detailed insight into the production of data by means of particle tracking simulations and their analysis to determine the edge effect. The results from the analysis of the edge effect are presented in Section 3.4.6. There, an 1-dimensional analytical model is compared to the more precise results from the tracking simulations. Despite both models coincidence within their error bars, the analytical model has some drawbacks. It doesnot respect

- the influence of $E \times B$ drifts due to E8, E16 (and E15) electrodes,

- the detector position and alignment,
- the 2-dimensional shape of the detector pads, and
- the detailed neutron beam distribution.

All the aforementioned points can be taken into account by simulations, to be presented in the following.

C.4.2.1. Simulation settings and statistics

To obtain the required information to quantify the edge effect full proton tracking simulations for seven analysing plane voltages were carried out ($U_{\mathrm{AP}} = \{0, 50, 250, 400, 500, 550, 600\}$ V). The particle generator, the tracking settings, and terminators were set to default. The set of voltages was necessary to describe the signature of the edge effect precisely (4^{th} order polynomial, see Figure 3.20).

Ideally the precision of the systematic correction is better than your measurement statistic, so that your not limited in the determination of a. In example, the measurement statistic for Config1 at 400 V is $\Delta y_{\mathrm{exp}}/y_{\mathrm{exp}} \sim 6 \cdot 10^{-4}$. If this is assumed as the typical required precision per retardation voltage, this means your simulation have to *detect* at least $N_{\mathrm{sim}} \approx \frac{1}{\sqrt{\Delta y_{\mathrm{exp}}/y_{\mathrm{exp}}}} \approx 3 \cdot 10^7$ protons per retardation voltage. Including the protons that miss the detector or reflected and are not relevant for the final analysis, it can be traced easily, that about 10^9 protons had to be simulated to obtain a precise correction for the edge effect.

The most important simulation output observables regarding the analysis are the incident position in the detector plane of the proton's guiding centre position (GCP) and the proton's real position (RP) (see Figure C.16). Both variables are related to each other in the following way: The cyclotron path of a charged particle in a magnetic field can be described by the superposition of the motion of the so-called guiding centre parallel to the magnetic field and a perpendicular drift (circular motion). The radius of the cyclotron motion is given by the gyration radius r_{g}, which is the perpendicular distance from the GCP. The RP is linked to the GCP by the radius r_{g} and the phase of motion ϕ_{g} defining the state of the circular motion. In case the charged particle is emitted with no angle to the magnetic field ($\vartheta = \{0, 180\}^\circ$), there will be no circular motion and the GC path coincidence with the RP path (provided that there are no of $E \times B$ drifts, also compare Figure C.6).

C.4.2.2. Analysis

The aim of the analysis is to achieve a functional dependence of the retardation voltage-dependent relative loss[2] of protons due to the edge effect. This means a function, that describes the data points $y^{\mathrm{ee}}_{\mathrm{sys}}(U_{\mathrm{AP}}) = N_{\mathrm{sim}}/N_{\mathrm{sim,\ ee\text{-}free}}$, where N_{sim} are the observed and $N_{\mathrm{sim,\ ee\text{-}free}}$ are

[2] Depending on the shape of the beam profile, the edge effect could also lead to a gain of protons.

the edge effect free counts from simulation. In the following it will not be distinguished between pads, beam profile, configuration and retardation voltage.

The aforementioned relation for $y_{\text{sys}}^{\text{ee}}$ requires clear definitions of $N_{\text{sim, ee-free}}$ and N_{sim}. These base on the proton's GCP and RP in relation to the pad's boundary resulting in the following categories of protons:

(i) GCP and RP inside the pad - N_{inside}

(ii) GCP inside, but RP outside the pad (lost protons) - $N_{\text{loss}}(>0)$

(iii) GCP outside, but RP inside the pad (gained protons) - $N_{\text{gain}}(>0)$

(iv) GCP and RP outside the pad - N_{outside}

The categorisation is depicted in Figure C.16 (b). The group (ii) and (iii) are those, which are relevant for the edge effect. If the proton's GCP is inside the pad, but its RP is outside the pad (group (ii)), this means the proton would have hitten the pad in absence of its circular motion. These protons are lost despite they fulfilled the transmission condition and started inside the decay volume, that is projected to the detector pad. The counts N_{loss} represent these protons. With the same arguments group (iii) in turn holds gained protons described by N_{gain}.

Now, back to the definitions of $N_{\text{sim, ee-free}}$ and N_{sim}: The observed counts N_{sim} are simply the number of protons, which RPs are inside the pad. Therefore the analysis tool checks if a proton is terminated by "Detector death" and if its RP is inside the pad's boundary. N_{sim} can also be obtained by adding the gained protons N_{gain} to and the lost protons N_{loss} from the edge effect free counts $N_{\text{sim, ee-free}}$:

$$N_{\text{sim}} = N_{\text{sim, ee-free}} + N_{\text{gain}} - N_{\text{loss}} \quad . \tag{C.37}$$

This makes sense, if one thinks about the two cases in which the edge effect vanishes:

(i) The detector area is large enough so that its boundary (edge) encloses the full projected magnetic flux tube plus the maximal gyration radius at the detector $r_{\text{g, max}}^{\text{detector}}$. If this is the case $N_{\text{loss}} = N_{\text{gain}} \equiv 0$ holds.

(ii) For a flat beam profile within $r_{\text{g, max}}^{\text{detector}}$ around the detectors boundary region. In this case, the edge effect is still present, but perfectly cancels out $N_{\text{loss}} = N_{\text{gain}}(\neq 0)$.

Both cases lead to the correct finding, that $N_{\text{sim}} \equiv N_{\text{sim, ee-free}}$, in case the edge effect vanishes.

The edge effect-free counts are given by the number of GCP inside the pad's boundary $N_{\text{GCP}} = N_{\text{sim, ee-free}}$. This becomes clear, when the number of RPs inside a pad are described by the categorisation above: $N_{\text{sim}} = N_{\text{inside}} + N_{\text{gain}}$. Combined with Equation (C.37) this results in the following equation

$$N_{\text{sim, ee-free}} = N_{\text{inside}} + N_{\text{loss}} = N_{\text{GCP}} \quad , \tag{C.38}$$

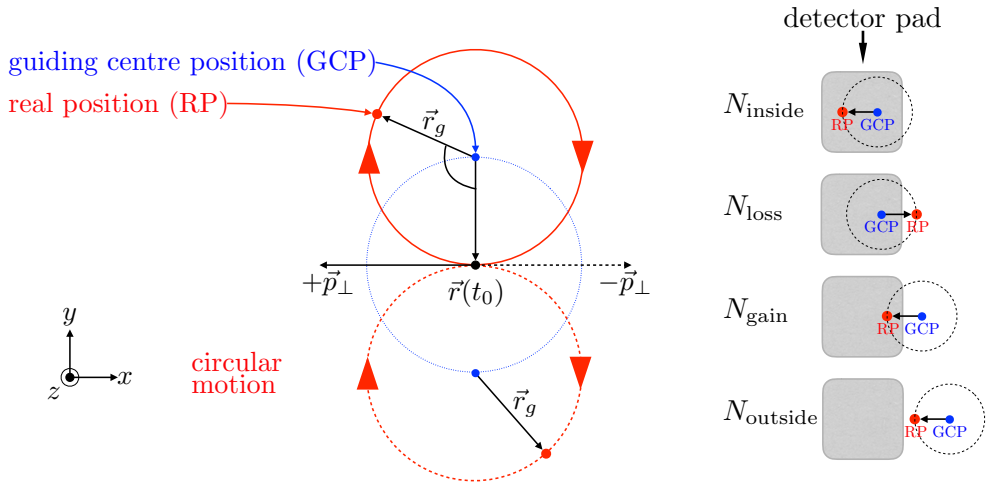

(a) Relation between GCP and RP

(b) Categorisation of incident protons at detector plane

Figure C.16.: Explanation of guiding centre and real position, and the categorisation based on them. (a) The scheme shows the protons motion projected on the x-y-plane. The magnetic field points towards the spectator ($+z$-direction). A proton generated at $\vec{r}(t_0)$ with $+\vec{p}_\perp$ (black dot) will take a clockwise *circular motion* (upper, red, solid circle). The current position during the circular motion (upper, red dot) is called the real position (RP). This can described by the gyration radius $\vec{r}_g$ circling around the guiding centre position (GCP; upper, blue dot). The GCP depends on the initial momentum $\vec{p}_\perp$, e.g., if the proton starts with $-\vec{p}_\perp$, then the proton's circular motion is described by the lower, red circle. This especially means, that two protons generated at $\vec{r}(t_0)$ with same, opposite momentum can have a maximum distance of $4\vec{r}_g$ of their RPs. The blue, dashed circle represents all possible GCPs depending on the direction of the initial momentum. (b) Shown are the four categorisation types of protons incident on the detector plane based on the relative position of RP and GCP to the detector pad.

where N_{GCP} is exactly the number of GCPs inside a pad, which can be traced easily. By means of this the relative loss due to the edge effect can be described by

$$y_{\mathrm{sys}}^{\mathrm{ee}}(U_{\mathrm{AP},i}) = N_{\mathrm{sim}}(U_{\mathrm{AP},i})/N_{\mathrm{GCP}}(U_{\mathrm{AP},i}) \quad , \tag{C.39}$$

where N_{sim} and N_{GCP} are direct accessible observables of the simulation output.

To obtain the $y_{\mathrm{sys}}^{\mathrm{ee(st/re)}}$ for the standard (st) and reduced (re) beam profile the counts $N_{\mathrm{sim/GCP}}$ are weighted with the corresponding beam profile at the position of generation of the proton, which is also part of the simulation output. This also allows easily to take the uncertainty of the beam profile relative to the detector position into account. Therefore the analysis was repeated for positions of the beam profile shifted by $\pm 1\,\mathrm{mm}$ in y/z-direction and the results compared. Also the differences between the two pads were investigated. Both systematics are well below the Monte Carlo statistics of $\Delta y_{\mathrm{sys}}^{\mathrm{ee}}/y_{\mathrm{sys}}^{\mathrm{ee}} \sim 2 \cdot 10^{-4}$, which is why the results are combined leading to the final results shown in Figure 3.20.

Figure C.17 shows the (binned) distribution for the two groups (ii) and (iii) around the detector boundary (black dashed line) as result from particle tracking with no retardation voltage applied ($U_{\mathrm{AP}} = 0\,\mathrm{V}$) and uniform beam profile. With increasing distance from the boundary the number of lost/gained protons decrease rapidly. The maximal observed distance measured orthogonal from the boundary is about 1.3 mm. This is easy understandable: A proton in the decay volume has a maximal gyration radius of about $r_{\mathrm{DVmax}} = \sqrt{2 m_{\mathrm{p}} T_{\mathrm{max}}}/eB_0 \approx 1.8\,\mathrm{mm}$ with $B_0 \approx 2.2\,\mathrm{T}$ (emission with maximal kinetic energy $T_{\mathrm{max}} \approx 751\,\mathrm{eV}$ perpendicular to the magnetic field line). The magnetic flux tube, and therefore the gyration radius, scales with $\sqrt{B_0/B(z)}$, where $B(z)$ is the magnetic flux density at z. At the position of the detector plane the field is $B(z_{\mathrm{detector}}) \approx 4.4\,\mathrm{T}$. This results in $r_{\mathrm{g,\,max}}^{\mathrm{detector}} = r_{\mathrm{g,\,max}}^{\mathrm{DV}} \sqrt{2.2\,\mathrm{T}/4.4\,\mathrm{T}} \approx 1.3\,\mathrm{mm}$.

C.4.3. Determination of the retardation voltage $\langle U_{\mathbf{A}} \rangle$ and magnetic field ratio $\langle r_{\mathbf{B}} \rangle$

As explained in Section 3.2.1 the input variables U_{A} and r_{B} to the transmission function have to be replaced by effective values $\langle U_{\mathrm{A}} \rangle$ and $\langle r_{\mathrm{B}} \rangle$ as they are effected by unavoidable electromagnetic field inhomogeneities. These values can only be obtained by tracking simulations. For exact determination of these sensitive parameters on *a* great effort was expended to pin down precise and accurate boundary conditions for the electromagnetic field calculations. This included the investigation and determination of the work function fluctuations of all relevant electrodes (Appendix A) and a magnetic field measurement by means of nuclear magnetic resonance (Section 3.4.2). In addition, the solution of a single electrostatic configuration including the detailed work function distributions was extremely computation power consuming ($\sim 2\,$weeks for single retardation voltage setting on a GPU). The tracking simulations themselves to determine $\langle r_{\mathrm{B}} \rangle$ and $\langle U_{\mathrm{A}} \rangle$ are straightforward and will be presented in the following. The results are already given in Section 3.4.3 or Section 3.4.2, respectively.

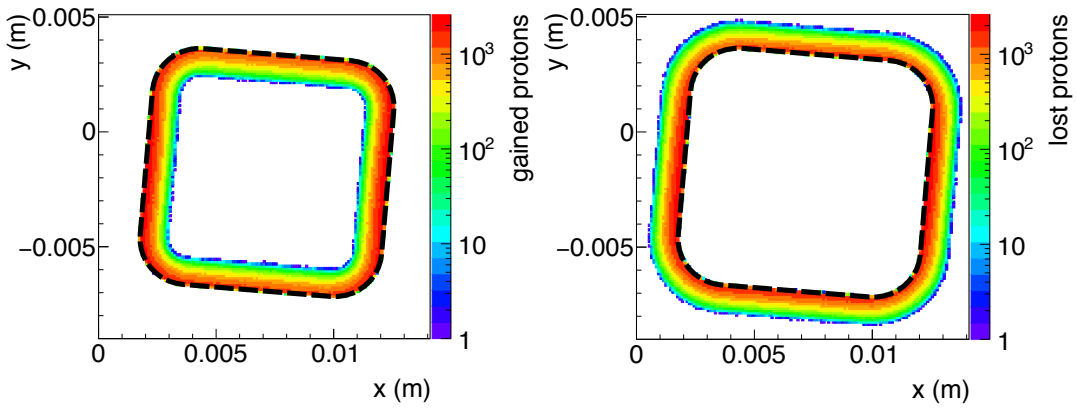

(a) Gained protons

(b) Lost protons

Figure C.17.: Distribution of gained and lost protons due to the edge effect. The plots visualize the lost and gained protons in the vicinity of pad 2's boundary (black dashed line) for a simulation with uniform beam profile at $U_{\mathrm{AP}} = 0\,\mathrm{V}$. (a) Plotted is the distribution of the incident RPs, which GCPs are outside the pad, but their RPs are inside the pad (group (iii)). (b) Plotted is the distribution of the incident RPs, which GCPs are inside the pad, but itheir RPs are outside the pad (group (ii)). The maximal width from the pad's boundary is given by the maximal possible gyration radius $r_{\mathrm{g,\,max}}^{\mathrm{detector}} \approx 1.3\,\mathrm{mm}$ at the detector. The probability to find a proton increases significant with shorter distance from the boundary, since the maximal distance of 1.3 mm can only be reached by a proton emitted with maximal kinetic energy $T_{\mathrm{max}} \approx 751\,\mathrm{eV}$ perpendicular to the magnetic field. But depending on the angle of emission it can also incident in-between $r_{\mathrm{g,\,max}}$ and the boundary. By integrating over all emission angles and energies the distribution can be reproduced.

C.4.3.1. Simulation settings and statistics

To obtain the required information to quantify the effective values full proton tracking simulations for four analysing plane voltages were carried out ($U_{\mathrm{AP},k} = 50, 250, 400, 600\,\mathrm{V}$). The particle generator, the tracking settings, and terminators were set to default.

The number of required tracks could not be pin downed prior to the simulation, since the widths of the distributions $\sigma_{\mathrm{RMS},r_\mathrm{B}}$ and $\sigma_{\mathrm{RMS},U_\mathrm{A}}$ were not known beforehand. Two criteria were used to verify for sufficient statistics: (i) The standard error of the mean should be $\sigma_{\mathrm{RMS},\langle r_\mathrm{B}\rangle}/N < 10^{-5}$ or $\sigma_{\mathrm{RMS},\langle U_\mathrm{A}\rangle}/N < 1\,\mathrm{meV}$, respectively. (ii) The values $\langle U_\mathrm{A}\rangle$ and $\langle r_\mathrm{B}\rangle$ plotted against the number of tracks shall exhibit convergence like behaviour.

The most important simulation output observables are the electric potential and magnetic field at place of generation, $\phi_{0,i}$ and $B_{z\ 0,i}$, and at the place of the proton's minimal longitudinal kinetic energy in the analysing plane region ($1.2\,\mathrm{m} \lesssim z \lesssim 1.4\,\mathrm{m}$), $\phi_{\mathrm{min\ long},i}$ and $B_{z\ \mathrm{min\ long}\ ,i}$. At this point a proton experiences the maximal amount of retardation, which is defined as the analysing plane.

C.4.3.2. Analysis

The aim of the analysis is to obtain functional dependencies, which correct the *ideal* input values U_AP [3] and r_B [4] of the transmission function by realistic, effective values with uncertainties taking field inhomogeneities into account.

Retardation voltage $\langle U_\mathrm{A}\rangle$

In case of the retardation voltage, it is targeted for a function that describes $\langle U_\mathrm{A}\rangle$ in dependence of the applied voltage $\langle U_\mathrm{A}\rangle = \langle U_\mathrm{A}\rangle(U_\mathrm{AP})$. For practical reasons the deviation from the ideal voltage is looked at:

$$y_\mathrm{sys}^{\langle U_\mathrm{A}\rangle}(U_{\mathrm{AP},k}) = \langle U_\mathrm{A}\rangle(U_{\mathrm{AP},k}) - U_{\mathrm{AP},k} \quad \text{with} \tag{C.40}$$

$$\langle U_\mathrm{A}\rangle(U_{\mathrm{AP},k}) = 1/N \sum_i^N U_{\mathrm{A},i}(U_{\mathrm{AP},k}) \tag{C.41}$$

The $U_{\mathrm{A},i}$'s are the retardation voltages of the single proton tracks P_i given by $U_{\mathrm{A},i}(U_{\mathrm{AP},k}) = \phi_{\mathrm{min\ long},i} - \phi_{0,i}$. These values were calculated for all protons from the simulation output, which are terminated by "Detector death" and incident inside a pad. The distributions $\{U_{\mathrm{A},i}\}$ are differentiated by pad 2 and pad 3, and configurations, in which the E15 electrode *was not* operated as dipole (Config 1,2,5,6 - E15sym) and in which E15 *was* operated as dipole

[3] Remember: in the ideal case, the retardation voltage U_A is identical to the applied voltage at the analysing plane U_AP.

[4] The ideal value defined by $r_B = B_{z,\ \mathrm{max\ AP}}/B_z(z = 0\,\mathrm{m})$, where $B_{z,\ \mathrm{max\ AP}}$ is the local magnetic field maximum in the analysing plane region, is a priori incorrect, since $B_z(z = 0\,\mathrm{m})$ neglects the gradient over the finite decay volume.

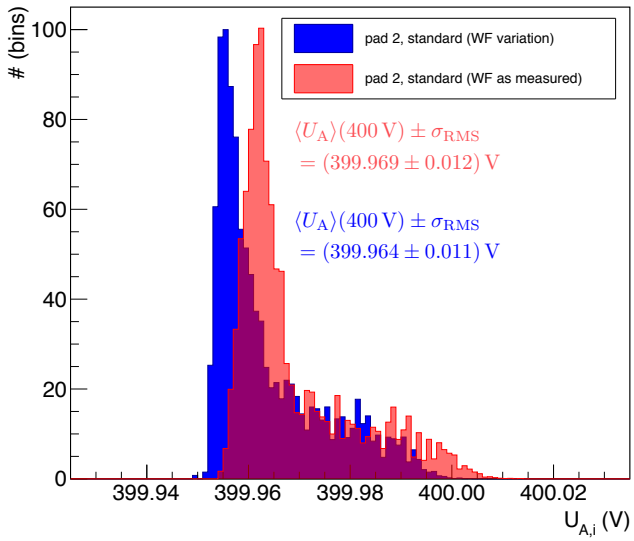

Figure C.18.: Distribution of ret. voltages of single proton tracks for pad 2 and E15sym configuration. The red distribution is the result from the work function distribution as measured and the blue distribution is the result from the statistically modification of the applied work function. The shape of the distributions doesn't change, only the mean value is shifted by $\sim -5\,\mathrm{mV}$.

(Config 3,4,7 - E15asym). The dipole mode shifts the analysing plane slightly in $-z$-direction resulting in different values $U_{\mathrm{A},i}$. The neutron beam profile was also taken into account by weighting of the values.

Figure C.18 shows the distribution of $\{U_{\mathrm{A},i}\}$ for $U_{\mathrm{AP}} = 400\,\mathrm{V}$ for pad 2, E15sym configuration, and weighting with the standard beam profile. The red distribution is the result from the work function distribution as measured. The blue distribution shall be ignored for a moment. The effective value is $\langle U_{\mathrm{A}}\rangle(400\,\mathrm{V}) = 399.969 \pm 0.012\,\mathrm{V}$ and is comparable to the rough estimation, in which one calculates the difference between the electric potential on-axis in the centre of the decay volume electrode $U_{\mathrm{A}}(z = 0\,\mathrm{cm}) = 0.020\,\mathrm{V}$ (see Figure 3.12) and the maximum potential in the analysing plane electrode $U_{\mathrm{A}}(z \approx 1.28\,\mathrm{cm}) = 399.986\,\mathrm{V}$ (see Figure 3.13), which is $\Delta U_{\mathrm{A}} = 399.966\,\mathrm{V}$.

In Figure C.19 the values $\langle U_{\mathrm{A}}\rangle(U_{\mathrm{AP},k}) - U_{\mathrm{AP},k}$ against U_{AP} are shown for pad 2 and 3 and for the reduced and standard beam profile. The uncertainties are given by the individual standard errors $\sigma_{\mathrm{RMS}}/\sqrt{N}$. The weighting with the beam profile has no significant influence. Also a variation of the position of the beam profile by $\pm 1\,\mathrm{mm}$ showed no significant effect (not shown). But the difference between the pads is clearly visible with an overall offset of about 4 mV. The reason for this are the individual proton path collected by the two pads. The further decrease of the values with increasing U_{AP} is due to the increasing influence of the field

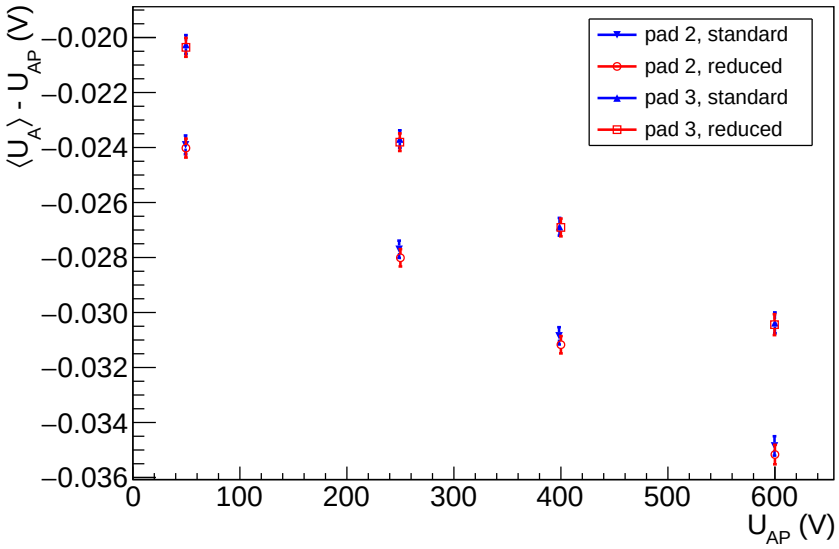

Figure C.19.: Difference to effective retardation voltages for reduced/standard beam profile for pad 2/3. Plotted are values $\langle U_\mathrm{A}\rangle(U_{\mathrm{AP},k}) - U_{\mathrm{AP},k}$ for pad 2 (lower points) and pad 3 (upper points) for weighting with the standard (blue points) and the reduced (red points) beam profile. The errors are given by their individual standard errors $\sigma_\mathrm{RMS}/\sqrt{N}$.

leakage from the E15 electrode. The data points per U_{AP} were combined by calculating the average per pad and by adding the systematic uncertainties due to the different beam profiles and position variation to the statistical error[5]. The same analysis was carried out for E15asym. The $y_{\mathrm{sys}}^{\langle U_{\mathrm{A}}\rangle}(U_{\mathrm{AP},k})$ can be described by a linear function $g_{\mathrm{sys}}^{\langle U_{\mathrm{A}}\rangle} = c_0^{\langle U_{\mathrm{A}}\rangle} + c_1^{\langle U_{\mathrm{A}}\rangle} \cdot U_{\mathrm{AP}}$. The final results are shown in Figure 3.14.

Besides the linear dependency of the retardation voltage from the applied voltage, there are several systematic uncertainties in the work function measurements resulting in a general offset $c_{\mathrm{AP,\,offset}}^{\langle U_{\mathrm{A}}\rangle}$ on $g_{\mathrm{sys}}^{\langle U_{\mathrm{A}}\rangle}$ (listed in Table 3.6). One contribution comes from the measurement accuracy of the work function fluctuations of $\pm 30\,\mathrm{meV}$. To take account for this the work function of the individual electrode segments were modified statistically by a work function offset drawn from a gaussian distribution with mean 0 meV and $\sigma = 30\,\mathrm{meV}$. Each modification required a further, extensive computation of the charge densities (~ 2 weeks per U_{AP}). Due to limited computing power this could only be done two times for the given set of the four U_{AP}'s. This resulted in a single GPU computation time of 32 weeks (work function as measured for E15sym and E15asym and 2 variations, for each 4 U_{AP}'s, each two weeks: ((2+2)*4*2) = 32 weeks). In Figure C.18 the red distribution shows the result from a variation. The shape is similar but shifted by about +5 meV. The electric potential in the decay volume is influenced by the work function of 28 electrode segments, which means that a variation results in a uncertainty of $30\,\mathrm{meV}/\sqrt{28} \approx 6\,\mathrm{meV}$ (first order). In case of the analysing plane the influence is due to 40 electrode segments $30\,\mathrm{meV}/\sqrt{40} \approx 5\,\mathrm{meV}$. However, the measurement accuracy is taken into account with 10 meV (see Table 3.6), which tends to overestimate the effect.

Magnetic field ratio $\langle r_{\mathbf{B}} \rangle$

From the same tracking simulations the distributions $\{r_{\mathrm{B},i}\}$ with $r_{\mathrm{B},i} = B_{z\ \mathrm{min\ long},i}/B_{z\ 0,i}$ were extracted for the different voltages $U_{\mathrm{AP},k}$. In Figure C.20 the distribution is shown for $U_{\mathrm{AP}} = 50\,\mathrm{V}$, weighting with the standard beam profile and E15asym. It can be traced easily, that the width of the distribution is basically caused by the magnetic field gradient in the decay volume (Figure 3.11) over the extent of the neutron beam in z-direction.

In Figure C.21 the averages of the distributions $\{r_{\mathrm{B},i}\}$ and their standard error $\sigma_{\mathrm{RMS}}/\sqrt{N}$ are plotted against U_{AP} for the standard and reduced beam profile and both pads for E15asym configuration. No voltage dependency can be identified, which is expected, since a dependency can only occur if the position of the analysing plane would change with the applied voltage. The difference in the weighting with standard (blue points) and reduced (red points) beam profile is marginal. The deviation between pad 2 (lower points) and 3 (upper points) is due to the radial decrease of the magnetic field from the symmetry axis of *a*SPECT.

Finally, four values $\langle r_{\mathrm{B}} \rangle$ are sufficient to describe the transmission: two for the differentiation between E15sym/asym and for the two detector pads. The final uncertainties are dom-

[5] The statistical error doesnot decrease by the combination, since the data from the variation and weighting with the beam profile stem from the same statistics.

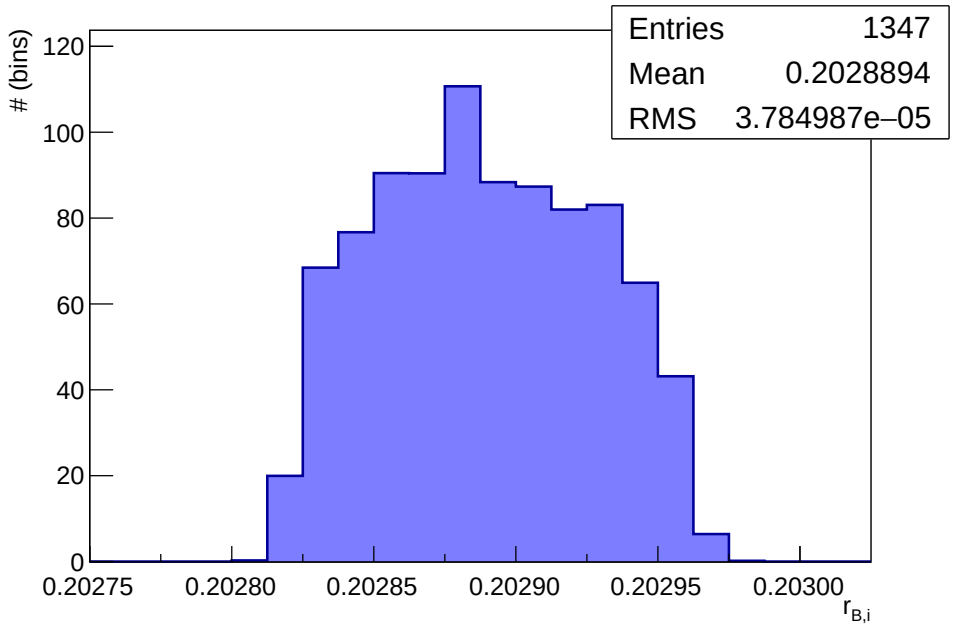

Figure C.20.: Distribution $\{r_{\mathrm{B},i}\}$ for E15asym configurations. The histograms shows the distribution of $\{r_{\mathrm{B},i}\}$ for pad 2, $U_{\mathrm{AP}} = 50\,\mathrm{V}$, and weighting with the standard beam profile. The width is basically caused by the magnetic field gradient in the decay volume over the extent of the neutron beam.

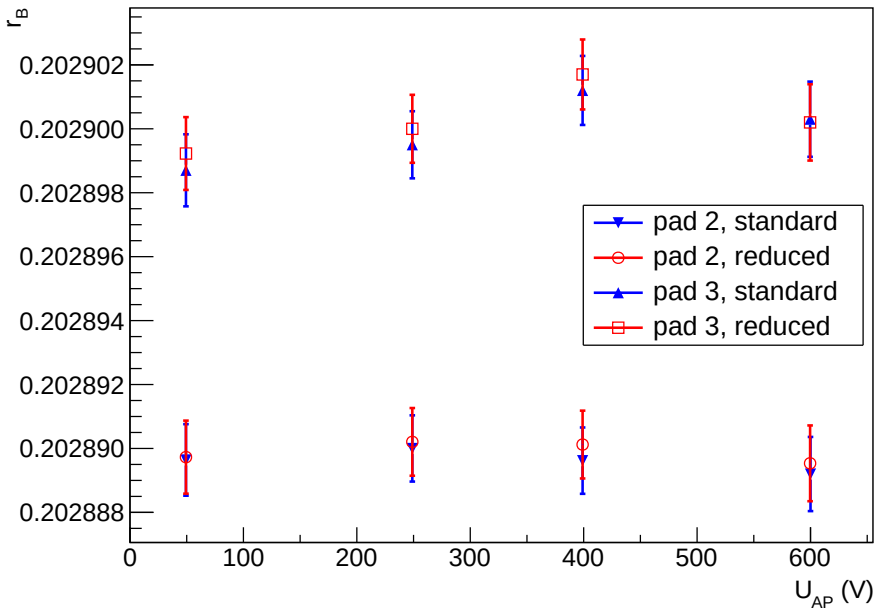

Figure C.21.: Magnetic field ratio r_B against U_{AP}. Plotted are the averages of the magnetic field ratios with their statistical errors from the distributions $\{r_{B,i}\}$ (Figure C.20) for pad 2 (lower points) and pad 3 (upper points) for weighting with the reduced (red points) and standard (blue points) beam profile for E15asym configurations against the voltage U_{AP}. No voltage dependency is visible. The effect of weighting with the beam profile is well below the statistical error ($\sim 1 * 10^{-6}$).

inated by the simulation statistics, but also include the small differences due to the variation of the beam profile by ± 1 mm and the weighting with the standard and reduced beam profile. The final results were already presented in Table 3.4.

C.4.4. Proton traps in the decay volume

In Section 3.4.9 it was shown, that the inhomogeneous electric fields, as a result of field leakage and work function fluctuations, in combination with the applied axial magnetic field gradient lead to Penning like traps in the decay volume. This is problematic, since trapped protons are lost for the measurement. As the condition for trapping basically depends on the protons initial longitudinal energy this leads to a retardation voltage dependent effect on the integral spectrum.

In Figure C.22 the electric potential including the work function fluctuations $\phi_{wf}(z)$ (solid blue line), without the work function fluctuations (dashed blue line) and the magnetic field

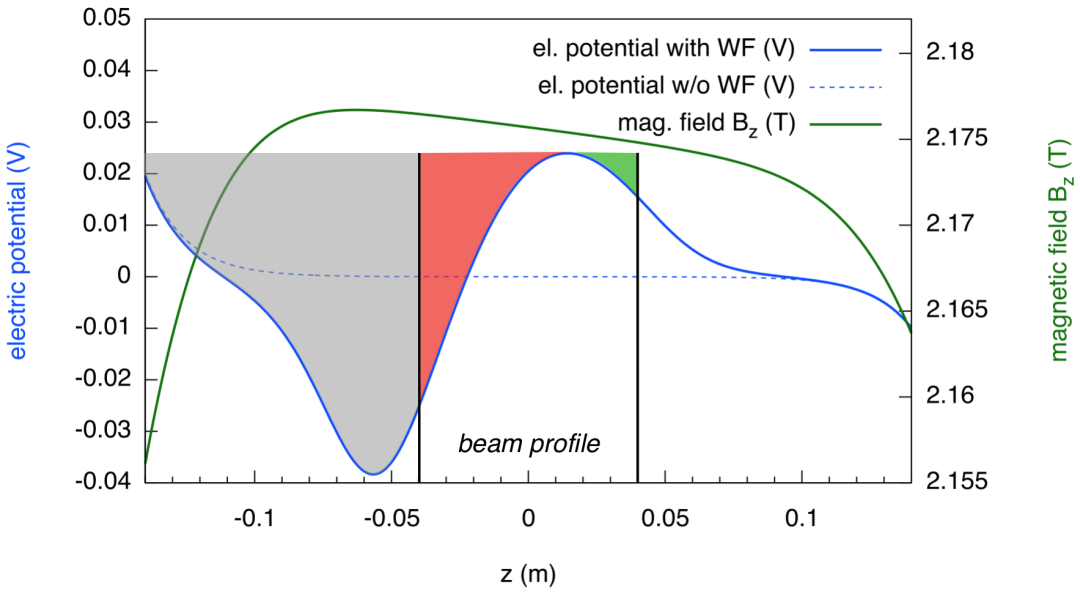

Figure C.22.: Proton trap in the decay volume. Shown is the electric potential with a clear minima and maxima due to field leakage and work function distribution (blue line). The blue dashed line is the potential in absence of these influences. The axial magnetic gradient is given by the green line. This electromagnetic field combination lead to Penning like traps for protons (greyish and reddish area). For details see text.

$B_z(z)$ (green line) in the decay volume are shown. The extent of the beam profile in z-direction is indicated by two black vertical lines at $\pm 0.04\,\mathrm{m}$. In absence of the measured work function fluctuations the electric potential (dashed blue line) is almost flat ($\sim 0\,\mathrm{V}$) over the decay volume. In combination with the magnetic field no particles are stored. In the case with work function fluctuations applied the electric potential reveals two extrema: A maxima at $0.015\,\mathrm{m}$ with $\sim 24\,\mathrm{mV}$ and a minima at $-0.055\,\mathrm{m}$ with $\sim -39\,\mathrm{mV}$. In combination with the magnetic field protons generated at $z < 0.015\,\mathrm{m}$ (reddish area) can potentially be stored between the maxima and the electrostatic mirror (greyish area). In example, a proton, which is generated at $z = -0.04\,\mathrm{m}$ with $\theta_0 = 0^\circ$ can only overcome the maxima, if its initial kinetic energy is at least $T_0 > e \cdot \phi_{\mathrm{wf}}(0.015\,\mathrm{m}) - e \cdot \phi_{\mathrm{wf}}(-0.04\,\mathrm{m}) = 24\,\mathrm{meV} - (-25\,\mathrm{meV}) = 49\,\mathrm{meV}$. As *a*SPECT only measures protons with $T_0 > 50\,\mathrm{eV}$ ($U_{\mathrm{AP}} = 50\,\mathrm{V}$), these low energetic ones do not influence the measured integral spectrum. But protons with $T_0 > 50\,\mathrm{eV}$ can also be stored, if they are emitted with an angle of $\theta_0 \approx 90^\circ$. Then, their longitudinal energy is too low to exit the decay volume. In example, by means of the so-called adiabatic transmission function (see [GBB$^+$05] Eq. (3)) it can be calculated analytically, that a proton, which is emitted at $z = -0.04\,\mathrm{m}$ with $\theta_0 \approx 90^\circ$ requires $T_0 \gtrsim 180\,\mathrm{eV}$ to exit the decay volume. The adiabatic transmission function respects the conversion of axial kinetic energy to longitudinal energy due to the axial magnetic field gradient in the decay volume. This helps to suppress the trapping of protons. Without this gradient protons from all energies would be stored only depending on the angle of emission θ_0, which would be worse. This emphasises the importance of the axial magnetic gradient in the decay volume as a design goal.

However, based on the on-axis fields shown in Figure C.22 and the adiabatic transmission function a simplified, 1-dimensional model is used in Section 3.4.9 to calculate the retardation voltage-dependent relative proton loss (Equation (3.32)) analytically. The result is shown in Figure 3.27 (red line). The model already indicates, that the effect on a is small (real a_{ref} is shifted by $\sim +0.3\,\%$, see Table 3.7). To respect also the x,y-distribution of the electromagnetic fields, potential $E \times B$ drifts of trapped protons and the correct projection onto the detector particle tracking is necessary. The aim of the simulation is to obtain the phase space $\Omega(\theta_0, T_0)$ of the trapped protons, which is finally the inset of Figure 3.27.

C.4.4.1. Simulation settings and statistics

To obtain the distribution $\Omega(\theta_0, T_0)$ it is sufficient to simulate for the single retardation voltage $U_{\mathrm{AP}} = 50\,\mathrm{eV}$, since the depth and shape of the trap is independent of the retardation voltage and protons with $T_0 < 50\,\mathrm{eV}$ are not relevant for the determination of a. The effect for retardation voltages $U_{\mathrm{AP}} > 50\,\mathrm{eV}$ can be deduced from this result. The particle generator and the tracking settings were set to default.

To identify a trapped proton in the simulation the terminator settings are of utmost importance. It was identified that a proton has to be detected after at least $3 \cdot 10^5$ steps, which is why this is the default setting for the "Maximum steps death" terminator. This limit is now raised to 10^7 steps. This means a proton, which is terminated by this modified terminator is

trapped between the electrostatic mirror and the decay volume (Protons, which are reflected between the decay volume and the analysing plane are terminated by "AP reflection death"). The "Trapped death" terminator was switched off completely.

The most important output variables are the initial kinetic energy T_0 and the initial polar angle to the magnetic field θ_0 of the protons terminated by "Maximal steps death". These are used to obtain $\Omega(\theta_0, T_0)$.

C.4.4.2. Analysis

All protons, which where terminated by "Maximum steps death", are used to fill the 2D-histogram $\Omega_{\mathrm{tr}}(\theta_0, T_0)$ for pad 2 and pad 3. But these protons have to meet the following requirements:

- Initial position $z_0 \lesssim 0.015\,\mathrm{m}$
  As shown in Figure C.22 only protons generated before the potential maximum can be trapped.

- Final position $z_0 \lesssim 0.015\,\mathrm{m}$
  If a proton is really be trapped, the "Maximum step death" terminator must take effect between the maximum in the decay volume and the electrostatic mirror.

- Proton stems from decay volume of pad 2 or 3
  If a proton is identified as trapped, this doesn't automatically mean it is lost for the measurement. It have to be checked if the proton even had the chance to hit one of the detector pads. Therefore it have to stem from the *actual* decay volume of one of the pads. These decay volumes could be reconstructed by determination of the volume, which is occuppied by the detected protons.

Furthermore, the detected protons are filled in $\Omega_{\mathrm{det}}(\theta_0, T_0)$.

To calculate the relative loss for the different retardation voltages $y^{\mathrm{tr}}_{\mathrm{sys}}(U_{\mathrm{AP},k})$ the so-called adiabatic transmission energy $T_{\mathrm{trans}}(\theta_0, U_{\mathrm{AP},k})$ is used (see [GBB$^+$05] Eq. (4)):

$$T_{\mathrm{trans}}(\theta_0, U_{\mathrm{AP},k}) = \frac{eU_{\mathrm{AP},k}}{1 - r_{\mathrm{B}} \sin^2 \theta_0} \quad . \tag{C.42}$$

The adiabatic transmission energy T_{trans} returns the minimal kinetic energy, which is required by a proton, depending on its initial polar angle θ_0, to be transmitted. This means, in case $T_0 \geq T_{\mathrm{trans}}$ the proton is transmitted, but if $T_0 < T_{\mathrm{trans}}$ it is not. This behaviour can be summarised by a Heaviside step function H:

$$H(T_0 - T_{\mathrm{trans}}(\theta_0, U_{\mathrm{AP},k})) = \begin{cases} 0: & T_0 - T_{\mathrm{trans}} < 0 \\ 1: & T_0 - T_{\mathrm{trans}} \geq 0 \end{cases} \quad . \tag{C.43}$$

By means of this Heaviside step function, the number of trapped protons from $\Omega_{\mathrm{tr}}(\theta_0, T_0)$ can be extracted, which would have been detected, if they were not trapped:

$$N_{\mathrm{tr},k} = \iint \Omega_{\mathrm{tr}}(\theta_0, T_0)\, H(T_0 - T_{\mathrm{trans}}(\theta_0, U_{\mathrm{AP},k}))\, d\theta\, dT_0 \quad . \tag{C.44}$$

This is almost the same as a vertical cut to the inset of Figure 3.27 at $T_{\mathrm{trans}}(\theta_0, U_{\mathrm{AP},k}) = \frac{eU_{\mathrm{AP},k}}{1-r_{\mathrm{B}}}$, as $\sin^2\theta_0 \approx 1$, and adding up the remaining bins. Since the simulation is performed for the single retardation voltage $U_{\mathrm{AP}} = 50\,\mathrm{V}$, this has also to be applied onto the distribution of the detected protons $\Omega_{\mathrm{det}}(\theta_0, T_0)$:

$$N_{\mathrm{det},k} = \iint \Omega_{\mathrm{det}}(\theta_0, T_0)\, H(T_0 - T_{\mathrm{trans}}(\theta_0, U_{\mathrm{AP},k}))\, d\theta\, dT_0 \quad . \tag{C.45}$$

Finally the relative loss can be calculated as follows:

$$y^{\mathrm{tr}}_{\mathrm{sys}}(U_{\mathrm{AP},k}) = \frac{N_{\mathrm{tr},k}}{N_{\mathrm{tr},k} + N_{\mathrm{det},k}} \tag{C.46}$$

The number of trapped protons depends predominately on the depth of the trap, which is formed by field leakage and the electrodes' work function fluctuations. To take account for the measurement accuracy of the work function fluctuations, the same analysis were conducted for electric potentials as result from statistically modified potentials of the electrode segments by a work function offset drawn from a gaussian distribution with mean 0 meV and $\sigma = 30\,\mathrm{meV}$ (just like in the case of $\langle U_{\mathrm{A}} \rangle$, Appendix C.4.3.2). As the distance from the electrode surfaces to the actual decay volume is large and it is surrounded by several electrodes segments, the deviation from the *original* potential is small. However, the uncertainties $y^{\mathrm{tr}}_{\mathrm{sys}}$ take this into account, as well as the Monte Carlo statistics and the uncertainties due to the positioning of the neutron beam profile.

Bibliography

[Abe08] H. Abele. "The neutron. Its properties and basic interactions". Progress in Particle and Nuclear Physics, volume 60 (2008) (1), 1 – 81. ISSN 0146-6410. URL http://www.sciencedirect.com/science/article/pii/S0146641007000622.

[ACH+17] C. Alexandrou et al. "Nucleon axial form factors using $N_f = 2$ twisted mass fermions with a physical value of the pion mass". Phys. Rev. D, volume 96 (2017), 054507. URL https://link.aps.org/doi/10.1103/PhysRevD.96.054507.

[ADH+06] H. Abele et al. "Characterization of a ballistic supermirror neutron guide". Nuclear Instruments and Methods in Physics Research Section A: Accelerators, Spectrometers, Detectors and Associated Equipment, volume 562 (2006) (1), 407 – 417. ISSN 0168-9002. URL http://www.sciencedirect.com/science/article/pii/S0168900206005328.

[AGL05] J. Ahrens, B. Geveci and C. Law. "ParaView: An End-User Tool for Large Data Visualization". Visualization Handbook, (2005).

[AHK+14] F. Allmendinger et al. "New Limit on Lorentz-Invariance- and *CPT*-Violating Neutron Spin Interactions Using a Free-Spin-Precession ^{3}He-^{129}Xe Comagnetometer". Phys. Rev. Lett., volume 112 (2014), 110801. URL https://link.aps.org/doi/10.1103/PhysRevLett.112.110801.

[BAB+08] Baeßler, S. et al. "First measurements with the neutron decay spectrometer a SPECT". Eur. Phys. J. A, volume 38 (2008) (1), 17–26. URL https://doi.org/10.1140/epja/i2008-10660-0.

[BBPP14] S. Baeßler et al. "New precision measurements of free neutron beta decay with cold neutrons". Journal of Physics G: Nuclear and Particle Physics, volume 41 (2014) (11), 114003. URL http://stacks.iop.org/0954-3899/41/i=11/a=114003.

[BCC+12] T. Bhattacharya et al. "Probing novel scalar and tensor interactions from (ultra)cold neutrons to the LHC". Phys. Rev. D, volume 85 (2012), 054512. URL https://link.aps.org/doi/10.1103/PhysRevD.85.054512.

[BD64] J. Bjorken and S. Drell. Relativistic quantum mechanics. International series in pure and applied physics (McGraw-Hill, 1964). URL https://books.google.de/books?id=pAdRAAAAMAAJ.

[BDA+18] M. A.-P. Brown et al. "New result for the neutron β-asymmetry parameter A_0 from UCNA". Phys. Rev. C, volume 97 (2018), 035505. URL https://link.aps.org/doi/10.1103/PhysRevC.97.035505.

[BDH+86] P. Bopp et al. "Beta-Decay Asymmetry of the Neutron and $\frac{g_A}{g_V}$". Phys. Rev. Lett., volume 56 (1986), 919–922. URL https://link.aps.org/doi/10.1103/PhysRevLett.56.919.

[BDvdG+02] J. Byrne et al. "Determination of the electron-antineutrino angular correlation coefficient a 0 and the parameter $|\lambda| = |\frac{G_A}{G_V}|$ in free neutron β-decay from measurements of the integrated energy spectrum of recoil protons stored in an ion trap". Journal of Physics G: Nuclear and Particle Physics, volume 28 (2002) (6), 1325. URL http://stacks.iop.org/0954-3899/28/i=6/a=314.

[BM94] S. Balashov and Y. Mostovoy. Preprint IAE-5718/2 (1994).

[Bor10] M. Borg. The electron antineutrino angular correlation coefficient a in free neutron decay: Testing the standard model with the aSPECT-spectrometer. Ph.D. thesis, Johannes Gutenberg-Universität Mainz (2010).

[Bow05] J. Bowman. "On the measurement of the electron-neutrino correlation in neutron beta decay". Journal of Research of the National Institute of Standards and Technology, volume 110 (2005) (4), 407. ISSN 1044-677X. URL http://dx.doi.org/10.6028/jres.110.061.

[BPT80] G. Beamson, H. Q. Porter and D. W. Turner. "The collimating and magnifying properties of a superconducting field photoelectron spectrometer". Journal of Physics E: Scientific Instruments, volume 13 (1980) (1), 64. URL http://stacks.iop.org/0022-3735/13/i=1/a=018.

[BR97] R. Brun and F. Rademakers. "ROOT - An object oriented data analysis framework". Nuclear Instruments & Methods in Physics Research Section A-Accelerators Spectrometers Detectors and Associated Equipment, volume 389 (1997) (1-2), 81–86. ISSN 0168-9002. URL http://root.cern.ch, 5th International Workshop on Software Engineering, Neural Nets, Genetic Algorithms, Expert Systems, Symbolic Algebra and Automatic Calculations in Physics Research (AIHENP 96), Lausanne, Switzerland, Sep 02-06, 1996.

[BTS+13] N. Bundaleski et al. "Influence of the patch field on work function measurements based on the secondary electron emission". Journal of Applied Physics, volume 113 (2013) (18), 183720. URL https://doi.org/10.1063/1.4804663.

[But08] J. C. Butcher. Numerical Methods for Ordinary Differential Equations, Second Edition (John Wiley & Sons, 2008), 2. ed. edition.

[BVB+10] Beck, M. et al. "Effect of a sweeping conductive wire on electrons stored in a Penning-like trap between the KATRIN spectrometers". Eur. Phys. J. A, volume 44 (2010) (3), 499–511. URL https://doi.org/10.1140/epja/i2010-10959-1.

[Cab63] N. Cabibbo. "Unitary Symmetry and Leptonic Decays". Phys. Rev. Lett., volume 10 (1963), 531–533. URL http://link.aps.org/doi/10.1103/PhysRevLett.10.531.

[CDMD+19] S. Capitani et al. "Isovector axial form factors of the nucleon in two-flavor lattice QCD". International Journal of Modern Physics A, volume 34 (2019) (02), 1950009. URL https://doi.org/10.1142/S0217751X1950009X.

[CMS18] A. Czarnecki, W. J. Marciano and A. Sirlin. "Neutron Lifetime and Axial Coupling Connection". Phys. Rev. Lett., volume 120 (2018), 202002. URL https://link.aps.org/doi/10.1103/PhysRevLett.120.202002.

[CNR+18] C. C. Chang et al. "A per-cent-level determination of the nucleon axial coupling from quantum chromodynamics". Nature, volume 558 (2018) (7708), 91–94. ISSN 1476-4687. URL http://dx.doi.org/10.1038/s41586-018-0161-8.

[Cor14] T. Corona. Methodology and Application of High Performance Electrostatic Field Simulation in the KATRIN Experiment. Ph.D. thesis, University of North Carolina, Chapel Hill, NC (2014).

[CRM13] V. Cirigliano and M. J. Ramsey-Musolf. "Low energy probes of physics beyond the standard model". Progress in Particle and Nuclear Physics, volume 71 (2013), 2 – 20. ISSN 0146-6410. URL http://www.sciencedirect.com/science/article/pii/S0146641013000215, fundamental Symmetries in the Era of the {LHC}.

[DBD+17] G. Darius et al. "Measurement of the Electron-Antineutrino Angular Correlation in Neutron β Decay". Phys. Rev. Lett., volume 119 (2017), 042502. URL https://link.aps.org/doi/10.1103/PhysRevLett.119.042502.

[Dob74] R. Dobrozemsky. "Production of a clean neutron gas for decay and scattering experiments". Nuclear Instruments and Methods, volume 118 (1974) (1), 1 – 37. ISSN 0029-554X. URL http://www.sciencedirect.com/science/article/pii/0029554X74906818.

[DS11] D. Dubbers and M. G. Schmidt. "The neutron and its role in cosmology and particle physics". Rev. Mod. Phys., volume 83 (2011), 1111–1171. URL http://link.aps.org/doi/10.1103/RevModPhys.83.1111.

[Dub91] D. Dubbers. "Particle physics with cold neutrons". Prog. Part. Nucl. Phys., volume 26 (1991), 173–252.

[FBP+16] Finlay, P. et al. "First high-statistics and high-resolution recoil-ion data from the WITCH retardation spectrometer". Eur. Phys. J. A, volume 52 (2016) (7), 206. URL https://doi.org/10.1140/epja/i2016-16206-y.

[Fer34] E. Fermi. "Versuch einer Theorie der β-Strahlen. I". Zeitschrift für Physik, volume 88 (1934) (3), 161–177. ISSN 0044-3328. URL https://doi.org/10.1007/BF01351864.

[FGM58] R. P. Feynman and M. Gell-Mann. "Theory of the Fermi Interaction". Phys. Rev., volume 109 (1958), 193–198. URL https://link.aps.org/doi/10.1103/PhysRev.109.193.

[FGT+17] D. Furse et al. "Kassiopeia: a modern, extensible C++ particle tracking package". New Journal of Physics, volume 19 (2017) (5), 053012. URL http://stacks.iop.org/1367-2630/19/i=5/a=053012.

[FGV+14] F. M. Fränkle et al. "Penning discharge in the KATRIN pre-spectrometer". Journal of Instrumentation, volume 9 (2014) (07), P07028. URL http://stacks.iop.org/1748-0221/9/i=07/a=P07028.

[FLC+12] J. A. Formaggio et al. "SOLVING FOR MICRO- AND MACRO-SCALE ELECTROSTATIC CONFIGURATIONS USING THE ROBIN HOOD ALGORITHM". Progress In Electromagnetics Research B, volume 39 (2012), 1–37. ISSN 1937-6472. URL http://dx.doi.org/10.2528/PIERB11112106.

[Fur15] D. L. Furse. Techniques for direct neutrino mass measurement utilizing tritium β-decay. Ph.D. thesis, Massachusetts Institute of Technology (2015).

[GAC16] M. González-Alonso and J. M. Camalich. "Global effective-field-theory analysis of new-physics effects in (semi)leptonic kaon decays". Journal of High Energy Physics, volume 2016 (2016) (12). ISSN 1029-8479. URL http://dx.doi.org/10.1007/JHEP12(2016)052.

[GANCS19] M. González-Alonso, O. Naviliat-Cuncic and N. Severijns. "New physics searches in nuclear and neutron β decay". Progress in Particle and Nuclear Physics, volume 104 (2019), 165 – 223. ISSN 0146-6410. URL http://www.sciencedirect.com/science/article/pii/S0146641018300735.

[Gar63] M. W. Garrett. "Calculation of Fields, Forces, and Mutual Inductances of Current Systems by Elliptic Integrals". Journal of Applied Physics, volume 34 (1963) (9), 2567–2573. URL https://doi.org/10.1063/1.1729771.

[GBB+05] F. Glück et al. "The neutron decay retardation spectrometer aSPECT: Electromagnetic design and systematic effects". European Physical Journal A, volume 23 (2005) (1), 135–146. ISSN 1434-6001.

[GCP06] L. Giordano, F. Cinquini and G. Pacchioni. "Tuning the surface metal work function by deposition of ultrathin oxide films: Density functional calculations". Phys. Rev. B, volume 73 (2006), 045414. URL https://link.aps.org/doi/10.1103/PhysRevB.73.045414.

[GDL+13] F. Glück et al. "Electromagnetic design of the large-volume air coil system of the KATRIN experiment". New Journal of Physics, volume 15 (2013) (8), 083025. URL http://stacks.iop.org/1367-2630/15/i=8/a=083025.

[GGS58] M. Goldhaber, L. Grodzins and A. W. Sunyar. "Helicity of Neutrinos". Phys. Rev., volume 109 (1958), 1015–1017. URL https://link.aps.org/doi/10.1103/PhysRev.109.1015.

[GGVN68] V. K. Grigoriev et al. "Measurement of Angular $(e,\overline{\nu})$ Correlation at Free Neutron Decay". Sov. J. Nucl. Phys., volume 6 (1968), 239.

[GJL95] F. Glück, I. Joo and J. Last. "Measurable parameters of neutron decay". Nuclear Physics A, volume 593 (1995) (2), 125 – 150. ISSN 0375-9474. URL http://www.sciencedirect.com/science/article/pii/0375947495003544.

[GJY+18] R. Gupta et al. "Isovector charges of the nucleon from $2+1+1$-flavor lattice QCD". Phys. Rev. D, volume 98 (2018), 034503. URL https://link.aps.org/doi/10.1103/PhysRevD.98.034503.

[Gla61] S. L. Glashow. "Partial-symmetries of weak interactions". Nuclear Physics, volume 22 (1961) (4), 579 – 588. ISSN 0029-5582. URL http://www.sciencedirect.com/science/article/pii/0029558261904692.

[GLG16] P. G. Geoffrey L. Greene. "The neutron enigma". Scientific American, volume 314 (2016) (4), 36–41.

[Glü93] F. Glück. "Measurable distributions of unpolarized neutron decay". Physical Review D, volume 47 (1993) (7), 2840–2848.

[Glu11] F. Gluck. "AXISYMMETRIC MAGNETIC FIELD CALCULATION WITH ZONAL HARMONIC EXPANSION". Progress In Electromagnetics Research B, volume 32 (2011), 351–388. ISSN 1937-6472. URL http://dx.doi.org/10.2528/PIERB11042108.

[Gro15] S. Groh. Modeling of the response function and measurement of transmission properties of the KATRIN experiment. Ph.D. thesis, Karlsruher Instituts für Technologie (2015).

[GS63] B. Girard and M. Sauzade. "Calcul des solenoides compenses du 6éme ordre a volume de bobinage minimum". Nuclear Instruments and Methods, volume 25 (1963), 269 – 284. ISSN 0029-554X. URL http://www.sciencedirect.com/science/article/pii/0029554X63901988.

[GT36] G. Gamow and E. Teller. "Selection Rules for the β-Disintegration". Phys. Rev., volume 49 (1936), 895–899. URL http://link.aps.org/doi/10.1103/PhysRev.49.895.

[Gua11] F. A. Guardia. Characterization of electromagnetic fields in the aSPECT spectrometer and reduction of systematic errors. Ph.D. thesis, Johannes Gutenberg-Universität Mainz (2011).

[Hah70] T. A. Hahn. "Thermal Expansion of Copper from 20 to 800 K—Standard Reference Material 736". Journal of Applied Physics, volume 41 (1970) (13), 5096–5101. ISSN 1089-7550. URL http://dx.doi.org/10.1063/1.1658614.

[Hay12] W. Haynes. CRC Handbook of Chemistry and Physics, 93rd Edition. CRC Handbook of Chemistry and Physics (Taylor & Francis, 2012). ISBN 9781439880494.

[Hil17] D. F. R. Hilk. Electric field simulations and electric dipole investigations at the KATRIN main spectrometer. Ph.D. thesis, Karlsruher Institut für Technologie (KIT) (2017).

[HKH+04] C. D. Hoyle et al. "Submillimeter tests of the gravitational inverse-square law". Phys. Rev. D, volume 70 (2004), 042004. URL https://link.aps.org/doi/10.1103/PhysRevD.70.042004.

[Hor11] R. M. Horta. First measurements of the aSPECT spectrometer. Ph.D. thesis, Johannes Gutenberg-Universität Mainz (2011).

[HSW79] J. Hölzl, F. K. Schulte and H. Wagner. Solid surface physics. Springer tracts in modern physics (Springer, Berlin, 1979). URL https://cds.cern.ch/record/445669.

[HT15] J. C. Hardy and I. S. Towner. "Superallowed $0^+ \to 0^+$ nuclear β decays: 2014 critical survey, with precise results for V_{ud} and CKM unitarity". Phys. Rev. C, volume 91 (2015), 025501. URL http://link.aps.org/doi/10.1103/PhysRevC.91.025501.

[Jac98] J. Jackson. Classical electrodynamics (Wiley, 1998), 3 edition.

[JTW57] J. Jackson, S. Treiman and H. Wyld. "Coulomb corrections in allowed beta transitions". Nuclear Physics, volume 4 (1957), 206 – 212. ISSN 0029-5582. URL http://www.sciencedirect.com/science/article/pii/0029558287900198.

[KD03] J. Kyte and J. Dennison. "Electron emission cross sections from a polycrystalline gold surface". In "Proceedings of the 9th Rocky Mountain NASA Space Grant Consortium Symposium", (Salt Lake City, Utah, 2003).

[KGB+14] G. Konrad et al. "The magnetic shielding for the neutron decay spectrometer aSPECT". Nuclear Instruments and Methods in Physics Research Section A: Accelerators, Spectrometers, Detectors and Associated Equipment, volume 767 (2014), 475 – 486. ISSN 0168-9002. URL http://www.sciencedirect.com/science/article/pii/S0168900214010109.

[KHB+10] G. KONRAD et al. "IMPACT OF NEUTRON DECAY EXPERIMENTS ON NON-STANDARD MODEL PHYSICS". In "Physics Beyond the Standard Models of Particles, Cosmology and Astrophysics", pages 660–672 (2010). URL https://www.worldscientific.com/doi/abs/10.1142/9789814340861_0061.

[KM73] M. Kobayashi and T. Maskawa. "CP-Violation in the Renormalizable Theory of Weak Interaction". Progress of Theoretical Physics, volume 49 (1973) (2), 652–657. ISSN 0033-068X. URL https://doi.org/10.1143/PTP.49.652.

[Kon11] G. E. Konrad. Measurement of the proton recoil spectrum in neutron beta decay with the spectrometer aSPECT : study of systematic effects. Ph.D. thesis, Universität Mainz (2011). URL http://tocs.ub.uni-mainz.de/pdfs/290221056.pdf, enth. dt. und engl. Zsfassung.

[KSB+05] M. Kreuz et al. "A measurement of the antineutrino asymmetry B in free neutron decay". Physics Letters B, volume 619 (2005) (3), 263 – 270. ISSN

0370-2693. URL http://www.sciencedirect.com/science/article/pii/S0370269305007598.

[Leo94] W. Leo. Techniques for Nuclear and Particle Physics Experiments: A How-to Approach (Springer, 1994). ISBN 9780387572802.

[LKS+03] T. C. Leung et al. "Relationship between surface dipole, work function and charge transfer: Some exceptions to an established rule". Phys. Rev. B, volume 68 (2003), 195408. URL https://link.aps.org/doi/10.1103/PhysRevB.68.195408.

[LS85] V. Lobashev and P. Spivak. "A method for measuring the electron antineutrino rest mass". Nuclear Instruments and Methods in Physics Research Section A: Accelerators, Spectrometers, Detectors and Associated Equipment, volume 240 (1985) (2), 305 – 310. ISSN 0168-9002. URL http://www.sciencedirect.com/science/article/pii/0168900285906400.

[LŠA06] P. Lazić, H. Štefančić and H. Abraham. "The Robin Hood method – A novel numerical method for electrostatic problems based on a non-local charge transfer". Journal of Computational Physics, volume 213 (2006) (1), 117 – 140. ISSN 0021-9991. URL http://www.sciencedirect.com/science/article/pii/S0021999105003712.

[LŠA08] P. Lazić, H. Štefančić and H. Abraham. "The Robin Hood method—A new view on differential equations". Engineering Analysis with Boundary Elements, volume 32 (2008) (1), 76 – 89. ISSN 0955-7997. URL http://www.sciencedirect.com/science/article/pii/S0955799707001026.

[LSK+97] P. Liaud et al. "The measurement of the beta asymmetry in the decay of polarized neutrons". Nuclear Physics A, volume 612 (1997) (1), 53 – 81. ISSN 0375-9474. URL http://www.sciencedirect.com/science/article/pii/S0375947496003259.

[LY56] T. D. Lee and C. N. Yang. "Question of Parity Conservation in Weak Interactions". Phys. Rev., volume 104 (1956), 254–258. URL http://link.aps.org/doi/10.1103/PhysRev.104.254.

[LYD+18] J. Liang et al. "Quark spins and anomalous Ward identity". Phys. Rev. D, volume 98 (2018), 074505. URL https://link.aps.org/doi/10.1103/PhysRevD.98.074505.

[Mai14] R. Maisonobe. Measurement of the angular correlation coefficient a between electron and antineutrino in neutron β-decay with the spectrometer aSPECT. Ph.D. thesis, Universite de Grenoble (2014).

[MGK+06] A. Mann et al. "A Sampling ADC Data Acquisition System for Positron Emission Tomography". IEEE Transactions on Nuclear Science, volume 53 (2006) (1), 297.

[MHP+07] A. Müller et al. "PAFF, a low-energy, low-flux proton accelerator for detector tests". Nuclear Instruments and Methods in Physics Research Section A: Accelerators, Spectrometers, Detectors and Associated Equipment, volume 582 (2007) (2), 395 – 400. ISSN 0168-9002. URL http://www.sciencedirect.com/science/article/pii/S0168900207019559.

[MKS+01] Y. A. Mostovoi et al. "Experimental value of GA/GV from a measurement of both P-odd correlations in free-neutron decay". Physics of Atomic Nuclei, volume 64 (2001) (11), 1955–1960. ISSN 1562-692X. URL https://doi.org/10.1134/1.1423745.

[MMD+13] D. Mund et al. "Determination of the Weak Axial Vector Coupling $\lambda = g_A/g_V$ from a Measurement of the β-Asymmetry Parameter A in Neutron Beta Decay". Phys. Rev. Lett., volume 110 (2013), 172502. URL https://link.aps.org/doi/10.1103/PhysRevLett.110.172502.

[MMS+18] B. Märkisch et al. "Measurement of the Weak Axial-Vector Coupling Constant in the Decay of Free Neutrons Using a Pulsed Cold Neutron Beam". arXiv e-prints, (2018), arXiv:1812.04666.

[mog19] "High performance computing Johannes Guternberg-Universität Mainz" (2019). URL https://hpc.uni-mainz.de.

[M.R98] L. K. G. D. L. F. M.R.I. "V. Contact electricity of metals". The London, Edinburgh, and Dublin Philosophical Magazine and Journal of Science, volume 46 (1898) (278), 82–120. URL https://doi.org/10.1080/14786449808621172.

[MS06] W. J. Marciano and A. Sirlin. "Improved Calculation of Electroweak Radiative Corrections and the Value of V_{ud}". Phys. Rev. Lett., volume 96 (2006), 032002. URL https://link.aps.org/doi/10.1103/PhysRevLett.96.032002.

[MY12] S. Mugo and J. Yuan. "Influence of Surface Adsorption on Work Function Measurements on Gold-Platinum Interface Using Scanning Kelvin Probe Microscopy". Journal of Physics: Conference Series, volume 371 (2012), 012030. URL https://doi.org/10.1088%2F1742-6596%2F371%2F1%2F012030.

[Nor61] T. G. Northrop. "The guiding center approximation to charged particle motion". Annals of Physics, volume 15 (1961) (1), 79 – 101. ISSN 0003-4916. URL http://www.sciencedirect.com/science/article/pii/0003491661901671.

[OHM+18] K. Ottnad et al. "Nucleon charges and quark momentum fraction with $N_f=2+1$ Wilson fermions". arXiv e-prints, (2018), arXiv:1809.10638.

[PAA+09] D. Pocanic et al. "Nab: Measurement principles, apparatus and uncertainties". Nuclear Instruments and Methods in Physics Research Section A: Accelerators, Spectrometers, Detectors and Associated Equipment, volume 611 (2009) (2–3), 211 – 215. ISSN 0168-9002. URL http://www.sciencedirect.com/science/article/pii/S0168900209015289, particle Physics with Slow Neutrons.

[PB72] M. R. Pinnel and J. E. Bennett. "Mass diffusion in polycrystalline copper/-electroplated gold planar couples". Metallurgical and Materials Transactions B, volume 3 (1972) (7), 1989–1997. ISSN 1543-1916. URL https://doi.org/10.1007/BF02642589.

[PBB+92] A. Picard et al. "A solenoid retarding spectrometer with high resolution and transmission for keV electrons". Nuclear Instruments and Methods in Physics Research Section B: Beam Interactions with Materials and Atoms, volume 63 (1992) (3), 345–358. ISSN 0168-583X. URL http://www.sciencedirect.com/science/article/pii/0168583X9295119C.

[PGG09] Padovani, M., Galli, D. and Glassgold, A. E. "Cosmic-ray ionization of molecular clouds". A&A, volume 501 (2009) (2), 619–631. URL https://doi.org/10.1051/0004-6361/200911794.

[Pin79] M. R. Pinnel. "Diffusion-related behaviour of gold in thin film systems". Gold Bulletin, volume 12 (1979) (2), 62–71. ISSN 2190-7579. URL https://doi.org/10.1007/BF03216542.

[PRMT07] S. Profumo, M. J. Ramsey-Musolf and S. Tulin. "Supersymmetric contributions to weak decay correlation coefficients". Phys. Rev. D, volume 75 (2007), 075017. URL https://link.aps.org/doi/10.1103/PhysRevD.75.075017.

[RD77] L. Reimer and H. Drescher. "Secondary electron emission of 10-100 keV electrons from transparent films of Al and Au". Journal of Physics D: Applied Physics, volume 10 (1977) (5), 805. URL http://stacks.iop.org/0022-3727/10/i=5/a=022.

[RL15] R. Rahemi and D. Li. "Variation in electron work function with temperature and its effect on the Young's modulus of metals". Scripta Materialia, volume 99 (2015), 41 – 44. ISSN 1359-6462. URL http://www.sciencedirect.com/science/article/pii/S135964621400493X.

[Sal68] A. Salam. "Weak and Electromagnetic Interactions". Conf. Proc., volume C680519 (1968), 367–377.

[SBNC06] N. Severijns, M. Beck and O. Naviliat-Cuncic. "Tests of the standard electroweak model in nuclear beta decay". Rev. Mod. Phys., volume 78 (2006), 991–1040. URL http://link.aps.org/doi/10.1103/RevModPhys.78.991.

[SDW78] C. Stratowa, R. Dobrozemsky and P. Weinzierl. "Ratio $|\frac{g_A}{g_V}|$ derived from the proton spectrum in free-neutron decay". Phys. Rev. D, volume 18 (1978), 3970–3979. URL http://link.aps.org/doi/10.1103/PhysRevD.18.3970.

[SGB+09] M. Simson et al. "Measuring the proton spectrum in neutron decay—Latest results with aSPECT". Nuclear Instruments and Methods in Physics Research Section A: Accelerators, Spectrometers, Detectors and Associated Equipment, volume 611 (2009) (2), 203 – 206. ISSN 0168-9002. URL http://www.sciencedirect.com/science/article/pii/S0168900209015265, particle Physics with Slow Neutrons.

[SHM+07] M. Simson et al. "Detection of low-energy protons using a silicon drift detector". Nuclear Instruments and Methods in Physics Research Section A: Accelerators, Spectrometers, Detectors and Associated Equipment, volume 581 (2007) (3), 772 – 775. ISSN 0168-9002. URL http://www.sciencedirect.com/science/article/pii/S0168900207018608.

[Sim10] M. Simson. Measurement of the electron antineutrino angular correlation coefficient a with the neutron decay spectrometer aSPECT. Dissertation, Technische Universitaet Muenchen, Muenchen (2010).

[SKD+08] M. Schumann et al. "Measurement of the Proton Asymmetry Parameter in Neutron Beta Decay". Phys. Rev. Lett., volume 100 (2008), 151801. URL https://link.aps.org/doi/10.1103/PhysRevLett.100.151801.

[SKD+17] M. Sasao et al. "Negative ion formation by proton reflection from a molybdenum surface at a shallow incidence angle". AIP Conference Proceedings, volume 1869 (2017) (1), 020008. URL https://aip.scitation.org/doi/abs/10.1063/1.4995714.

[SML06] W. J. Schroeder, K. Martin and W. E. Lorensen. The visualization toolkit (Kitware, Clifton Park, NY, 2006), 4. ed. edition. ISBN 1-930934-19-X and 978-1-930934-19-1.

[SSS68] G. B. Scott, M. Springford and J. R. Stockton. "Use of a magnetoresistor to measure the magnetic field in a superconducting magnet". Journal of Physics E: Scientific Instruments, volume 1 (1968) (9), 925. URL http://stacks.iop.org/0022-3735/1/i=9/a=309.

[SVK+05] A. Serebrov et al. "Measurement of the neutron lifetime using a gravitational trap and a low-temperature Fomblin coating". Physics Letters B, volume 605 (2005) (1), 72 – 78. ISSN 0370-2693. URL http://www.sciencedirect.com/science/article/pii/S0370269304015552.

[TAB+13] K. Tullney et al. "Constraints on Spin-Dependent Short-Range Interaction between Nucleons". Phys. Rev. Lett., volume 111 (2013), 100801. URL https://link.aps.org/doi/10.1103/PhysRevLett.111.100801.

[TBC+13] V. Tishchenko et al. "Detailed report of the MuLan measurement of the positive muon lifetime and determination of the Fermi constant". Phys. Rev. D, volume 87 (2013), 052003. URL http://link.aps.org/doi/10.1103/PhysRevD.87.052003.

[THH+18] M. Tanabashi et al. "Review of Particle Physics". Phys. Rev. D, volume 98 (2018), 030001. URL https://link.aps.org/doi/10.1103/PhysRevD.98.030001.

[TP76] H. G. Tompkins and M. R. Pinnel. "Low temperature diffusion of copper through gold". Journal of Applied Physics, volume 47 (1976) (9), 3804–3812. URL https://doi.org/10.1063/1.323265.

[VWT15] K. K. Vos, H. W. Wilschut and R. G. E. Timmermans. "Symmetry violations in nuclear and neutron β decay". Rev. Mod. Phys., volume 87 (2015), 1483–1516. URL https://link.aps.org/doi/10.1103/RevModPhys.87.1483.

[WAH+57] C. S. Wu et al. "Experimental Test of Parity Conservation in Beta Decay". Phys. Rev., volume 105 (1957), 1413–1415. URL http://link.aps.org/doi/10.1103/PhysRev.105.1413.

[WBC+09] F. Wietfeldt et al. "aCORN: An experiment to measure the electron–antineutrino correlation in neutron decay". Nuclear Instruments and Methods in Physics Research Section A: Accelerators, Spectrometers, Detectors and Associated Equipment, volume 611 (2009) (2–3), 207 – 210. ISSN 0168-9002. URL http://www.sciencedirect.com/science/article/pii/S0168900209015277, particle Physics with Slow Neutrons.

[WBD+18] F. E. Wietfeldt et al. "Measurement of the electron-antineutrino correlation in neutron beta decay: aCORN experiment". arXiv e-prints, (2018), arXiv:1810.00857.

[Wei67] S. Weinberg. "A Model of Leptons". Phys. Rev. Lett., volume 19 (1967), 1264–1266. URL http://link.aps.org/doi/10.1103/PhysRevLett.19.1264.

[WF72] R. L. Wells and T. Fort. "Adsorption of water on clean gold by measurement of work function changes". Surface Science, volume 32 (1972) (3), 554 – 560. ISSN 0039-6028. URL http://www.sciencedirect.com/science/article/pii/0039602872901823.

[WG11] F. E. Wietfeldt and G. L. Greene. "Colloquium: The neutron lifetime". Rev. Mod. Phys., volume 83 (2011), 1173–1192. URL https://link.aps.org/doi/10.1103/RevModPhys.83.1173.

[Wun16] A. G. Wunderle. Precision Measurement of the $\beta - \overline{\nu}_e$ angular correlation coefficient a in free neutron decay. Ph.D. thesis, Johannes Gutenberg-Universität Mainz (2016).

[Yer04] B. Yerozolimsky. "New Approaches to Investigations of the Angular Correlations in Neutron Decay". arXiv e-prints, (2004), nucl-ex/0401014.

[YKMS97] B. Yerozolimsky et al. "Corrigendum: Corrected value of the beta-emission asymmetry in the decay of polarized neutrons measured in 1990". Physics Letters B, volume 412 (1997) (3), 240 – 241. ISSN 0370-2693. URL http://www.sciencedirect.com/science/article/pii/S0370269397010046.

[YSH+08] J.-S. Yoon et al. "Cross Sections for Electron Collisions with Hydrogen Molecules". Journal of Physical and Chemical Reference Data, volume 37 (2008) (2), 913–931. URL https://doi.org/10.1063/1.2838023.

[ZBvdG+00] O. Zimmer et al. ""aspect" – a new spectrometer for the measurement of the angular correlation coefficient a in neutron beta decay". Nuclear Instruments and Methods in Physics Research Section A: Accelerators, Spectrometers, Detectors and Associated Equipment, volume 440 (2000) (3), 548 – 556. ISSN 0168-9002. URL http://www.sciencedirect.com/science/article/pii/S0168900299010359.

[Zis32] W. A. Zisman. "A NEW METHOD OF MEASURING CONTACT POTENTIAL DIFFERENCES IN METALS". Review of Scientific Instruments, volume 3 (1932) (7), 367–370. URL https://doi.org/10.1063/1.1748947.

[ZZB10] J. F. Ziegler, M. Ziegler and J. Biersack. "SRIM – The stopping and range of ions in matter (2010)". Nuclear Instruments and Methods in Physics Research Section B: Beam Interactions with Materials and Atoms, volume 268 (2010) (11), 1818 – 1823. ISSN 0168-583X. URL http://www.

sciencedirect.com/science/article/pii/S0168583X10001862, 19th International Conference on Ion Beam Analysis.